

**DOE-ER-0313/40  
Distribution  
Categories  
UC-423, -424**

**FUSION MATERIALS  
SEMIANNUAL PROGRESS REPORT  
FOR THE PERIOD ENDING  
June 30, 2006**

**Prepared for  
DOE Office of Fusion Energy Sciences  
(AT 60 20 10 0)**

**DATE PUBLISHED: September 2006**

**Prepared for  
OAK RIDGE NATIONAL LABORATORY  
Oak Ridge, Tennessee 37831  
Managed by  
UT-Battelle, LLC  
For the  
U.S. DEPARTMENT OF ENERGY**

## FOREWORD

This is the fortieth in a series of semiannual technical progress reports on fusion materials science activities supported by the Fusion Energy Sciences Program of the U.S. Department of Energy. This report focuses on research addressing the effects on materials properties and performance from exposure to the neutronic, thermal, and chemical environments anticipated in the chambers of fusion experiments and energy systems. This research is a major element of the national effort to establish the materials knowledge base of an economically and environmentally attractive fusion energy source. Research activities on issues related to the interaction of materials with plasmas are reported separately.

The results reported are the product of a national effort involving a number of national laboratories and universities. A large fraction of this work, particularly in relation to fission reactor irradiations, is carried out collaboratively with partners in Japan, Russia, and the European Union. The purpose of this series of reports is to provide a working technical record for the use of program participants, and to provide a means of communicating the efforts of fusion materials scientists to the broader fusion community, both nationally and worldwide.

This report has been compiled and edited under the guidance of R. L. Klueh and Teresa Roe, Oak Ridge National Laboratory. Their efforts, and the efforts of the many persons who made technical contributions, are gratefully acknowledged.

G. R. Nardella  
Research Division  
Office of Fusion Energy Sciences



## TABLE OF CONTENTS

<b>1.0</b>	<b><i>VANADIUM ALLOYS</i></b>	<b>1</b>
<b>1.1</b>	<b>PROGRESS IN CONSTRUCTION OF A V-4CR-4TI THERMAL CONVECTION LOOP AND TEST FACILITY—B. A. Pint, S. J. Pawel, and J. L. Moser (Oak Ridge National Laboratory)</b>	<b>2</b>
	A vacuum chamber and ancillary equipment are being assembled for the experiment. A loop design has been formalized and V-4Cr-4Ti tubing has been received and examined prior to fabrication of the loop. Specimens and wire for the hot and cold leg have been fabricated. Specimens have been prepared for two layer MHD coatings at Lawrence Livermore National Laboratory.	
<b>2.0</b>	<b><i>CERAMIC COMPOSITE MATERIALS</i></b>	<b>6</b>
<b>2.1</b>	<b>IRRADIATION CREEP OF CHEMICALLY VAPOR DEPOSITED SILICON CARBIDE AS ESTIMATED BY BEND STRESS RELAXATION METHOD—Y. Katoh, L. L. Snead, S. Kondo (Oak Ridge National Laboratory), T. Hinoki, A. Kohyama (Kyoto University)</b>	<b>7</b>
	Bend stress relaxation technique was successfully applied for the study on irradiation creep of chemically vapor-deposited beta-phase silicon carbide (SiC) ceramics and vapor-infiltrated composites. Samples machined into thin strips were held within a curved gap in the silicon carbide fixture, and irradiated in High Flux Isotope Reactor at Oak Ridge National Laboratory and Japan Materials Test Reactor at Japan Atomic Energy Agency to the maximum neutron fluences of $0.74 \times 10^{25} \text{ n/m}^2$ ( $E > 0.1 \text{ MeV}$ ) at 400–1030°C. Irradiation creep strain for SiC exhibited weak temperature dependence in the temperature range studied. The creep strain appeared highly non-linear to neutron fluence due to the early domination of the initial transient irradiation creep. The transient creep was speculated to have caused by the rapid development of defect clusters and the structural relaxation of as-grown defects during early stages of irradiation damage accumulation. Steady-state irradiation creep compliance of SiC was conservatively estimated to be $2\text{--}3 \times 10^{-32} \text{ (MPa-n/m}^2\text{)}^{-1}$ at $\sim 600\text{--}\sim 1,100^\circ\text{C}$ . The observed smaller irradiation creep strains for the monocrystalline SiC and the uni-directional composites than for the polycrystalline SiC were attributed to differences in the transient creep strain.	
<b>3.0</b>	<b><i>FERRITIC/MARTENSITIC STEELS AND ODS STEELS</i></b>	<b>16</b>
<b>3.1</b>	<b>EVALUATION OF FRACTURE TOUGHNESS MASTER CURVE SHIFT OF JMTR IRRADIATED F82H USING SMALL SPECIMENS—T. Yamamoto, G. R. Odette, D. Gragg, W. J. Yang (University of California, Santa Barbara), H. Kurishita, H. Matsui, M. Narui, M. Yamazaki (Tohoku University, Japan)</b>	<b>17</b>

Small to ultra-small 1/3 size pre-cracked Charpy and 1.67 x 1.67 x 9.2 mm deformation and fracture minibeam (DFMB) specimens of the F82H IEA heat were irradiated to 0.02 and 0.12 dpa at 290°C in the Japanese Materials Test Reactor. Nominal cleavage transition temperature shifts, based on the measured toughness,  $K_{Jm}(T)$ , data ( $\Delta T_m$ ) as well as reference temperature shifts ( $\Delta T_o$ ) found after size-adjusting the  $K_{Jm}(T)$  data yielded  $\Delta T_{m/o} \approx 27 \pm 10$  and  $44 \pm 10$  at the two doses, respectively. Using measured yield stress changes ( $\Delta \sigma_y$ ), the  $C_o = \Delta T_o / \Delta \sigma_y = 0.58 \pm 0.14$  at 0.12 dpa, is in good agreement with data in the literature. The dynamic transition temperature shift,  $\Delta T_d$ , derived from DFMB tests, was  $\approx 30 \pm 20^\circ\text{C}$  at 0.1 dpa, also in good agreement with the estimated  $\Delta T_o$  shifts. The  $\Delta T_d$  and  $\Delta T_o$  are also in excellent agreement with a  $\Delta T_o = C_o \Delta \sigma_y(\text{dpa}, T_i)$  hardening-shift model, where the  $\Delta \sigma_y(\text{dpa}, T_i)$  was found by fitting a large database on tensile properties.

- 3.2 EFFECTS OF CONSOLIDATION TEMPERATURE, STRENGTH AND MICROSTRUCTURE ON FRACTURE TOUGHNESS OF NANOSTRUCTURED FERRITIC ALLOYS—P. Miao, G. R. Odette, T. Yamamoto (University of California, Santa Barbara), M. Alinger (University of California, Santa Barbara, University of California, Berkeley), D. Hoelzer (Oak Ridge National Laboratory), and D. Gragg (University of California, Santa Barbara)** **25**

Fully consolidated nanostructured ferritic alloys (NFAs) were prepared by attritor milling pre-alloyed Fe-14Cr-3W-0.4Ti and 0.3wt%  $Y_2O_3$  powders, followed by hot isostatic pressing (HIPing) at 1000°C and 1150°C and 200 MPa for 4 h. Transmission electron microscopy (TEM) revealed similar bimodal distributions of fine and coarse ferrite grains in both cases. However, as expected, the alloy microhardness decreased with increasing in HIPing temperature. Three point bend tests on single edge notched specimens, with a nominal root radius  $\rho = 0.15$  mm, were used to measure the notch fracture toughness,  $K_{Ic}$ , as a function of test temperature. The  $K_{Ic}$  curves were found to be similar for both alloys. It appears that the coarser ferrite grains control cleavage fracture, in a way that is independent of alloy strength and hiping temperature.

- 3.3 THE MICROSTRUCTURE AND STRENGTH PROPERTIES OF MA957 NANOSTRUCTURED FERRITIC ALLOY JOINTS PRODUCED BY FRICTION STIR AND ELECTRO-SPARK DEPOSITION WELDING—P. Miao, G. R. Odette (University of California, Santa Barbara), J. Gould, J. Bernath (Edison Welding Institute), R. Miller (DDL-OMNI), M. Alinger (University of California, Santa Barbara, University of California, Berkeley) and C. Zanis (DDL-OMNI)** **30**

The nanostructured ferritic alloy (NFA) MA957 was joined by friction stir welding (FSW) and electro-sparked deposition (ESD) welding. Transmission electron microscopy (TEM) and small angle neutron scatter (SANS) characterization studies showed a uniform fine-scale equiaxed ferrite structure with a high density of dislocations and only slightly coarsened nm-scale particles in the joint region of the FSW weld compared to the base metal. Microhardness and tensile measurements on the FSW showed a modest reduction in the strength of the joint compared to the as-processed MA957. In contrast, the ESD welds contained considerable porosity and the nm-scale particles dissolved or coarsened significantly, resulting in a larger degradation of the joint region strength. Thus FSW is a promising method for joining NFAs.

- 3.4 MECHANICAL PROPERTIES OF NEUTRON-IRRADIATED NICKEL-CONTAINING MARTENSITIC STEELS: I. EXPERIMENTAL STUDY—R. L. Klueh, N. Hashimoto, and M. A. Sokolov (Oak Ridge National Laboratory), K. Shiba and S. Jitsukawa (Japan Atomic Energy Research Institute)** **53**

The 9Cr-1MoVNb and 12Cr-1MoVW steels and these steels with 2% Ni additions were irradiated in HFIR to  $\approx 10$  dpa at 300°C and  $\approx 12$  dpa at 400°C and in FFTF to  $\approx 15$  dpa at 393°C. After irradiation in HFIR, steels with 2% Ni hardened more than steels without a nickel addition. When 9Cr-1MoVNb-2Ni, 12Cr-1MoVW, and 12Cr-1MoVW-2Ni steels were irradiated in HFIR at 400°C, they hardened more than when irradiated in FFTF at 393°C. The 9Cr-1MoVNb steel hardened to the same level in both FFTF and HFIR. For all but the 9Cr-1MoVNb steel, shifts in DBTT of the steels irradiated in HFIR were greater than shifts for the same steels irradiated in FFTF. Irradiation in HFIR at 300 and 400°C caused a larger shift for the steels containing 2% Ni than for the steels with no nickel addition. The increase in DBTT was related to the increase in yield stress. Despite the uncertainty inherent in the experiments, the results lead to the conclusion that helium caused an increment of hardening that contributed to the extra shift in DBTT over that observed after irradiation in FFTF where little helium formed.

**3.5 ON THE RELATION BETWEEN IRRADIATION INDUCED CHANGES IN THE MASTER CURVE REFERENCE TEMPERATURE SHIFT AND CHANGES IN STRAIN HARDENED FLOW STRESS—G. R. Odette, M. Y. He, and T. Yamamoto (University of California, Santa Barbara)**

69

Irradiation hardening produces increases in the cleavage transition fracture toughness reference temperature ( $\Delta T_o$ ). It is traditional to relate  $\Delta T_o$  to the corresponding changes in the yield stress,  $\Delta\sigma_y$ , as  $C_o = \Delta T_o / \Delta\sigma_y$ . However, it is a strain-hardened flow stress,  $\sigma_{fl}$ , in the fracture process zone that controls cleavage, rather than  $\sigma_y$ . Thus, irradiation induced decreases in the strain hardening  $\Delta\sigma_{sh}$  ( $< 0$ ) must be considered along with  $\Delta\sigma_y$  ( $> 0$ ) in evaluating  $\Delta T_o$ . The  $\Delta\sigma_{sh}$  in reactor pressure vessel (RPV) steels irradiated to low doses at around 300°C are small, even for large  $\Delta\sigma_y$ . However, the  $\Delta\sigma_{sh}$  are much greater for high dose irradiations of tempered martensitic steels (TMS) that are candidates for fusion applications. As a result, for the TMS case the  $C_o$  are less, and in some instances much less, than for RPV steels and irradiation conditions. We address two key questions. First, how does  $\Delta\sigma_{sh}$  influence the  $C_o = \Delta T_o / \Delta\sigma_y$  relation? Second, is it possible to derive a universal relation between  $\Delta T_o$  and  $\Delta\sigma_{fl}$  averaged over a pertinent range of  $\epsilon$ ,  $\langle \Delta\sigma_{fl} \rangle$ , such that a  $C_o' = \Delta T_o / \langle \Delta\sigma_{fl} \rangle$  is independent of the individual values of  $\Delta\sigma_y$  and  $\Delta\sigma_{sh}$ ? The results of this study suggest that  $\langle \Delta\sigma_{fl} \rangle$  averaged between 0 and 0.1 provides a similar  $C_o'$  for various assumptions about the effect of irradiation on  $\Delta\sigma_{sh}$ . Notably, changes in indentation hardness,  $\Delta H$ , are also directly related to this same  $\langle \Delta\sigma_{fl} \rangle$ . Hence, measurements of  $\Delta H$  should provide a good basis for assessing  $\Delta T_o$  for a wide range of alloys and irradiation conditions.

**3.6 ON THE INTRINSIC INITIATION AND ARREST CLEAVAGE FRACTURE TOUGHNESS OF FERRITE—M. L. Hribernik, G. R. Odette, and M. Y. He (University of California, Santa Barbara)**

74

The results of the crack arrest fracture toughness ( $K_a$ ) measurements on cleavage oriented Fe single crystals from -196 to 0°C are reported. Arrest measurements were performed on four low toughness cleavage orientations; (100)[010], (100)[011], (110)[001] and (110)[110]. Reliable and consistent measurements were obtained for the (100) cleavage planes, however inconsistent measurements were observed for the (110) planes as cleavage cracks always reverted back to the (100) planar orientation. The corresponding static ( $K_{ic}$ ) and dynamic ( $K_{id}$ ) cleavage initiation toughness for the (100) planes from -196 to 50°C were also measured over a range of applied stress intensity rates ( $\dot{K}$ ) from  $\approx 0.1$  to  $10^4$  MPa $\sqrt{m/s}$ . The  $K_{ia}(T)$ ,  $K_{ic}(T)$  and  $K_{id}(T)$  gradually increase with temperature from a minimum average  $K_{ia}$  value of approximately 4 MPa $\sqrt{m}$  up to a rapid BDT at  $\approx 0^\circ\text{C}$ . The BDT temperature increases with higher  $\dot{K}$ , and is highest for  $K_{ia}$ . The  $\dot{K}$  dependence of  $K_{ic/d}(T)$  is consistent with the strain rate dependence of thermally activated flow stress of Fe. The  $K_{ic}(T)$  for single crystal Fe and W are also reasonably similar when plotted on a homologous temperature scale. The  $K_{ia}(T)$  for Fe at  $\approx -40^\circ\text{C}$  is similar to that for Fe-3wt%Si at  $\approx 110^\circ\text{C}$ . This 150°C shift can be reasonably rationalized by the solid solution lattice strengthening of Si. The  $K_{ia}(T)$  for Fe must be shifted up by  $\approx 220^\circ\text{C}$  to approximate the temperature dependence of the  $K_{id}(T)$  that is consistent with a universal  $K_{ic}(T)$  master curve shape. This magnitude of shift may be caused by a combination of thermally activated (rate-dependent) solid solution lattice strengthening, complemented by long-range internal stress fields.

**3.7 SWELLING AND MICROSTRUCTURE OF PURE Fe AND Fe-Cr ALLOYS AFTER NEUTRON IRRADIATION TO ~26 DPA AT 400°C**—Yu V. Konobeev, A. M. Dvoriashin, S. I. Porollo (The Institute of Physics and Power Engineering, Russia), F. A. Garner (Pacific Northwest National Laboratory) **80**

The microstructures of pure Fe and various Fe-Cr binary alloys in both the annealed and heavily cold worked conditions were investigated after irradiation to 25.8 dpa at  $4 \times 10^{-7}$  dpa/s in the BR-10 fast reactor. Microscopy has shown that the largest swelling of 4.5% was observed in the cold worked pure iron while that of annealed Fe is only 1.7%. Additions of 2% chromium resulted in a decrease of swelling, but the swelling of cold worked Fe-2Cr alloy was still higher than that of the annealed condition. Independent of the initial starting condition, swelling in the Fe-6Cr alloy was completely suppressed. In alloys with higher chromium content swelling of 0.04–0.05% was observed only in samples irradiated in the annealed condition. There were also significant changes in dislocation and precipitate microstructure following irradiation.

**4.0 COPPER ALLOYS** **86**

*No contributions.*

**5.0 REFRACTORY METALS AND ALLOYS** **87**

*No contributions.*

**6.0 AUSTENITIC STAINLESS STEELS** **88**

**6.1 THE MECHANISM OF STRESS INFLUENCE ON SWELLING OF 20% COLD WORKED 16Cr15Ni2MoTiMnSi STEEL**—I. A. Portnykh, A. V. Kozlov, V. L. Panchenko (FSUE Institute of Nuclear Materials), V. M. Chernov (A. A. Bochvar Institute of Inorganic Materials), and F. A. Garner (Pacific Northwest National Laboratory) **89**

Argon-pressurized tubes of 20% cold-worked 16Cr15Ni2MoTiMnSi steel were irradiated at hoop stresses of 0, 100, and 200 MPa at ~740K in the BN-600 fast reactor to 108 dpa. Following nondestructive measurements of strain, density measurements and microscopy were conducted. Voids were categorized into three types depending on their association with other microstructural features. Stress enhanced the nucleation of all void types, but nucleation of voids associated with dislocations was increased the most. Swelling increased as a consequence, even though the average size of each type void decreases. Swelling measured by TEM and density change gave identical results.

**6.2 THE INFLUENCE OF COLD-WORK LEVEL ON THE IRRADIATION CREEP AND SWELLING OF AISI 316 STAINLESS STEEL IRRADIATED AS PRESSURIZED TUBES IN THE EBR-II FAST REACTOR**—E. R. Gilbert and F. A. Garner (Pacific Northwest National Laboratory) **95**

Pressurized tubes of AISI 316 stainless steel irradiated in the P-1 experiment in the EBR-II fast reactor have been measured to determine the dependence of irradiation-induced strains resulting from plastic deformation, irradiation creep, void swelling and precipitation. It is shown that the Soderberg relation predicting no axial creep strains in biaxially-loaded tubes is correct for both plastic and creep strains. Swelling strains are shown to be isotropically distributed both for stress-free and stress-affected swelling, while precipitation strains are somewhat anisotropic in their distribution. When corrected for stress-enhancement of swelling, the derived irradiation creep strains appear to be identical for both annealed and 20% cold-worked specimens, and also for tubes strained by rise to power increases in pressure. For relatively small creep strains it is often difficult to separate the creep and non-

creep components of deformation.

- 6.3 RECENT EXPERIMENTAL RESULTS ON NEUTRON-INDUCED VOID SWELLING OF AISI 304 STAINLESS STEEL CONCERNING ITS INTERACTIVE DEPENDENCE ON TEMPERATURE AND DISPLACEMENT RATE—F. A. Garner (Pacific Northwest National Laboratory), B. J. Makenas (Fluor Hanford Company) 104**

The objective of this effort is to explore the response of austenitic steels in diverse nuclear environments. Since light water reactors generate helium/dpa levels comparable to fusion devices, there is considerable overlap in relevance. In addition, the focus on AISI 304, while not of direct application to fusion devices, is useful because this simple steel does not have a very complicated phase evolution, allowing study of radiation-induced microstructural evolution without the complications associated with precipitation.

- 7.0 MHD INSULATORS, COATINGS, INSULATING CERAMICS, AND OPTICAL MATERIALS 115**

- 7.1 INVESTIGATION OF Pb-Li COMPATIBILITY FOR THE DUALCOOLANT TEST BLANKET MODULE—B. A. Pint and J. L. Moser (Oak Ridge National Laboratory) 116**

Static capsule tests in Pb-17Li were performed on coated and uncoated type 316 stainless steel and Al-containing alloys at 800°C and the Pb-Li was analyzed after each capsule test. Chemical vapor deposited (CVD) aluminide coatings on type 316 substrates reduced dissolution by ~50X at 800°C compared with uncoated samples. Little effect of pre-oxidation was observed for the performance of the coating. These results indicate that aluminide coatings may be a viable option to allow conventional Fe- or Ni-base tubing alloys to carry Pb-Li from the first wall to the heat exchanger. Future work will need to include testing in a flowing system with a thermal gradient to fully determine the compatibility of these materials. In order to test the viability of using a thermal convection loop made of quartz, a quartz ampoule was filled with Pb-Li and exposed for 1000h at 800°C. No Si was detected in the Pb-Li after the test indicating that quartz may be a low cost construction option.

- 8.0 BREEDING MATERIALS 120**

*No contributions.*

- 9.0 RADIATION EFFECTS, MECHANISTIC STUDIES, AND EXPERIMENTAL METHODS 121**

- 9.1 MODELLING THERMODYNAMICS OF ALLOYS FOR FUSION APPLICATION—A. Caro, M. Caro, J. Marian (Lawrence Livermore National Laboratory), E. Lopasso (Centro Atomico Bariloche, Argentina), and D. Crowson (Virginia Polytechnic Institute) 122**

Atomistic simulations of alloys at the empirical level face the challenge of correctly modeling basic thermodynamic properties. In this work we develop a methodology to generalize many-body classic potentials to incorporate complex formation energy curves. Application to Fe-Cr allows us to predict the implications of the ab initio results of formation energy on the phase diagram of this alloy and to get a detailed insight into the processes leading to precipitation of  $\alpha'$  phase under irradiation.

- 9.2 THERMAL HELIUM DESORPTION OF HELIUM-IMPLANTED IRON—D. Xu, T. Bus, S. C. Glade, and B. D. Wirth (University of California, Berkeley) 128**

Following the last report, we have performed new implantations at energies lower than 100 keV, with an aim of reducing the penetration depth of helium atoms and the structural damage, and thus reducing the He-point defect interaction complexity during desorption experiments. Initial measurements on the new samples have revealed a large number of

desorption peaks within both the bcc and fcc temperature ranges. These peaks are well fit with first order reaction kinetics, which reveal activation energies ranging from ~1.9 to ~3.5 eV. The number and the relative intensities of detected desorption peaks within the bcc temperature range appear to increase with decreasing implantation energy. Previously reported spurious peaks and a non-1st-order sharp peak are now better understood and described in the current report.

**9.3 HELIUM IN IRRADIATED IRON: A MULTI-SCALE STUDY—T. Seletskaya, Yu. N. Osetsky, R. E. Stoller, and G. M. Stocks (Oak Ridge National Laboratory) 140**

Helium is produced in neutron-irradiated metals as the result of (n,  $\alpha$ ) transmutation reactions and plays a significant role in microstructure evolution and mechanical properties degradation [1,2]. Due to helium's high mobility via an interstitial migration mechanism and its strong binding with vacancies, information on its atomistic behavior is hard to assess from experiments. The only way to obtain such information is from first-principles electronic structure calculations. However, electronic structure calculations can not be used on the time and size scales needed to simulate the important evolution of helium-vacancy clusters that ultimately leads to bubble formation. A multi-scale approach, based on constructing an empirical potential and employing this potential in classical molecular dynamics, seems to be the only practical approach currently available to study He behavior in metals on the desired scale.

**9.4 MODELING THE INTERACTION OF HELIUM WITH DISLOCATIONS AND GRAIN BOUNDARIES IN ALPHA-IRON—H. L. Heinisch, F. Gao, and R. J. Kurtz (Pacific Northwest National Laboratory) 147**

Molecular statics, molecular dynamics and the dimer method of potential surface mapping are being used to study the fate of helium in the vicinity of dislocations and grain boundaries in alpha-iron. Even at very low temperatures interstitial helium atoms can migrate to dislocations and grain boundaries, where they are strongly bound. The binding energies of helium to these microstructural features, relative to the perfect crystal, and the migration energies of helium diffusing within them have a strong correlation to the excess atomic volume that exists in these extended defects. Helium atom migration energies within the dislocations and grain boundaries studied are in the range of 0.4–0.5 eV. Helium “kick out” mechanisms have been identified within dislocations and grain boundaries by which interstitial helium atoms replace a Fe lattice atom, creating a stable He-vacancy complex that may be a nucleation site for a He bubble.

**10.0 DOSIMETRY, DAMAGE PARAMETERS, AND ACTIVATION CALCULATIONS 154**

*No contributions.*

**11.0 MATERIALS ENGINEERING AND DESIGN REQUIREMENTS 155**

*No contributions.*

**12.0 IRRADIATION FACILITIES AND TEST MATRICES 156**

**12.1 IRRADIATION OF FUSION MATERIALS IN THE BR2 REACTOR: THE FRISCO-F EXPERIMENT—E. Lucon (SCK•CEN) and M. A. Sokolov (Oak Ridge National Laboratory) 157**

Tensile and miniature Compact Tension specimens of eight high chromium steels of fusion relevance have been irradiated in the BR2 reactor in the framework of a collaborative project between Oak Ridge National Laboratory (ORNL) and SCK•CEN. All samples have been irradiated at a nominal temperature of 300°C in the in-pile section 2 (IPS-2) for five cycles (02/2005 to 01/2006) up to an average fast neutron fluence of 8.02

× 1020 n/cm<sup>2</sup> or 1.20 dpa. The rig was rotated three times by 180° in order to reduce the radial and azimuthal neutron flux gradients.

## **1.0 VANADIUM ALLOYS**

## **PROGRESS IN CONSTRUCTION OF A V-4CR-4TI THERMAL CONVECTION LOOP AND TEST FACILITY—B. A. Pint, S. J. Pawel, and J. L. Moser (Oak Ridge National Laboratory)**

### **OBJECTIVE**

The objective of this project is to operate a flowing Li experiment to test the Li compatibility in a thermal gradient of V-4Cr-4Ti and a multi-layer electrically-insulating coating needed to reduce the magneto hydrodynamic (MHD) force in the first wall of a lithium cooled blanket. The experiment is planned to start in January of 2007 and run for 1,000h at 750°C.

### **SUMMARY**

A vacuum chamber and ancillary equipment are being assembled for the experiment. A loop design has been formalized and V-4Cr-4Ti tubing has been received and examined prior to fabrication of the loop. Specimens and wire for the hot and cold leg have been fabricated. Specimens have been prepared for two layer MHD coatings at Lawrence Livermore National Laboratory.

### **PROGRESS AND STATUS**

#### **Introduction**

A self-cooled lithium blanket concept is attractive for a fusion reactor because of lithium's tritium breeding capability and excellent heat transfer characteristics. Due to compatibility issues at >500°C, vanadium alloys [1] are the most likely structural materials for this concept. One of the critical issues for this, and any liquid-metal concept, is the need to reduce the pressure drop associated with the magneto hydrodynamic (MHD) force due to the high magnetic field in the reactor [2,3]. One solution to the MHD problem is to apply an electrically insulating coating to decouple the structural wall from the liquid metal [4]. The coating must be thin, durable and have a high electrical resistivity. It also must be almost crack-free to prevent shorting [5,6]. The current focus of the U.S. program on reducing the MHD pressure drop is on durable multi-layer coatings or a flow-channel insert [7,8]. Both of these solutions have been previously proposed [4,9,10]; however, little experimental verification has been conducted. Both concepts rely on excellent compatibility of a relatively thin V or V alloy layer to prevent Li from contacting and degrading the insulating ceramic layer. Initial capsule and in-situ testing of multi-layer coatings have shown promising results [11]. However, a flowing Li test with a temperature gradient is needed to validate the compatibility of such thin layers. A brief summary of the vanadium-lithium compatibility literature [12] showed a wide range of results with no systematic study of the effects or relative importance of alloying elements and Li impurities. Ideally, a monometallic loop with relatively high purity Li and V specimens is needed to clarify the range of results found for V alloys in Li and preparations for a flowing Li thermal convection loop experiment are currently underway. The current plan is to run the loop for 1000h with a maximum temperature of 750°C beginning in January 2007. The loop will be destructively evaluated after the test with characterization completed by the end of March 2007.

#### **Results and Discussion**

A vacuum of  $\sim 10^{-6}$  Pa is needed to run a high temperature V-4Cr-4Ti loop to avoid excessive oxygen uptake, and subsequent embrittlement, by the vanadium alloy tubing during the experiment [13]. A vacuum chamber with control system has been delivered and installed and is undergoing initial test out at ORNL, Figure 1a. To reach the required vacuum, the entire chamber must be baked out requiring an insulating cover for the system, Figure 1b. The heating elements are located in the panel behind the chamber. The unit was tested to the specified vacuum at the manufacturer prior to

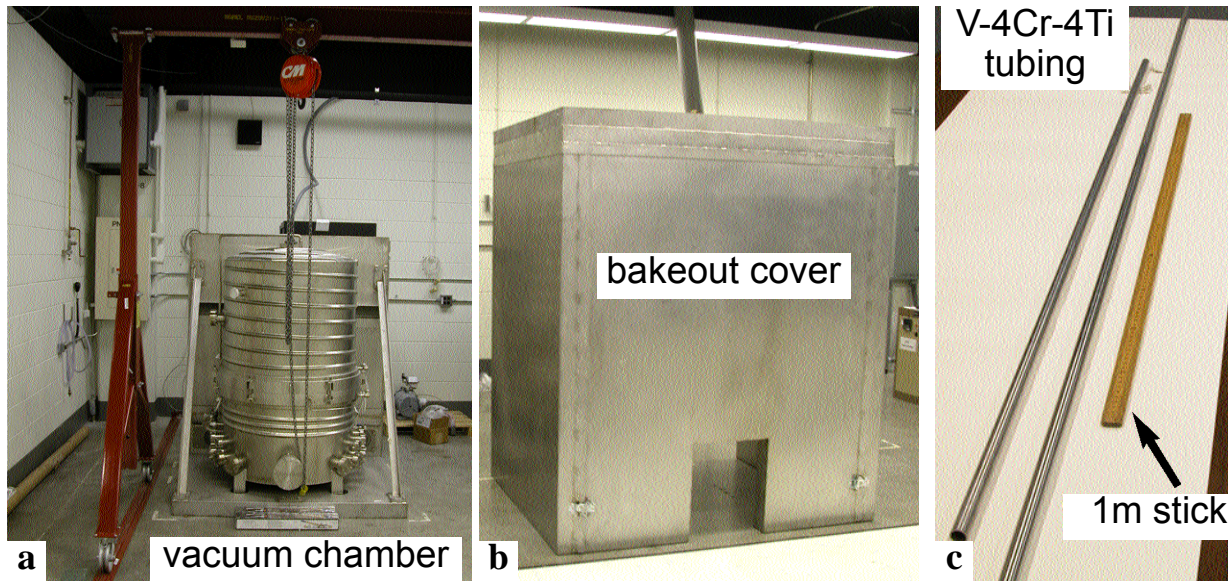


Figure 1. Photographs of (a) the vacuum chamber (base vacuum of  $<10^{-6}$ Pa) and overhead crane, (b) the bakeout furnace and (c) the V-4Cr-4Ti tubing.

shipment. A crane also has been installed to move the cover and raise the top of the chamber to install the loop. Three Mo heaters have been ordered. Two will heat the hot leg of the loop and the third will heat the Li in the fill tank to begin the experiment.

**Loop construction.** A simple loop design will be used. It was developed for a recently cancelled program and based on early ORNL designs. To construct the loop, V-4Cr-4Ti tubing and sheet are needed. Approximately 4 m of V-4Cr-4Ti tubing (19mm OD, 1.6mm wall thickness) was procured and delivered in March 2006. To qualify the material, the tubing first was visually examined and metallography was performed to examine defects. Figure 2a shows a representative longitudinal section of the tubing. The grain size was uniform across most of the thickness and only near the surface was the grain size small

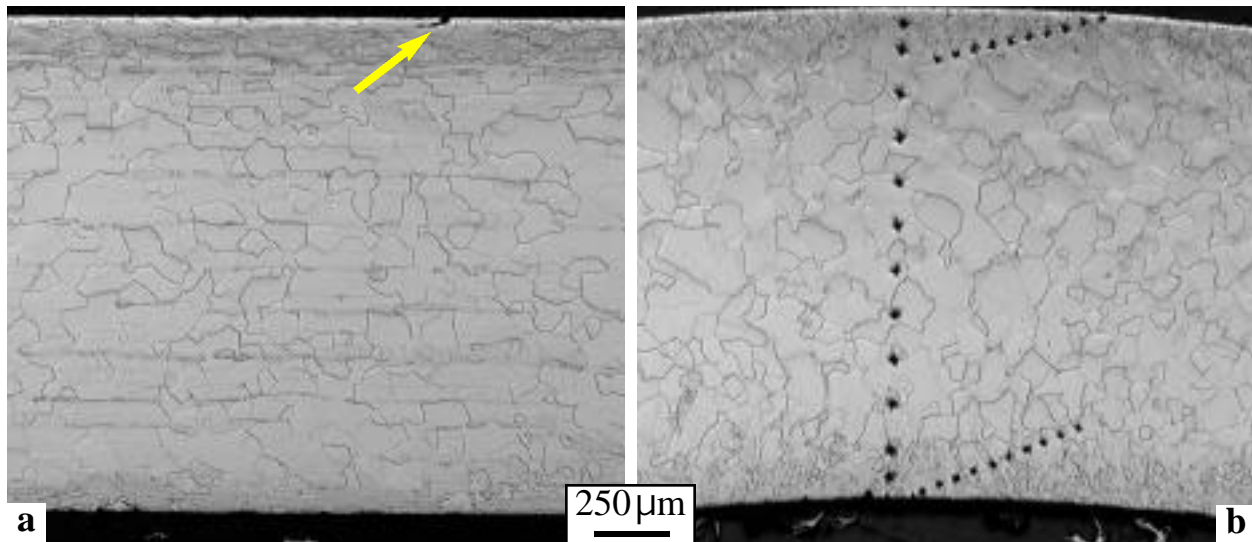


Figure 2. Light microscopy of the V-Cr-4Ti tubing (a) longitudinal section and (b) cross-section. A crack was observed in (a) and hardness tests are shown in (b). The etchant was  $60\text{H}_2\text{O}-30\text{HNO}_3-10\text{HF}$ .

and disturbed. There is some evidence of banding. A small crack is marked (arrow) on the outside surface. The effect of the structure gradient was measured by hardness testing. The hardness in the central, equiaxed grain portion is routinely  $H_V$  148-152. Near cracks the hardness increases to  $H_V$  165-172 while near both surfaces the hardness is typically  $H_V$  132-138.

One of the worst sections from visual examination was sectioned and deeper cracks were observed with the deepest (~52% of wall thickness) shown in Figure 3a. Finer grains and possibly some inclusions surround this crack. A more nominal depth for the flaws was 15-20% of the wall thickness, e.g., Figure 3b. Most cracks were not perpendicular to the outer surface. At the higher magnification in Figure 3b, the transgranular crack propagated through the fine-grained layer that was more heavily etched, perhaps indicating more precipitates. Also, a ~5 $\mu$ m surface layer (arrow) can be seen that has not been identified. The layer almost bridges the crack. Cracking also was observed on the inner diameter with the deepest being 12% of wall thickness but most only 1-2%, Figure 3c. Some of the wider, shallow cracks suggest "grain dropping" and were visible to the naked eye when the tubing was cut open.

The room temperature ductility was assessed by flattening sections of tubing in a bench vise. Defects in each section were placed perpendicular to the platens to place maximum tensile stress on the defects. In each case, the flaw opened cleanly but there was no indication of propagation and the remaining section was fully ductile. To further assess the overall tubing quality, a helium pressure test (690kPa, 100psig) was performed on each of the three tubing sections. Swagelok fittings were placed on each end of the entire tube length along with a pressure gage. The pressure remained steady and unchanged for 24h for all three tubes. The tubes are expected to contain a much lower pressure (~100kPa) so the as-received material appears to be adequate for loop construction. The final characterization planned is to use the tubing to make a capsule and perform a 1000h 800°C Li capsule test to ensure that the tubing has compatibility similar to the prior V alloy capsule tests performed at ORNL [7,14].

**Compatibility specimens.** Specimens of V-4Cr-4Ti to be placed in the hot and cold legs of the loop have been fabricated, Figure 4. Tensile specimens (SS-3 type) will be used in order to determine post-test mechanical properties along with 0.75mm thick tab or spacer specimens that center the specimen chain in the tube, top of Figure 4. Also, 0.75mm diameter V-4Cr-4Ti wire has been made to connect the loop specimens. Ten, 1mm thick spacer specimens were sent for coating using electron-beam physical vapor

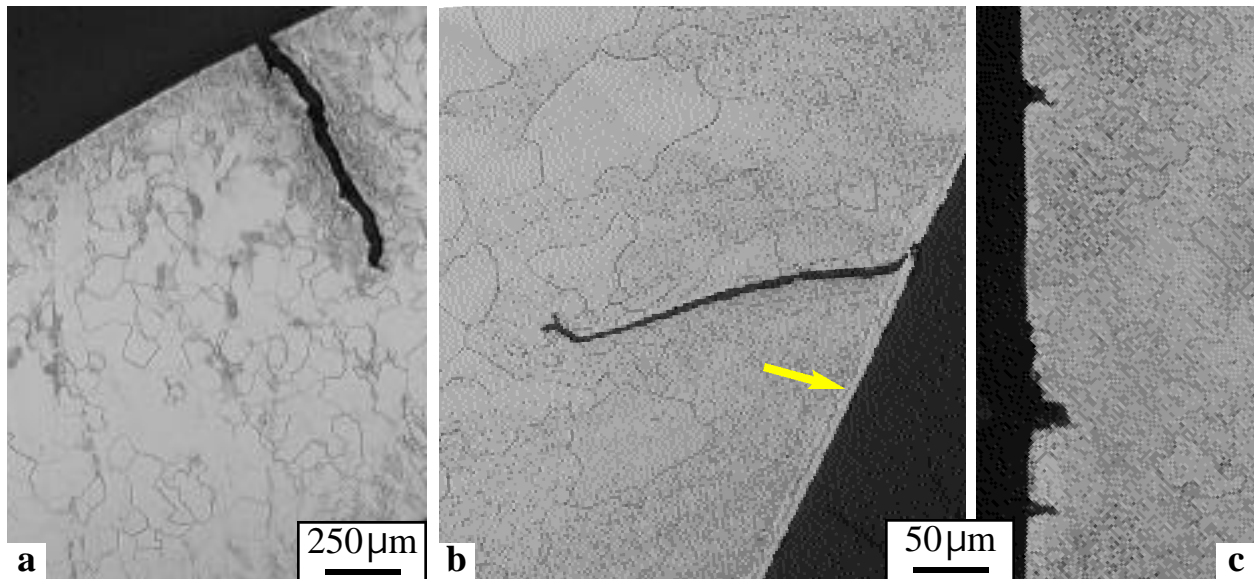


Figure 3. Light microscopy of cross-section of the V-Cr-4Ti tubing showing cracks on the (a,b) outer diameter and (c) inner diameter. Arrow in (b) marks unidentified outer layer.

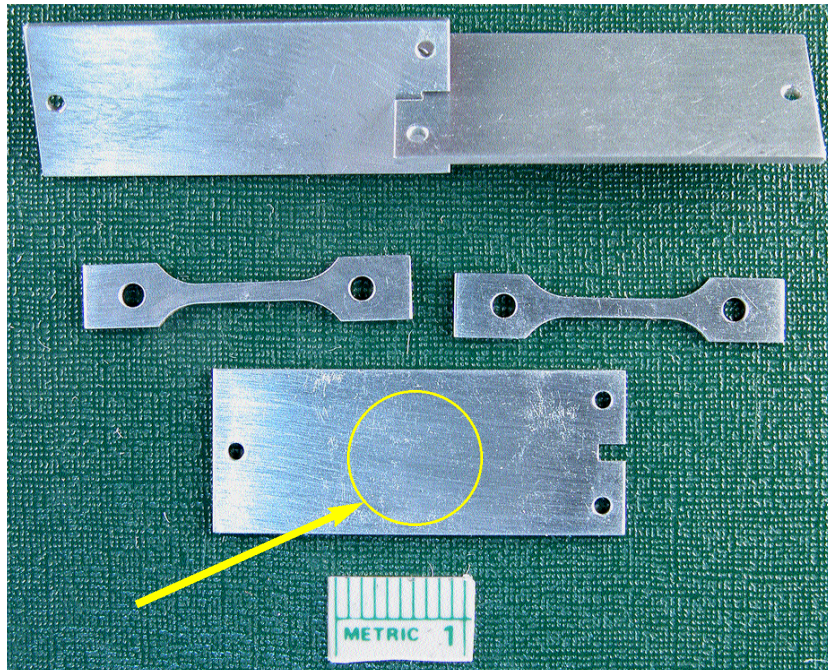


Figure 4. Photograph of examples of V-4Cr-4Ti tab and SS-3 tensile specimens prepared for the loop experiment. The circle (arrow) gives an indication of the PVD oxide ( $Y_2O_3$  or  $Er_2O_3$ ) coatings that will be applied to some specimens and then overcoated with  $10\mu\text{m}$  of vanadium.

deposition (EB-PVD) at Lawrence Livermore National Laboratory (LLNL). Half will be coated with  $Er_2O_3$  and half with  $Y_2O_3$ . The approximate size of the oxide coating is shown by the circle in Figure 4. All of the specimens will then be overcoated with a  $10\mu\text{m}$  layer of vanadium layer. One of each type will be kept to measure the as-coated resistance. Coated specimens will be placed in both the hot and cold legs of the loop but more will be placed in the hot leg.

## References

- [1] R. J. Kurtz, K. Abe, V. M. Chernov, D. T. Hoelzer, H. Matsui, T. Muroga, and G. R. Odette, *J. Nucl. Mater.* 329-333 (2004) 47.
- [2] I. R. Kirillov, C. B. Reed, L. Barleon, and K. Miyazaki, *Fusion Eng. Des.* 27 (1995) 553.
- [3] L. Barleon, V. Casal, and L. Lenhart, *Fusion Eng. Des.* 14 (1991) 401.
- [4] S. Malang, H. U. Borgstedt, E. H. Farnum, K. Natesan, and I. V. Vitkovski, *Fusion Eng. Des.* 27 (1995) 570.
- [5] L. Bühler, *Fusion Eng. Des.* 27 (1995) 650.
- [6] A. Y. Ying and A. A. Gaizer, *Fusion Eng. Des.* 27 (1995) 634.
- [7] B. A. Pint, P. F. Tortorelli, A. Jankowski, J. Hays, T. Muroga, A. Suzuki, O. I. Yeliseyeva, and V. M. Chernov, *J. Nucl. Mater.* 329-333 (2004) 119.
- [8] B. A. Pint, J. L. Moser, and P. F. Tortorelli, *Fusion Eng. Des.* 81 (2006) 901.
- [9] Y. Y. Liu and D. L. Smith, *J. Nucl. Mater.* 141-43 (1986) 38.
- [10] I. V. Vitkovsky et al., *Fusion Eng. Des.* 61-62 (2002) 739.
- [11] B. A. Pint, J. L. Moser, A. Jankowski, and J. Hayes, *Journal of Nuclear Materials* (in press).
- [12] B. A. Pint, K. L. More, H. M. Meyer, and J. R. DiStefano, *Fusion Sci. Technol.* 47 (2005) 851.
- [13] B. A. Pint and J. R. DiStefano, *Oxid. Met.* 62 (2005) 33.
- [14] B. A. Pint, J. H. DeVan, and J. R. DiStefano, *J. Nucl. Mater.* 307-311 (2002) 1344.

## **2.0 CERAMIC COMPOSITE MATERIALS**

**IRRADIATION CREEP OF CHEMICALLY VAPOR DEPOSITED SILICON CARBIDE AS ESTIMATED BY BEND STRESS RELAXATION METHOD—Y. Katoh, L. L. Snead, S. Kondo (Oak Ridge National Laboratory), T. Hinoki, A. Kohyama (Kyoto University)**

**OBJECTIVE**

The objective of this work was to develop a technique to experimentally determine the neutron irradiation-induced creep deformation behavior of brittle bulk ceramics and fibrous ceramic composites, and to study the irradiation creep of chemically vapor-deposited silicon carbide and uni-directionally reinforced silicon carbide fiber, chemically vapor-infiltrated silicon carbide matrix composites. The initial experimental result is discussed in this report.

**SUMMARY**

Bend stress relaxation technique was successfully applied for the study on irradiation creep of chemically vapor-deposited beta-phase silicon carbide (SiC) ceramics and vapor-infiltrated composites. Samples machined into thin strips were held within a curved gap in the silicon carbide fixture, and irradiated in High Flux Isotope Reactor at Oak Ridge National Laboratory and Japan Materials Test Reactor at Japan Atomic Energy Agency to the maximum neutron fluences of  $0.74 \times 10^{25}$  n/m<sup>2</sup> ( $E > 0.1$  MeV) at 400–1030°C. Irradiation creep strain for SiC exhibited weak temperature dependence in the temperature range studied. The creep strain appeared highly non-linear to neutron fluence due to the early domination of the initial transient irradiation creep. The transient creep was speculated to have caused by the rapid development of defect clusters and the structural relaxation of as-grown defects during early stages of irradiation damage accumulation. Steady-state irradiation creep compliance of SiC was conservatively estimated to be  $2\text{--}3 \times 10^{-32}$  (MPa-n/m<sup>2</sup>)<sup>-1</sup> at ~600–~1,100°C. The observed smaller irradiation creep strains for the monocrystalline SiC and the uni-directional composites than for the polycrystalline SiC were attributed to differences in the transient creep strain.

**PROGRESS AND STATUS**

**Introduction**

Silicon carbide (SiC) and composite materials of SiC are among the key engineering materials for nuclear applications including fusion and advanced fission energy and nuclear propulsion systems [1–3]. The promises and attractiveness of SiC ceramics rely on their unique combined properties such as neutron irradiation resistance, high temperature strength and inertness, low electrical conductivity, low activation / low decay heat, low tritium permeability, and low specific mass. Recent advancement of SiC-based ceramic composite technology has triggered the efforts toward practical applications of continuous SiC fiber-reinforced SiC-matrix ceramic composites (SiC/SiC composites) to the fusion blanket structural and multi-functional components [1,4] and the gas-cooled fission reactor core components [5,6].

One of the most critical issues which have not yet been addressed for SiC ceramics and composites for nuclear structural applications is irradiation creep [7]. Irradiation creep is the anisotropic plastic deformation driven by external or internal stresses, and induced or enhanced by irradiation in excess of thermal creep deformation. Irradiation creep generally dominates creep deformation of irradiated materials

Table 1. List of materials irradiated in this work.

Material	Crystal Structure	Manufacturer	Density (g/cm <sup>3</sup> )	Purity (%)		
CVD SiC	Polycrystalline beta	Rohm & Haas	3.21	>99.9995		
3C SiC	Monocrystalline beta	Hoya	3.21	~99.99 <sup>1)</sup>		
Material	Fiber / Architecture	Interphase	Matrix	V <sub>f</sub> <sup>2)</sup> (%)	Density (g/cm <sup>3</sup> )	Porosity (%)
UD-TySA/PyC <sup>3)</sup>	Tyranno™-SA	PyC <sup>520nm</sup>	SiC <sup>CVI</sup>	~30	~2.6	~17
UD-TySA/ML <sup>4)</sup>	Uni-directional	5x(PyC <sup>20nm</sup> /SiC <sup>100nm</sup> )				

<sup>1)</sup> Doped nitrogen as major impurity. <sup>2)</sup> Fiber volume fraction. <sup>3)</sup> Pyrolytic carbon interphase <sup>4)</sup> Multilayered interphase.

at temperatures below thermal creep practically operates for conventional metals and alloys.

Studies on irradiation creep of SiC (-based materials) are so far very limited. Irradiation creep of chemically vapor-deposited SiC has been studied by Price in 1977 [8]. In that work, elastically bent strip samples of chemically vapor-deposited (CVD) SiC were irradiated in a fission reactor, and the creep compliance was estimated to be  $\sim 1 \times 10^{-6} \text{ MPa}^{-1} \text{ dpa}^{-1}$  at 780–1130°C. Scholz and co-workers [9–12] measured the creep deformation of SCS-6 CVD SiC-based fiber, which was torsionally loaded under penetrating proton or deuteron beam irradiation. They reported several important observations including the linear stress and flux dependency of the tangential creep rate at 600°C, and an approximate irradiation creep compliance of  $\sim 1 \times 10^{-5} \text{ MPa}^{-1} \text{ dpa}^{-1}$ , which is only weakly and non-monotonically dependent on irradiation temperature in 450–1,100°C range. The adopted experimental method and setup in this work are reliable. However, the determined irradiation creep compliances are more than an order larger than those reported for neutron irradiation by Price [8]. Moreover, the CVD SiC fiber used is known to exhibit anomalous thermal creep behavior presumably due to excess silicon on grain boundaries [13].

For high purity, stoichiometric, vapor-deposited SiC, which is relevant to SiC ceramics and SiC/SiC composites' constituents considered for nuclear applications, there have not been convincing neutron irradiation creep compliance data available. The present work is intended to help understanding the creep behavior of such materials under neutron irradiation at elevated temperatures. An experimental method utilizing the technique of bend stress relaxation was employed. This paper describes the experimental method adopted, reports the initial results, and discusses their implication.

## Experimental Procedures

The bend stress relaxation (BSR) technique was adopted by Morscher and DiCarlo for evaluation of thermal creep behavior of ceramic fibers [14]. In a BSR irradiation creep experiment, samples in a form of straight thin fiber or strip are constrained to the bend radius  $R_0$  at temperature  $T$  and damage rate  $\phi$  for a period  $t$ . The bend stress retention ratio (BSR ratio,  $m$ ) is defined by

$$m(\phi, T, t) = \frac{\sigma_a}{\sigma_0} = 1 - \frac{R_0}{R_a} \quad (1)$$

where  $\sigma_a$  and  $\sigma_0$  are the initial and the final bend stresses, respectively, and  $R_a$  is the unconstrained bend radius after heat treatment, assuming a constant elastic modulus. When a linear stress dependence of steady-state irradiation creep rate  $\dot{\epsilon}_{ic}$  is assumed,

$$\dot{\epsilon}_{ic} = \kappa \sigma \phi \quad (2)$$

the irradiation creep compliance  $\kappa$  can be derived by the following equation,

$$\kappa = \frac{\ln(m_1/m_2)}{E\phi(t_2 - t_1)} \quad (3)$$

using  $m$  values at two different dose levels.

Compared to the conventional experimental techniques for irradiation creep studies such as the pressurized tube creep and externally loaded in-pile tensile or compressive creep techniques, BSR technique requires only very small specimens in a simple geometry. However, the successful application of BSR technique to irradiation creep study of bulk ceramics hinges upon preparation of thin strip samples with sufficient flexural strength and the appropriate design of specimen holders that ensure the thermal contact with the specimens without imposing undesired interactions.

For the first set of experiment, thin strip samples with dimensions of 25 or 40 mm x 1 mm x 50  $\mu$ m were prepared. Materials used were high purity (>99.9995%) beta-phase (3C) CVD SiC manufactured by Rohm and Haas Co., Advanced Materials (Waborn, Massachusetts, USA), and a free-standing monocrystalline

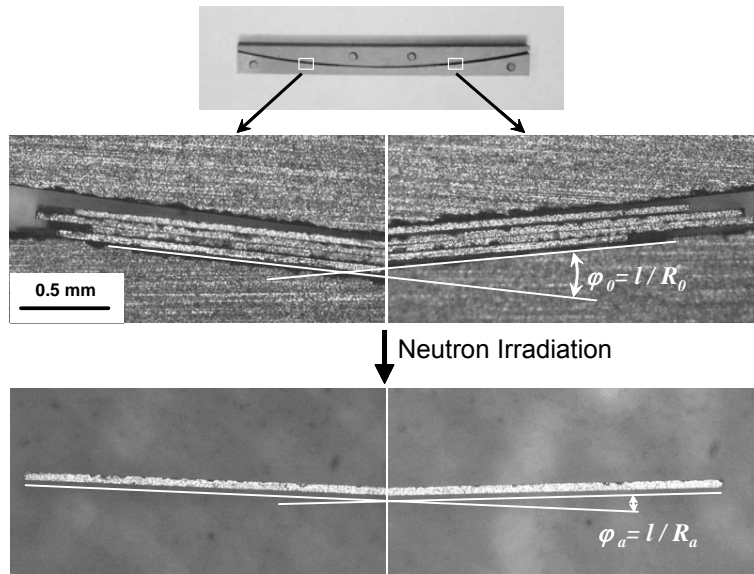


Fig. 1. Appearance of assembled BSR irradiation creep holder (top) and magnified views of end sections of thin strip specimens before (middle) and after (bottom) creep deformation.

Table 2. Summary of irradiation condition and result of BSR irradiation creep experiment.

Material	T <sub>irr</sub> °C	Fluence x10 <sup>25</sup> n/m <sup>2</sup>	Reactor	Initial / final bend stress MPa	Initial / final bend strain x10 <sup>-4</sup>	Creep strain x10 <sup>-4</sup>	BSR ratio <i>m</i>	Average creep compliance x10 <sup>-37</sup> (Pa-n/m <sup>2</sup> ) <sup>-1</sup>
CVD SiC	400	0.6	JMTR	82 / 60	1.80 / 1.39	0.41	0.77	0.97
	600	0.2	JMTR	81 / 57	1.80 / 1.31	0.49	0.73	3.5
		0.6	JMTR	81 / 46	1.80 / 1.05	0.75	0.58	2.0
	700*	0.66	HFIR	58 / 45**	1.52 / 1.04**	0.48**	0.69	1.3**
	750	0.6	JMTR	80 / 55	1.80 / 1.27	0.53	0.71	1.3
	1030*	0.74	HFIR	86 / 53**	1.94 / 1.23**	0.71**	0.63	1.4**
3C SiC	700*	0.66	HFIR	68 / 58**	1.52 / 1.32**	0.20**	0.87	0.47**
	1030*	0.74	HFIR	86 / 74**	1.94 / 1.22**	0.72**	0.88	0.40**
UD-TySA/PyC	600	0.2	JMTR	59 / 48	1.80 / 1.50	0.30	0.83	2.8
UD-TySA/ML	600	0.2	JMTR	63 / 55	1.80 / 1.62	0.18	0.90	1.5

\*Calculated temperature. \*\*Rough measurement; to be updated.

wafer of 3C-SiC with {100} surface orientation provided by Hoya Advanced Semiconductors Technologies, Inc. (Tokyo, Japan). The monocrystalline specimens were machined so that the longitudinal direction is in parallel with one of the <011> orientations. The specimens, after the finish-grinding with diamond paste, exhibited typical flexural strength of ~400 MPa, which enables the minimum bending radius of ~30 mm. In addition to the monolithic CVD SiC materials, small number of uni-directionally reinforced Tyranno™-SA fiber, chemically vapor-infiltrated SiC matrix composites were included to the materials to be evaluated. The SiC ceramics and composites tested are summarized in [Table 1](#).

The specimen holder was designed to retain the thin strip samples in a narrow gap with a curvature of 100mm radius. The appearance of the assembled specimen holder and the procedure to measure the constrained and the unconstrained specimen curvatures are shown in [Fig. 1](#). CVD SiC and Hexoloy™ SA were used as the holder materials in order to avoid potential chemical interactions with the SiC specimens during irradiation. The bend radii were determined by measuring the differential tangential angles at both ends of the sample strips before (constrained) and after (unconstrained) irradiation, as shown in Fig. 1. The accuracy of bend angle measurement by optical microscopy was <0.1°, which gives <1% error in determination of the BSR ratios.

The irradiation was performed at High Flux Isotope Reactor (HFIR), Oak Ridge National Laboratory (Oak Ridge, Tennessee, USA), and Japan Materials Test Reactor (JMTR), Japan Atomic Energy Agency (Oarai, Japan) to the maximum neutron fluence of 7.4x10<sup>24</sup> n/m<sup>2</sup> (E>0.1 MeV, the same shall apply hereinafter). The nominal irradiation temperatures were 700 and 1,030°C for HFIR, and 400, 600, and 750°C for JMTR. Details of the irradiation conditions are summarized in [Table 2](#).

## Results

The result of strain measurement is summarized in Table 2. The strain and stress values are the maximum that occurs at the tensile and compressive surfaces of bent specimens. The creep strain corresponds to the unconstrained residual strain, and the final bend strain was determined by subtracting the creep strain from the initial elastic strain. The initial and the final bend stresses were determined using temperature-dependent Young's modulus data for non-irradiated CVD SiC [15]. The linear-averaged irradiation creep compliances,  $\bar{\kappa}$ , were derived by dividing the creep strain by the product of fluence and the linear-averaged stress.

Neutron irradiation is known to lower Young's modulus of CVD SiC by a few to several percent at the temperatures for this experiment [16]. Such change in Young's modulus occurs mostly before a few dpa of irradiation damage is achieved. Since the irradiation effect on elastic modulus was neglected here, the  $\bar{\kappa}$  data may involve a few percent errors due to this.

In Fig. 2, the irradiation-creep BSR ratios are plotted as a function of irradiation temperature for the polycrystalline ('CVD SiC') and monocrystalline ('3C SiC') materials. The obvious features are: 1) the general lack of temperature dependence, 2) the distinctively smaller creep deformation for the monocrystalline samples, and 3) a reasonable agreement between data from HFIR and JMTR. A slightly negative correlation between the BSR ratio and irradiation temperature could be noticed, but the temperature effect does not appear significant compared to the error bars shown. The error bars correspond to the ranges of scatter for the data from JMTR, whereas they represent the maximum cumulative uncertainty associated with the bend radius measurement for the data from HFIR.

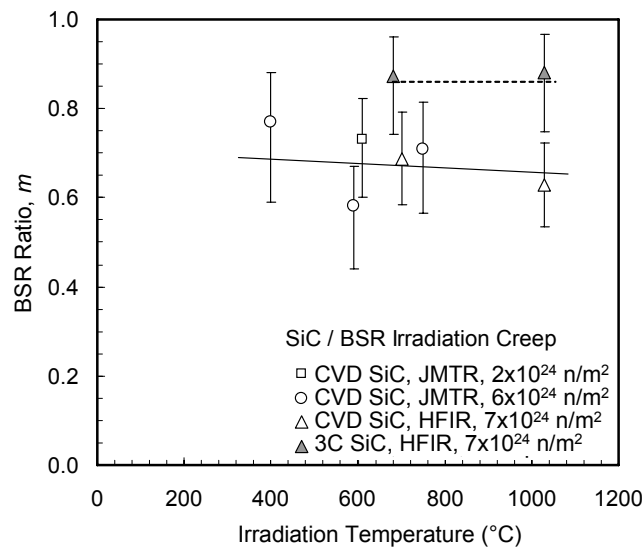


Fig. 2. Bend stress retention ratios for the irradiated polycrystalline ('CVD SiC') and monocrystalline ('3C SiC') vapor-deposited beta-phase SiC, as a function of irradiation temperature.

## Discussion

The linear-averaged irradiation creep compliance values,  $\bar{\kappa}$ , in Table 2, which have been obtained by putting  $t_l = 0$  and  $m_l = 1$  in Eq. 3, are obviously not appropriate for predicting the long-range irradiation creep behavior of SiC. For the light ion-irradiated SCS-6 fiber, Scholz et al. reports domination of the primary transient creep until at least 0.05 dpa, potentially followed by a transition into the steady-state-like creep, at 600°C [12]. They attributed the primary creep behavior to anisotropic partitioning of excess vacancies in association with the rapid interstitial cluster formation during the initial phase of irradiation process in SiC, by correlating the transient creep rate with the swelling rate of SiC at the relevant temperatures [12]. The fluence dependence of the BSR ratio observed at 600°C in this work supports the early domination of transient irradiation creep. Meanwhile, Eq. 2 also assumes the linear dependence of irradiation creep rate on the stress magnitude and neutron flux. The assumptions of linear stress and flux dependence may be adequate because of the light-ion data reported by Scholz et al. [9] but will have to be confirmed by neutron irradiation in future work.

Fig. 3 presents the irradiation creep BSR ratios obtained from this work and calculated from data published by Price [8], as a function of neutron fluence. Those data do not indicate constant creep compliance but represent a rather steep stress relaxation before a fluence of  $0.2 \times 10^{25}$  n/m<sup>2</sup> is achieved and the domination of that initial relaxation to the total stress relaxation at  $\sim 0.6 \times 10^{25}$  n/m<sup>2</sup>. It is not clear if the fluence of  $\sim 0.6 \times 10^{25}$  n/m<sup>2</sup> is still within the transient creep regime or not. However, at 600–750°C, the BSR ratios similar to that at  $0.2 \times 10^{25}$  n/m<sup>2</sup> suggest that it is close to the end of the transient creep regime at  $\sim 0.6 \times 10^{25}$  n/m<sup>2</sup>. The near-saturation of swelling at <1 dpa in this temperature range [17] also supports this implication, assuming the correlation of irradiation creep and low temperature swelling proposed by Scholz [12].

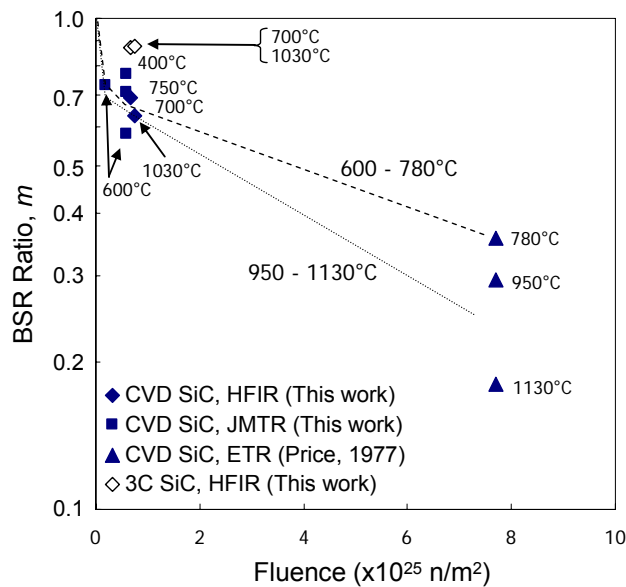


Fig. 3. Neutron fluence dependence of irradiation creep BSR ratio. Note that slope is proportional to irradiation creep compliance.

In ion-irradiated CVD SiC, Kondo et al. found that the number density of Frank faulted loops of interstitial type is strongly dependent on the relative orientation to the surface [18]. In their observation, loops on a {111} family plane that was near parallel to the free surface were abundantly present, whereas those on planes near perpendicular to the surface were notably rare. Because of the shallow damage range ( $\sim 2 \mu\text{m}$ ) in their ion irradiated sample, significant lateral compressive stress develops by swelling during the early irradiation. Therefore, the observation implies that the nucleation of interstitial loops was allowed only in orientations which do not cause expansion to the compressively stressed directions. Anisotropic swelling and/or creep by the mechanism of stress-induced preferred nucleation (SIPN) of dislocation loops was concluded in that work. Although this observation was at  $1,400^\circ\text{C}$ , it may be possible that a similar mechanism operates at lower temperatures for present work, since dislocation loop-like interstitial clusters develop even at below  $800^\circ\text{C}$  and low doses [19]. Assuming that the rapid production of aligned interstitial clusters are contributors to the initial transient creep, it is reasonable to expect the regime of steady-state(-like) creep follows through the growth and progressive nucleation of those clusters.

Based on the discussion above, it is possible that a steady-state irradiation creep is almost achieved at  $\sim 0.6 \times 10^{25} \text{ n/m}^2$ . Under such an assumption, steady-state creep compliances of  $\sim 2 \times 10^{-32}$  and  $\sim 3 \times 10^{-32} (\text{MPa}\cdot\text{n/m}^2)^{-1}$  at  $600\text{--}780^\circ\text{C}$  and  $950\text{--}1,030^\circ\text{C}$ , respectively, can be derived from data shown in Fig. 3. They are plotted in Fig. 4, along with the linear-averaged irradiation creep compliance values from the present work and by Price [8], and the light-ion creep compliance values published by Scholz [12]. Fig. 4 clearly depicts that the linear-averaged compliance values are strongly affected by the transient creep component. For the same reason, the steady-state creep compliance determined upon the relaxation

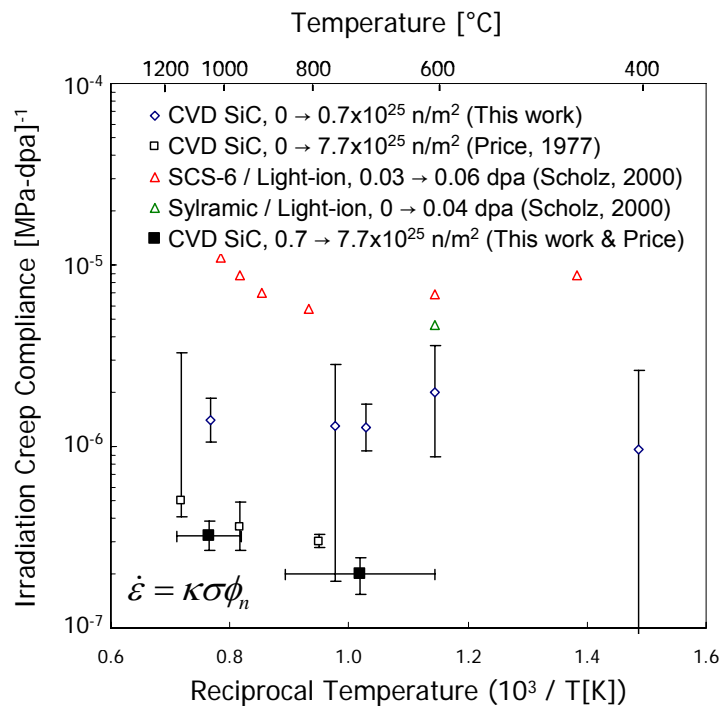


Fig. 4. Irradiation creep compliance of chemically vapor deposited SiC and SiC-based materials estimated by various experiments.

behavior between  $\sim 0.6$  and  $7.7 \times 10^{25}$  n/m<sup>2</sup> may still be a conservative estimation. The very large compliance values for the light ion irradiation creep are primarily due to the fact that they represent tangent compliances at a certain dose within the transient creep regime, while the presumably higher defect production efficiency by light ions and the non-stoichiometric grain boundary chemistry might have contributed as well.

The observed difference in stress relaxation behavior between the polycrystalline and monocrystalline materials is notable. The possible explanations include: 1) crystallographic orientation effect and 2) the influence of as-grown defects including grain boundaries. Assuming {111} as the primary habit planes for the responsible microstructural defects, in the monocrystalline specimens, two planes are in parallel and the other planes are  $\sim 53^\circ$  inclined to the stress axis. On the other hand, in the polycrystalline specimens, one of the {111} planes is in parallel and three others are  $0\text{--}71^\circ$  inclined to the stress axis. Hence, significant crystallographic orientation effect is not anticipated in this situation. As to the effect of as-grown defects, the polycrystalline material contains grain and subgrain boundaries and stacking faults, twin boundaries, and dislocations, whereas only the very low density stacking faults have been observed in the monocrystalline material [20]. It's been speculated that the thermally activated relaxation of these defects are partly responsible for the primary thermal creep deformation of stoichiometric SiC [21]. The primary thermal creep strain in CVD SiC is known to reach as high as  $>1 \times 10^{-4}$  at  $1500^\circ\text{C}$ , and it is reasonable to assume that a similar deformation mechanism can operate at significantly lower temperatures in assist of irradiation. Therefore, the effect of as-grown defects is more likely than the effect of crystallographic orientation as the reason for the different irradiation creep strains at a low dose.

It is also interesting to note the significantly smaller fractional stress relaxation for the uni-directional composites than for polycrystalline monolithic SiC. Since the composites consists primarily of beta-phase polycrystalline SiC, and the pyrolytic carbon interphase itself should exhibit much larger irradiation creep compliance than SiC [22], there seems to be no reasonable explanation for a smaller steady-state creep for composites than for monolithic SiC. Moreover, typically the chemically vapor-infiltrated SiC matrix is microstructurally more defected than monolithic CVD SiC in an as-grown condition. Therefore, the most likely cause is the smaller transient creep for the SiC fiber than CVD SiC. In the production process, Tyranno<sup>TM</sup>-SA fiber is final heat-treated at  $\sim 1,800^\circ\text{C}$  under substantial tensile stress, which might have already modified the microstructural defects anisotropically so that the additional relaxation in favor of longitudinal tensile deformation is impeded. There has also been a proposed mechanism of grain boundary strengthening for Tyranno<sup>TM</sup>-SA fiber by nano-scopic precipitation of aluminum compound that obstructs high temperature deformation associated with grain boundary sliding and/or rearrangement [23], which may also affect the transient irradiation creep behavior. In either case, it is worth noting that the anticipated creep vulnerability of carbon interphase did not impose a detectable detrimental effect on irradiation creep of the composites.

## Conclusions

Irradiation creep of vapor-deposited beta-phase SiC and uni-directional SiC composites were studied by BSR experiments in fission reactors. Irradiation creep strain for monolithic SiC exhibited weak temperature dependence in the  $400\text{--}1,030^\circ\text{C}$  range. The creep strain appeared highly non-linear to neutron fluence due to the early domination of the initial transient irradiation creep. The transient creep was speculated to have caused by the rapid development of defect clusters and the structural relaxation of as-grown defects

during early stages of irradiation damage accumulation. Steady-state irradiation creep compliance of SiC was conservatively estimated to be  $2\text{--}3 \times 10^{-32} \text{ (MPa}\cdot\text{n/m}^2\text{)}^{-1}$  at  $\sim 600\text{--}\sim 1,100^\circ\text{C}$ .

Both the monocrystalline beta-phase SiC and the uni-directionally reinforced Tyranno™-SA fiber, vapor-infiltrated SiC matrix composites exhibited substantially smaller creep strain than the polycrystalline beta-phase SiC at  $0.2\text{--}0.74 \times 10^{24} \text{ n/m}^2$  and  $600\text{--}1,030^\circ\text{C}$ . These were attributed to differences in the transient irradiation creep strain, and several potential mechanisms were discussed.

## References

- [1] Y. Katoh et al., Current Status and Critical Issues for Development of SiC Composites for Fusion Applications, *Journal of Nuclear Materials* (submitted).
- [2] S. J. Zinkle, *Fusion Sci. Technol.* 47 (2005) 821–828.
- [3] R. Naslain, *Compos. Sci. Technol.* 64 (2004) 155–170.
- [4] M. Abdou, D. Sze, C. Wong, M. Sawan, A. Ying, N. B. Morley, and S. Malang, *Fusion Sci. Technol.* 47 (2005) 475–487.
- [5] G. O. Hayner et al., INEEL/EXT-04-02347, Rev. 1, Idaho National Engineering and Environmental Laboratory, Idaho Falls (2004).
- [6] A. Kohyama, T. Hinoki, T. Mizuno, T. Kunugi, M. Sato, Y. Katoh, and J. S. Park, R&D of Advanced Material Systems for Reactor Core Component of Gas Cooled Fast Reactor, Proceedings of the International Congress on Advances in Nuclear Power Plants, May 15–19, 2005, Seoul.
- [7] A. R. Raffray, R. Jones, G. Aiello, M. Billone, L. Giancarli, H. Golfier, A. Hasegawa, Y. Katoh, A. Kohyama, S. Nishio, B. Riccardi, and M. S. Tillack, *Fusion Eng. Des.* 55 (2001) 55–95.
- [8] R. J. Price, *Nucl. Technol.* 35 (1977) 320–336.
- [9] R. Scholz, *J. Nucl. Mater.* 258–263 (1998) 1533–1539.
- [10] R. Scholz, *J. Nucl. Mater.* 254 (1998) 74–77.
- [11] R. Scholz and G. E. Youngblood, *J. Nucl. Mater.* 283–287 (2000) 372–375.
- [12] R. Scholz, R. Mueller, and D. Lesueur, *J. Nucl. Mater.* 307–311 (2002) 1183–1186.
- [13] J. A. DiCarlo, *J. Mater. Sci.* 21 (1986) 217–224.
- [14] G. N. Morscher and J. A. DiCarlo, *J. Am. Ceram. Soc.* 75 (1992) 136–140.
- [15] Y. Katoh and L. L. Snead, *Ceram. Eng. Sci. Proc.* 26, No. 2 (2005) 265–272.
- [16] Y. Katoh and L. L. Snead, *J. ASTM Int.* 2 (2005) 12377-1-13.
- [17] Y. Katoh, H. Kishimoto, and A. Kohyama, *J. Nucl. Mater.* 307–311 (2002) 1221–1226.
- [18] S. Kondo et al., *Journal of Nuclear Materials* (submitted).
- [19] Y. Katoh, N. Hashimoto, S. Kondo, L. L. Snead, and A. Kohyama, Microstructural Development in Cubic Silicon Carbide during Irradiation at Elevated Temperatures, *Journal of Nuclear Materials* (in press).
- [20] E. Polychroniadis, M. Syvajarvi, R. Yakimova, and J. Stoemenos, *J. Cryst. Growth* 263 (2004) 68–75.
- [21] G. N. Morscher, C. A. Lewinsohn, C. E. Bakis, R. E. Tressler, and T. Wagner, *J. Am. Ceram. Soc.* 78 (1995) 3244–3255.
- [22] T. D. Burchell, *Carbon Materials for Advanced Technologies*, Ed., T. D. Burchell (Pergamon, 1999).
- [23] T. Shibayama, private communication.

**3.0 FERRITIC/MARTENSITIC STEELS  
AND  
ODS STEELS**

**EVALUATION OF FRACTURE TOUGHNESS MASTER CURVE SHIFT OF JMTR IRRADIATED F82H USING SMALL SPECIMENS**—T. Yamamoto, G. R. Odette, D. Gragg, W. J. Yang (University of California, Santa Barbara), H. Kurishita, H. Matsui, M. Narui, M. Yamazaki (Tohoku University, Japan)

**OBJECTIVE**

In this study, we characterize the effects of low dose irradiation on the IEA heat of F82H using small to ultra-small specimens. Our primary objectives are to:

- Evaluate the use and limitations of using small bend bars with dimensions one-third and one-sixth of standard Charpy specimens to evaluate static  $\Delta T_o$  (1/3PCC) and dynamic  $\Delta T_d$  (so-called deformation and fracture minibeam, DFMBs) transition toughness temperature shifts,
- Compare the  $\Delta T_o$  based directly on the measured toughness ( $K_{Jm}$ ) to that determined from estimates of the corresponding small scale yielding toughness at a reference size ( $K_{Jr}$ ) derived using a physically based size adjustment procedure,
- Compare the  $\Delta T_o$  and  $\Delta T_d$  to hardening model predictions and general  $\Delta T_o$ - $\Delta\sigma_y$  trends.

**SUMMARY**

Small to ultra-small 1/3 size pre-cracked Charpy and 1.67 x 1.67 x 9.2 mm deformation and fracture minibeam (DFMB) specimens of the F82H IEA heat were irradiated to 0.02 and 0.12 dpa at 290 °C in the Japanese Materials Test Reactor. Nominal cleavage transition temperature shifts, based on the measured toughness,  $K_{Jm}(T)$ , data ( $\Delta T_m$ ) as well as reference temperature shifts ( $\Delta T_o$ ) found after size-adjusting the  $K_{Jm}(T)$  data yielded  $\Delta T_{m/o} \approx 27 \pm 10$  and  $44 \pm 10$  at the two doses, respectively. Using measured yield stress changes ( $\Delta\sigma_y$ ), the  $C_o = \Delta T_o / \Delta\sigma_y = 0.58 \pm 0.14$  at 0.12 dpa, is in good agreement with data in the literature. The dynamic transition temperature shift,  $\Delta T_d$ , derived from DFMB tests, was  $\approx 30 \pm 20^\circ\text{C}$  at 0.1 dpa, also in good agreement with the estimated  $\Delta T_o$  shifts. The  $\Delta T_d$  and  $\Delta T_o$  are also in excellent agreement with a  $\Delta T_o = C_o \Delta\sigma_y(\text{dpa}, T_i)$  hardening-shift model, where the  $\Delta\sigma_y(\text{dpa}, T_i)$  was found by fitting a large database on tensile properties.

**PROGRESS AND STATUS**

**Introduction**

A key issue in developing 8-9Cr-1-2W normalized and tempered martensitic steels (TMS) for fusion reactor applications is irradiation embrittlement, as characterized by upward shifts ( $\Delta T_o$ ) in the cleavage fracture toughness master curve (MC) [1-5]. At irradiation temperatures less than  $\approx 400^\circ\text{C}$ , the  $\Delta T_o$  are primarily due to irradiation hardening,  $\Delta\sigma_y$  [1,6,7]. However, the weakening of grain boundaries by very high levels of helium may also interact synergistically with large  $\Delta\sigma_y$ , resulting in very large  $\Delta T_o$  [1,7]. Assessment of  $\Delta T_o$  requires utilization of small specimens due to both limited space and high heating rates in available irradiation facilities. However, the fracture toughness measured using small specimens,  $K_{Jm}$ , is generally higher relative to values obtained from larger, conventional specimens, due to both statistical and constraint loss size effects [1,4,8]. It has been shown that physically based models can be used to adjust  $K_{Jm}$  data to full constraint conditions (plane strain, small scale yielding)  $K_{Jr}$  at a reference size [4,8]. For example, application of the adjustment procedure to a large F82H  $K_{Jm}$  database obtained from 13 types of specimens resulted in a self-consistent population of  $K_{Jr}$  data well described by a single MC of  $T_o \approx -100 \pm 3^\circ\text{C}$  [4].

In the hardening dominated regime,  $T_o \approx C_o \Delta\sigma_y$ , where estimates of  $C_o$  range from  $\approx 0.7^\circ\text{C}/\text{MPa}$  for reactor pressure vessel (RPV) steels and low dose (dpa) irradiations at  $T_i \approx 300^\circ\text{C}$  [1,9] to less than  $\approx 0.4^\circ\text{C}/\text{MPa}$  for higher dose TMS alloys, particularly for irradiations at lower temperatures [1,10-11]. Odette et al. reported a  $C_o \approx 0.58^\circ\text{C}/\text{MPa}$  for F82H irradiated between  $\approx 250$  to  $380^\circ\text{C}$  [1,10]. It has also been shown that the lower  $C_o$  for TMS alloys and irradiation conditions, compared to the RPV case, can be attributed

to much larger reduction of strain hardening after irradiation to high dose [1,10,12]. If  $C_o$  is assumed to be approximately constant for a particular alloy and irradiation regime, then  $T_o$  can be related to  $\Delta\sigma_y$ , or other measures of irradiation-induced strength increases, such as measured by Vickers microhardness ( $\Delta H_v$ ) [13,14]. A large database on  $\Delta\sigma_y$  in irradiated TMS compiled by Yamamoto et al. [6] was used to derive a semi-empirical model for  $\Delta\sigma_y$  ( $dpa, T_i, T_t$ ), where  $T_t$  is the test temperature. This work showed that the hardening model could be combined with hardening-shift coefficients for Charpy ( $C_c$ ) tests and  $C_o$  to predict  $\Delta T_c = C_c \Delta\sigma_y$  ( $dpa, T_i$ ) and  $T_o = C_o \Delta\sigma_y$  ( $dpa, T_i$ ), respectively.

In this study, we characterize the effects of low dose irradiation on the IEA heat of F82H using small to ultra-small specimens. Our primary objectives were to:

- evaluate the use and limitations of using small bend bars with dimensions one-third and one-sixth of standard Charpy specimens to evaluate static  $\Delta T_o$  (1/3PCC) and dynamic  $\Delta T_d$  (so-called deformation and fracture minibeams, DFMBs) transition toughness temperature shifts;
- compare the  $\Delta T_o$  based directly on the measured toughness ( $K_{Jm}$ ) to that determined from estimates of the corresponding small scale yielding toughness at a reference size ( $K_{Jr}$ ) derived using a physically based size adjustment procedure;
- compare the  $\Delta T_o$  and  $\Delta T_d$  to hardening model predictions and general  $\Delta T_o$  -  $\Delta\sigma_y$  trends.

## Experimental Procedure

Detailed information on the IEA heat of F82H characterized in this study is summarized elsewhere [15]. The 1/3PCC specimens with dimensions of  $W = 3.33$ ,  $B = 3.33$  and  $L = 18.3$  mm were fabricated in L-T orientation, where  $W$ ,  $B$  and  $L$  are the specimen width, thickness and length, respectively. The fatigue pre-cracks were grown to nominal  $a/W$  of  $\approx 0.5$ , where  $a$  is the crack length, at a final maximum peak stress intensity factor of  $\approx 18$  MPa $\sqrt{m}$ . DFMBs, with dimensions  $W = 1.67$ ,  $B = 1.67$  and  $L = 9.2$  mm, were fabricated in T-S orientation from pre-cracked coupons using special procedures described elsewhere [16]. SS-J2-type sheet dogbone tensile specimens, with gauge section dimensions of  $W = 1.2$ ,  $L = 5$  and  $t = 0.5$  mm, were also fabricated in L-axis orientation. Irradiations were carried out in the Japan Materials Test Reactor (JMTR) at 290°C. The 1/3PCC and the tensile specimens were irradiated to between  $\approx 0.02$  and 0.12 dpa, while the DFMB specimens were irradiated to  $\approx 0.1$  dpa.

The post irradiation mechanical tests were carried out in the hot cell facility at the IMR-Oarai Center, Tohoku University in Oarai, Japan. The 1/3PCCs were tested statically on a screw driven load frame. The bending fixture, with a span of 6.6 mm, and specimen were immersed in a isopentane cooling bath, and stabilized to within  $\pm 1$  °C of  $T_t$  for at least ten minutes prior to testing at a displacement rate is 2  $\mu\text{m/s}$ . Tensile tests were performed in the same bath at a nominal strain rate of  $6.67 \times 10^{-4}$  on the same load frame. The DFMB specimens were tested in a so-called IZOD configuration [17] on an oil pressure driven drop tower impact tester. An impact displacement at 1 m/s was applied by an instrumented striker at a distance 3.3 mm from the crack line, near the end the cantilevered beam specimen. Data for DFMB control specimens tested at UCSB, both in 3 point bending and in a similar IZOD configuration, were generally consistent with the Oarai results. In all cases the load-time data was converted to load-displacement curves that were analyzed for  $K_{Jm}$  and  $K_{Jd}$  using the procedures in ASTM E1921-05 [5].

## Size Effect Adjustments of Fracture Toughness Data

Cleavage fracture initiates in the high stress region near the tip of a blunting crack [1,18-21]. The crack tip fields can be described by isostress contours that reach peak values of 3 to 5 times  $\sigma_y$ , depending on the alloy strain-hardening rate [1,18-21]. Under plane strain, small-scale yielding (SSY) conditions for specimens with  $a/W \approx 0.5$ , the spatial dimensions of the stress field scale with the crack tip opening displacement,  $\delta \approx K_J^2 / 2\sigma_y E$  [1,18,20]. However, if the deformation level, hence the  $\delta$ , in a small specimen that is required to produce cleavage is not very small compared to the characteristic dimension of the

specimen, typically taken as the uncracked ligament length,  $b = W - a$ , then the crack tip stress fields fall below small scale yielding values. The reduction of the stress fields at higher  $\delta/b$  is known as constraint loss (CL) [1,8,21]. Constraint loss begins at  $\delta/b \approx 0.01$  and becomes significant at values of 0.02 [1,8]. Assuming an irradiated  $\sigma_y \approx 600$  MPa and  $\delta/b = 0.02$  suggests that the maximum toughness that can be measured without significant constraint loss is about  $65 \text{ MPa}\sqrt{\text{m}}$ . Beyond this limiting value, the  $K_{Jm}/K_{Jc}$  increase rapidly. Thus rapid CL with increasing toughness and  $T_i$ , is marked by a very steep slope of the  $K_{Jm}(T_i)$  curves for small specimens in the cleavage transition.

A simple but powerful micromechanical model proposes that cleavage occurs when a critical stress ( $\sigma^*$ ) encompasses a critical volume  $V^*$  of material near a crack tip [1,8,21]. Three dimensional finite element (FE) simulations were performed to obtain the average stressed areas ( $\langle A \rangle$ ) along the crack front as a function of the alloys constitutive law,  $\sigma(\epsilon)$ , applied loading  $K_J$ , and normalized stress  $\sigma_{22}/\sigma_y$  perpendicular to the crack plane, for both of large scale yielding (LSY) condition and the actual specimen geometry as well as the SSY condition [1,4,8]. The CL size adjustment is defined as the ratio,  $[K_J/K_{SSY}]$  of the LSY- $K_J$  at  $K_{Jm}$  to the corresponding SSY  $K_{SSY}$  at  $K_{Jc}$  for the same stressed  $\langle A \rangle$  at a specified  $\sigma^*/\sigma_y$ , where  $\sigma^*$  is the critical microcleavage fracture stress [1,8,19]. Thus,  $K_{Jc}(B) = K_{Jm}/[K_J/K_{SSY}]$ . A second statistical stressed volume (SSV) size adjustment relates to the variations in the probability of initiating weakest link cleavage as a function of the total volume ( $V$ ) of material under high stress. Since for SSY conditions,  $\langle A \rangle$  scales with  $K_J^4$  and  $V^* = B\langle A \rangle^*$ , simple theory suggests that  $K_{Jc}$  scales as  $\approx B^{-1/4}$  [1,8]. However, other mechanistic considerations and empirical observations show that this  $B^{-1/4}$ -scaling is modified by a minimum toughness,  $K_{min}$ , as  $K_{Jr}(B_r) = [K_{Jc}(B) - K_{min}][B_r/B]^{1/4} + K_{min}$  [1,5,8]. The ASTM MC standard E1921-05, specifies a  $K_{min} \approx 20 \text{ MPa}\sqrt{\text{m}}$  and a reference thickness  $B_r = 25.4 \text{ mm}$  [5]. More detailed description on the CL and SSV size effects adjustment procedures can be found in the literature [1,8].

## Results and Discussion

The  $K_{Jm}(T)$  data for the 1/3PCC specimens irradiated in JMTR to 0.02 and 0.12 dpa at 290 °C are shown in Figures 1a. The measured shifts,  $\Delta T_m$ , evaluated by the temperatures marking the sharp toughness transitions, as indicated by the lines, are about  $24 \pm 10$  and  $44 \pm 10$  °C for doses of 0.02 and 0.12 dpa, respectively. Figure 1b shows  $K_{Jm}$  data adjusted to the toughness,  $K_{JB}$ , at a reference thickness  $B_r = 25.4 \text{ m}$ , using the ASTM E1921 statistical adjustment procedure cited above [5]. Unirradiated  $K_{JB}$  toughness values for the same heat of F82H reported by Wallin [3] from tests on similar bend specimens with dimensions of  $W = 4$ ,  $B = 3$  and  $L = 27 \text{ mm}$ , shown in Figure 1b for comparison, and are generally consistent with our unirradiated control  $K_{JB}$  data. A multi-temperature MC analysis based on ASTM E1921 procedure [5] yields a  $T_o \approx -126$  °C. The deviation of  $\approx -26$  °C for the small 1/3PPC specimens relative to full constrain conditions is consistent with previous observations [2,3,4]. The corresponding adjusted  $T_o$  values of the irradiated specimens -99 and -76 °C, yielding  $\Delta T_o \approx 27 \pm 8$  and  $50 \pm 7$  °C, for irradiations to 0.02 and 0.12 dpa, respectively. Note, the data in Figures 1a and 1b do not account for CL effects, which are discussed below.

The  $[K_J/K_{SSY}]$  CL adjustment factors were determined from FE simulations for  $\sigma^* = 2100$  MPa using the  $\sigma(\epsilon)$  from the -100°C tensile test data on the unirradiated control and the specimens irradiated to 0.12 dpa. The  $\sigma^*$  was calibrated by fitting a MC shape to the SSY  $K_{Jc}(T_i)$  curve for F82H [4]. The magnitude of the adjustment,  $K_{Jm} - K_{Jc}$ , plotted versus  $K_{Jm}$  in Figure 2a, is similar in both cases. Thus the fitted relation in Figure 2a was used for CL adjustments of the  $K_{Jm}$  data obtained from the 1/3PCC specimens irradiated to 0.02 dpa. Figure 1c shows the corresponding CL and SSV adjusted,  $K_{Jr}$  data. Multi-temperature MC analyses resulted in  $T_o$  values of -77, -48 and -34°C, yielding  $\Delta T_o$  of  $29 \pm 8$  and  $43 \pm 7$  °C for 0.02 and 0.12 dpa irradiation conditions, respectively. These  $\Delta T_o$  are very similar to the other estimates, with overall averages are  $27 \pm 2$  °C and  $44 \pm 6$  °C for the 0.02 and 0.12 dpa irradiations, respectively. However, the estimated  $T_o$  for the unirradiated F82H is  $\approx 23$  °C higher than the nominal full constraint  $K_{Jr}$  value of  $\approx$

-100°C. This difference suggests that the combined CL and SSV procedures consistently over adjust the  $K_{Jm}$  data for these very small specimens.

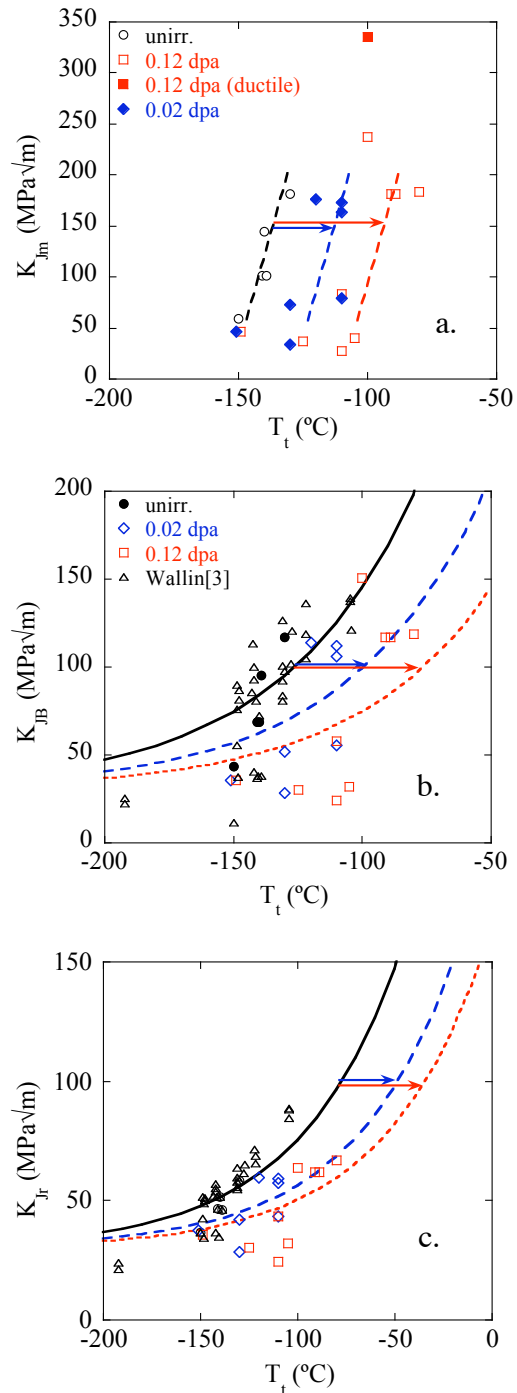


Figure 1. (a) Measured fracture toughness data,  $K_{Jm}$ , on the F82H IEA 1/3PCC specimens before and after the neutron irradiations at 290 °C in JMTR; (b) MC curves derived based on ASTM E1921-05 SSV adjustment procedure; (c) MC curves derived based on the combined CL and SSV adjustment procedure.

Tensile tests performed at 15°C showed  $\Delta\sigma_y = 74 \pm 10$  MPa at 0.12 dpa. Using this and the average  $\Delta T_o = 44 \pm 10$  °C yields a  $C_o = 0.58 \pm 0.14$  °C/MPa at 0.12 dpa, in good agreement with previous estimates for F82H [1,10]. Assuming a  $\Delta\sigma_y = K(\text{dpa})^{1/2}$  dose scaling, where  $K = 213$  MPa for the 0.12 dpa case, the estimated average  $\Delta\sigma_y \approx 30 \pm 4$  MPa at 0.02 dpa. Taking the average  $\Delta T_o = 27 \pm 10$  °C, the corresponding  $C_o = 0.9$ °C/MPa. The higher value in this case may be partly due to a smaller loss of strain hardening for the low dose irradiation condition [12]. Note the uncertainties in the  $C_o$  estimates are large and are estimated to be  $\approx \pm 0.3$ °C/MPa. Indeed, a better demonstration of the consistency of these new results with previous observations is shown in Figure 2b plotting  $\Delta T_o$  versus  $\Delta\sigma_y$  for all available data on F82H [11,22-23].

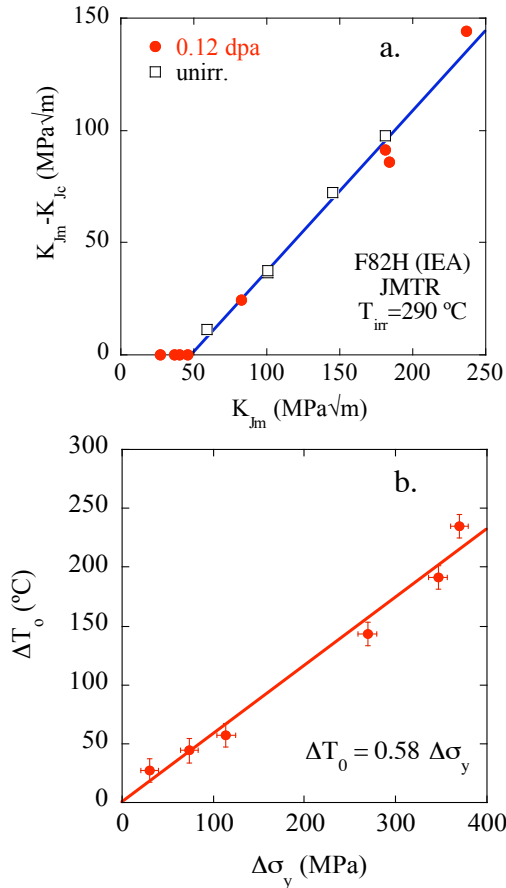


Figure 2. (a) The magnitude of the CL adjustment as function of  $K_{fm}$  for both the unirradiated control and the 0.12 dpa irradiation conditions; (b)  $\Delta T_o$  versus  $\Delta\sigma_y$  for data available on F82H irradiated between 250 and 380°C.

Figure 3a shows  $K_{jd}$  data from dynamic fracture tests on the DFMB specimens irradiated to 0.1 dpa at 290 °C. The estimated  $T_{du}$  for the unirradiated control specimen at an impact velocity 1m/s impact rate is about -60 °C, while that for 0.2m/s tests is  $\approx 10$  °C lower. This difference is consistent with the temperature shift in  $\sigma_y$  due to higher (h) to lower (l) strain-rates given by  $\Delta T_{gr} = -CT_{ll} \ln(\epsilon'_h/\epsilon'_l) \approx -10$  °C, for a nominal value of  $C = 0.03$ , where  $T_{ll}$  is the absolute temperature at the lower loading rate [24]. The corresponding  $T_{di}$  for the 0.1 dpa irradiation condition is  $\approx -35$  °C, yielding a  $\Delta T_d \approx 25$  °C. Thus  $\Delta T_d$  is less than the corresponding static  $\Delta T_o$ . Estimating  $\Delta\sigma_{yd} = \Delta\sigma_y = 68$  MPa at 0.1 dpa, the  $C_d = \Delta T_d / \Delta\sigma_{yd} = 0.36$ °C/MPa. This low value of  $C_d$  is similar to the  $C_c$  typically measured in subsized Charpy V-notch impact tests [1].

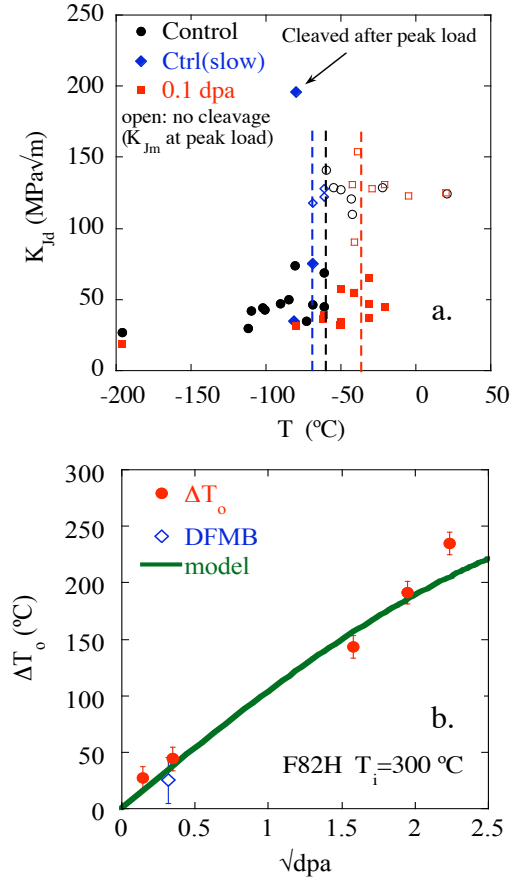


Figure 3. (a) Dynamic toughness measured by IZOD-type impact tests on F82H IEA DFMB specimens in the unirradiated condition and irradiated to 0.1 dpa at 290 °C in JMTR; (b) the composite model prediction of the  $\Delta T_o$  vs dose ( $\sqrt{dpa}$ ) for  $T_i=300$  °C.

Assuming a factor of  $\approx 5 \times 10^5$  higher loading rate in the dynamic versus static tests the  $\Delta T_{\epsilon'} = -CT_{th} \ln(\epsilon'_h/\epsilon'_l)$  relation can be used to estimate a  $T_m$  for static DFMB tests as  $\approx -144$ °C. The corresponding  $T_o$  for the DFMB tests evaluated by the ASTM E1921 procedure would be expected to be about 28°C less than for the 1/3PCC, as expected due to the additional loss of constraint in this case.

We can also estimate  $\Delta T_o$  based on the hardening-shift relation  $\Delta T_o = C_o \Delta \sigma_y(dpa, T_i)$ , where the  $\Delta \sigma_y(dpa, T_i)$  was derived from our analysis of the larger TMS database study. For  $T_i = 300$ °C and using the  $\sigma_y(dpa, T_i)$  correlation for  $T_i = 23$ °C and the  $C_o = 0.58$ °C/MPa from the fit shown in Figure 2b,

$$\Delta T_o = 296[1 - \exp(-dpa/7.7)]^{1/2} \quad (1)$$

As shown in Figure 3b, the hardening-shift model  $\Delta T_o(dpa)$  predictions are in good agreement with experimental data for  $T_i=290$  to 300 °C (note,  $\Delta T_o(290) - \Delta T_o(300) \approx 3$ °C at around 0.1 dpa, which is within the experimental error). Figure 3b also shows that the  $\Delta T_o$  prediction is within the estimated errors for the  $\Delta T_d$  from the DFMB tests

## Conclusions

Fracture toughness tests for 1/3PCC specimens of F82H IEA irradiated to 0.02 and 0.12 dpa at 290 °C in JMTR were carried out to estimate MC reference temperature shift,  $\Delta T_o$ , using variety of procedures,

yielded average  $27\pm 10$  and  $44\pm 10^\circ\text{C}$ , respectively. These results indicate that  $\Delta T_m$  directly evaluated from the  $K_{Jm}$  data can be used to estimate  $\Delta T_o \approx \Delta T_m$ , in spite of the large CL suffered by these small specimens. As expected both the unirradiated  $T_d$  and that for irradiations at  $290^\circ\text{C}$  to  $0.1$  dpa from the dynamic DFMB tests were higher than their static counterparts. The nominal  $\Delta T_d = 25\pm 20^\circ\text{C}$  determined from dynamic tests is somewhat smaller than the estimated  $\Delta T_o$  for the same irradiation conditions of  $\approx 40^\circ\text{C}$ , but the difference is within the estimated data uncertainties. Likewise, the individual values of  $C_o$  and  $C_d$  for these small specimen tests varied between about but averaged about  $0.58^\circ\text{C}/\text{MPa}$ , consistent with previous observations. Indeed  $\Delta T_o$  and  $\Delta T_d$  predicted by a simple hardening shift model based on this  $C_o$  and  $\Delta\sigma_y(\text{dpa}, T_i)$  derived from an analysis of a large database and is also consistent with experimental estimates within expected data errors.

### Acknowledgements

This research was the result of a collaborative agreement between University of California, Santa Barbara, and the Tohoku University Institute for Materials Research with support from the U.S. Department of Energy, Office of Fusion Science (Grant #DE-FG03-94ER54275) and MEXT (Japan).

### References

- [1] G. R. Odette, T. Yamamoto, H. J. Rathbun, M. Y. He, M. L. Hribernik, and J. W. Rensman, *J. Nucl. Mater.* 323 (2003) 313.
- [2] G. E. Lucas, G. R. Odette, M. Sokolov, P. Spatig, T. Yamamoto, and P. Jung, *J. Nucl. Mater.* 307-311 (2002) 1600.
- [3] K. Wallin, A. Laukkanen, and S. Tahtinen, *Small Specimen Test Techniques 4*, ASTM STP 1418 (2002) 33.
- [4] G. R. Odette, T. Yamamoto, H. Kishimoto, M. Sokolov, P. Spätig, W. J. Yang, J.-W. Rensman, and G. E. Lucas, *J. Nucl. Mater.* 329-333 (2004) 1243.
- [5] ASTM E 1921-05, Standard Test Method for Determination of Reference Temperature,  $T_o$ , for Ferritic Steels in the Transition Range, ASTM (2005).
- [6] T. Yamamoto, G. R. Odette, H. Kishimoto, J.-W. Rensman, and P. Miao, *J. Nucl. Mater.* (in press).
- [7] R. Kasada, T. Morimura, A. Hasegawa, and A. Kimura, *J. Nucl. Mater.* 299 (2001) 83.
- [8] H. J. Rathbun, G. R. Odette, M. Y. He, and T. Yamamoto, *Engineering Fracture Mechanics* (in press).
- [9] M. A. Sokolov and R. K. Nanstad, *Effects of Irradiation on Materials-18th International Symposium*, ASTM STP 1325 (1999) 167.
- [10] G. R. Odette, H. J. Rathbun, J. W. Rensman, and F. P. van den Broek, *J. Nucl. Mater.* 307-311 (2002) 1624.
- [11] J.-W. Rensman, NRG Irradiation Testing: Report on  $300^\circ\text{C}$  and  $60^\circ\text{C}$  Irradiated RAFM Steels, NRG Petten 20023/05.68497/P.
- [12] M. Y. He, G. R. Odette, and T. Yamamoto, *Journal of Nuclear Materials* (submitted).
- [13] G. R. Odette, M. Y. He, and D. Klingensmith, *Fusion Materials Semiannual Report DOE/ER-313/37* (2005) 109.
- [14] M. Y. He, G. R. Odette, T. Yamamoto, and D. Klingensmith, *Journal of Nuclear Materials* (submitted).
- [15] S. Jitsukawa, M. Tamura, B. van der Schaaf, R. L. Klueh, A. Alamo, C. Peterson, M. Schirra, P. Spaetig, G. R. Odette, A. A. Tavassoli, K. Shiba, A. Kohyama, and A. Kimura, *J. Nucl. Mater.* 307-311 (2002) 179.
- [16] G. R. Odette, M. He, D. Gragg, D. Klingensmith, and G. E. Lucas, *J. Nucl. Mater.* 307-311 (2002) 1643.
- [17] D5941-96 Standard Test Method for Determination of Izod Impact Strength (withdrawn 1998).
- [18] K. Edsinger, G. R. Odette, G. E. Lucas, and B. D. Wirth, *ASTM STP 1270* (1996) 670.

- [19] G. R. Odette, *J. Nucl. Mater.* 212-215 (1994) 45.
- [20] T. L. Anderson, *Fracture Mechanics: Fundamentals and Applications*, Third Edition, CRC Press, (Boca Raton, Florida, 2005).
- [21] M. Y. He, G. R. Odette, and T. Yamamoto, *Journal of Nuclear Materials* (submitted).
- [22] P. Spatig, Small-scale fracture mechanics – modeling of brittle to ductile transition behaviors using appropriate theories. Formation of rules for transferability to standards and fusion components, TTW2-TTMS-005b, CPPI, Switzerland (2005).
- [23] M. A. Sokolov, R. L. Klueh, G. R. Odette, K. Shiba, and H. Tanigawa, *ASTM STP 1447* (2004) 408.
- [24] P. Spatig, G. R. Odette, and G. E. Lucas, *J. Nucl. Mater.* 275 (1999) 324.

**EFFECTS OF CONSOLIDATION TEMPERATURE, STRENGTH AND MICROSTRUCTURE ON FRACTURE TOUGHNESS OF NANOSTRUCTURED FERRITIC ALLOYS**—P. Miao, G. R. Odette, T. Yamamoto (University of California, Santa Barbara), M. Alinger (University of California, Santa Barbara, University of California, Berkeley), D. Hoelzer (Oak Ridge National Laboratory), and D. Gragg (University of California, Santa Barbara)

## OBJECTIVE

This work is to investigate fracture toughness of hot-isostatic-processed (HIPed) nanostructured ferrite alloys and the effects of HIPing parameters and microstructures on the fracture toughness.

## SUMMARY

Fully consolidated nanostructured ferritic alloys (NFAs) were prepared by attritor milling pre-alloyed Fe-14Cr-3W-0.4Ti and 0.3wt%  $Y_2O_3$  powders, followed by hot isostatic pressing (HIPing) at 1000°C and 1150°C and 200 MPa for 4 h. Transmission electron microscopy (TEM) revealed similar bimodal distributions of fine and coarse ferrite grains in both cases. However, as expected, the alloy microhardness decreased with increasing in HIPing temperature. Three point bend tests on single edge notched specimens, with a nominal root radius  $\rho = 0.15$  mm, were used to measure the notch fracture toughness,  $K_{Ic}$ , as a function of test temperature. The  $K_{Ic}$  curves were found to be similar for both alloys. It appears that the coarser ferrite grains control cleavage fracture, in a way that is independent of alloy strength and HIPing temperature.

## PROGRESS AND STATUS

### Introduction

Nanostructured ferritic alloys (NFAs) containing 12 to 14%Cr and a very high density of nm-scale Y-Ti-O precipitate phases have outstanding low temperature tensile ( $> 1$  GPa) and high temperature creep strengths [1-3] and offer a potential for mitigating radiation damage, including the effects of high helium levels [4, 5] in fusion reactor structures. However, a significant challenge to the development of NFAs is maintaining adequate fracture toughness, in combination with high strength. Various approaches to optimizing the fracture toughness of NFAs, including alternative processing paths [5-7] and alloy designs [5, 8], have been, or are being, studied.

Previous investigations [1] of the fracture toughness of an extruded MA957 NFA revealed a strong dependence on microstructural anisotropy. This anisotropy is manifested as elongated grains in the extrusion direction, with a length to diameter aspect ratio of  $\approx 10$ -20 [7], along with preferred longitudinal  $\langle 110 \rangle$ -fiber texture [9]. This MA957 heat alloy also contained  $Al_2O_3$  impurity inclusion stringers that were elongated in the extrusion direction. As a result, orientations with the crack plane normal perpendicular to the extrusion direction (C-R and C-L) have lower toughness. The lowest toughness is when the cracks grow in the extrusion direction (C-L). In contrast, the toughness is higher and transition temperature (TT) is lower when the crack plane normal is parallel to the extrusion direction (L-R). Thus, the purpose of this study was to evaluate the toughness in a nominally clean (inclusion free), isotropic and equiaxed alloys produced by HIPing.

### Experimental Procedure

The NFAs were prepared by mechanically alloying Fe-14Cr-3W-0.4Ti powder with 0.3wt%  $Y_2O_3$  for 40h in an attritor mill with an argon atmosphere. The milled powders were then vacuum canned and consolidated by HIPing at 200MPa for 4h at 1000°C (14YWT1000) and 1150°C (14YWT1150). The alloy densities were measured using a MicroMeritics AccuPyc 1330 pycnometer. Their potential porosity was examined by optical microscopy. The microstructure of the alloy was characterized by TEM (JEOL2010HR). The TEM specimens were prepared by grinding 3mm diameter discs to a thickness of

~0.15mm, followed by thinning to electron transparency in a TENUPOL twin-jet electro-polisher with  $\text{H}_2\text{SO}_4 + 80\%\text{CH}_3\text{OH}$  at room temperature.

The flow strength of the NFAs was evaluated by diamond pyramid Vicker's microhardness (DPH) measurements using a 1kg load at room (~23°C) and liquid-nitrogen (-196°C) temperatures. Notch fracture toughness was measured in three-point-bending on an MTS servohydraulic load frame at a displacement rate of 0.08mm/min over the temperature range from -100°C to 205°C. The fracture specimens (B=1.65, W=3.3 and L = 18 mm) were by EDM notched with a 0° flank angle to an  $a/W \approx 0.5$  with a nominal root radius  $r = 0.15$  mm that was then razor-press sharpened prior to testing. However, since they were not fatigue pre-cracked, the sharp *notch* fracture toughness is designated as  $K_{Ic}$ . Fractographic characterization was carried out using a SEM FEI XL-40.

## Results and Discussion

The densities of 14YWT1000 and 14YWT1150 were  $7.91 \pm 0.02$  and  $7.92 \pm 0.06$ , respectively, indicating full consolidation. For example, the density of a wrought alloy with a similar composition (~81wt%Fe, 13%Cr, 3%W) is  $7.86 \text{ g/cm}^3$  [10]. This conclusion was further supported by the failure to observe porosity by optical microscopy.

TEM showed similar, roughly 50-50% fine and coarse ferrite mixture of ferrite grains (see Figures. 1a and c) in both 14YWT1000 and 14YWT1150. The fine ferrite grains are ~200 nm in diameter. The coarser grains have wide size distribution, ranging from about one to several tens of  $\mu\text{m}$ . The larger ferrite grains are presumably the result of recovery and growth in regions with a lower density of fine scale precipitates phases, including both nm scale Y-Ti-O clusters and slightly larger  $\text{Ti}_2\text{Y}_2\text{O}_7$  pyrochlore oxides [11]. Similar bimodal distributions have also been observed in ODS Eurofer [12]. Dislocation densities in the fine ferrite grains are higher than in the coarse grains (Figures 1b and d).

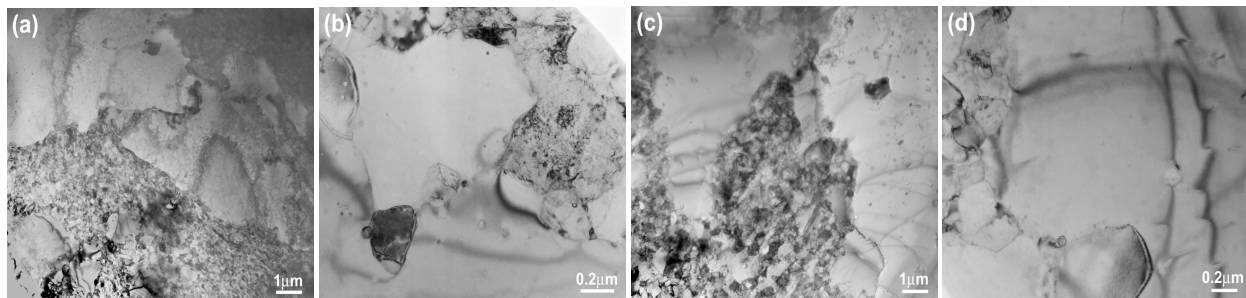


Figure 1. Microstructure of (a) and (b) 14YWT1000 and (c) and (d) 14YWT1150 at low (a and c) and medium (b and d) resolution.

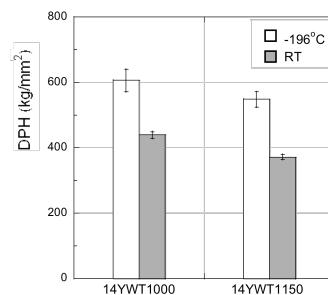


Figure 2. The effect of the HIPing temperature on microhardness.

As shown in Figure 2, hardness at room temperature and  $-196^{\circ}\text{C}$  decreases with increasing in HIPing temperature. These results are reasonably consistent with previous data on similar alloys reported by Alinger et al [5, 13], who found that the nano-sized particles sizes increase and their number densities decrease with higher HIPing temperature. The similarity in the grain structures in 14YWT1000 and 14YWT1150 suggests that the recovery and grain growth is resisted in regions with high nano-scale particle densities in both cases.

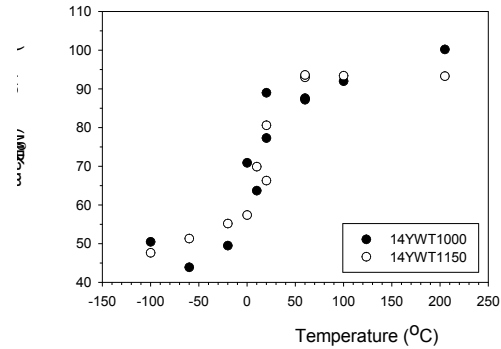


Figure 3. The variation of  $K_p$  with temperature for 14YWT1000 and 14YWT1150.

The variation of the  $K_p$  of 14YWT1000 and 14YWT1150 with temperature is shown in Figure 3. Although the strengths of these alloys are different, their TT of  $\approx 10^{\circ}\text{C}$  and  $K_p(T)$  curves are nearly identical.

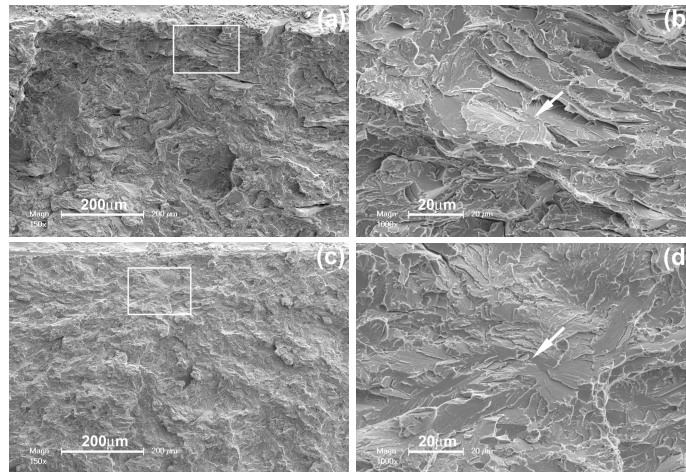


Figure 4. Low (a and c) and intermediate (b and d) magnification fractographic images of 14YWT1000 (a and b) 14YWT1150 (c and d) specimens fractured at  $-100^{\circ}\text{C}$ .

These results may suggest that the bimodal grain structure may be more important than strength in controlling fracture in these NFAs. Fractographic observations support this hypothesis. Figures 4 and 5 show fracture on the lower shelf at  $-100^{\circ}\text{C}$  by pure cleavage (Figure 4), and by a ductile microvoid nucleation, growth and coalescence on the upper-shelf at  $200^{\circ}\text{C}$  (Figure 5). However, even at the higher temperatures, isolated cleavage facets are observed. Higher magnification examination of suspected initiation sites (framed and arrowed in Figures 4) at  $-100^{\circ}\text{C}$  suggest that the cleavage is triggered by the fracture of large particles or, perhaps extra hard grains, surrounded by facet sizes that are larger than  $\approx 5$  to  $10\ \mu\text{m}$ , consistent with the corresponding sizes of the coarser ferrite grains. The conclusion is even

clearer in the fractographs shown in Figure 5 showing disproportionate importance of the larger grains in cleavage fracture at 200°C.

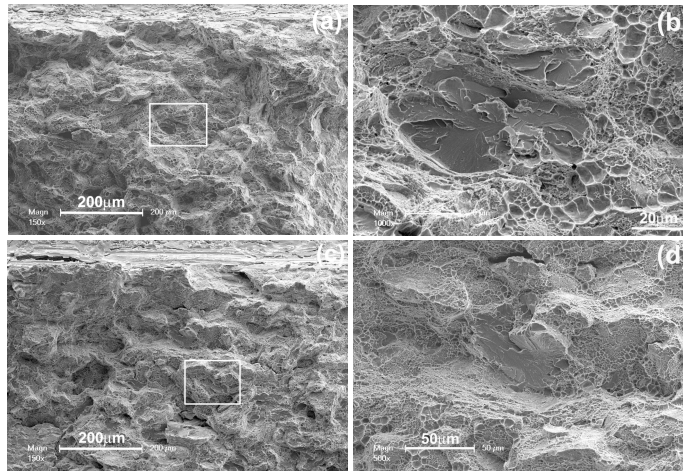


Figure 5. Low (a and c) and intermediate (b and d) magnification fractographic images of 14YWT1000 (a and b) 14YWT1150 (c and d) specimens fractured at 200°C.

## Discussion

The breakdown in the usual higher strength-lower toughness relation is not fully understood. One possibility is that dislocation pile-ups in the larger and softer coarse grains trigger cleavage, perhaps by fracturing smaller harder grains or brittle particles. In this case, differences in the average strength of the alloy may be less significant than similarities in the grain structures. Indeed, if the larger grains are softer, the effect on the size of the pile up may offset the corresponding effect of higher strength.

Nano-indentation studies will be used to explore strength variations between larger and smaller grains. Additional studies to characterize the NFAs nano-microstructures, constitutive properties and sharp fatigue pre-crack fracture toughness are ongoing. Note this study will be extended to HIPing at 850°C, which was part of the original test matrix; however, due to a failure in the HIP in this case, the resulting 14YWT850 alloy, with a DPH of  $588 \pm 25 \text{ kg/mm}^2$ , was not fully consolidated. Hence, the 14YWT850 was not fracture tested.

These preliminary results suggest that producing alloys with a more uniform and finer distribution of grain sizes would lead to higher toughness and lower TT. Of course, developing processing routes that lead to more homogeneous nano-microstructures is a more generally desirable objective.

## Concluding Remarks

High density, pore-free 14YWT NFAs were processed by HIPing mechanically alloyed powders at 1000°C and 1150°C. Both alloys contained similar distributions of fine ( $\approx 200\text{nm}$ ) and coarse (one to several tens of  $\mu\text{m}$ ) ferrite grains. The 14YWT1000 is substantially stronger than 14YWT1150, as expected. However, both alloys have similar notch fracture toughness with a TT  $\approx 10^\circ\text{C}$ . We hypothesize that the toughness is primarily mediated by the coarser ferrite grains in a way that is relatively insensitive to the alloy strength. Processing paths that produce finer and more homogeneous microstructures offer the promise of higher toughness, along with an optimized balance of properties.

**References**

- [1] M. J. Alinger, G. R. Odette, and G. E. Lucas, J. Nucl. Mater. 307-311 (2002) 484.
- [2] R. L. Klueh, J. P. Shingledecker, R. W. Swindeman, and D. T. Hoelzer, J. Nucl. Mater. 341 (2005) 103.
- [3] R. L. Klueh, P. J. Maziasz, I. S. Kim, L. Heatherly, D. T. Hoelzer, N. Hashimoto, E. A. Kenik, and K. Miyahara, J. Nucl. Mater. 307-311 (2002) 773.
- [4] T. Yamamoto et al., Journal of Nuclear Materials (to be published).
- [5] M. J. Alinger, G. R. Odette, and D. T. Hoelzer, J. Nucl. Mater. 329-333 (2004) 382.
- [6] S. Ukai and M. Fujiwara, J. Nucl. Mater. 307-311 (2002) 749.
- [7] A. Alamo, V. Lambard, X. Averty, and M. H. Mathon, J. Nucl. Mater. 329-333 (2004) 333.
- [8] T. Kuwabara, H. Kurishita, S. Ukai, M. Narui, and S. Mizuta, J. Nucl. Mater. 258-263 (1998) 1236.
- [9] T. S. Chou and H.K.D.H. Bhadeshia, Metall. Trans. 24A (1993) 773.
- [10] C. T. Lynch, CRC Handbook of Materials Science, CRC Press, Cleveland, Ohio, 1974, Vol. 2, 105.
- [11] H. Kishimoto, M. J. Alinger, G. R. Odette, and T. Yamamoto, J. Nucl. Mater. 329-333 (2004) 369.
- [12] C. Cayron, E. Rath, I. Chu, and S. Launois, J. Nucl. Mater. 335 (2004) 83.
- [13] M. J. Alinger, Ph.D. dissertation, University of California, Santa Barbara, 2004.

**THE MICROSTRUCTURE AND STRENGTH PROPERTIES OF MA957 NANOSTRUCTURED FERRITIC ALLOY JOINTS PRODUCED BY FRICTION STIR AND ELECTRO-SPARK DEPOSITION WELDING**—P. Miao, G. R. Odette (University of California, Santa Barbara), J. Gould, J. Bernath (Edison Welding Institute), R. Miller (DDL-OMNI), M. Alinger (University of California, Santa Barbara, University of California, Berkeley) and C. Zanis (DDL-OMNI)

## **OBJECTIVE**

This work is to investigate joining methods and their effects on microstructures and mechanical properties of nanostructured ferrite alloys.

## **SUMMARY**

The nanostructured ferritic alloy (NFA) MA957 was joined by friction stir welding (FSW) and electro-sparked deposition (ESD) welding. Transmission electron microscopy (TEM) and small angle neutron scatter (SANS) characterization studies showed a uniform fine-scale equiaxed ferrite structure with a high density of dislocations and only slightly coarsened nm-scale particles in the joint region of the FSW weld compared to the base metal. Microhardness and tensile measurements on the FSW showed a modest reduction in the strength of the joint compared to the as-processed MA957. In contrast, the ESD welds contained considerable porosity and the nm-scale particles dissolved or coarsened significantly, resulting in a larger degradation of the joint region strength. Thus FSW is a promising method for joining NFAs.

## **PROGRESS AND STATUS**

### **Introduction**

Nanostructured Fe-14Cr-W-Ti-Y<sub>2</sub>O<sub>3</sub> dispersion strengthened ferritic alloys (NFAs) have outstanding low temperature tensile (> 1 GPa) and high temperature creep strengths [1-3] and also offer a potential for mitigating radiation damage, including the effects of high helium levels [4, 5] in fusion reactor environments. The excellent properties of NFAs primarily derive from a very high density of Y-Ti-O nm-scale precipitate phases that form when mechanically alloyed powders (pre-alloyed Fe-14Cr-W-Ti plus Y<sub>2</sub>O<sub>3</sub>) by milling are consolidated by hot isostatic pressing (HIPing) or extrusion [5-8]. These phases include small solute clusters rich in Y-Ti and O and slightly larger Ti<sub>2</sub>Y<sub>2</sub>O<sub>7</sub> pyrochlore oxides. Henceforth, we will refer to these features as nm-scale particles (NSP) encompassing a size range up to ≈ 8 nm. Thus, a critical issue is producing and maintaining the NSP through all stages processing and fabrication, as well as in high temperature service in irradiation environments.

Thus a major challenge to the use of NFAs is joining. Conventional fusion welding methods are generally not useful, since the NSP would be expected to dissolve during typical melting-solidification processes. Joining processes, that either avoid melting completely, or that involve very rapid melting and re-solidification, may preserve the NSP. In this work we explore two such possible joining methods. FSW is a solid-state joining process that involves mechanical mixing of base metals under severe deformation conditions [9, 10]. The material in and near a FSW joint experiences a moderately high temperature cycle, with peak temperatures up to ≈1300 to 1400°C, but there is no melting. Thus, in principle, FSW may or may not severely damage the NSP. Further, dynamic recrystallization during FSW refines the grains in the stir zone, and further severe deformation induces a high dislocation density [11, 12]. Thus, fine scale FSW microstructures may provide an optimal balance of mechanical properties. ESD welding uses a rapid discharge power source to supply short-duration current pulses to a moving electrode in contact with a substrate [13]. The pulses produce extremely rapid heating, leading to melt droplet formation and deposition in the weld zone as relatively thin splats that cool at very high rates. Thus, in principle, the rapid ESD temperature cycle might allow some of the NSP to survive in the joint region.

## Experimental

A commercial MA957 alloy bar of 25mm (diameter)  $\times$  100mm (length) with a nominal composition of Fe-14wt% Cr, 0.9% Ti, 0.3% Mo, and 0.25%  $Y_2O_3$  was sectioned into  $100 \times 17 \times 2 \text{ mm}^3$  and  $10 \times 17 \times 2 \text{ mm}^3$  slabs for FSW and ESD welding, respectively. FSW butt-welding in the long dimension direction was produced at a tool spindle speed of 130 to 160 rpm and travel speed of 150 – 200 mm/min [10]. Other details of the FSW method and tooling are proprietary. The ESD but-welding was performed with an electrode ground from the MA957 using an Advanced Surfaces and Processes (ASAP) system at a pulse rate of 400 Hz and voltage of 150 V. The butted base metal sections were ground to a  $\approx$  half thickness radius and then filled by the ESD deposit, one side at a time.

The nano-microstructures of the MA957 weld and base metals were characterized by TEM (JEOL2010HR), SANS (NG1 at the National Institute of Standards and Technology) and optical microscopy. Standard 3 mm TEM discs, either centered in the weld region or taken from the base metal, were ground to a thickness of  $\sim 0.15 \text{ mm}$  and then thinned to electron transparency in a TENUPO twin-jet electro-polisher with  $H_2SO_4 + 80\%CH_3OH$  at room temperature. TEM images for the measurement of the NSP and larger oxide particles were taken in the same foil orientation (near [011]) for the MA957 weld and base metals. Details of the experiment, data reduction and analysis for SANS are given elsewhere [14].

The room temperature strength of the FSW and ESD-welded MA957 were evaluated both by microhardness traverses across the weld and tensile tests using subsized flat dogbone specimens with a reduced gauge section in the weld and heat-affected zone transverse to the weld axis. The corresponding tensile tests carried out on the base metal were for the same orientation.

## Results and Discussion

As seen in Figure 1a, the MA957 base metal has typical fine scale elongated ferrite grains along the extrusion direction. In contrast, as seen in Figure 1b, the severe plastic deformation during FSW produces a uniform distribution of fine scale equiaxed grains, containing a significant density of dislocations. The optical macro and micrographs in Figure 2 show that after the ESD welding process produces a layered structure, composed of large number of droplet-scale deposits (Figure 2a) along with considerable porosity (Figure 2b). Such structures are typical of ESD depositions carried out in air, and clearly do not represent an acceptable joint product. Note, however, the process could be modified to minimize the porosity. Thus the major issue of concern here for the ESD welds is the fate of the NSP.

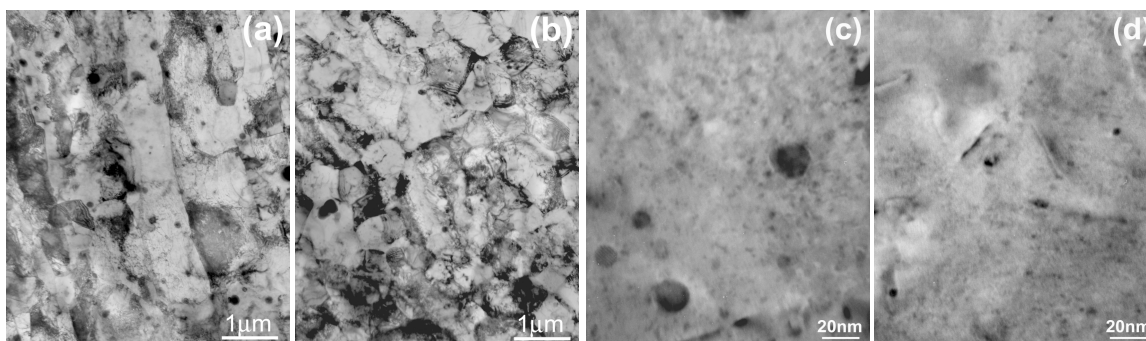


Figure 1. TEM image of the grain and dislocation microstructure in the MA957 (a) base metal and (b) FSW and the NSP and larger oxide particles in (c) base metal and (d) FSW.

As seen in the TEM micrographs in Figures 1c and d, there is a high density of NSP in both the base (Figure 1c) and FSW weld (Figure 1d) metals. Based on convergent beam estimates of the foil thickness, the particle size and volume fraction distributions are shown in Figures 3a and b and the corresponding

NSP parameter averages are shown in Table 1. Note rather large particles, with diameters greater than about 8 nm, are included in these assessments, and represent what is considered to be a second population of oxide phases that contribute significantly to the overall volume fraction estimated by TEM.

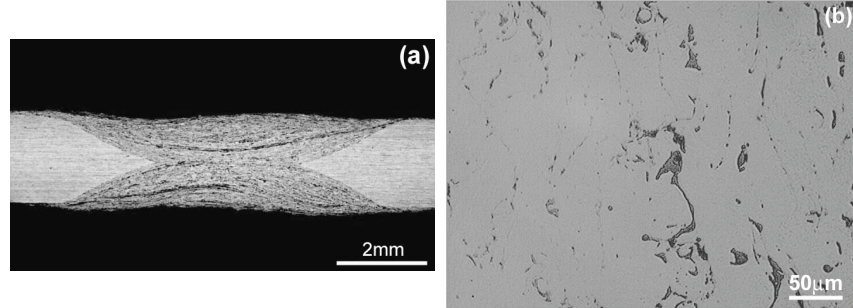


Figure 2. (a) Macrograph and (b) micrograph (unetched) of the MA957 ESD weld.

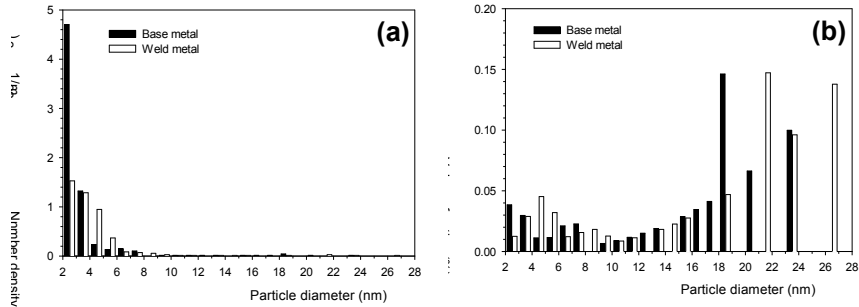


Figure 3. (a) The number density and (b) the volume fraction of the NSP and larger oxide particles in the MA957 FSW and base metal found in the TEM studies.

Table 1. The average NSP and larger oxide particle parameters found in the TEM studies and NSP parameters measured by the SANS in the MA957 FSW, ESD and base metal

NSP and Larger Oxide Parameters		Base metal	FSW	ESD
Average diameter (nm)	TEM	3.4	4.1	
	SANS	2.4	2.5	4.7
Number density ( $\times 10^{23}$ , $1/m^3$ )	TEM	0.68	0.45	
	SANS	8.5	3.5	0.25
Volume fraction (%)	TEM	0.61	0.69	
	SANS	0.6	0.25	0.12

The TEM on the FSW shows only a slight coarsening of the NSP, with a nominal increase in the particle diameter from  $\approx 3.4$  to  $4.1$  nm and a reduction in number density from  $\approx 0.68$  to  $0.45 \times 10^{23}/m^3$ . The volume fraction is approximately constant of  $\approx 0.67\%$  (FSW) versus  $0.6\%$  (base metal). However, there are two important caveats. First, the smallest NSP cannot be imaged in TEM. Second the features observed in TEM may include some surface deposit artifacts. Both of these limitations indicate the need for the use of other techniques.

SANS characterization of both the FSW and ESD joints was carried out on the NG1 instrument at NIST. Because of the small size and somewhat irregular shape of the weld specimens, it was not possible to

experimentally establish the magnetic to nuclear scattering ratio (M/N) in this case. However, the relative shapes and positions of the SANS curves at  $45^\circ$  to the direction of the magnetic field, shown in Figure 4, can be qualitatively interpreted to show that FSW decreases the number density and volume fraction and spreads the size distribution of NSP. The ESD process has a larger effect, leading to a greater increase in the size and a large reduction in the number density and volume fraction of the NSP. The absolute magnitudes of the scattering curves can be estimated assuming a typical  $M/N = 1$  for MA957. Corresponding fits to these cross sections, assuming the particles are non-magnetic, can be used to derive the NSP parameters that are summarized in Table 1.

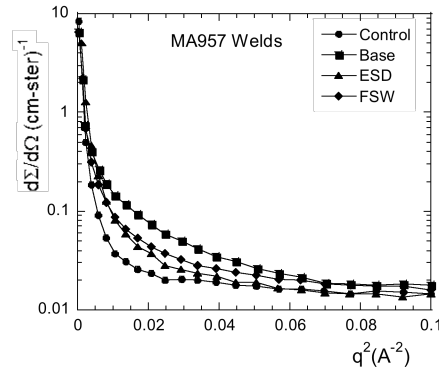


Figure 4. SANS cross section curves at a  $45^\circ$  angle to the direction of the magnetic field.

Clearly the SANS shows the presence of smaller and more numerous NSP compared to TEM. This is expected since: a) the SANS is optimized to detect small NSP features while it is blind to the larger features; and b) TEM does not see the smallest and most numerous NSP.

Because of their limitations, neither the SANS nor TEM quantitative results should be taken too literally. However, they are broadly consistent with each other, and clearly show that while FSW reduces the number and volume fraction of NSP, the overall effects are relatively modest. In contrast the ESD welding process has a much larger effect on the NSP, consistent with a larger reduction in their hardening contribution, by estimated factors of at least 2 to 4, depending on assumptions about changes in the particle strength factors as obstacles to dislocation glide.

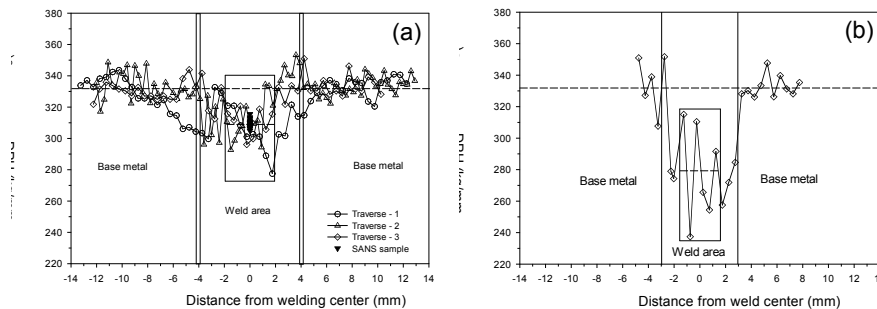


Figure 5. Microhardness profile across the welds of (a) FSW- and (b) ESD-welded MA957.

Vicker's diamond pyramid hardness (DPH) traverses at 500g load across the FSW and ESD welds are shown in Figure 5. Figure 5a for the FSW also includes measurements on a SANS specimen on the weld axis. The strength decreases from the edge of the weld and is a minimum near the center. The average DPH value in the central weld region of the FSW-welded MA957 for various indent sequences ranged from  $309 \pm 10 \text{ kg/mm}^2$  or about 7% lower than for the base metal value of  $332 \pm 10 \text{ kg/mm}^2$ . In contrast, the

average DPH ( $279 \pm 31 \text{ kg/mm}^2$ ) in the central weld region of the ESD-weld shown in Figure 5b is  $\approx 16\%$  lower compared the base metal.

As shown in Table 2, the ultimate tensile strength UTS was decreased by  $\approx 9\%$  in the FSW and by  $\approx 37\%$  in the ESD weld. Thus tensile results for the FSW are consistent with the decrease in hardness in the weakest part stir zone. The larger decrease in the tensile strength of the ESD weld, compared to the hardness drop, is probably due to the presence of porosity in this case.

Table 2. UTS of base and weld metal in the FSW- and ESD-welded MA957

Property	Base metal	FSW	ESD
UTS (MPa)	$1035 \pm 3$	942	$656^a$

<sup>a</sup>Only one specimen was tested.

## Discussion

With regard to the key question about the fate of the NSP, the SANS results of this study suggest that FSW produces a larger degradation of the smallest features, but even in this case it is on the order of a 50% reduction in the number density and volume fraction. Somewhat larger features are only slightly coarsened. This behavior may be due to a combination of the transient high temperatures during FSW, and very severe deformation that results in mechanical dissolution of the small particles by dislocation cutting processes. This conclusion is consistent with the previous observation that small NSP are not strong dislocation Orowan-type barriers. Note, such mechanical cutting may also play a role in the initial mechanical alloying process. The FSW also produces beneficial changes in the microstructure, by refining the grains and making them equiaxed, as well as increasing the dislocation density. The net result is a minimal decrease in the strength of the FSW joint ( $<10\%$ ). In contrast to the FSW case, the ESD joining process appears to be far less promising. In spite of the rapid sequence of melting and solidification the NSP are severely degraded.

## Summary and Conclusions

The FSW produced an attractive high strength joint of MA957 with a uniform fine-scale and equiaxed ferrite structure as well as a significant density of dislocations in the severely plastically deformed joint stir region. The NSP were only slightly degraded during welding in this case. FSW decreased the alloy hardness and ultimate tensile strength by less than 10% compared to the base metal. The ESD MA957 welds contained porosity and the NSP were severely degraded during the melting-resolidification sequence. These microstructural changes resulted in a significant degradation of mechanical properties from  $\approx 16\%$  (hardness) to  $\approx 37\%$  (UTS) compared to the MA957 base metal. Hence, ESD welding does not appear to be a promising method for joining NFA.

## References

- [1] M. J. Alinger, G. R. Odette, and G. E. Lucas, *J. Nucl. Mater.* 307-311 (2002) 484.
- [2] R. L. Klueh, J. P. Shingledecker, R. W. Swindeman, and D. T. Hoelzer, *J. Nucl. Mater.* 341 (2005) 103.
- [3] R. L. Klueh, P. J. Maziasz, I. S. Kim, L. Heatherly, D. T. Hoelzer, N. Hashimoto, E. A. Kenik, and K. Miyahara, *J. Nucl. Mater.* 307-311 (2002) 773.
- [4] T. Yamamoto et al., *Journal of Nuclear Materials* (to be published).
- [5] M. J. Alinger, G. R. Odette, and D. T. Hoelzer, *J. Nucl. Mater.* 329-333 (2004) 382.
- [6] M. K. Miller, D. T. Hoelzer, E. A. Kenik, and K. F. Russel, *J. Nucl. Mater.* 329-333 (2004) 338.
- [7] S. Ukai and M. Fujiwara, *J. Nucl. Mater.* 307-311 (2002) 749.
- [8] M. Klimenkov, R. Lindau, and A. Möslang, *J. Crystal Growth* 249 (2003) 381.
- [9] W. M. Thomas and E. D. Nicholas, *Materials & Design* 18 (1997) 269.
- [10] J. Bernath and J. Gould, Report on Development of Candidate Joining Technology for MA957 Sheet, March 2005, Edison Welding Institute, Columbus, Ohio, USA.

- [11] Y. S. Sato, T. W. Nelson, C. J. Sterling, R. J. Steel, and C.-O. Pettersson, *Mater. Sci. Eng. A397* (2005) 376.
- [12] K. V. Jata, K. K. Sankaran, and J. J. Ruschau, *Metall. Mater. Trans. 31A* (2000) 2181.
- [13] G. L. Sheldon and R. N. Johnson, *Electro-spark deposition—a technique for producing wear resistant coatings*, Ed., K. C. Ludema, *Wear of Materials*, ASME, New York, 1985.
- [14] M. J. Alinger, Ph.D. dissertation, University of California, Santa Barbara, 2004.

**MECHANICAL PROPERTIES OF NEUTRON-IRRADIATED NICKEL-CONTAINING MARTENSITIC STEELS: I. EXPERIMENTAL STUDY\***—R. L. Klueh, N. Hashimoto, and M. A. Sokolov (Oak Ridge National Laboratory), K. Shiba and S. Jitsukawa (Japan Atomic Energy Research Institute)

**OBJECTIVE**

Tensile and Charpy specimens of 9Cr-1MoVNb (modified 9Cr-1Mo) and 12Cr-1MoVW (Sandvik HT9) steels and these steels doped with 2% Ni were irradiated at 300 and 400°C in the High Flux Isotope Reactor (HFIR) up to  $\approx 12$  dpa and at 393°C in the Fast Flux Test Facility (FFTF) to  $\approx 15$  dpa. In HFIR, a mixed-spectrum reactor, (n,  $\alpha$ ) reactions of thermal neutrons with  $^{58}\text{Ni}$  produce helium in the steels. Little helium is produced during irradiation in FFTF.

After HFIR irradiation, the yield stress of all steels increased, with the largest increases occurring for nickel-doped steels. The ductile-brittle transition temperature (DBTT) increased up to two times and 1.7 times more in steels with 2% Ni than in those without the nickel addition after HFIR irradiation at 300 and 400°C, respectively. Much smaller differences occurred between these steels after irradiation in FFTF. The DBTT increases for steels with 2% Ni after HFIR irradiation were 2–4 times greater than after FFTF irradiation. Results indicated there was hardening due to helium in addition to hardening by displacement damage and irradiation-induced precipitation.

**SUMMARY**

The 9Cr-1MoVNb and 12Cr-1MoVW steels and these steels with 2% Ni additions were irradiated in HFIR to  $\approx 10$  dpa at 300°C and  $\approx 12$  dpa at 400°C and in FFTF to  $\approx 15$  dpa at 393°C. After irradiation in HFIR, steels with 2% Ni hardened more than steels without a nickel addition. When 9Cr-1MoVNb-2Ni, 12Cr-1MoVW, and 12Cr-1MoVW-2Ni steels were irradiated in HFIR at 400°C, they hardened more than when irradiated in FFTF at 393°C. The 9Cr-1MoVNb steel hardened to the same level in both FFTF and HFIR. For all but the 9Cr-1MoVNb steel, shifts in DBTT of the steels irradiated in HFIR were greater than shifts for the same steels irradiated in FFTF. Irradiation in HFIR at 300 and 400°C caused a larger shift for the steels containing 2% Ni than for the steels with no nickel addition. The increase in DBTT was related to the increase in yield stress. Despite the uncertainty inherent in the experiments, the results lead to the conclusion that helium caused an increment of hardening that contributed to the extra shift in DBTT over that observed after irradiation in FFTF where little helium formed.

**PROGRESS AND STATUS**

**Introduction**

Irradiation of a ferritic/martensitic steel first wall of a tokamak fusion reactor by 14 MeV neutrons from the deuterium/tritium fusion reaction will cause displacement damage and production of large amounts of transmutation helium ( $\approx 10$  appm He/dpa) in the steel. Because no fusion reactor or intense 14-MeV neutron source exists, fusion neutron irradiation effects cannot be studied directly at appropriate damage levels. Fission reactors with neutron energies greater than  $\approx 0.1$  MeV can be used to study displacement damage. However, helium formed in a fusion reactor first wall is produced by high-energy neutrons ( $\geq 5$  MeV), and in the absence of an intense 14 MeV neutron source, special techniques are required to simulate the simultaneous production of helium and displacement damage.

Simultaneous displacement damage and helium formation can be produced in alloys containing nickel by irradiating in a mixed-spectrum fission reactor, where displacement damage is produced by fast neutrons in the spectrum, and helium forms by a two-step reaction of  $^{58}\text{Ni}$  with thermal neutrons in the spectrum. Natural nickel contains 68%  $^{58}\text{Ni}$ . For steel with  $\approx 2\%$  Ni, irradiation to  $\geq 10$  dpa in the mixed-spectrum High Flux Isotope Reactor (HFIR) at the Oak Ridge National Laboratory (ORNL) produces a similar

---

\*This paper has been accepted for publication in *Journal of Nuclear Materials*.

helium to displacement damage ratio ( $\approx 10$  appm/dpa) as attained in the undoped steel in a tokamak first wall. Below  $\approx 10$  dpa, the ratio is somewhat lower.

Previous papers reported on the tensile [1–3] and Charpy [4–7] behavior of commercial 9Cr-1MoVNb (modified 9Cr-1Mo) and 12Cr-1MoVW (Sandvik HT9)<sup>†</sup> steels and these steels with 1 and 2% Ni after irradiation in HFIR, where larger amounts of helium form, and in the Experimental Breeder Reactor (EBR-II) and Fast Flux Test Facility (FFTF), fast reactors where little helium forms. In this paper, results are presented from further studies of these steels irradiated in the FFTF and HFIR.

## Experimental Procedure

Electroslag remelted heats of 9Cr-1MoVNb ( $\approx 0.1\%$  Ni) and 12Cr-1MoVW ( $\approx 0.5\%$  Ni) steels were prepared by Combustion Engineering Inc., Chattanooga, Tennessee. Similar compositions with 2% Ni, designated 9Cr-1MoVNb-2Ni and 12Cr-1MoVW-2Ni, were also produced. Chemical compositions are given in Table 1.

Table 1. Composition of the steels (wt %)

Element <sup>a</sup>	9Cr-1MoVNb		12Cr-1MoVW	
	Standard	2% Ni	Standard	2% Ni
C	0.09	0.064	0.21	0.20
Mn	0.36	0.36	0.50	0.49
P	0.008	0.008	0.011	0.011
S	0.004	0.004	0.004	0.004
Si	0.08	0.08	0.18	0.14
Ni	0.11	2.17	0.43	2.27
Cr	8.62	8.57	11.99	11.71
Mo	0.98	0.98	0.93	1.02
V	0.209	0.222	0.27	0.31
Nb	0.063	0.066	0.018	0.015
Ti	0.002	0.002	0.003	0.003
Co	0.013	0.015	0.017	0.021
Cu	0.03	0.04	0.05	0.05
Al	0.013	0.015	0.030	0.028
W	0.01	0.01	0.54	0.54
As	<0.001	<0.001	<0.001	<0.002
Sn	0.003	0.003	0.003	0.002
N	0.050	0.053	0.020	0.017
O	0.007	0.006	0.005	0.007

<sup>a</sup><0.001 B, <0.001 Zr, balance Fe

Sheet tensile specimens 25.4-mm long with a reduced gage section 7.62-mm long by 1.52-mm wide by 0.76-mm thick were machined from 0.76-mm sheet. Miniature ( $\frac{1}{3}$ -size) Charpy specimens 3.3 mm x 3.3 mm x 25.4 mm with 0.51-mm-deep notch and 0.05-0.08-mm root radius were machined from 16-mm thick plates.

Steels were irradiated in the normalized-and-tempered condition: austenitization was 0.5 h at 1050°C followed by a rapid cool in flowing helium gas; tempering was 5 h at 700°C.

Two irradiation capsules containing sixteen 25.4-mm-long specimen positions were irradiated in the HFIR peripheral target positions with specimens at nominal temperatures of 300 and 400°C. At each position, either four  $\frac{1}{3}$ -size Charpy specimens, four SS-3 tensile specimens, or about 100 transmission electron

<sup>†</sup>The commercial steels modified 9Cr-1Mo and Sandvik HT9 will be referred to by the generic designations 9Cr-1MoVNb and 12Cr-1MoVW, respectively.

microscopy (TEM) specimens in a 12Cr steel subcapsule were enclosed in 12Cr steel holders that were then encapsulated in aluminum sleeves. To control the temperature by nuclear heating, the gas gap between the outer diameter of the steel specimen holder and the aluminum sleeve was adjusted to compensate for the variation in nuclear heating rate along the length of the capsule. A thermal gradient of  $<45^{\circ}\text{C}$  was calculated to exist from the interior to the exterior of the Charpy specimens.

Each capsule contained three flux monitors to determine fluence as a function of distance from the HFIR midplane. Total maximum fluence at the midplane was  $6.9 \times 10^{26} \text{ n/m}^2$ , with a thermal fluence of  $3.2 \times 10^{26} \text{ n/m}^2$  ( $<0.5\text{eV}$ ) and a fast fluence of  $1.68 \times 10^{26} \text{ n/m}^2$  ( $>0.1 \text{ MeV}$ ). Maximum displacement damage at the midplane was  $\approx 12 \text{ dpa}$ . Only specimens at the center position along the length of the capsule received the peak fluence. Therefore, displacement damage and the helium concentration of the specimens varied depending on their position in the capsule relative to the reactor midplane.

Two tensile specimens and 4–6 Charpy specimens of each steel were irradiated. Specimens irradiated at  $300^{\circ}\text{C}$  were at the ends of the capsules and received 9–10 dpa. Displacement damage in specimens irradiated at  $400^{\circ}\text{C}$  was 11–12 dpa.

Charpy and tensile specimens were also irradiated at  $\approx 393^{\circ}\text{C}$  in the FFTF in the Materials Open Test Assembly (MOTA), where the temperature of the specimens was monitored and maintained at  $\pm 5^{\circ}\text{C}$ . Tensile specimens were irradiated to  $3.59 \times 10^{26} \text{ n/m}^2$  ( $E > 0.1 \text{ MeV}$ ),  $\approx 15 \text{ dpa}$ , and Charpy specimens were irradiated to  $2.99 \times 10^{26} \text{ n/m}^2$  ( $E > 0.1 \text{ MeV}$ ),  $\approx 12.4 \text{ dpa}$ .

The TEM specimens were thinned using an automatic Tenupol electropolishing unit located in a shielded glove box. Disks were examined using a JEM-2000FX ( $\text{LaB}_6$ ) transmission electron microscope. Foil thickness was measured using thickness fringes in order to evaluate quantitative defect density values.

## Results

### Tensile Behavior

Before irradiation, there was little difference in the yield stress and ultimate tensile strength of the respective steels with and without the 2% Ni addition (Table 2). Irradiation in HFIR caused an increase in the 0.2% offset yield stress and ultimate tensile strength, with the largest effect at  $300^{\circ}\text{C}$ . The 9Cr-1MoVNb-2Ni steel hardened more than 9Cr-1MoVNb, and the 12Cr-1MoVW-2Ni hardened more than 12Cr-1MoVW at both 300 and  $400^{\circ}\text{C}$ , indicating a possible helium (or nickel) effect. Irradiation caused a decrease in uniform and total elongations (Table 2).

After irradiation in FFTF, there was little difference in the increase in yield stress ( $\Delta\sigma_y$ ) of the steels with different nickel concentrations (Table 2). The  $\Delta\sigma_y$  for 9Cr-1MoVNb without and with nickel were 135 and 165 MPa, respectively, and for 12Cr-1MoVW without and with nickel were 255 and 254 MPa, respectively.

When the steels irradiated in HFIR and FFTF are compared, there is no difference in yield stress [Fig. 1(a)] and ultimate tensile strength [Fig. 1(b)] of 9Cr-1MoVNb steel irradiated in HFIR and FFTF at 400 and  $393^{\circ}\text{C}$ , respectively, but the rest of the specimens showed more hardening after irradiation in HFIR. For the yield stress, a 15, 10, and 17% difference was observed for the 9Cr-1MoVNb-2Ni, 12Cr-1MoVW, and 12Cr-1MoVW-2Ni steels, respectively. Differences in the ultimate tensile strengths were slightly less.

### Charpy Behavior

Irradiation caused an increase in the DBTT ( $\Delta\text{DBTT}$ ) and a reduction in the USE for all specimens irradiated at 300 and  $400^{\circ}\text{C}$  in HFIR and at  $393^{\circ}\text{C}$  in FFTF (Table 3). The HFIR results indicated a larger  $\Delta\text{DBTT}$  for steels irradiated at  $300^{\circ}\text{C}$  than at  $400^{\circ}\text{C}$  (Fig. 2). Irradiations at  $300^{\circ}\text{C}$  produced a larger shift in DBTT for the steels with the 2% Ni, with the largest effect occurring for the 9Cr-1MoVNb-2Ni steel, where the shift was over twice that for the steel with no nickel addition. A smaller difference ( $\approx 1.4$  times)

Table 2. Tensile properties<sup>a</sup> of steels unirradiated and irradiated in HFIR<sup>b</sup> and FFTF<sup>c</sup>

Steel	Irradiation T(°C)/dpa/He(appm)	Strength <sup>d</sup> (MPa)		Elongation (%)		$\Delta\sigma_y$ (MPa)
		Yield	Ultimate	Uniform	Total	
9Cr-1MoVnb	300	673	734	3.5	12.3	
HFIR	300/7/7	1078	1078	0.3	6.4	405
	400	633	693	2.5	10.6	
HFIR	400/12/12	772	792	1.1	7.2	139
FFTF	393/15/<3	768	795	1.4	5.3	135
9Cr-1MoVnb-2Ni	300	679	768	3.3	11.0	
HFIR	300/8/68	1234	1241	0.5	6.0	555
	400	645	723	2.7	9.3	
HFIR	400/12/129	958	958	0.4	6.3	313
FFTF	393/15/<3	810	840	1.6	5.8	165
12Cr-1MoVW	300	690	804	5.5	11.7	
HFIR	300/6/11	1135	1150	0.8	5.0	445
	400	665	763	3.7	10.1	
HFIR	400/12/31	1025	1048	0.8	2.6	360
FFTF	393/15/<3	920	973	1.8	5.1	255
12Cr-1MoVW-2Ni	300	641	818	4.0	10.7	
HFIR	300/6/48	1165	1206	2.6	2.9	524
	400	649	781	3.6	10.4	
HFIR	400/12/141	1093	1113	1.0	1.9	444
FFTF	393/15/<3	903	965	1.8	5.4	254

<sup>a</sup>Values are the average of two tests.

<sup>b</sup>Specimens were irradiated in HFIR to 9–10 dpa at 300°C and 11–12 dpa at 400°C.

<sup>c</sup>Specimens were irradiated in FFTF to  $\approx 15$  dpa at 393°C.

<sup>d</sup>The test temperature was the same as the irradiation temperature for the HFIR-irradiated specimens; it was 400°C for the FFTF-irradiated specimens.

occurred for the 12 Cr steels, where the difference in helium concentration of the two steels was less (Table 1). A similar effect was observed for the steels after irradiation in HFIR at 400°C, where the  $\Delta$ DBTT for 9Cr-1MoVnb-2Ni was  $\approx 1.7$  times that for 9Cr-1MoVnb and that for 12Cr-1MoVW-2Ni was  $\approx 1.6$  times that for 12Cr-1MoVW.

The  $\Delta$ DBTTs for the 9Cr-1MoVnb steel were similar after irradiation at 400°C in HFIR and 393°C in FFTF (Fig. 2). For the 9Cr-1MoVnb-2Ni steel, however, the  $\Delta$ DBTT after HFIR irradiation at 400°C was four times greater than after irradiation in FFTF at 393°C. The  $\Delta$ DBTTs for the 12Cr-1MoVW and 12Cr-1MoVW-2Ni after irradiation in HFIR at 400°C were both nearly twice as large as after irradiation in FFTF at 393°C.

The reduction in USE was generally greater for the steels irradiated in HFIR than FFTF (Fig. 3). The difference in USE between steels irradiated at 300 and 400°C in HFIR was generally quite small.

#### Transmission Electron Microscopy (TEM) and Scanning Electron Microscopy (SEM)

Specimens of 9Cr-1MoVnb and 9Cr-1MoVnb-2Ni steels irradiated in HFIR at 400°C were examined by TEM (no TEM was obtained for the 12Cr steels) [10]. Both the 9Cr-1MoVnb and 9Cr-1MoVnb-2Ni steels irradiated in HFIR at 400°C developed  $a_0\langle 100 \rangle$  and  $(a_0/2)\langle 111 \rangle$  dislocation loops with the number density slightly larger and the loops slightly smaller for 9Cr-1MoVnb-2Ni (Fig. 4). Dislocation loop densities and sizes were as follows:  $a_0\langle 100 \rangle$  were  $5 \times 10^{21} \text{ m}^{-3}$ , 21 nm and  $7 \times 10^{21} \text{ m}^{-3}$ , 20 nm for 9Cr-1MoVnb and 9Cr-1MoVnb-2Ni, respectively;  $(a_0/2)\langle 111 \rangle$  were  $4 \times 10^{21} \text{ m}^{-3}$ , 25 nm and  $6 \times 10^{21} \text{ m}^{-3}$ , 24 nm for 9Cr-1MoVnb and 9Cr-1MoVnb-2Ni, respectively.

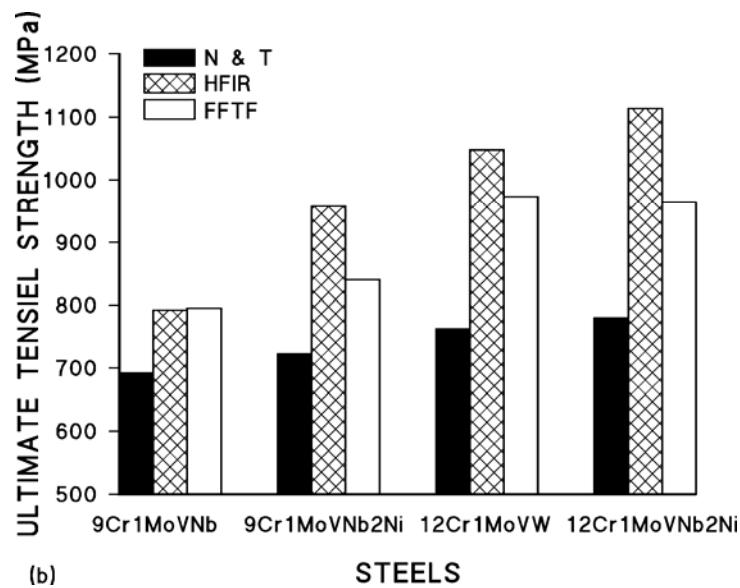
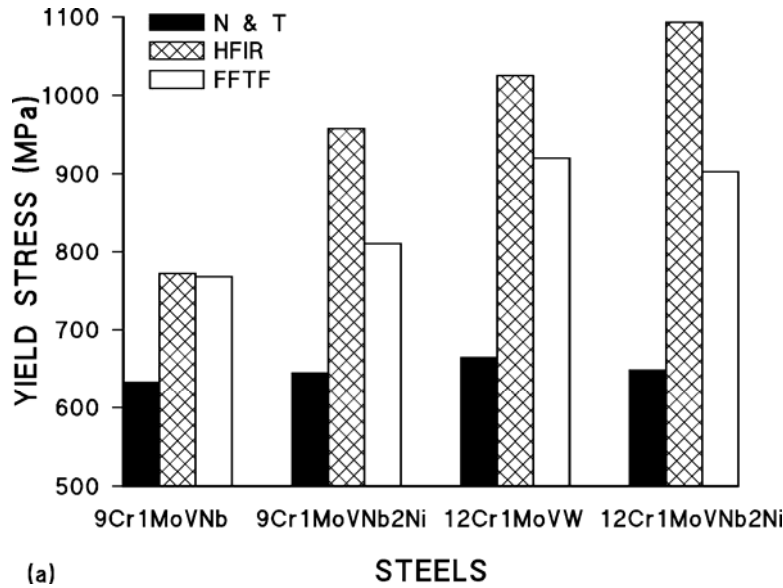


Fig. 1. A comparison of the (a) yield stress and (b) the ultimate tensile strength of steels in the normalized-and tempered condition and after irradiation in HFIR at 400°C and in FFTF at 393°C.

Cavities also developed, with 9Cr-1MoVNb-2Ni steel having a higher number density ( $9 \times 10^{21}$  vs.  $3 \times 10^{21} \text{ m}^{-3}$ ) and smaller average size (5 vs. 9 nm) (Fig. 5). For these low irradiation doses, there was little difference in swelling for the two steels: 9Cr-1MoVNb was estimated at 0.17%, and 9Cr-1MoVNb-2Ni was estimated at 0.15%.

Precipitate microstructures before irradiation consisted primarily of  $M_{23}C_6$  on lath and prior-austenite grain boundaries with similar quantities ( $< 1 \times 10^{20} \text{ m}^{-3}$ ) and average sizes ( $\approx 100 \text{ nm}$ ) in both the 9Cr-1MoVNb and 9Cr-1MoVNb-2Ni steels. There were also a few widely scattered MX particles within the matrix. Irradiation caused little change in the  $M_{23}C_6$  structure for either 9Cr steel, and no new precipitates formed in the 9Cr-1MoVNb [Fig 6 (a)]. However, a irradiation-induced precipitate identified as  $M_2X$  at a number density of  $5 \times 10^{20} \text{ m}^{-3}$  and a mean size of 54 nm was observed in the 9Cr-1MoVNb-2Ni steel [Fig. 6(b)].

Table 3. Impact properties of steels unirradiated and irradiated in HFIR<sup>a</sup> and FFTF<sup>b</sup>

Steel, Reactor	Irradiation Temperature, °C	Transition Temperature, °C <sup>c</sup>	$\Delta$ DBTT, °C	Upper-Shelf Energy, J
9Cr-1MoVNb	Unirradiated	-1		10.0
HFIR	300	143	144	4.1
HFIR	400	93	94	5.7
FFTF	393	99	100	6.4
9Cr-1MoVNb-2Ni	Unirradiated	-117		9.0
HFIR	300	181	298	4.0
HFIR	400	47	164	6.3
FFTF	393	-76	41	6.4
12Cr-1MoVW	Unirradiated	-39		7.1
HFIR	300	147	186	3.7
HFIR	400	84	123	3.5
FFTF	393	26	65	4.0
12Cr-1MoVW-2Ni	Unirradiated	-75		6.3
HFIR	300	185	260	3.5
HFIR	400	118	193	3.4
FFTF	393	25	100	4.8

<sup>a</sup>Specimens were irradiated in HFIR to 9–10 dpa at 300°C and 11–12 dpa at 400°C.

<sup>b</sup>Specimens were irradiated in FFTF to  $\approx$ 15 dpa at 393°C.

<sup>c</sup>Taken at one-half the upper-shelf energy.

Fracture surfaces of Charpy specimens from the lower- and upper-shelf regions of the Charpy curve for each steel were examined by SEM. The fracture surfaces of specimens from lower-shelf regions exhibited typical cleavage fractures, and those from upper-shelf regions exhibited ductile-type shear, which is similar to observations on the surfaces of specimens in the unirradiated condition.

## Discussion

In previous studies on nickel-doped steels, different tempering treatments were used on the steels with 2% Ni (5 h at 700°C) and the standard steels (1 h at 760°C for the 9Cr-1MoVNb and 2.5 h at 780°C for the 12Cr-1MoVW; these are recommended tempering treatments for commercial 9Cr-1MoVNb and 12Cr-1MoVW steels, respectively) [1–7]. The lower tempering temperature was used for steels with 2% Ni to avoid tempering above  $A_1$ , the equilibrium temperature above which ferrite begins to transform to austenite;  $A_1$  is lowered by nickel. An attempt was made to temper to similar room-temperature hardnesses (strengths) using the different tempering conditions. Unfortunately, even though hardnesses were similar for the different tempering conditions, the yield stresses at room temperature and the irradiation temperatures before irradiation turned out to be somewhat different, which complicated the comparison after irradiation [1–7].

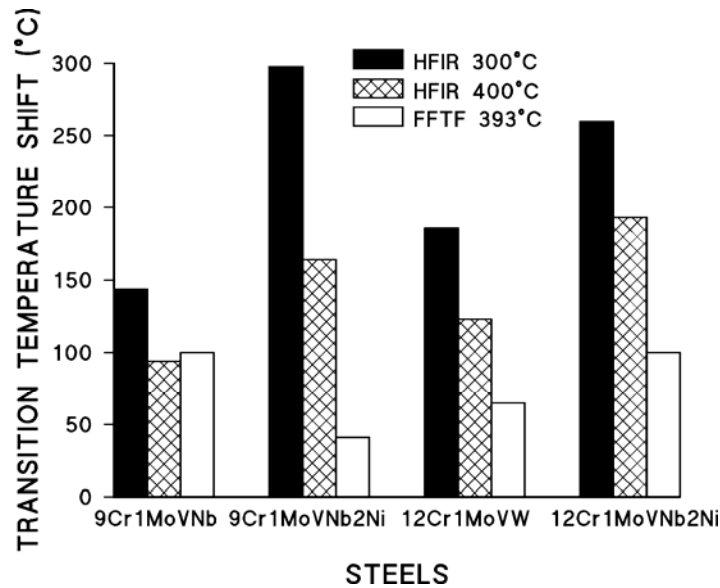


Fig. 2. Shift in ductile-brittle transition temperature of the steels after irradiation in HFIR at 300 and 400°C and in FFTF at 393°C.

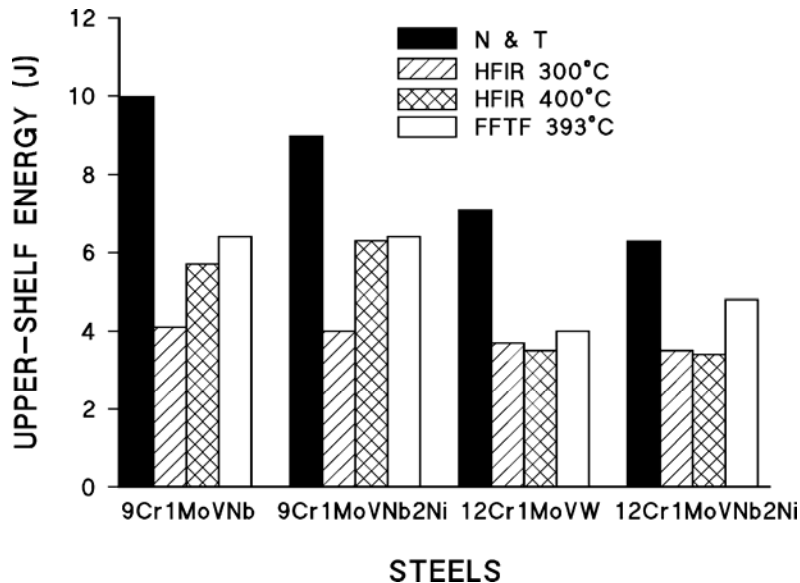


Fig. 3. Upper-shelf energy of the steels in the normalized-and tempered (unirradiated) condition and after irradiation in HFIR at 300 and 400°C and in FFTF at 393°C.

For the present experiments, the same tempering treatment was used for all steels (5 h at 700°C). Although this heat treatment produced similar strengths for all steels at room temperature, 300, and 400°C, the new tempering conditions changed the DBTTs of the standard steels: the DBTT of the 9Cr-1MoVNb increased from -29 to -1°C and that for 12Cr-1MoVW decreased from -18 to -39°C. The steels with 2% Ni had lower DBTTs than the respective steels without the nickel addition. In other words, it was not possible to have both the DBTT and yield stress of the standard steels and the steels with 2% Ni similar prior to irradiation. The lower DBTT for the nickel-containing steels before irradiation (Table 3) reflects the well-known fact that nickel lowers the transition temperature of steels [11].

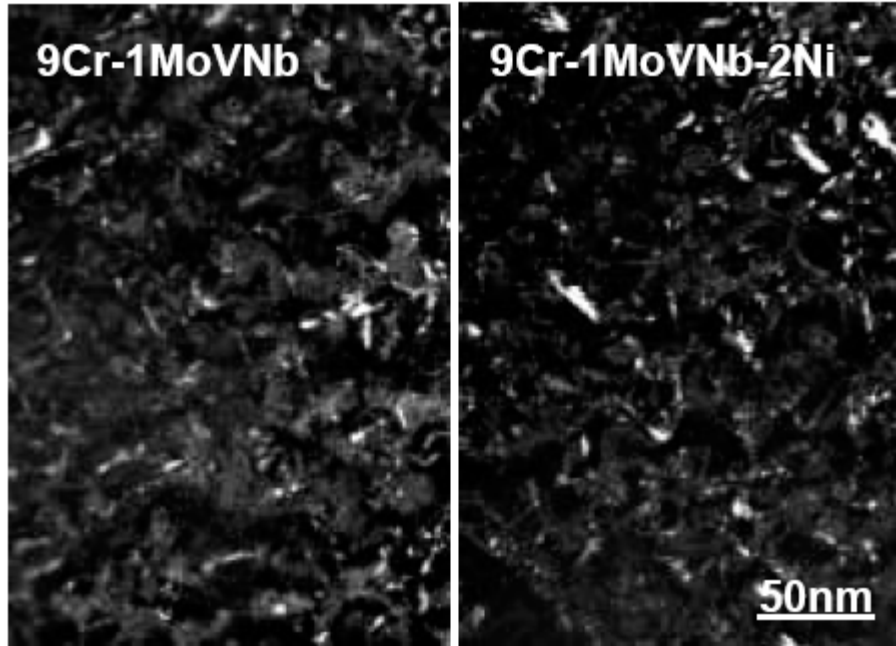


Fig. 4. Dislocation segments and loops in 9Cr-1MoVNb and 9Cr-1MoVNb-2Ni irradiated in HFIR to  $\approx 12$  dpa at 400°C using diffraction conditions:  $g=110$  ( $g,4g$ ).

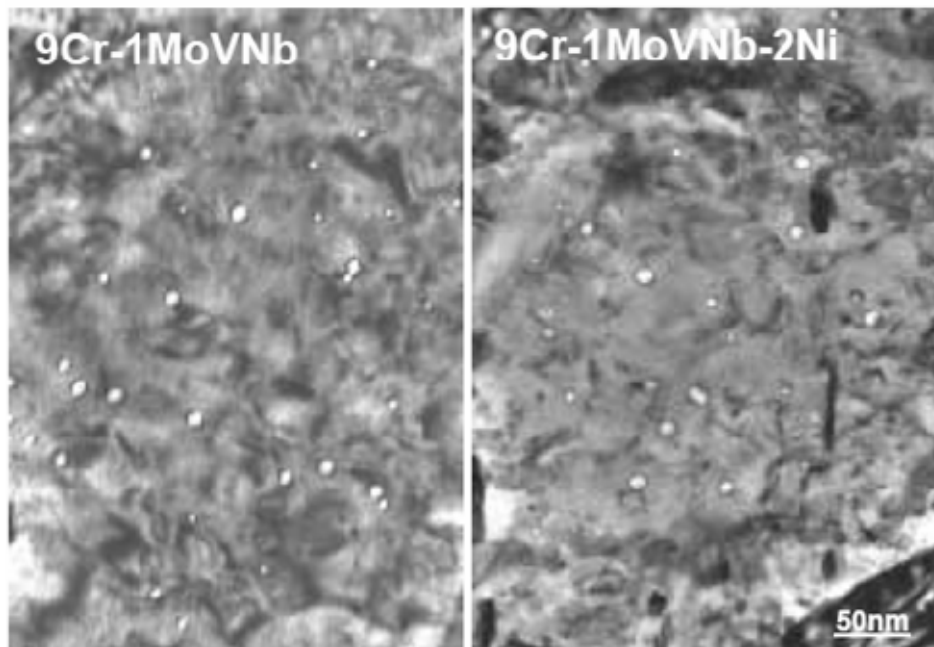


Fig. 5. Cavities in 9Cr-1MoVNb and 9Cr-1MoVNb-2Ni irradiated in HFIR to  $\approx 12$  dpa at 400°C.

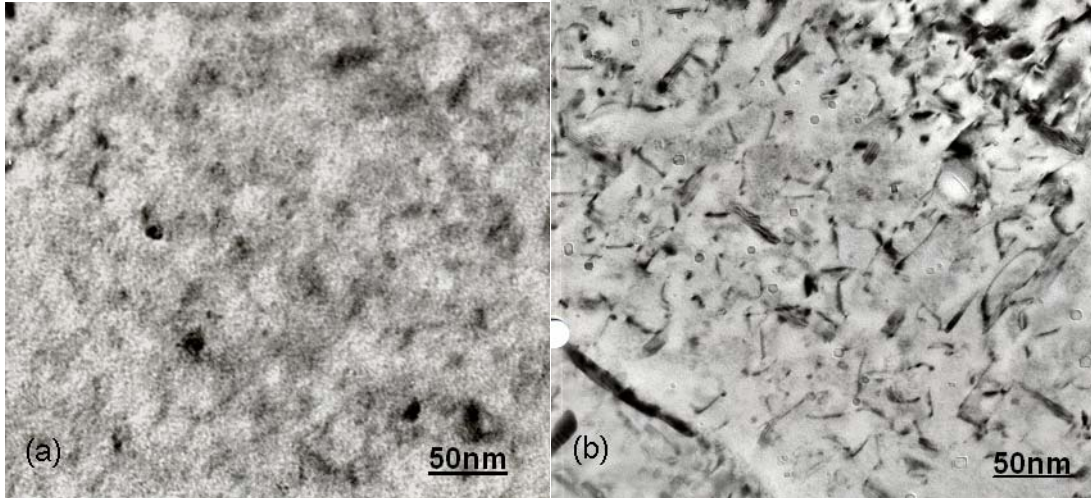


Fig. 6. Precipitates in the matrix of (a) 9Cr-1MoVNb and (b) 9Cr-1MoVNb-2Ni steels irradiated in HFIR to  $\approx 12$  dpa at 400°C.

#### Irradiation Hardening and Embrittlement

When the steels with and without the nickel additions were given the same tempering treatments, they had similar strengths at 300 and 400°C before irradiation (Table 2). The greater hardening after irradiation in the HFIR at 300 than at 400°C is expected [1–3]. After irradiation in HFIR, the respective yield stress increases for 9Cr-1MoVNb, 9Cr-1MoVNb-2Ni, 12Cr-1MoVW, and 12Cr-1MoVW-2Ni were respectively 405, 555, 445, and 524 MPa at 300°C and 139, 313, 360, and 444 MPa at 400°C. These results indicate a larger increase at both 300 and 400°C for the steels with 2% Ni than their counterparts without a nickel addition.

After irradiation in FFTF at 393°C, yield stress increased 135, 165, 255, and 254 MPa for 9Cr-1MoVNb, 9Cr-1MoVNb-2Ni, 12Cr-1MoVW, and 12Cr-1MoVW-2Ni, respectively. With the exception of the 9Cr-1MoVNb, the yield stress increases for the different steels were smaller after FFTF irradiation than after HFIR irradiation (Fig. 1). A similar increase occurred for 9Cr-1MoVNb at 393°C in FFTF and at 400°C in HFIR. Since there was only a small difference in displacement damage in the two reactors and hardening saturates with fluence at  $<10$  dpa at  $\approx 400^\circ\text{C}$  [2,3,12], similar hardening might be expected, as observed for the 9Cr-1MoVNb, because it contains the least nickel and, therefore, the least helium. The 15, 10, and 17% higher yield stress in HFIR over that in FFTF for the 9Cr-1MoVNb-2Ni, 12Cr-1MoVW, and 12Cr-1MoVW-2Ni, respectively, are not all that large, especially considering the change in DBTT to be discussed in the next section. However, note that the largest changes are for the steels with 2% nickel and the 12Cr-1MoVW, which contains 0.43% Ni; 9Cr-1MoVNb contains 0.11%Ni (Table 1). This implies that an argument can be made that helium caused much of the difference because, as discussed below, similar precipitate phases are expected during irradiation in the two reactors.

In Fig. 7(a),  $\Delta\text{DBTT}$  is plotted against  $\Delta\sigma_y$  for results from irradiation in HFIR at 300 and 400°C; Fig. 7(b) shows the same data along with data from the FFTF irradiation at 393°C. The data were fit by linear regression with lines through the origins and had slopes of 0.46 (correlation coefficient  $r=0.94$ ) and 0.45 ( $r=0.92$ ), for Figs. 7(a) and 7(b), respectively. All indications are that the results follow linear relationships, indicating the shift in transition temperature is proportional to hardening.

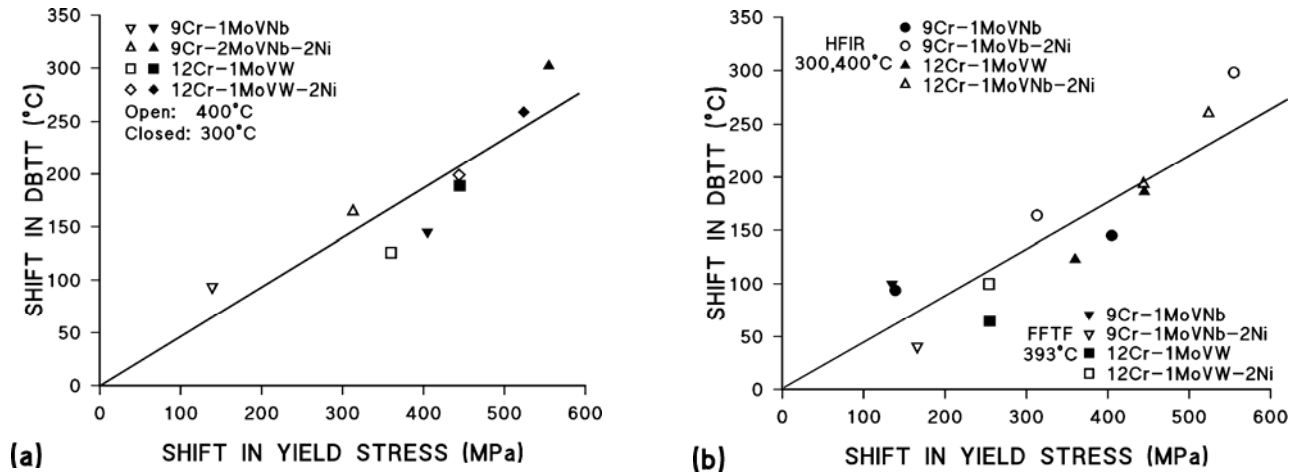


Fig. 7. Shift in ductile-brittle transition temperature plotted against shift in yield stress for 9Cr-1MoVNb, 9Cr-1MoVNb-2Ni, 12Cr-1MoVW, and 12Cr-1MoVW-2Ni steels irradiated in (a) HFIR at 300 and 400°C and (b) HFIR at 300 and 400°C and FFTF at 393°C.

Figure 8 shows just the data for the 400°C irradiations in HFIR and the 393°C irradiations in FFTF with a regression line of slope 0.42 ( $r=0.86$ ). There was both more hardening and a larger shift in transition temperature for the 9Cr-1MoVNb-2Ni, 12Cr-1MoVW, and 12Cr-1MoVW-2Ni steels irradiated in HFIR at 400°C than in FFTF at 393°C, even though displacement damage in the two reactors was similar and saturation with fluence would be expected for these doses at these temperatures [2,3,12]. There was no difference for the two reactors for 9Cr-1MoVNb, which contained the least helium after HFIR irradiation.

Although there is no difference between the  $\Delta$ DBTT for the 9Cr-1MoVNb in FFTF at 393°C and HFIR at 400°C in the present irradiations, there are differences for the 9Cr-1MoVNb-2Ni, 12Cr-1MoVW, and 12Cr-1MoVW-2Ni steels (Fig. 8). For the latter three steels, the  $\Delta$ DBTT values after irradiation in HFIR are 2–4 times greater than in FFTF, which is consistent with a helium effect. This might be expected since the 9Cr-1MoVNb steel contained a calculated value of only about 12 appm He after irradiation in HFIR, compared to  $\approx 31$ , 129, and 141 for the 12Cr-1MoVW, 9Cr-1MoVNb-2Ni, and 12Cr-1MoVW-2Ni steels, respectively. Thus, a larger effect would be expected for the latter steels if it is a helium effect. Since there was a similar difference in the hardening of the steels depending on the helium concentration, it is concluded that there is a contribution to hardening due to helium that is over and above the hardening due to displacement damage and irradiation-induced precipitation, and that hardening by helium causes a further increase in  $\Delta$ DBTT after irradiation in HFIR.

After irradiation at 300°C, where no comparison is possible with irradiation in a fast reactor, the  $\Delta$ DBTT for the 9Cr-1MoVNb was again the smallest (144°C), followed by 12Cr-1MoVW (186°C), 12Cr-1MoVW-2Ni (260°C), and 9Cr-1MoVNb-2Ni (298°C). This is also in line with  $\Delta\sigma_y$  [Fig. 5(a)] and the amount of helium present in the respective steels (the 9Cr-1MoVNb, 12Cr-1MoVW, 12Cr-1MoVW-2Ni and 9Cr-1MoVNb-2Ni steels contain  $\approx 8$ , 20, 48, and 47 appm He, respectively).

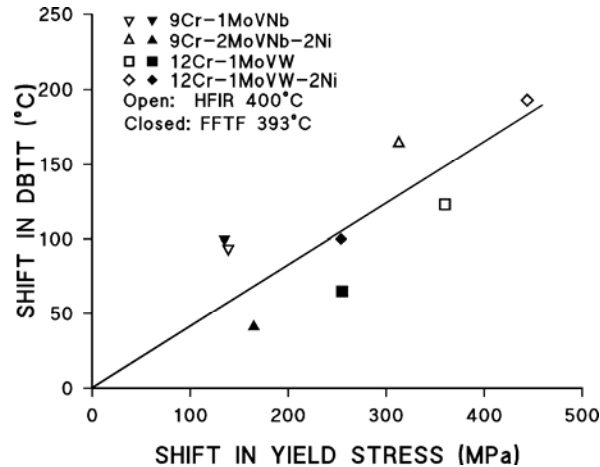


Fig. 8. Shift in ductile-brittle transition temperature plotted against shift in yield stress for 9Cr-1MoVNb, 9Cr-1MoVNb-2Ni, 12Cr-1MoVW, and 12Cr-1MoVW-2Ni irradiated in HFIR at 400°C and FFTF at 393°C

Tensile and Charpy results from the present HFIR and FFTF irradiations will now be compared to results from previous studies of the same steels irradiated in HFIR and EBR-II (Experimental Breeder Reactor), where it was concluded that helium affected impact properties [2–4,6,7]. One reason for this conclusion is shown in Fig. 9, where  $\Delta$ DBTT for 9Cr-1MoVNb and 12Cr-1MoVW steels are shown after irradiation in HFIR [6] and EBR-II [12], a fast reactor where little helium forms. After irradiation in EBR-II at 390°C, the  $\Delta$ DBTTs after 13 and 26 dpa ( $<0.1$  appm He) were similar, indicating the expected saturation with fluence ( $\Delta$ DBTT  $\approx 54^\circ\text{C}$  for the 9Cr-1MoVNb and  $\approx 140^\circ\text{C}$  for the 12Cr-1MoVW). This saturation did not occur for 9Cr-1MoVNb and 12Cr-1MoVW steels irradiated to  $\approx 40$  dpa at 400°C in HFIR, where  $\approx 30$  and 120 appm He formed, and the  $\Delta$ DBTTs were 207 and 242°C, respectively. The irradiation-induced shift in DBTT after irradiation in EBR-II was attributed to irradiation hardening caused by the dislocation loops from displacement damage and any hardening due to radiation-induced precipitation [6,12]. These processes undoubtedly also occurred during HFIR irradiation, but in this case, there was an additional increment in  $\Delta$ DBTT that was attributed to helium [6].

Another reason for concluding there was a helium effect was that after the 9Cr-1MoVNb-2Ni and 12Cr-1MoVW-2Ni steels were irradiated in HFIR to  $\approx 40$  dpa at 400°C and  $\approx 400$  appm helium, the  $\Delta$ DBTT values were 348 and 328°C, respectively [6]. This was over three times the value obtained for 12Cr-1MoVW-2Ni irradiated in FFTF at 390°C [5], where the  $\Delta$ DBTT at saturation was 90°C (9Cr-1MoVNb-2Ni was not irradiated at 390°C), and it was over 1.5 times that of the steels with no nickel additions (less helium) irradiated in HFIR. Hardening results from the previous irradiations in FFTF agreed with the recent observations on the hardening of the steels irradiated in the fast reactor, that is, steels without nickel showed similar hardening and shifts in DBTT to those with nickel. However, for the HFIR irradiations, there was no additional increment of hardening that could be attributed to helium [3], as was the case in the present experiments.

Specimens were also previously irradiated to  $\approx 27$  dpa at 300°C in HFIR [5]; the helium concentrations were  $\approx 20$ , 230, 70, and 240 appm for the 9Cr-1MoVNb, 9Cr-1MoVNb-2Ni, 12Cr-1MoVW, and 12Cr-1MoVW-2Ni, respectively. A helium effect was suggested by the larger  $\Delta$ DBTT for the 9Cr-1MoVNb-2Ni and 12Cr-1MoVW-2Ni steels compared to steels without nickel. Since no fast reactor comparisons are possible for this HFIR-irradiation temperature, these results will not be discussed further here.

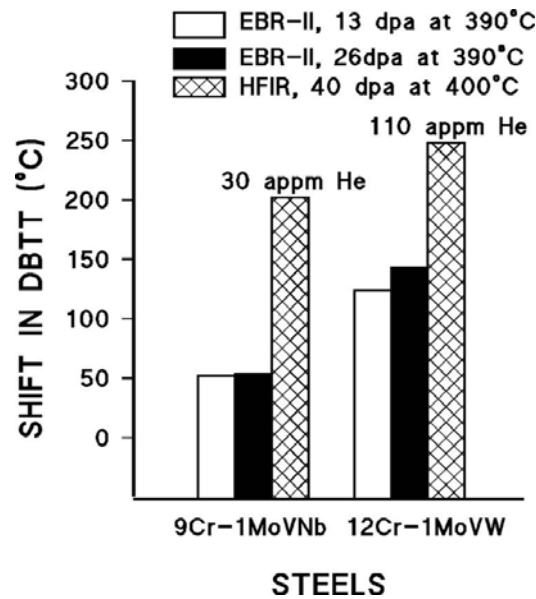


Fig. 9. Shift in ductile-brittle transition temperature for 9Cr-1MoVNb and 12Cr-1MoVW irradiated the HFIR at 400°C and EBR-II at 390°C [5].

Figure 10 shows data from Fig. 8 of the present HFIR (HFIR #2) and FFTF experiments at 400°C to  $\approx 12$  dpa and 393°C to  $\approx 15$  dpa, respectively, to which were added data from the previous HFIR (HFIR #1) experiment at 400°C to  $\approx 40$  dpa [2-4,6,7]. The linear-regression line fitting the data from the present HFIR and FFTF irradiations in Fig. 8 is also shown. Although data are limited, the results from the previous experiment deviate significantly from the line obtained for the recent results. For the high-dose data, there is a much larger  $\Delta\text{DBTT}/\Delta\sigma_y$  compared to the lower-dose data. That is, the previous high-dose data do not appear to harden in accordance with the regression line. In fact, it appears that softening occurred at 400°C for these tests relative to the recent tests. The previous results were attributed to a change in brittle fracture mode from transgranular cleavage to intergranular. This difference will be discussed in greater detail in the companion paper (Part II) [13], where mechanisms will be analyzed.

The question has been debated whether the nickel additions for the high-dose irradiations changed the microstructure to give the differences observed [14-16]. As discussed in the following section, irradiation at  $\approx 400^\circ\text{C}$  produced a high density of fine  $\text{M}_6\text{C}$  precipitates in 9Cr-1MoVNb-2Ni and 12Cr-1MoVW-2Ni steels during irradiation in FFTF, where little helium formed, and in HFIR, where  $\approx 400$  appm He formed [17,18]. Therefore, the extra shift in DBTT in HFIR could not be attributed to irradiation-induced precipitation.

Although a helium effect was used to explain the large deviation from the linear relationship of the 40 dpa data (Fig. 10) [5,6], the results of the present experiment then present a dilemma. In the lower-dose experiment, the steels with 2% Ni developed a larger  $\Delta\text{DBTT}$  than the respective steels without the added nickel, but they did not show the large differences observed for the higher fluences in HFIR. There was also no change in fracture mode. Figure 7 provides the limited evidence in the recent results that suggests the steels with 2% Ni hardened significantly more during HFIR irradiation than the steels without a nickel addition. Similar excess hardening for the nickel-doped steels is not evident in FFTF. If there is no difference in precipitation between the fast and mixed-spectrum reactor, the helium generated in HFIR must play a role in the hardening for similar displacement damage in the two reactors. It needs to be emphasized, however, that this difference is small ( $<20\%$ ), and there is considerable scatter in the data. If helium affects the DBTT, then there should be a correlation between  $\Delta\text{DBTT}$  and helium concentration. This appears to be true for 400°C data (Fig. 11), although the reliability of the correlation suffers from a scarcity of results on steels containing high helium concentrations.

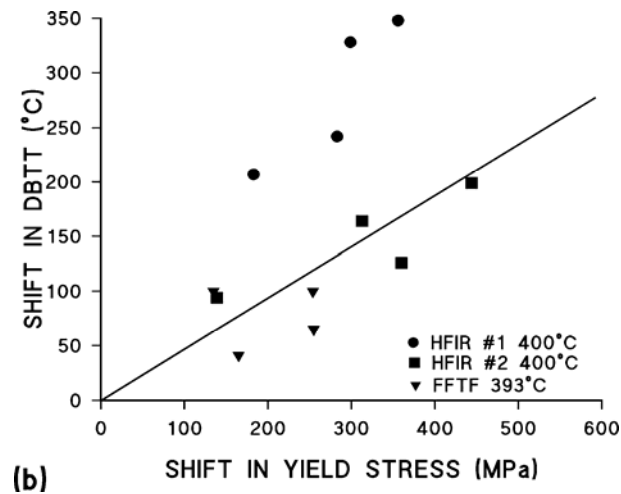


Fig. 10. Shift in ductile-brittle transition temperature plotted against the increase in yield stress for 9Cr-1MoVNb, 9Cr-1MoVNb-2Ni, 12Cr-1MoVW, and 12Cr-1MoVW-2Ni steels irradiated in the present (HFIR #2) and previous (HFIR #1) HFIR experiments at 400°C and in FFTF at 393°C.

### Microstructure

As pointed out in earlier papers describing irradiation experiments with the nickel-doped steels, irradiation-induced nickel-containing  $M_6C$  formed in the 9Cr-1MoVNb-2Ni and 12Cr-1MoVW-2Ni steels during HFIR irradiation to  $\approx 40$  dpa at 400°C [17,18]. However, the same  $M_6C$  precipitates formed in irradiations of the steels to  $\approx 47$  dpa at 407°C in the fast reactor FFTF (Fig. 12) [17,18]. If the precipitates caused hardening in the HFIR-irradiated steel, they should have caused a similar effect in FFTF for similar doses. Therefore, it was concluded that the larger  $\Delta DBTT$  after irradiation in HFIR was due to helium, since helium formation in the nickel-containing steels irradiated in HFIR was the only obvious difference compared to irradiation in FFTF [5,6]. One difference in microstructure that was observed was that there was more void swelling in the HFIR-irradiated specimen.

The microstructural observations on 9Cr-1MoVNb-2Ni in the present experiment differed from the earlier studies, because no high number density of nickel-rich  $M_6C$  particles was observed after irradiation. Instead,  $M_2X$  particles were observed [Fig. 6(b)]. However, the presence of  $M_2X$  is not too surprising, because this precipitate is a chromium-rich nitride (basically  $Cr_2N$ ) with some of the chromium replaced by other solutes and some nitrogen replaced by carbon. It can form more easily in 9Cr-1MoVNb steel because the specification for this steel includes 0.03–0.07% N, and the 9Cr-1MoVNb and 9Cr-1MoVNb-2Ni steels in this experiment contained 0.05% N (Table 1). Because of the relatively large size and small number density of  $M_2X$  precipitates, it would not be expected to contribute much to hardening. A similar precipitation sequence should also occur for irradiation to a similar dose in FFTF.

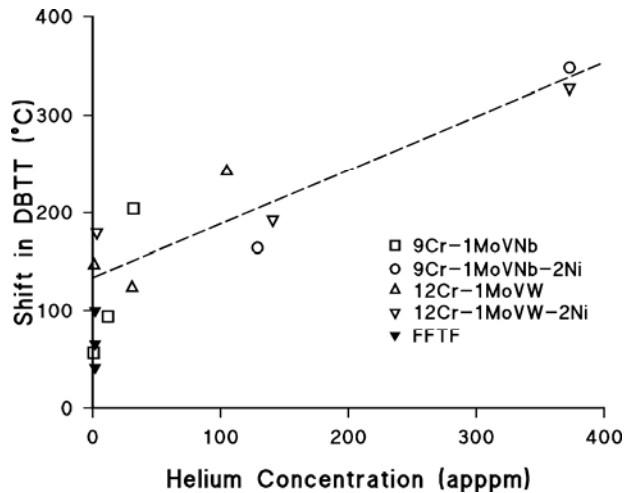


Fig. 11. Shift in ductile-brittle transition temperature plotted against helium concentration for 9Cr-1MoVNb, 9Cr-1MoVNb-2Ni, 12Cr-1MoVW, and 12Cr-1MoVW-2Ni steels irradiated in the present (HFIR #2) and previous (HFIR #1) HFIR experiments at 400°C and in FFTF at 393°C.

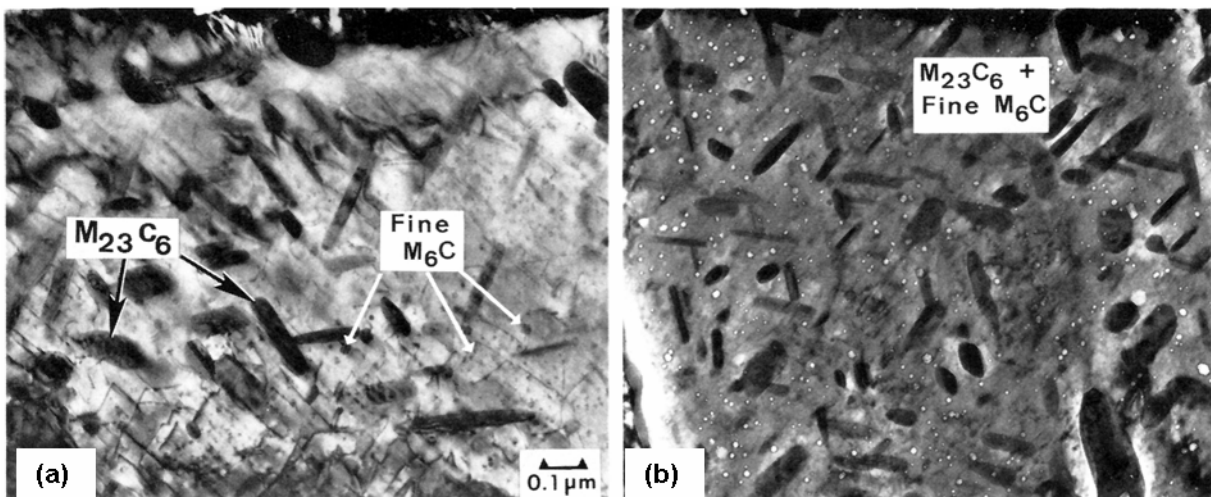


Fig. 12. Transmission electron micrographs of 9Cr-1MoVNb-2Ni steel irradiated in (a) FFTF to  $\approx 47$  dpa and  $\approx 5$  appm He and (b) HFIR at 400°C to  $\approx 37$  dpa and  $\approx 410$  appm He.

A possible explanation for the absence of  $M_6C$  in the irradiated 9Cr-1MoVNb-2Ni, as observed in higher-dose irradiations [17,18], is that  $M_2X$  is an intermediate phase, or the small amounts present can form more quickly, and more time—a higher irradiation dose—is required for  $M_6C$  to form in sizes that can be observed and identified. Irradiations were to  $\approx 40$  dpa and higher where  $M_6C$  was observed, compared to about 12 dpa for the steels irradiated in the present experiment. The  $M_6C$  was previously analyzed as being rich in Cr, Ni, and Si, along with some iron and traces of Mo, P, and V [17,18]. A similar precipitate was detected in 12Cr-1MoVW steel irradiated in EBR-II, but in that case it was identified as G-phase, and for that steel the precipitate composition was determined as Ni-24.1Fe-12.7Si-8.7Mn-3.8Mo-1.9Cr [19].

In the irradiation capsule used for the present HFIR experiment, the reduced-activation steel 9Cr-2WVTa and that steel with 2% Ni (9Cr-2WVTa-2Ni) were also irradiated [20]. Before irradiation, the microstructures of these steels were respectively similar to those of 9Cr-1MoVNb and 9Cr-1MoVNb-2Ni—tempered martensite with  $M_{23}C_6$  and MX precipitates. Likewise, there was only a minor difference in

the dislocation loop structure after irradiation. However, the 9Cr-2WVTa-2Ni contained a high number density ( $2 \times 10^{21} \text{ m}^{-3}$ ) of small (average size 7 nm) irradiation-induced particles identified as  $\text{M}_6\text{C}$  (Fig. 13). The size was less and the number density higher than for  $\text{M}_2\text{X}$  in 9Cr-1MoVNb-2Ni (54 nm and  $5 \times 10^{20} \text{ m}^{-3}$ ) [compare Figs. 13 and 6(b)]. Based on the above hypothesis, the absence of  $\text{M}_2\text{X}$  in the 9Cr-2WVTa is not unexpected, since this steel contains only about 0.01% N. The microstructure of 9Cr-2WVTa-2Ni was similar to structures found for 9Cr-1MoVNb-2Ni after higher-dose irradiations, supporting the hypothesis concerning the kinetics of  $\text{M}_6\text{C}$  formation in 9Cr-1MoVNb-2Ni.

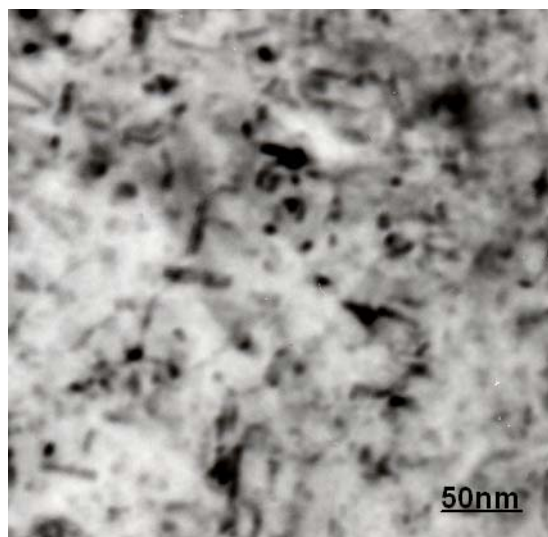


Fig. 13. Irradiation-induced  $\text{M}_6\text{C}$  precipitates in the matrix of 9Cr-2WVTa-2Ni steel irradiated in HFIR to 12 dpa at 400°C. Compare with Fig. 6 that shows 9Cr-1MoVNb-2Ni irradiated similarly but containing irradiation-induced  $\text{M}_2\text{X}$ .

#### Problems with Nickel Doping

There has been concern about using nickel-doped steels to determine helium effects, because of the effect nickel might have on the microstructure and mechanical properties [21–25]. Excess hardening in terms of an increased yield stress was observed on the reduced-activation steel JLF-1 (9Cr-2WVTa) containing 1% Ni relative to the undoped steel after irradiation to  $\approx 0.15$  dpa at 170°C in the Japan Materials Test Reactor (JMTR) [23,24]. No excess hardening was observed for similar irradiation at 220°C. Irradiation of these steels in the Advanced Test Reactor (ATR) to 2.2 and 3.8 dpa at 270 and 348°C, respectively, produced excess hardening (up to 350 MPa) for the 270°C irradiation. Similar strengths were observed for the two steels irradiated at 348°C [25]. The excess hardening was accompanied by a larger increase in DBTT for the nickel-containing steel.

Microstructural observations by TEM revealed that irradiation-induced dislocation loops were finer and denser in the 1% Ni steel than in the undoped steel, which suggested that the nickel addition affected nucleation and growth of dislocation loops to produce excess hardening and embrittlement [25]. Little difference in loop structure was observed in the TEM studies on the 9Cr steels irradiated in HFIR at 400°C to 12 dpa. Likewise, no hardening attributable to nickel was observed previously for neutron irradiations of the nickel-doped 9Cr-1MoVNb and 12Cr-1MoVW steels at 300 and 400°C [1–3], temperatures above those where the excess hardening was observed in JMTR and ATR [22–25].

In dual ion-beam irradiations (6.4 MeV  $\text{Fe}^{3+}$  and degraded 1 MeV  $\text{He}^+$ ) to 5 dpa of F82H without nickel and with 1% and 2% Ni, hardness measurements by an ultra-microindentation technique indicated excess hardening in the 2% Ni irradiated at 350°C [26]. However, it is unclear how this might compare with neutron irradiation, since ion irradiations are at a dose rate several orders of magnitude higher than for fast-reactor irradiations. Results from neutron irradiations indicated a two-step hardening-recovery

process for the irradiated steels, with the second step occurring at  $\geq 300^{\circ}\text{C}$  [23]. Presumably, recovery would proceed simultaneously with hardening during irradiation, thus explaining the effect of temperature on the excess hardening. Such recovery would not occur during ion irradiations to 5 dpa, which are completed within several hours, compared with several months for irradiation to 10 dpa and higher. Nevertheless, the possibility of excess hardening for the  $300^{\circ}\text{C}$  tests must be kept in mind when evaluating these results, since there are no FFTF experiments at this temperature to determine the effect of the nickel.

### Helium Effects

As with all irradiation experiments, the results of this experiment involve uncertainty introduced by the small number of tests (due to limited reactor space for inserting specimens). Within the limits of such uncertainties, the present results lead to some conclusions concerning the effect of helium on mechanical properties. If similar displacement damage and precipitation occurs in the steels irradiated in FFTF and HFIR at similar temperatures, as previously observed [17,18], then the results from the present irradiations indicate there was a component of hardening that must be attributed to helium. It therefore follows that this hardening produced an increment of increase in transition temperature in the Charpy tests over and above the hardening caused by displacement damage and any irradiation-induced precipitation. Mechanisms for how helium may affect hardening will be discussed in part II [13].

Several investigators have published studies providing evidence for a helium effect on the mechanical properties of irradiated steels using other experimental techniques other than nickel doping. Also, as discussed above, the results of the present work showing a hardening effect due to helium differ from the previous high-dose experiments, where embrittlement occurred without an increase in hardness that could be attributed to helium [6,7]. In part II that accompanies this contribution, the present results will be examined in light of the previous experiments [16].

### **Acknowledgement**

We wish to thank the following people who helped in the completion of this work: L. T. Gibson, N. H. Rouse, and E. T. Manneschildt carried out the experimental tests and procedures; Dr. L. R. Greenwood analyzed the dosimetry specimens in the irradiation capsules and calculated the helium concentrations; Drs. D. R. Harries, L. K. Mansur, R. G. Stoller, and S. J. Zinkle reviewed the manuscript and provided helpful discussion of the work.

This research was sponsored by the Office of Fusion Energy Sciences, U.S. Department of Energy, under contract DE-AC05-00OR22725 with UT-Battelle, LLC.

### **References**

- [1] R. L. Klueh, P. J. Maziasz, and J. M. Vitek, *J. Nucl. Mater.* 141–143 (1986) 960.
- [2] R. L. Klueh and J. M. Vitek, *J. Nucl. Mater.* 150 (1987) 272.
- [3] R. L. Klueh and P. J. Maziasz, *J. Nucl. Mater.* 187 (1992) 43.
- [4] J. M. Vitek, W. R. Corwin, R. L. Klueh, and J. R. Hawthorne, *J. Nucl. Mater.* 141–143 (1986) 948.
- [5] W. R. Corwin, J. M. Vitek, and R. L. Klueh, *J. Nucl. Mater.* 149 (1987) 312.
- [6] R. L. Klueh and D. J. Alexander, *J. Nucl. Mater.* 187 (1992) 60.
- [7] R. L. Klueh and D. J. Alexander, *J. Nucl. Mater.* 218 (1995) 151.
- [8] D. J. Alexander, R. K. Nanstad, W. R. Corwin, and J. T. Hutton, in *Applications of Automation Technology to Fatigue and Fracture Testing*, ASTM STP 1092, Eds., A. A. Braun, N. E. Ashbaugh, and F. M. Smith (American Society for Testing and Materials, Philadelphia, 1990) 83.
- [9] M. A. Sokolov and R. K. Nanstad, in *Effects of Radiation on Materials: 17<sup>th</sup> International Symposium*, ASTM STP 1270, Eds., D. S. Gelles, R. K. Nanstad, A. S. Kumar, and E. A. Little (American Society for Testing and Materials, Philadelphia, 1996) 384.
- [10] N. Hashimoto and R. L. Klueh, *J. Nucl. Mater.* 305 (2002) 153.
- [11] W. C. Leslie, *The Physical Metallurgy of Steels* (McGraw-Hill, New York, 1981) 123.
- [12] W. L. Hu and D. S. Gelles, in *Influence of Radiation on Material Properties: 13th International Symposium (Part II)*, ASTM STP 956, Eds., F. A. Garner, C. H. Henager, Jr., and N. Igata (American

Society for Testing Materials, Philadelphia, 1987) 83.

[13] R. L. Klueh, N. Hashimoto, M. A. Sokolov, K. Shiba, and S. Jitsukawa, *Journal of Nuclear Materials* (in press).

[14] D. S. Gelles, *J. Nucl. Mater.* 230 (1996) 187.

[15] R. L. Klueh and D. J. Alexander, *J. Nucl. Mater.* 230 (1996) 191.

[16] N. Hashimoto and R. L. Klueh, *J. Nucl. Mater.* 305 (2002) 153.

[17] P. J. Maziasz, R. L. Klueh, and J. M. Vitek, *J. Nucl. Mater.* 141–143 (1986) 929.

[18] P. J. Maziasz, R. L. Klueh, in *Effects of Radiation on Materials: 14th International Symposium*, ASTM STP 1046, Eds., N. H. Packen, R. E. Stoller, and A. S. Kumar (American Society for Testing and Materials, Philadelphia, 1990) 35.

[19] D. S. Gelles and L. E. Thomas, in *Ferritic Steels for use in Nuclear Energy Technologies*, Eds., J. W. Davis and D. J. Michel (The Metallurgical Society of AIME, Warrendale, Pa., 1984) 559.

[20] R. L. Klueh, M. A. Sokolov, K. Shiba, Y. Miwa, and J. P. Robertson, *J. Nucl. Mater.* 283–287 (2000) 478.

[21] D. S. Gelles, G. L. Hankin, and M. L. Hamilton, *J. Nucl. Mater.* 251 (1997) 188.

[22] D. S. Gelles, in *Effects of Radiation on Materials: 18th International Symposium*, ASTM STP 1325, Eds., R. K. Nanstad, M. L. Hamilton, G. A. Garner, and A. S. Kumar (American Society for Testing and Materials, Philadelphia, 1997) 899.

[23] R. Kasada, A. Kimura, H. Matsui, and M. Narui, *J. Nucl. Mater.* 258–263 (1998) 1199.

[24] R. Kasada, T. Morimura, H. Matsui, M. Narui, and A. Kimura, in *Effects of Radiation on Materials: 19<sup>th</sup> International Symposium*, ASTM STP 1366, Eds., M. L. Hamilton, A. S. Kumar, S. T. Rosinski, and M. L. Grossbeck (American Society for Testing and Materials, West Conshohocken, Pa., 2000) 448.

[25] R. Kasada and A. Kimura, *Mater. Trans.* 46 (2005) 475.

[26] M. Ando, H. Tanigawa, S. Jitsukawa, T. Sawai, Y. Katoh, A. Kohyama, K. Nakamura, and H. Takeuchi, *J. Nucl. Mater.* 307–311 (2002) 260–265.

**MECHANICAL PROPERTIES OF NEUTRON-IRRADIATED NICKEL-CONTAINING MARTENSITIC STEELS: II. REVIEW AND ANALYSIS OF HELIUM-EFFECTS STUDIES**—R. L. Klueh, N. Hashimoto, M. A. Sokolov, and P. J. Maziasz (Oak Ridge National Laboratory), K. Shiba and S. Jitsukawa (Japan Atomic Energy Research Institute)

**OBJECTIVE**

In part I of this helium-effects study on ferritic/martensitic steels, results were presented on tensile and Charpy impact properties of 9Cr-1MoVNb (modified 9Cr-1Mo) and 12Cr-1MoVW (Sandvik HT9) steels and these steels containing 2% Ni after irradiation in the High Flux Isotope Reactor (HFIR) to 10–12 dpa at 300 and 400°C and in the Fast Flux Test Facility (FFTF) to 15 dpa at 393°C. The results indicated that helium caused an increment of hardening above irradiation hardening produced in the absence of helium. In addition to helium-effects studies on ferritic/martensitic steels using nickel doping, studies have also been conducted over the years using boron doping, ion implantation, and spallation neutron sources. In these previous investigations, observations of hardening and embrittlement were made that were attributed to helium. In this paper, the new results and those from previous helium-effects studies are reviewed and analyzed.

**SUMMARY**

Without a fusion test reactor or other intense 14 MeV neutron source, simulation techniques are required to study the possible effects of neutron irradiation from the deuterium-tritium fusion reaction that will cause the simultaneous production of displacement damage and transmutation helium in a martensitic steel first wall of a fusion reactor. In part I of this work, results from the irradiation of modified 9Cr-1Mo (9Cr-1MoVNb), Sandvik HT9 (12Cr-1MoVW),\* and these steels with 2% Ni (9Cr-1MoVNb-2Ni and 12Cr-1MoVW-2Ni) in the High Flux Isotope Reactor (HFIR) and the Fast Flux Test Facility (FFTF) were presented [1]. Tensile results indicated helium-induced hardening caused an increase in the ductile-brittle transition temperature (DBTT) above that caused by displacement damage and irradiation-induced precipitation effects occurring in the absence of helium. Previous work on the nickel-doped steels irradiated to a much higher dose [2–6] indicated helium caused embrittlement, but without detectable hardening above that attributed to displacement damage and irradiation-induced precipitation [5,6].

In this paper, results from these helium-effects studies using nickel doping and other simulation techniques are reviewed and analyzed. The objective is to place the recent results [1] in context with previous studies to demonstrate the effect of helium on mechanical properties of irradiated ferritic/martensitic steels.

**Experimental Techniques**

Several techniques have been used to study helium effects, including nickel doping [1–7], boron doping [8,9], helium implantation with accelerators [10–14] and injector foils [15–17], and spallation neutron sources [18–25]. All but the injector foils have been employed for mechanical properties studies, which are the subject of this paper. In this section, the techniques used to study mechanical properties will be briefly described.

Nickel Doping

Simultaneous displacement damage and helium formation is produced in alloys containing nickel irradiated in a mixed-spectrum fission reactor. Displacement damage is produced by fast neutrons in the spectrum, and helium forms by a two-step reaction of  $^{58}\text{Ni}$  with thermal neutrons in the spectrum [7]:  $^{58}\text{Ni}(n,\gamma)^{59}\text{Ni}(n,\alpha)^{56}\text{Fe}$  (natural nickel contains 68%  $^{58}\text{Ni}$ ). For ferritic/martensitic steels with about 2% Ni, irradiation in a mixed-spectrum reactor such as HFIR at the Oak Ridge National Laboratory (ORNL)

---

\*The commercial steels modified 9Cr-1Mo and Sandvik HT9 will be referred to by the generic designations 9Cr-1MoVNb and 12Cr-1MoVW, respectively.

produces a similar helium to displacement damage ratio ( $\approx 10$  appm/dpa) to that attained in a tokamak first wall in the steel without the nickel when irradiated to  $\geq 10$  dpa. Atom recoil resulting from the  $(n,\alpha)$  reaction produces displacement damage in the metal lattice that needs to be accounted for [26].

As part I of this work, tensile and Charpy results were published for 9Cr-1MoVNb and 12Cr-1MoVW steels and these steels with 2% Ni that were irradiated to 12 dpa at 400°C in HFIR and to 15 dpa at 393°C in the FFTF [1]. The technique was also used in earlier experiments for irradiation of the steels up to  $\approx 40$  dpa at 400°C in HFIR and FFTF [2–6]. To determine whether there is a helium effect, tensile and Charpy data for steels with and without nickel additions were compared after irradiation in HFIR, and data for steels irradiated in HFIR were compared with those irradiated in FFTF, where very little helium is produced.

Uncertainties in the nickel-doping technique involve the possible effect of nickel on the microstructure. Irradiations of nickel-containing 9Cr steels to low doses in the Japan Materials Test Reactor [27] and the Advanced Test Reactor [28] at temperatures below 300°C indicated an effect of nickel on hardening. As discussed in detail in part I [1], no such hardening has been observed for irradiations at 300 and 400°C in HFIR and at 393°C in FFTF, which are the focus of this discussion.

### Boron Doping

Boron-containing steels have been used to study helium effects [8,9,29–33], because during neutron irradiation, helium forms by the  $^{10}\text{B}(n,\alpha)^7\text{Li}$  reaction. The cross section for the  $(n,\alpha)$  reaction is greatest for low-energy (thermal) neutrons, which means irradiation in a mixed-spectrum reactor such as HFIR will cause all the  $^{10}\text{B}$  to transform within 1–2 dpa, compared to a much longer time in a fast reactor. Natural boron contains about 19.9%  $^{10}\text{B}$ , the remainder  $^{11}\text{B}$ .

The energies of the lithium ion and the  $\alpha$ -particle (0.87 and 1.53 MeV, respectively) produced by the reaction create a significant number of atomic displacements as they slow down to thermal energy, and these additional displacements could cause an increase in the local defect concentration [34]. Boron can segregate to interfaces and form precipitates or be incorporated in precipitates, such as  $\text{B}_4\text{C}$  and  $\text{M}_{23}(\text{CB})_6$  [35,36]. When the boron is contained in precipitates, neutron irradiation can lead to cavities forming in a “halo” around the boron-containing precipitate particles, the size of the halos being characteristic of the energy of the  $\alpha$ -particles released by the  $(n,\alpha)$  reaction. Sometimes two rings are observed, one for the  $\alpha$ -particle and one for the lithium [35,36]. The presence of the lithium could present a source of confusion in the interpretation of the results.

### Helium Implantation

Helium can be implanted in miniature tensile or Charpy specimens by  $\alpha$ -particle injection in a cyclotron [10–14]. An injected specimen can then be compared to a similar specimen irradiated by neutrons in a reactor to a similar dose, but where much less helium is formed. Alternatively, the implanted specimen can be compared with an unimplanted specimen [11–14]. A problem with this technique is that it produces a higher He/dpa ratio than fusion, and it is generally limited to low doses.

### Spallation Neutron Source Irradiation

Obviously, nickel doping, boron doping, and helium implantation experiments are not ideal for simulating helium effects for fusion applications. An ideal experiment would produce helium during irradiation without altering the steel composition, as in a fusion reactor or an intense 14 MeV neutron source. Although different from fusion conditions, high-energy proton or neutron irradiation in spallation neutron sources have been used to investigate simultaneous production of helium and displacement damage without introducing another element or implanting helium [18–25]. In such facilities, irradiation is by very high-energy particles, much higher than the 14 MeV neutrons emanating from the deuterium-tritium fusion reaction.

Most of the studies discussed below were carried out on ferritic/martensitic steels irradiated by 600–750 MeV protons in SINQ (Swiss Spallation Neutron Source) at the Paul Scherrer Institute in Switzerland [18–22]. Studies have also been carried out in the LANSCE (Los Alamos Neutron Science Center) accelerator at Los Alamos, New Mexico [23–25]. Problems with spallation neutron irradiation include a much higher He/dpa ratio compared to that for an intense 14 MeV neutron source, and in addition to helium, large amounts of hydrogen are also produced.

## Review of Experimental Results

All four experimental techniques introduced in the previous section have produced results that were interpreted to indicate a helium effect on swelling and embrittlement of ferritic/martensitic steels. In this section, similarities and differences in these results will be summarized and discussed.

### Nickel Doping

Nickel doping has been used to examine the effect of helium on swelling [37,38] and tensile [1–4] and impact properties [1,5,6,39] of ferritic/martensitic steels by comparing the effects when irradiated in the mixed-spectrum HFIR reactor and the FFTF fast reactor. Although an increase in swelling has been attributed to the higher helium generated in HFIR when nickel-doped steels irradiated in the HFIR and FFTF reactors were compared, there was no apparent difference in precipitation during irradiation [37,38]. Precipitates in the 9Cr-1MoVNb and 12Cr-1MoVW steel with and without the nickel additions were examined by transmission electron microscopy (TEM) after irradiation at 407°C to  $\approx 47$  dpa in FFTF and at 400°C to  $\approx 38$  dpa in HFIR [37,38]. The same high density of tiny  $M_6C$  precipitates formed in 9Cr-1MoVNb-2Ni and 12Cr-1MoVW-2Ni during irradiation in FFTF as formed in HFIR.

In the most recent experiment with nickel-doped steels to examine the effect of helium on mechanical properties, 9Cr-1MoVNb, 9Cr-1MoVNb-2Ni, 12Cr-1MoVW, and 12Cr-1MoVW-2Ni steels were irradiated in HFIR to  $\approx 10$  dpa at 300°C and  $\approx 12$  dpa at 400°C and to  $\approx 15$  dpa at 393°C in the FFTF [1]. The results indicated that the 9Cr-1MoVNb-2Ni (129 appm He), 12Cr-1MoVW (31 appm He), and 12Cr-1MoVW-2Ni (141 appm He) irradiated in HFIR hardened more—showed a larger increase in yield stress,  $\Delta\sigma_y$ —than the same steels irradiated in FFTF at 393°C ( $< 0.5$  appm He). The 9Cr-1MoVNb steel, which contained the least helium (12 appm), hardened to about the same level in both FFTF and HFIR. These results along with the 300°C results from HFIR for the steels with and without the nickel additions led to the conclusion that helium caused a larger  $\Delta\sigma_y$  than that due to displacement damage and any irradiation-induced precipitation hardening [1].

The increment of hardening contributed to an increase in DBTT ( $\Delta DBTT$ ) over and above that when there was no helium present. Irradiation in HFIR at 300 and 400°C caused a larger  $\Delta DBTT$  for the steels containing 2% Ni than for those with no nickel addition. There was a linear relationship between  $\Delta DBTT$  and  $\Delta\sigma_y$ , and the data were fit by linear regression through the origin. Since there were no FFTF irradiations for comparison for the 300°C HFIR irradiations, this discussion will emphasize the 400°C HFIR data and the 393°C FFTF data, for which the slope of the  $\Delta DBTT$ - $\Delta\sigma_y$  relationship was 0.42 [1].

In the previous paper, these data for the 10–15 dpa HFIR and FFTF irradiations were compared with previous 40 dpa irradiations in HFIR [5] at 400°C and high-dose irradiations in EBR-II at 390°C [40]. The high-dose results also provided indications of a helium effect on fracture, because there was a much larger  $\Delta DBTT$  for the HFIR-irradiated specimens compared to the EBR-II-irradiated specimens and a larger  $\Delta DBTT$  for the nickel-doped specimens compared to the undoped specimens irradiated in HFIR.

There were some differences between the high-dose and low-dose irradiations. First, fracture of the nickel-doped specimens from the high-dose irradiations displayed an intergranular fracture mode on the lower shelf [5], compared to transgranular cleavage for the low-dose irradiations [1]. Secondly, the data for the high-dose HFIR experiment (HFIR #1) [5] did not fit on the linear  $\Delta DBTT$ - $\Delta\sigma_y$  relationship (Fig. 1) obtained from the recent HFIR experiment (HFIR #2) [1]. Figure 1 indicates a much larger  $\Delta DBTT$  for the high-dose data than would be predicted from the linear relationship based on the low-dose data. It appears that softening occurred for the high-dose specimens compared to the linear relationship of the

low-dose specimens. For the combined data for the two studies, there appeared to be a relationship between  $\Delta$ DBTT and helium concentration [1].

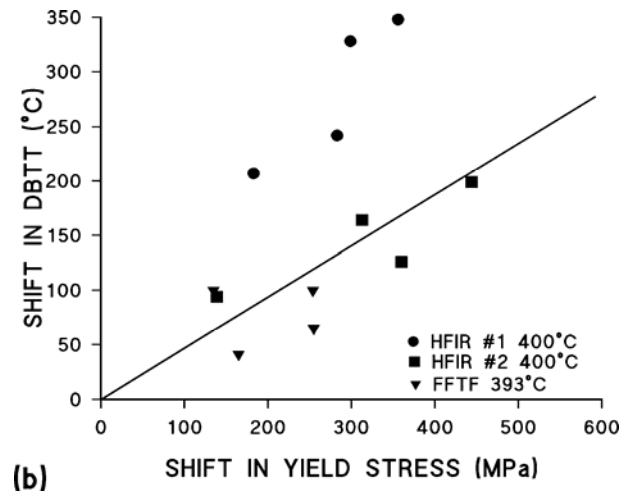


Fig. 1. Shift in ductile-brittle transition temperature plotted against the increase in yield stress for 9Cr-1MoVNb, 9Cr-1MoVNb-2Ni, 12Cr-1MoVW, and 12Cr-1MoVW-2Ni steels irradiated in the present (HFIR #2) and previous (HFIR #1) HFIR experiments at 400°C and in FFTF at 393°C.

### Boron Doping

The effect of helium on swelling was investigated in the reduced-activation steel F82H (nominally Fe-2.0W-0.20V-0.04Ta-0.10C) with 4–8 and 60 ppm natural boron ( $\approx 6$  and 60 appm He) and 58 ppm  $^{10}\text{B}$  ( $\approx 300$  appm He). Irradiation at 400°C in HFIR to  $\approx 7$ , 26, and 51 dpa [41] demonstrated that swelling and the number density of cavities increased with helium concentration.

Tensile specimens of the reduced-activation steel F82H with the above boron concentrations were irradiated in HFIR at 400 and 500°C to 11 to 34 dpa [8,9]. Tests at the irradiation temperatures indicated that any effect of helium on strength or ductility was small, and the differences generally fell within the scatter of the data. These steels were also irradiated in the Japan Materials Test Reactor (JMTR) to 0.8 dpa at 250–265°C [8,9]. For tensile tests over the range from room temperature to 400°C, irradiation hardening for the two steels was similar, with boron-doped F82H showing a slightly lower strength. However, the steel with the higher helium concentration had a considerably lower total elongation and reduction of area [9].

Several irradiation experiments indicated that specimens with 300 appm He from  $^{10}\text{B}$  had a much larger  $\Delta$ DBTT than specimens without the presence of helium or with much lower helium concentrations [8,9,29–33]. Irradiation of  $^{10}\text{B}$ -doped specimens and undoped specimens at 355–375°C to 0.3–0.5 dpa in JMTR and the Japan Research Reactor (JRR-2) to produce 300 appm He in the doped F82H produced a DBTT in the doped steel  $\approx 15^\circ\text{C}$  higher than in the undoped steel [8]. No shift in transition temperature was observed when irradiated at 500–590°C.

A larger effect with  $^{10}\text{B}$  doping was obtained for F82H irradiated at lower temperatures (260–360°C) to 0.3–0.6 dpa in JMTR [9]. Although a complete Charpy curve was not determined (because of temperature limitations of the Charpy test rig) for the  $^{10}\text{B}$ -doped steel with 100 appm He, the  $\square$ DBTT appeared to be well above room temperature (Fig. 2) and much larger than for the standard F82H irradiated similarly. There was no difference in the yield stress of the  $^{10}\text{B}$ -containing steel and a steel without the  $^{10}\text{B}$  addition. Both hardened by a similar amount, although there was a slight loss of ductility for the  $^{10}\text{B}$ -containing steel [9].

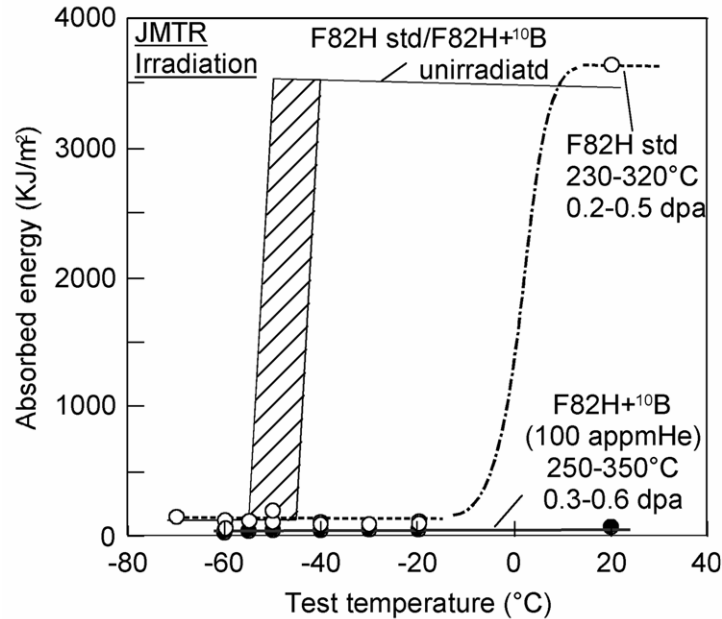


Fig. 2. Charpy impact curves for standard F82H and  $^{10}\text{B}$ -doped F82H in the unirradiated condition and after irradiation to 0.2–0.6 dpa at 250–350°C in JMTR [9].

In another experiment, the reduced-activation steel JLF-1 (nominally Fe-9Cr-2.0W-0.20V-0.07Ta-0.05N-0.10C) and this steel with 0.0022% B was irradiated to 2.5 dpa at 300°C in the High Flux Reactor (HFR), a mixed-spectrum reactor in the Netherlands [29]. Before irradiation, the steels had similar Charpy curves. After irradiation, the DBTT of the boron-containing steel with  $\approx 23$  appm He was about 70°C higher than for the steel without the boron addition.

The relative shift in DBTT obtained from irradiation in HFR of four reduced-activation steels and two conventional Cr-Mo steels after 0.2, 0.8, and 2.4 dpa at 250–450°C was attributed to the different levels of helium in the steels due to different levels of boron [30–32]. In Fig. 3, the  $\Delta\text{DBTT}$  data for these steels are shown as a function of dose for the 300°C irradiation along with the boron content of each steel. It was observed that the higher the boron content, the steeper the slope of the curve and the higher the  $\Delta\text{DBTT}$  for the individual steels. A curve for the  $^{10}\text{B}$ -to-He transformation is also shown, and it has the same characteristics as the embrittlement curves. Over 99% of the  $^{10}\text{B}$  has transformed to helium by 1.6 dpa, which is near where saturation in  $\Delta\text{DBTT}$  with fluence occurred for the MANET I steel.

Maximum helium in the steels was calculated as 85, 70, 60, 60, <20, and <10 appm for MANET I, MANET II, OPTIFER Ia, OPTIFER II, F82H, and ORNL 9Cr-2WVTa, respectively. The  $\Delta\text{DBTT}$ s for the steels scale with the boron content and, therefore, the helium content; the ratio of  $\Delta\text{DBTT}$  to helium was essentially the same for all of the steels at  $\approx 2\text{--}3^\circ\text{C}/\text{appm He}$  [30–32]. The effect of helium (boron) was subsequently “verified” by irradiating OPTIFER steels with reduced boron concentrations [33]. These steels showed significantly less embrittlement than the same steels containing the higher boron concentrations.

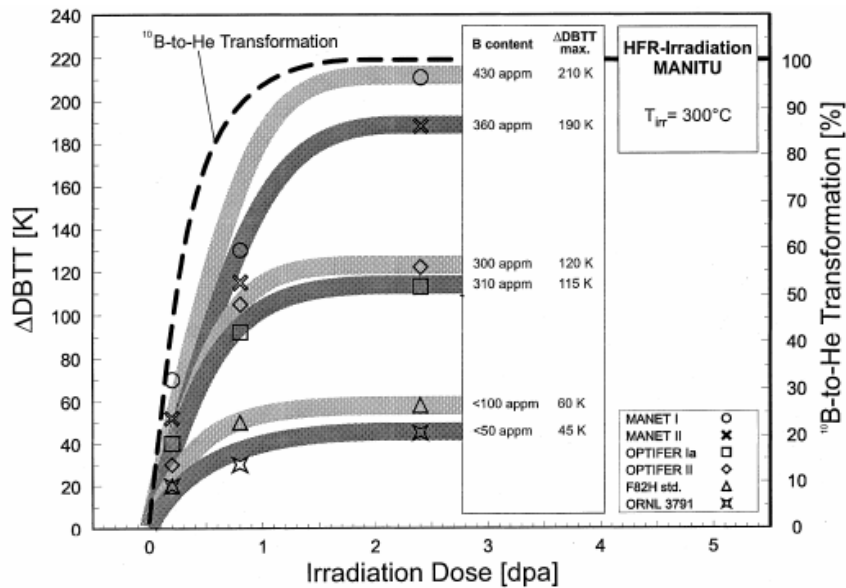


Fig. 3. Shift in DBTT vs. irradiation dose of six steels irradiated in HFR showing how the shift in DBTT correlates with boron content and, therefore, helium content [30].

#### Helium Implantation

To investigate the effect of helium on embrittlement, 300 appm He (0.2 dpa) was implanted in miniature Charpy specimens of F82H by  $\alpha$ -particle injection in a cyclotron [10]. For comparison, similar specimens were irradiated in the HFR to the same dose but with <8 appm He. The  $\Delta$ DBTT of the latter specimen was 18°C compared to 44°C for the implanted specimen. The results were interpreted to mean helium exacerbated the shift in DBTT [10].

In another study, up to 5000 appm He was implanted at 150–550°C in 100  $\mu\text{m}$ -thick tensile specimens of normalized-and-tempered modified 9Cr-1Mo (9Cr-1MoVNb) and EM10 (Fe-8.8Cr-1.1Mo-0.5Mn-0.2Ni-0.4Si-0.1C that is essentially unmodified 9Cr-1Mo steel) [11]. Tests at room temperature and the implantation temperature indicated that implanted helium caused hardening and embrittlement, which increased with increasing helium and decreasing implantation temperature. For steels containing about 2500 appm He, scanning electron microscopy (SEM) revealed intergranular failures. For irradiation at 250°C and testing at either room temperature or 250°C, failure occurred with little or no necking, and the fracture surface was essentially completely intergranular. It was stated that tests on steel irradiated at 550°C, “displayed some necking and ductile appearance is retained...” [11].

In more recent work, these investigators implanted 2500 appm He in miniature tensile specimens and the notch region of Charpy specimens at 250°C with a displacement damage of 0.4 dpa [13,14]. Room-temperature 0.2% yield stress increased by  $\approx$ 50% after implantation, with an accompanying decrease in ductility; total elongation decreased from about 9% to about 1%. Although SEM of fracture surfaces indicated a ductile failure, there were indications of secondary cracks on grain boundaries. Charpy specimens were tested in static three-point bending at room temperature. Bending curves indicated a “pop-in” in a narrow loading range, indicating the initiation and propagation of a brittle crack. A fully brittle fracture containing intergranular and cleavage fracture modes was observed by SEM in the helium-implanted region, whereas a ductile failure mode was observed in the non-implanted region. Finite-element analysis of the bending tests demonstrated that helium caused a decrease in the critical stress for intergranular fracture [13].

The TEM observations on EM10 and modified 9Cr-1Mo (identified in the studies as T91—the ASTM designation for modified 9Cr-1Mo tubing) specimens irradiated at 250 and 550°C with 5000 appm He showed high number densities of helium bubbles, similar in appearance for both steels [12]. The helium bubbles in specimens irradiated at 250°C were too small to detect by TEM, but black-dot damage was observed. Small-angle scattering verified the presence of bubbles in these specimens. Bubbles were observed by TEM in specimens irradiated at 550°C. They were estimated at 2.5–3 nm in diameter at a number density of  $3\text{--}4 \times 10^{22} \text{ m}^{-3}$ ; they were inhomogeneously distributed in the matrix, on lath boundaries and prior-austenite grain boundaries, on dislocations, and at carbide/matrix interfaces. It was concluded that the bubble pressures were close to thermodynamic equilibrium, and hardening was due to the high density of helium bubbles that leads to the intergranular fracture, and the [12], “brittle, intergranular fracture mode results from the combination of pronounced hardening and weakening of PAG [prior-austenite grain] boundaries due to helium.” In the second experiment where implantation was to 2500 appm at 250°C, the number density of small (<1 nm) bubbles was estimated at  $3\text{--}4 \times 10^{23} \text{ m}^{-3}$  [14].

It is interesting to note that since the objective of these tests was the determination of the feasibility of using martensitic steels for the target of a European Spallation Source (ESS), the results were taken as putting into question [12], “...the suitability of martensitic steels as structural materials for the ESS container window, which will operate below 250°C.” Applications at temperatures significantly higher than 250°C were deemed possible.

#### Spallation Neutron Source Irradiation

Studies on microstructure [18,21,22], tensile properties, and impact properties [18–22] were conducted on several martensitic steels after irradiation by 600–750 MeV protons in SINQ. Most of the observations were on T91 (9Cr-1MoVNb) and F82H. Two SINQ irradiations were carried out, one to doses up to 12 dpa and 1120 appm He at 90 to 360°C and the other up to 20.3 dpa and 1695 appm He at 118 to 400°C [18–22].

Helium bubbles 1–1.5 nm diameter formed in the steels irradiated at 175 to 360°C up to  $\approx 12$  dpa and 1100 appm He; there a slight increase in size with irradiation temperature. Number density remained relatively constant over the temperature range at  $\approx 5 \times 10^{23} \text{ m}^{-3}$ . No bubbles could be resolved for irradiations below about 5.8 dpa, indicating helium concentration was not high enough [18,22].

In the second experiment on F82H irradiated at 400°C to 20.3 dpa and 1695 appm He, a bimodal distribution of bubbles and/or voids was observed. The size of the cavities reached 60 nm, thus indicating the large effect of helium and temperature [22] relative to studies in the first experiments at lower temperatures and doses [18,22].

Tensile tests on steels irradiated at 90 to 360°C up to 12 dpa indicated hardening increased with dose. Sufficient specimens were not available to determine whether saturation in strength occurred with increasing dose [19,22].

Small-punch (SP) testing was used to determine a  $DBTT_{SP}$  [19,21,22], as differentiated from Charpy V-notch (CVN) tests, which were also conducted to determine  $DBTT_{CVN}$  [22]. The  $\Delta DBTT_{SP}$  increased linearly with dose up to 6–7 dpa and about 400 appm He, above which there was a large increase for both F82H and T91. There was no saturation of  $\Delta DBTT_{SP}$  with dose. Based on the determined relationship  $DBTT_{SP} = 0.4 DBTT_{CVN}$ , a shift of  $DBTT_{CVN}$  of 295°C was calculated for T91 irradiated to 9.4 dpa at 280°C. A linear relationship between  $\Delta DBTT_{SP}$  and helium concentration was observed [22], similar to that obtained for the nickel-doping experiments [1].

A limited number of tests on CVN specimens of T91 and F82H irradiated to 7.5 dpa at 120 to 195°C also showed the non-linear increase with dose indicated in the SP tests. These tests verified the relationship between  $DBTT_{SP}$  and  $DBTT_{CVN}$  [21]. There was no indication of a saturation with dose.

In the second, higher-dose experiment, SP specimens of F82H were irradiated up to 18.4 dpa and  $\approx 1530$  appm He at an average temperature of 380°C. The  $\Delta\text{DBTT}_{\text{SP}}$  was 291°C, which gives a calculated  $\Delta\text{DBTT}_{\text{CVN}}$  of 727°C. These results combined with the other results reinforced the conclusions that  $\Delta\text{DBTT}$  does not saturate with dose, and there is a linear relationship between  $\Delta\text{DBTT}$  and helium concentration for the steels irradiated over the range 2.5–18.4 dpa and 85 to 1530 appm He [22]. With SEM observations on tested small-punch specimens, it was possible to observe the change in fracture mode from brittle to ductile with increasing test temperature. Brittle fracture appeared to be highly intergranular.

Evidence that helium can promote intergranular fracture was obtained in a related experiment in SINQ, where tensile specimens of EM10 were irradiated in the normalized-and-tempered, quenched, and cold-worked-and-tempered conditions [42,43]. Average irradiation conditions were  $\approx 100$ –330°C, 4–12 dpa, and 150–940 appm He. The quenched steel is of interest for this discussion because after irradiation at an average temperature of 287°C to 9.8 dpa and 750 appm He, the specimen tested at room temperature fractured without necking, and SEM indicated that [43], "...the fracture surface, which lies strictly perpendicular to the specimen axis, displays a fully brittle, intergranular appearance." This observation contrasted with the unirradiated steel that displayed a fracture that "is clearly fully ductile as shown by the well defined dimples."

Results from this irradiation in SINQ were compared with irradiation to 0.8–9 dpa at 325°C of the same EM10 in the quenched condition in the mixed-spectrum OSIRIS Reactor [41]. Despite even greater hardening of the quenched steel irradiated in OSIRIS, it was stated that the specimen can [43] "still retain some ductility... whereas the SINQ-irradiated specimens display a complete loss of ductility." Reduction of area for a room-temperature test was  $>50\%$  for the OSIRIS-irradiated specimen, compared to essentially no reduction of area for the SINQ-irradiated specimen, indicating the complete embrittlement of this specimen [43].

It appears that in all attempts to study helium effects, interpretation of results is always associated with inherent uncertainties, and these experiments are no exception. Although helium is implicated in the intergranular fracture, the investigators pointed out that considerable hydrogen (over 4000 appm) was generated during the SINQ irradiation, and it could be a contributing factor [43]. However, they concluded that a substantial amount of this hydrogen should diffuse from the steel during irradiation. To support this, work was cited that showed only 10% of the hydrogen generated in F82H irradiated in SINQ at 295°C remained in the steel following irradiation [44]. The quenched EM10 was irradiated at 287°C. It was also pointed out that if hydrogen was the source of the intergranular failure, then a similar effect might be expected for the normalized-and-tempered and cold-worked-and-tempered steels [43]. Also, the helium-implantation study discussed in the previous section [11,12] that gave similar intergranular fractures without the presence of hydrogen was cited to support the conclusion that intergranular fracture was caused by the helium.

Several ferritic/martensitic steel tensile specimens were irradiated in LANSCE and HFIR, including modified 9Cr-1Mo and the reduced-activation steel ORNL 9Cr-2WVTa. Irradiation was at 60 to 100°C at doses up to 1.2 dpa in HFIR and 60 to 164°C at doses of 0.026 to 10 dpa in LANSCE [24,25]. The interesting observation for this discussion is the conclusion that [25]: "there are signs of a small radiation strengthening contribution attributable to the presence of helium." This hardening due to helium appears similar to that observed in the low-dose irradiations of the nicked-doped steels [1].

## Discussion

### Analysis of Data

In the recent irradiation experiments on nickel-doped and undoped 9Cr-1MoVNb and 12Cr-1MoVW steels irradiated to 12–15 dpa in HFIR and FFTF at  $\approx 400^\circ\text{C}$ , the results indicated that helium increased the hardening and embrittlement over that due to displacement damage and irradiation-induced precipitation [1]. These results agreed with previous experiments at low irradiation temperatures [2,39], but they differed from previous HFIR experiments on these same steels irradiated to 40 dpa at  $400^\circ\text{C}$  (Fig. 1) that led to the conclusion that helium causes embrittlement by causing a change in fracture mode [5,6].

Reasons for concluding there was a helium effect in the recent experiments were: (1) the  $\Delta\text{DBTTs}$  for the HFIR-irradiated steels with the highest helium concentrations were greater than for the same steels with much less helium after irradiation in FFTF to similar doses, (2)  $\Delta\text{DBTTs}$  of the HFIR-irradiated 9Cr-1MoVNb-2Ni and 12Cr-1MoVW-2Ni steels were greater than those for the steels without nickel additions, and (3) HFIR-irradiated steels with the highest helium concentrations generally hardened more than the same steels irradiated in FFTF.

A similar hardening effect due to helium was recently observed in dual-ion irradiations [45]. Specimens of reduced-activation steel JLF-1 were irradiated with single-beam 6.4 MeV  $\text{Fe}^{3+}$  ions and with the double-beam 6.4 MeV  $\text{Fe}^{3+}$  ions and 1.0 MeV  $\text{He}^{3+}$  ions at  $420^\circ\text{C}$  up to 60 dpa. Dual-ion irradiation produced finer defect clusters than single-ion irradiation. Nano-indentation hardness measurements indicated much more hardening for the dual-ion irradiated specimens. Further, the hardening appeared to saturate for the single-ion-irradiated specimens, but not for the dual-ion-irradiated specimens, even after 60 dpa [45].

The  $\Delta\text{DBTTs}$  in the recent work [1] were not as large as in the previous experiment on nickel-doped steels (Fig. 1) [5]. Furthermore, there appeared to be a correlation between  $\Delta\text{DBTT}$  and  $\Delta\sigma_y$  for the recent experiments, which is contrary to the previous high-dose experiments at  $400^\circ\text{C}$ , where no hardening in  $400^\circ\text{C}$  tensile tests was attributable to helium [3,4]. Also, in the recent experiments, there was no indication of intergranular fracture. As discussed below, it was previously suggested that helium can promote intergranular fracture in an impact test, and intergranular fracture was observed on nickel-containing steels irradiated to  $>60$  dpa and up to  $>700$  appm He [4,5].

The TEM on the 9Cr-1MoVNb-2Ni steel irradiated at  $400^\circ\text{C}$  to about 12 dpa provided further support for the conclusion of a helium effect [1,46]. In this case, the high number density of small  $\text{M}_6\text{C}$  particles observed in the high-dose irradiations [37,38] was not observed. Instead, the irradiation-induced precipitate that appeared was  $\text{M}_2\text{X}$ , and it was present at a lower number density ( $5 \times 10^{20} \text{ m}^{-3}$ ) and a larger size (54 nm) than the  $\text{M}_6\text{C}$  in this steel irradiated to 38–47 dpa in HFIR and FFTF. Irradiation-induced  $\text{M}_6\text{C}$  was observed in a reduced-activation 9Cr-2WVTa steel containing 2% Ni (9Cr-2WVTa-2Ni); the number density was estimated to be  $2 \times 10^{21} \text{ m}^{-3}$  with an average size of 7 nm [1,46]. This irradiation was also to 12 dpa in HFIR at  $400^\circ\text{C}$ , and the specimen was contained in the same capsule used for the 9Cr-1MoVNb-2Ni. It is of interest to note that the hardening ( $\Delta\sigma_y$ ) in the two steels was similar (313 MPa for the 9Cr-1MoVNb-2Ni and 301 MPa for the 9Cr-2WVTa-2Ni), another indication, perhaps, that these particular irradiation-induced precipitates were not a major component of the hardening, given the large difference in size and number density of the precipitates in the two steels.

Although results from the recent experiment (to  $\approx 12$  dpa) and those from the previous experiment (to  $\approx 40$  dpa) for  $400^\circ\text{C}$  irradiations in HFIR led to conclusions of a helium effect on impact properties, there appear to be different mechanisms. In the first case, excess hardening by helium appeared to play a role [1]. In the second case, no excess hardening attributable to helium was observed. Instead, softening occurred relative to the steel irradiated to 12 dpa (Fig. 1), and helium appeared to promote intergranular failure [5].

According to Farrell [47,48], helium can affect the mechanical properties in three ways: (1) helium can stabilize vacancy clusters, thus causing an increase in the number of interstitial clusters that eventually grow into dislocations that increase the strength, (2) helium can stabilize the clusters to higher temperatures than in the absence of helium, and (3) helium can diffuse to grain boundaries and induce intergranular failure.

Another possible hardening mechanism for helium is a high number density of small helium-filled bubbles, such as those observed by helium implantation [11–14,49] and spallation neutron source irradiations [18,22,]. There are still some question of how much hardening occurs in this instance. Modeling of the interaction of an edge dislocation with voids showed that the voids down to 1 nm are strong obstacles for dislocations [50]. However, molecular dynamic simulations indicated voids are weak barriers, and helium-filled bubbles are only moderately more effective [51].

The transition temperature in an impact test can be increased by an increase in flow stress or a decrease in fracture stress. Displacement damage and irradiation-induced precipitation can cause embrittlement by increasing the flow stress. Hardening by helium should have the same effect. Since the shift in transition temperature for the high-dose experiments was not commensurate with the hardening observed—if anything, there was a relative softening—it was hypothesized that helium lowered the fracture stress [5,6]. An increase in DBTT due to a lower fracture stress can be caused by: (1) more or larger flaws at which a fracture initiates, (2) less resistance to initiation of a flaw, and (3) less resistance to the propagation of a flaw.

Inclusions or carbides are the usual source of the microcracks that initiate fracture in steels [52,53]. To explain a helium effect for the high-dose irradiations, a mechanism was hypothesized previously [5,6] that when steels contain sufficient helium, the microcrack source could be helium-containing bubbles on a prior austenite grain boundary, on a martensite lath boundary (subgrain boundary), or at a precipitate/matrix interface. Helium could collect in small bubbles that under stress become nuclei for fracture and/or enhance crack propagation, thus providing an explanation for observations of intergranular facets on the fracture surface [5]. Helium-caused flaws could induce brittle fracture, but the fracture mode would not be completely intergranular until a high concentration of helium is present. With higher helium concentrations at boundaries, resistance to crack propagation could be affected. A change to a fully intergranular fracture would be accelerated by increased helium and higher temperatures, where diffusion rates of helium to boundaries would be higher [5,6].

Such fine bubbles on boundaries have been observed on 9Cr-1MoVNb-2Ni irradiated at 400°C to  $\approx 75$  dpa and  $\approx 760$  appm He (Fig. 4) [54]. As seen in Fig. 4, an almost continuous layer of tiny bubbles cover the  $M_{23}C_6$  particles and the lath boundaries that contain the precipitate. These fine bubbles, some of which are also visible in the matrix, are distinct from the large polyhedral cavities in the matrix.

Results from the low- and high-dose experiments indicate that helium could affect embrittlement by two of Farrell's mechanisms [47]: (1) by a hardening mechanism at low doses and (2) by promotion of intergranular fracture at high doses. Hardening by helium-filled bubbles, such as those in the matrix in Fig. 4, could also contribute to hardening and embrittlement. This contribution would be expected to contribute most when the bubbles are smaller in the low-to-intermediate helium concentration regime.

The fact that  $\Delta$ DBTTs observed after 40 dpa at 400°C [5] did not correlate with the hardening (Fig. 1) observed in the recent experiment [1] can also be explained by the difference in dose. Hardening saturates with fluence in a fast reactor after a few ( $<10$ ) dpa at 400°C. As opposed to saturation occurring for higher-dose experiments in fast reactors (low helium), however, a maximum in yield strength and transition temperature with fluence has been observed for several steels [55–59], including 12Cr-1MoVW [58,59] and modified 9Cr-1MoVNb [58] irradiated in FFTF. When a maximum was observed near 400°C, it occurred at fluences of 25–30 dpa [55–59].

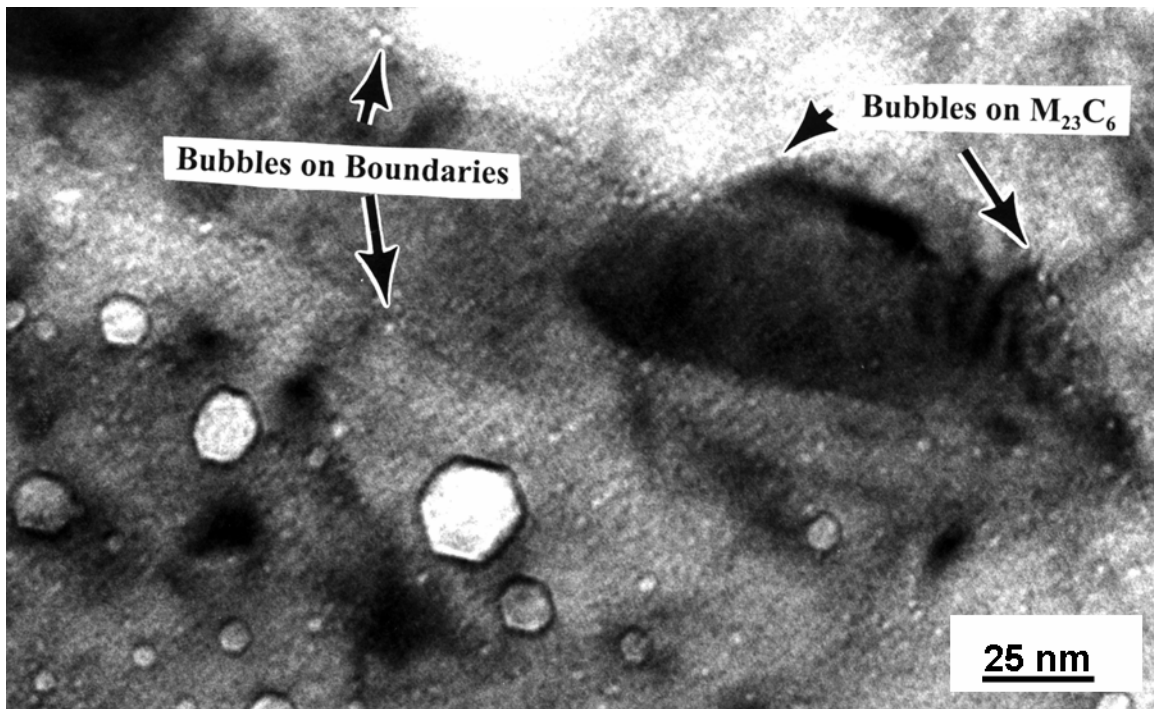


Fig. 4. Bubbles on martensite lath boundaries and on  $M_{23}C_6$  precipitates in 9Cr-1MoVW-2Ni steel irradiated in HFIR to  $\approx 75$  dpa (760 appm He) at 400°C [54].

An explanation for the maximum is that beyond the fluence for saturation, irradiation-enhanced softening proceeds to the point where it offsets some of the hardening. That is, thermal aging causes a reduction of strength due to precipitate coarsening and dislocation recovery [57]. In the absence of irradiation, such softening would occur at 400°C only after much longer thermal-aging times. Irradiation-enhanced diffusion accelerates the process to produce the maximum in strength. Therefore, the much larger shift in DBTT for a smaller shift in yield stress for steels irradiated to 40 dpa relative to the more recent tests can be explained. With less hardening, the only way to cause a larger shift in DBTT is for there to be a decrease in fracture stress caused by helium (Farrell's third mechanism [47]), as proposed previously [5,6].

This hypothesis can be applied to the latest results on the nickel-doped steels [1]. The lower fluence (12 dpa vs. 40 dpa for the previous work) means that less helium reaches boundaries that are potential sites for fracture initiation than in the 40 dpa tests. Therefore, the helium effect would be expected to be less for the 12 dpa specimens than for 40 dpa specimens, as has been observed. In this case embrittlement is aided by excess hardening by Farrell's first mechanism [47]. Lower helium plus lower irradiation-enhanced diffusion rates at 300°C provide reasons to expect even less of an effect at this and lower temperatures for the conditions of the recent and previous tests. Because of diffusion, the postulated mechanism would require less helium to produce complete intergranular fracture as the irradiation temperature increases. Furthermore, there appears to be a relationship between the  $\Delta$ DBTT and helium concentration at 400°C [1], further enhancing this hypothesis.

Helium generated from boron [8,9,29–33] appears to have a larger effect per amount of helium than helium formed in nickel-doped steels [1,5,6]. Boron can segregate to prior-austenite grain boundaries during austenitization [60–63]. This is a non-equilibrium process, and the amount of segregated boron at prior austenite grain boundaries depends on cooling rate from the austenitization temperature [63]. In recent work to understand stabilization of  $M_{23}C_6$  during creep of two 9Cr-W steels, it was determined that boron is incorporated in the  $M_{23}C_6$  precipitate to form  $M_{23}(C,B)_6$  [64,65]. This occurs during tempering, and the amount of boron in the  $M_{23}C_6$  depends on the tempering temperature, time, and the boron composition. For the irradiation studies on boron-containing steels, it is expected the boron will be

situated in  $M_{23}(C,B)_6$ , which is mainly at prior-austenite grain boundaries and lath boundaries. If, as hypothesized above, helium-containing cavities at boundaries act as crack-nucleation sites, then, in boron-doped steels, cavities should form at a lower total helium concentration, since helium from boron forms in the vicinity of the boundaries where fracture is nucleated, thus decreasing the diffusion distance.

Although there was much more helium in the steels irradiated in SINQ [18–22] and the helium-implantation studies than the nickel- and boron-doped steels, the results demonstrated that helium caused intergranular failure [12–14, 21,22]. Because of the high helium concentrations in those cases, completely intergranular fractures would be expected from the above hypothesis. That is what was observed, compared to an  $\approx 75\%$  intergranular fracture surface on a 12Cr-1MoVW-2Ni steel irradiated to 74 dpa and 760 appm He [5]. Henry et al. reached a similar conclusion to that reached from the irradiated nickel-doped steels [5,6] to explain their intergranular failures when they postulated that helium caused a decrease in the critical stress for intergranular fracture [13].

Odette, Yamamoto, and Kishimoto [66] recently proposed a mechanism to explain helium effects similar to that proposed previously [5,6] and discussed here. They posit critical fracture stresses for transgranular cleavage (TGC),  $\sigma_c^*$ , and intergranular fracture (IGF),  $\sigma_{ig}^*$ ; brittle fracture for either mode occurs when the critical stress is exceeded in front of a notch or crack tip. According to this formalism, "...gradual weakening of the PAGs [prior-austenite grain boundaries] by helium (and/or other mechanisms) would not be reflected in IGF until  $\sigma_{ig}^*$  falls below  $\sigma_c^*$ ..." However, the authors acknowledge that such an abrupt change would not be expected and, in reality, a gradual change from TGC to IGF would be expected [66], as was hypothesized previously [6].

#### Observations and Future Experiments

If the above interpretation of the nickel-doped results and other helium-effects studies is correct, then a large effect of helium on impact properties of high-temperature steels may occur for operating conditions in the first wall of a fusion reactor. Since ferritic/martensitic steels are currently the only viable structural material for this application, the need to understand helium effects is of utmost importance. These observations underscore the need for an intense 14 MeV neutron source, so the effect can be studied under conditions applicable to a fusion reactor first wall.

Since an intense 14 MeV neutron source is not on the near-term horizon, simulation experiments and the use of spallation neutron sources must continue to be applied to the problem. Results from the 12 dpa experiment [1] indicate nickel-doping has limitations for relatively low-dose, low-temperature irradiations, since relatively small effects are observed. Likewise, well-known problems are inherent in boron-doping experiments—surface segregation and the production of lithium in concert with helium. Nevertheless, properly planned experiments using nickel and boron isotopes should be possible to elucidate the problem.

Until now, most helium-effects studies have been restricted to  $\leq 425^\circ\text{C}$ , since irradiation hardening from displacement damage does not occur in ferritic/martensitic steels at  $\geq 425^\circ\text{C}$ . However, as pointed out previously [6], if the proposed mechanism for the effect of helium on fracture is correct, then under irradiation conditions where high helium concentrations form, much larger bubbles will form at boundaries in shorter times at higher irradiation temperatures.

Such bubble formation on boundaries has been observed in irradiation of nickel-doped steels irradiated in HFIR at  $600^\circ\text{C}$  to  $\approx 40$  dpa and  $\approx 400$  appm He (Fig. 5) [54]. In this case, relatively large bubbles formed on lath boundaries, but their numbers and the amount of boundary area covered were much less than observed for the same steel irradiated at  $400^\circ\text{C}$  (Fig. 4). This difference probably results from the change in bubble-nucleation kinetics with increasing temperature. The presence of fewer bubbles plus the absence of radiation hardening at higher temperatures might mitigate against embrittlement. However, the presence of bubbles on a boundary implies the presence of atomic helium on the boundary. Therefore, if helium lowers the resistance to crack propagation, then embrittlement may occur in the absence of any irradiation hardening, meaning the effect could appear above the temperature where

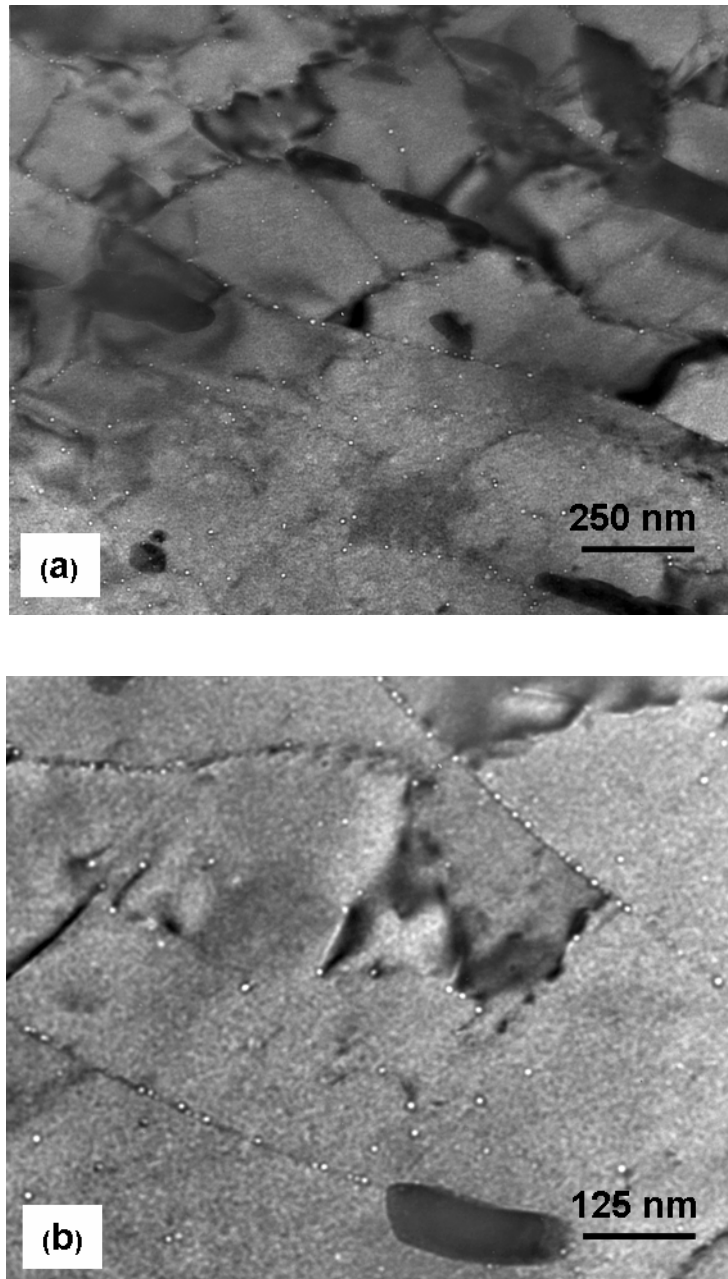


Fig. 5. Bubbles on (a) at low magnification indicating they formed on martensite lath boundaries and the matrix and (b) at higher magnification indicating their distribution in the 12Cr-1MoVW-2Ni steel irradiated in HFIR at 600°C to  $\approx 40$  dpa [54].

irradiation hardening ceases. At the higher temperatures, this is essentially classical elevated-temperature helium embrittlement. Creep and tensile tests at 600 and 700°C have shown that the ferritic/martensitic steels are relatively immune to this phenomenon [67], although no impact tests have been conducted.

## SUMMARY AND CONCLUSIONS

Based on nickel-doping studies along with results from studies using boron doping, helium implantation, and spallation neutron source techniques, it was concluded that helium plays a significant role in the hardening and embrittlement after irradiation at temperatures where irradiation hardening occurs ( $\leq 425\text{--}450^\circ\text{C}$ ). For low helium concentrations, hardening due to helium occurs over and above hardening due to displacement damage and irradiation-induced precipitation. The increased hardening due to helium causes further embrittlement as determined in an impact test. Helium is probably associated with a higher number density of irradiation-induced defects. It can stabilize vacancy clusters that can increase the number of interstitial clusters that eventually grow into dislocations as well as stabilize clusters to higher temperatures. Small bubbles may also contribute to hardening.

With increasing helium concentration, there is a decrease in fracture stress that is associated with a transition to helium-induced intergranular failure on the lower shelf in an impact test. Complete intergranular failure would not be expected until very large helium concentrations ( $>1000$  ppm) are reached. In the transition region between hardening and complete intergranular failure, it was suggested that small helium-filled cavities or bubbles could become nuclei for fracture and/or enhance crack propagation. Alternatively, or in combination with bubbles on the boundaries, helium atoms on the boundaries could promote fracture. Both processes are caused by the diffusion of helium to grain boundaries, subgrain (martensite lath) boundaries, and precipitate/lattice interfaces, where the small helium bubbles can form.

Although the results of a large number of helium-effects studies using simulation techniques indicate a helium effect on embrittlement of ferritic/martensitic steels, all of the techniques have problems associated with interpreting results. There is a critical need for an intense 14 MeV neutron source in which the problems inherent in the simulation techniques are eliminated.

## Acknowledgements

For reviewing the manuscript and for helpful discussions of the subject, Drs. D. R. Harries, L. K. Mansur, R. G. Stoller, and S. J. Zinkle are gratefully acknowledged. This research was sponsored by the Office of Fusion Energy Sciences, U.S. Department of Energy, under contract DE-AC05-00OR22725 with UT-Battelle, LLC.

## References

- [1] R. L. Klueh, N. Hashimoto, M. A. Sokolov, K. Shiba, and S. Jitsukawa, *Journal of Nuclear Materials* (in press).
- [2] R. L. Klueh and J. M. Vitek, *J. Nucl. Mater.* 161 (1989) 13.
- [3] R. L. Klueh and J. M. Vitek, *J. Nucl. Mater.* 150 (1987) 272.
- [4] R. L. Klueh and P. J. Maziasz, *J. Nucl. Mater.* 187 (1992) 43.
- [5] R. L. Klueh and D. J. Alexander, *J. Nucl. Mater.* 187 (1992) 60.
- [6] R. L. Klueh and D. J. Alexander, *J. Nucl. Mater.* 218 (1995) 15.
- [7] R. L. Klueh and E. E. Bloom, *Nucl. Eng. Design* 73 (1982) 101.
- [8] K. Shiba, I. Ioka, J. E. Robertson, M. Suzuki, and A. Hishinuma, in *Euromat 96: Conference on Materials and Nuclear Power* (Institute for Materials, London, 1996) 265.
- [9] K. Shiba and A. Hishinuma, *J. Nucl. Mater.* 283–287 (2000) 474.
- [10] R. Lindau, A. Möslang, D. Preininger, M. Rieth, and H. D. Röhrig, *J. Nucl. Mater.* 271 & 272 (1999) 450.
- [11] P. Jung, J. Henry, J. Chen, and J.-C. Brachet, *J. Nucl. Mater.* 318 (2003) 241.
- [12] J. Henry, M.-H. Mathon, and P. Jung, *J. Nucl. Mater.* 318 (2003) 249.
- [13] J. Henry, L. Vincent, X. Averty, B. Marini, and P. Jung, *Journal of Nuclear Materials* (in press).

- [14] J. Henry, L. Vincent, X. Averty, B. Marini, and P. Jung, *Journal of Nuclear Materials* (in press).
- [15] L. K. Mansur, A. F. Rowcliffe, M. L. Grossbeck, and R. E. Stoller, *J. Nucl. Mater.* 139 (1986) 228.
- [16] G. R. Odette, *J. Nucl. Mater.* 141–143 (1986) 1057.
- [17] L. K. Mansur and W. A. Coghlan, in *Effects of Irradiation on Materials: 14<sup>th</sup> International Symposium*, Vol. 1, ASTM STP 1046, Eds., N. J. Packan, R. E. Stoller, and A. S. Kumar (American Society for Testing and Materials, Philadelphia, 1989) 315.
- [18] X. Jia, Y. Dia, and M. Victoria, *J. Nucl. Mater.* 305 (2002) 1.
- [19] Y. Dai, X. Jia, and K. Ferrell, *J. Nucl. Mater.* 318 (2002) 192.
- [20] X. Jai and Y. Dia, *J. Nucl. Mater.* 323 (2003) 360.
- [21] Y. Dia and X. Jai, in *Proceedings of Conference on Accelerator Applications in a Nuclear Renaissance* (American Nuclear Society, La Grange Park, Ill., 2004) 857–863.
- [22] Y. Dia, X. Jai, R. Thermer, and F. Groeschel, *Irradiation Effects in Martensitic Steels Under Neutron and Proton Mixed Spectrum*, TM-34-04-08, Paul Scherrer Institute (2004).
- [23] S. A. Maloy, T. Romero, M. R. James, and Y. Dai, *Journal of Nuclear Materials* (in press).
- [24] K. Farrell and T. S. Byun, *J. Nucl. Mater.* 296 (2001) 129.
- [25] K. Farrell and T. S. Byun, *J. Nucl. Mater.* 318 (2003) 274.
- [26] L. R. Greenwood, *J. Nucl. Mater.* 115 (1983) 137.
- [27] R. Kasada, A. Kimura, H. Matsui, and M. Narui, *J. Nucl. Mater.* 258–263 (1998) 1199.
- [28] R. Kasada and A. Kimura, *Mater. Trans.* 46 (2005) 475.
- [29] E. V. van Osch, M. G. Horsten, G. E. Lucas, and G. R. Odette, in *Effects of Irradiation on Materials: 19<sup>th</sup> International Symposium*, ASTM STP 1366, Eds., M. L. Hamilton, A. S. Kumar, S. T. Rosinski, and M. L. Grossbeck (American Society for Testing and Materials, West Conshohocken, Pa., 2000) 612.
- [30] M. Rieth, B. Dafferner, and H. D. Röhrig, *J. Nucl. Mater.* 258–263 (1998) 1147.
- [31] E. I. Materna-Morris, M. Rieth, and K. Ehrlich, in *Effects of Irradiation on Materials: 19<sup>th</sup> International Symposium*, ASTM STP 1366, Eds., M. L. Hamilton, A. S. Kumar, S. T. Rosinski, and M. L. Grossbeck (American Society for Testing and Materials, West Conshohocken, Pa., 2000) 597.
- [32] H-C. Schneider, B. Dafferner, and J. Aktaa, *J. Nucl. Mater.* 295 (2001) 16.
- [33] H-C. Schneider, B. Dafferner, and J. Aktaa, *J. Nucl. Mater.* 321 (2003) 135.
- [34] L. R. Greenwood, *J. ASTM Int.* 3 (2006).
- [35] K. Farrell, J. T. Houston, A. Wolfenden, R. T. King, and A. Jostons, in *Radiation-Induced Voids in Metals*, Eds., J. W. Corbett and L. C. Ianniello, CONF-710601, U.S. Atomic Energy Commission (1972) 376.
- [36] D. S. Gelles and F. A. Garner, *J. Nucl. Mater.* 85&86 (1979) 689.
- [37] P. J. Maziasz, R. L. Klueh, and J. M. Vitek, *J. Nucl. Mater.* 141–143 (1986) 929.
- [38] P. J. Maziasz and R. L. Klueh, in *Effects of Radiation on Materials: 14th International Symposium*, Volume I, ASTM STP 956, Eds., N. H. Packan, R. E. Stoller, and A. S. Kumar (American Society for Testing and Materials, Philadelphia, 1987) 35.
- [39] R. L. Klueh, J. M. Vitek, W. R. Corwin, and D. J. Alexander, *J. Nucl. Mater.* 155–157 (1988) 973.
- [40] W. L. Hu and D. S. Gelles, in *Influence of Radiation on Material Properties: 13th International Symposium (Part II)*, ASTM STP 956, Eds., F. A. Garner, C. H. Henager, Jr., and N. Igata (American Society for Testing and Materials, Philadelphia, 1987) 83.
- [41] E. Wakai, N. Hashimoto, Y. Miwa, J. P. Robertson, R. L. Klueh, K. Shiba, and S. Jitsukawa, *J. Nucl. Mater.* 283–287 (2000) 334.
- [42] J. C. Brachet, X. Averty, P. Lamagnère, A. Alamo, F. Rosenblum, O. Raquet, and J. L. Bertin, in *Effects of Irradiation on Materials: 20<sup>th</sup> International Symposium*, ASTM STP 1405, Eds., S. T. Rosinski, M. L. Grossbeck, T. R. Allen, and A. S. Kumar (American Society for Testing and Materials, West Conshohocken, Pa., 2002) 500.
- [43] J. Henry, X. Averty, Y. Dia, P. Lamagnère, J. P. Pizzanelli, J. J. Espinas, and P. Wident, *J. Nucl. Mater.* 318 (2003) 215.
- [44] Y. Dia, Y. Foucher, M. James, and B. Oliver, *J. Nucl. Mater.* 318 (2003) 167.
- [45] H. Ogiwara, A. Kohyama, H. Tanigawa, and H. Sakasegawa, *Journal of Nuclear Materials* (in press).
- [46] N. Hashimoto and R. L. Klueh, *J. Nucl. Mater.* 305 (2002) 153.
- [47] K. Farrell, *Radiat. Eff.* 53 (1980) 175.
- [48] K. Farrell, P. J. Maziasz, E. H. Lee, and L. K. Mansur, *Radiat. Eff.* 78 (1983) 277.
- [49] J. Hunn, E. Lee, T. Byun, and L. Mansur, *J. Nucl. Mater.* 282 (2000) 131.
- [50] Y. Osetsky, D. Bacon, and V. Mohles, *Philos. Mag.* 83 (2003) 3623.

- [51] B. Wirth, G. Odette, J. Marian, L. Ventelon, J. Young-Vandersall, and L. Zepeda-Ruiz, *J. Nucl. Mater.* 329–333 (2004) 103.
- [52] R. W. Hertzberg, *Deformation and Fracture Mechanics of Engineering Materials*, 3<sup>rd</sup> Ed. (Wiley, New York, 1989) 253.
- [53] C. J. McMahon, Jr., *Fundamental Phenomena in the Materials Sciences*, Eds., L. J. Bonis, J. J. Duga, and J. J. Gilman, Vol. 4 (Plenum, New York, 1967) 247.
- [54] P. J. Maziasz, unpublished research.
- [55] A. Kohyama, A. Hishinuma, D. S. Gelles, R. L. Klueh, W. Dietz, and K. Ehrlich, *J. Nucl. Mater.* 233–237 (1996) 138.
- [56] K. Shiba, M. Suzuki, A. Hishinuma, and J. E. Pawel, in *Effects of Radiation on Materials: 17th International Symposium*, ASTM STP 1270, Eds., D. S. Gelles, R. K. Nanstad, A. S. Kumar, and E. A. Little (American Society for Testing and Materials, Philadelphia, 1996) 753.
- [57] V. S. Khabarov, A. M. Dvoriashin, and S. I. Porollo, *J. Nucl. Mater.* 233–237 (1996) 236.
- [58] S. A. Maloy, M. B. Toloczko, K. J. McClellan, T. Romero, Y. Kohno, F. A. Garner, R. J. Kurtz, and A. Kimura, *Journal of Nuclear Materials* (in press).
- [59] R. L. Klueh and D. J. Alexander, *J. Nucl. Mater.* 258–263 (1998) 1269.
- [60] W. C. Leslie, *The Physical Metallurgy of Steels* (McGraw-Hill Book Company, New York, 1981) 269.
- [61] F. B. Pickering, *Physical Metallurgy and the Design of Steels* (Applied Science Publishers Ltd, London, 1978) 103.
- [62] T. M. Williams, A. M. Stoneham, and D. R. Harries, *Met. Sci.* 10 (1976) 14.
- [63] D. R. Harries and A. D. Marwick, *Phil. Trans. Roy. Soc. London A295* (1980) 197.
- [64] A. Golpayegani, M. Hättestrand, and H-O. Andrén, in *Parsons 2003: Engineering Issues in Turbine Machinery, Power Plant and Renewables*, Eds., A. Strang, R. D. Conroy, W. M. Banks, M. Blackler, J. Leggett, G. M. McColvin, S. Simpson, M. Smith, F. Starr, and R. W. Vanstone (The Institute of Materials, Minerals and Mining, London, 2003) 347.
- [65] A. Czyska-Filemonowicz, K. Bryla, K. Spiradek-Hahn, H. Firganek, A. Zielinska-Lipiec, and P. J. Ennis, in *Advances in Materials Technology for Fossil Power Plants*, Eds., R. Viswanathan, D. Gandy, and K. Coleman (ASM International, Materials Park, Ohio, 2005) 365.
- [66] G. R. Odette, T. Yamamoto, and H. Kishimoto, *Fusion Materials Semiannual Progress Report for Period Ending December 31, 2003*, DOE/ER-313/35 (2004) 90.
- [67] R. L. Klueh and D. R. Harries, *High-Chromium Ferritic and Martensitic Steels for Nuclear Applications* (ASTM, West Conshohocken, Pa., 2001) 135.

## ON THE RELATION BETWEEN IRRADIATION INDUCED CHANGES IN THE MASTER CURVE REFERENCE TEMPERATURE SHIFT AND CHANGES IN STRAIN HARDENED FLOW STRESS—G. R. Odette, M. Y. He, and T. Yamamoto (University of California, Santa Barbara)

### OBJECTIVE

Relation between irradiation induced changes in the master curve reference temperature shift and changes in strain hardened flow.

### SUMMARY

Irradiation hardening produces increases in the cleavage transition fracture toughness reference temperature ( $\Delta T_o$ ). It is traditional to relate  $\Delta T_o$  to the corresponding changes in the yield stress,  $\Delta\sigma_y$ , as  $C_o = \Delta T_o / \Delta\sigma_y$ . However, it is a strain-hardened flow stress,  $\sigma_{fl}$ , in the fracture process zone that controls cleavage, rather than  $\sigma_y$ . Thus, irradiation induced decreases in the strain hardening  $\Delta\sigma_{sh}$  ( $< 0$ ) must be considered along with  $\Delta\sigma_y$  ( $> 0$ ) in evaluating  $\Delta T_o$ . The  $\Delta\sigma_{sh}$  in reactor pressure vessel (RPV) steels irradiated to low doses at around 300°C are small, even for large  $\Delta\sigma_y$ . However, the  $\Delta\sigma_{sh}$  are much greater for high dose irradiations of tempered martensitic steels (TMS) that are candidates for fusion applications. As a result, for the TMS case the  $C_o$  are less, and in some instances much less, than for RPV steels and irradiation conditions. We address two key questions. First, how does  $\Delta\sigma_{sh}$  influence the  $C_o = \Delta T_o / \Delta\sigma_y$  relation? Second, is it possible to derive a universal relation between  $\Delta T_o$  and  $\Delta\sigma_{fl}$  averaged over a pertinent range of  $\epsilon$ ,  $\langle \Delta\sigma_{fl} \rangle$ , such that a  $C_o' = \Delta T_o / \langle \Delta\sigma_{fl} \rangle$  is independent of the individual values of  $\Delta\sigma_y$  and  $\Delta\sigma_{sh}$ ? The results of this study suggest that  $\langle \Delta\sigma_{fl} \rangle$  averaged between 0 and 0.1 provides a similar  $C_o'$  for various assumptions about the effect of irradiation on  $\Delta\sigma_{sh}$ . Notably, changes in indentation hardness,  $\Delta H$ , are also directly related to this same  $\langle \Delta\sigma_{fl} \rangle$ . Hence, measurements of  $\Delta H$  should provide a good basis for assessing  $\Delta T_o$  for a wide range of alloys and irradiation conditions.

### PROGRESS AND STATUS

#### Introduction

The master curve (MC) method is based on the empirical observation that in the cleavage transition fracture toughness temperature curves [ $K_{Jc}(T)$ ], for a wide variety of ferritic alloys and alloy conditions, have an approximately constant shape [1-4]. The master curve shape can be indexed on a relative temperature scale  $[(T - T_o)]$  by a reference temperature ( $T_o$ ) at 100 MPa $\sqrt{m}$ . It is believed that the  $K_{Jc}(T - T_o)$  curve is invariant for a wide range of  $T_o$ , including following irradiation, leading to  $T_o$  shifts ( $\Delta T_o$ ). It is also well established that shifts in both Charpy indexed ( $\Delta T_c$ ) and fracture toughness ( $\Delta T_o$ ) cleavage transition temperatures induced by neutron irradiation below about 400°C are primarily due to hardening [1-3, 5-7]. Thus, it is common to correlate  $\Delta T_c$  and  $\Delta T_o$  with irradiation induced increases in the yield stress ( $\Delta\sigma_y$ ). Analysis of data for low dose (typically  $< 0.06$  dpa)  $\approx 300^\circ\text{C}$  irradiations of Mn-Mo-Ni low alloy reactor pressure vessel steels, shows that  $C_o = \Delta T_o / \Delta\sigma_y \approx 0.7 \pm 0.2^\circ\text{C}$  [2]. The corresponding values for higher dose ( $> 1$  dpa)  $\approx 300^\circ\text{C}$  irradiations of 9Cr tempered martensitic steels (TMS) are generally smaller with  $C_o < \approx 0.6^\circ\text{C}$ , and even much less in some cases, particularly for lower irradiation temperatures ( $T_i$ ) [1,7,12]. Thus, it is important to understand and model the mechanisms responsible for differences in  $C_o$ . In this paper, we focus on in the hardening dominated embrittlement regime, within the framework of a critical micro-cleavage stress ( $\sigma^*$ )-critical stressed volume ( $V^*$ ) model of  $K_{Jc}(T)$  [1,3,8-11,13,14]. However, in this case we use a two-dimensional small scale yielding model, with T-stresses equal to 0, where the local fracture properties are expressed in terms of a critical area ( $A^*$ ) within a specified  $\sigma_{22} = \sigma^*$  stress contour. Here,  $\sigma_{22}$  is the stress normal to the crack plane. For finite dimensions  $V^* = BA^*$ , where B is the crack front length, assuming full constraint.

### Effects of Irradiation on $\sigma_{fl}(\varepsilon)$

Within the framework of the hardening dominated shift model, the  $\Delta\sigma_{fl}(\varepsilon)$  is the strength property controlling  $\Delta T_o$ . Thus, it is critical to properly treat the combined effects of irradiation, alloy type, test temperature and strain rate over a proper  $\varepsilon$  range. Unfortunately, information needed to build appropriate  $\sigma_{fl}(\varepsilon)$  models is limited, especially for irradiated alloys with high  $\sigma_y$  and low  $\sigma_{sh}$ , leading to very low to negligible uniform strains, almost immediate necking upon yielding and, in many cases, internal flow localization. Conditions associated with post yield strain softening offer even greater complications. Thus, we will consider general trends between the unirradiated alloys and the corresponding irradiation conditions.

Figure 1a shows an example of the effect of low dose 0.025 dpa, 270°C irradiation on the room temperature  $\sigma_{sh}(\varepsilon)$  for high sensitivity (0.2% Cu and 1.6% Ni) RPV steel. Note, we show  $\sigma_{sh}(\varepsilon)$  rather than  $\sigma_{fl}(\varepsilon)$  to make the effects of irradiation on strain hardening more visible. In this extreme case producing a large  $\Delta\sigma_y \approx 400$  MPa,  $\Delta\sigma_{sh}(\varepsilon)$  is modest; for example, at  $\varepsilon = 0.025$ ,  $\Delta\sigma_{sh}(0.025) \approx -20$  MPa. For a lower  $\Delta\sigma_y \approx 200$  MPa case (CM19-T16 not shown) the  $\Delta\sigma_{sh}(0.025) \approx -10$  MPa. For RPV steels and irradiation conditions the general trend is  $\Delta\sigma_{sh}(0.025) \approx -0.05\Delta\sigma_y$ . Thus, irradiation induced  $\Delta\sigma_{sh}$  is expected to have little effect on the  $C_o = \Delta T_o/\Delta\sigma_y$  relation for RPV steels. Figure 1b shows the corresponding  $\sigma_{fl}(\varepsilon)$  for the TMS F82H. Note the strain hardening in the *unirradiated* TMS alloy is more rapid compared to the RPV steels. For example, at  $\varepsilon = 0.025$  the unirradiated  $\sigma_{sh}$  are  $\approx 115$  MPa and 50 MPa in the unirradiated TMS and RPV alloys, respectively. This difference is the consequence of the finer scale tempered martensite lath packet microstructure in TMS, compared to the bainitic microstructure RPV steels [16, 19-21].

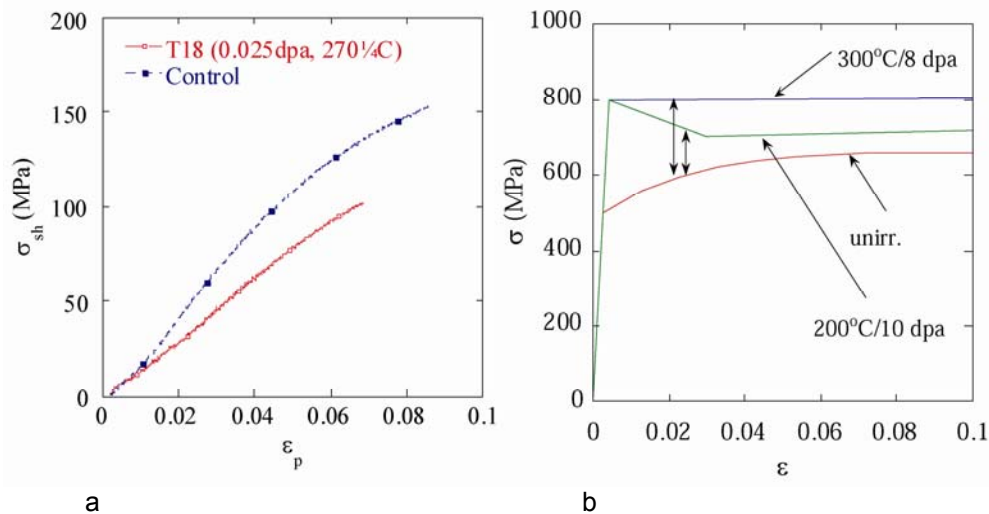


Fig. 1. a) an example of the effect of low dose 0.025 dpa, 270°C irradiation on the room temperature  $\sigma_{sh}(\varepsilon)$  for high sensitivity (0.2% Cu and 1.6% Ni) RPV steel and b)  $\sigma_{fl}(\varepsilon)$  curves for the F82H TMS unirradiated and irradiated to 10 dpa at 200°C and 8 dpa at 300 °C.

However, an even more significant effect is the much larger  $\Delta\sigma_{sh}$  following irradiation in the TMS case, leading to approximately perfectly plastic or even softening behavior at high  $\Delta\sigma_y$ . This is also illustrated in Figure 1b showing two examples of true stress-strain  $\sigma_{fl}(\varepsilon)$  curves that were derived using an finite element (FE) procedure, described elsewhere [16]. The procedure is based on simulating engineering stress-strain curves, accounting for geometry and stress state changes that occur during necking, to find a self-consistent  $\sigma_{fl}(\varepsilon)$ . The  $\Delta\sigma_y \approx 300$  MPa for test temperatures ( $T_i$ ) at  $T_i$  in both cases. The curve for a 300°C, 8 dpa irradiation is almost perfectly plastic, while that for a 200°C, 10 dpa irradiation shows softening at ( $\approx -100$  MPa at  $\varepsilon = 0.025$ ). Note, the assessment of strain hardening effects is further complicated by the fact that both  $\Delta\sigma_y$

(lower) and  $\Delta\sigma_{sh}$  (lower or higher) vary with lower  $T_t < T_i$ , as well as  $T_i$ . Nevertheless, as shown by the double arrow lines near  $\varepsilon = 0.025$ , the  $\Delta\sigma_{fl}/\Delta\sigma_y$  are much smaller than for TMS alloy and irradiation conditions compared to the RPV steel case. For example, assuming perfectly plastic behavior after irradiation resulting in  $\Delta\sigma_y = 300$  MPa, the TMS  $\Delta\sigma_{sh}(0.025) \approx -115$  MPa compared to an estimated  $\approx -15$  MPa for RPV steels and irradiation conditions. Again assuming  $\sigma_{fl}(0.025)$  is the controlling strength parameter, the difference in  $\Delta\sigma_{sh}(0.025)$  would result reduction in the nominal  $C_o = \Delta T_o/\Delta\sigma_y$  from  $\approx 0.7$  to  $\approx 0.46^\circ\text{C}/\text{MPa}$ . Assuming softening of 100 MPa following irradiation, would further reduce  $C_o$  to  $\approx 0.3^\circ\text{C}/\text{MPa}$ .

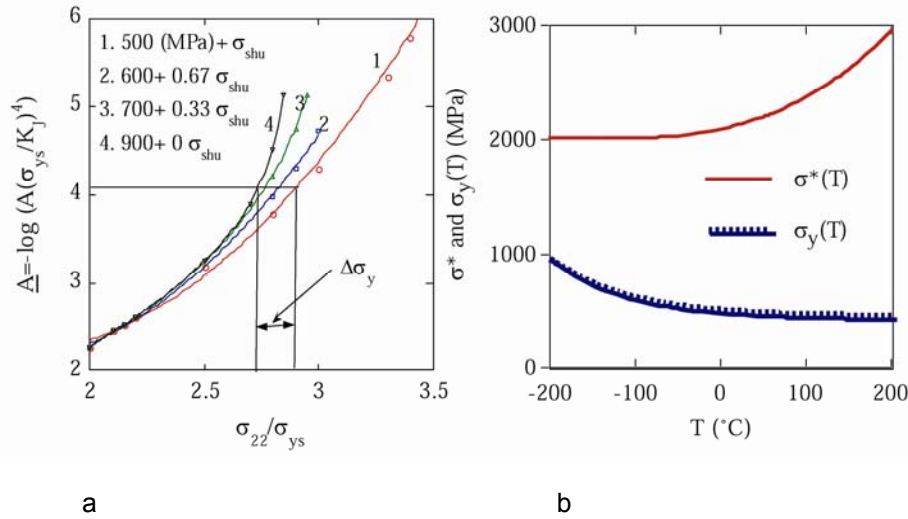


Fig. 2. a)  $\log A_o$  versus  $(\sigma_{22}/\sigma_y)$  derived from the FE calculations along with the corresponding polynomial fit lines and b)  $\sigma^*(T)$  fitted for the  $\sigma_y(T)$  derived from the least square fit to RPV and TMS database and  $A^* = 5 \times 10^{-9} \text{ m}^2$ .

## Results and Analysis

We have proposed a simple model for small scale yielding that cleavage, by either a single or few propagating micro-cracks, or quasi-cleavage involving extensive micro-cracking prior to cleavage, occurs when a  $\sigma_{22} = \sigma^*$  encompass a critical *area* ( $A^*$ ) [1, 7-11, 13, 14]. We further quantify these results based on an  $\sigma^*$ - $A^*$  cleavage model, using prototypical  $\sigma_{fl}(\varepsilon)$  that reflect the combined effects of irradiation on both  $\Delta\sigma_y$  and  $\Delta\sigma_{sh}$ , as:

$$\sigma_{fl}(\varepsilon) = \sigma_{yu} + \Delta\sigma_y + \sigma_{shu}(\varepsilon) + \Delta\sigma_{sh}(\varepsilon) \quad (1)$$

Here the subscript u designates the unirradiated condition and the  $\Delta\sigma_y$  and  $\Delta\sigma_{sh}(\varepsilon)$  represent the effects of irradiation on  $\sigma_y (> 0)$  and  $\sigma_{sh} (< 0)$ , respectively. Various  $\sigma_{fl}(\varepsilon)$  were used, based on guidance from assessing trends in a large database. We specifically assume the nominal  $\sigma_{shu}(\varepsilon)$  decreases by a factor of 1/3 for  $\Delta\sigma_y = 100$  MPa, 2/3 for  $\Delta\sigma_y = 200$  MPa and vanishes for  $\Delta\sigma_y \geq 300$  MPa.

Figure 3 shows the  $K_{Jc}(T)$  curves for  $\Delta\sigma_y$  from 0 to 400 MPa both with (solid lines) and without (dashed lines) corresponding reductions in  $\Delta\sigma_{sh}(\varepsilon)$ . The predicted  $K_{Jc}(T)$  curves (solid line) are reasonably consistent with the shape MC (dotted lines). Figure 4a shows the corresponding  $\Delta T_o$  plotted against the  $\Delta\sigma_y$ . The  $C_o$  found by least square fits are  $0.51^\circ\text{C}/\text{MPa}$  for the reduced  $\sigma_{sh}$  case versus  $0.66^\circ\text{C}/\text{MPa}$  for the assumption that  $\sigma_{sh}$  is not decreased by irradiation. The nominal relation for RPV steels is also shown for comparison. Figure 4 a also shows the effect of perfectly plastic strain softening of 100 MPa, resulting in a  $C_o \approx 0.36^\circ\text{C}/\text{MPa}$  for  $\Delta\sigma_y = 300$  and 400 MPa resulting in corresponding  $\Delta\sigma_{fl} = 200$  and 300 MPa, respectively.

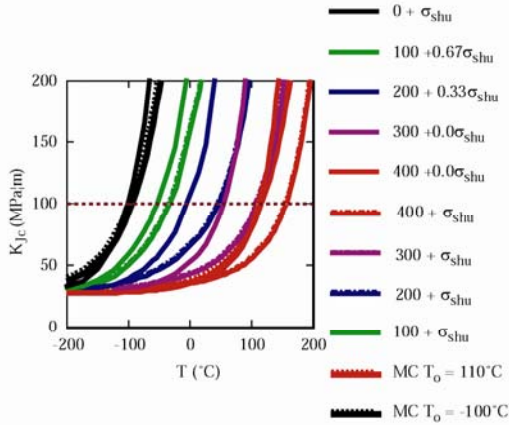


Fig. 3.  $K_{Jc}(T)$  curves for  $\Delta\sigma_y$  from 0 to 400 MPa both with (solid lines) and without (dashed lines) corresponding reductions in  $\Delta\sigma_{sh}(\varepsilon)$ .

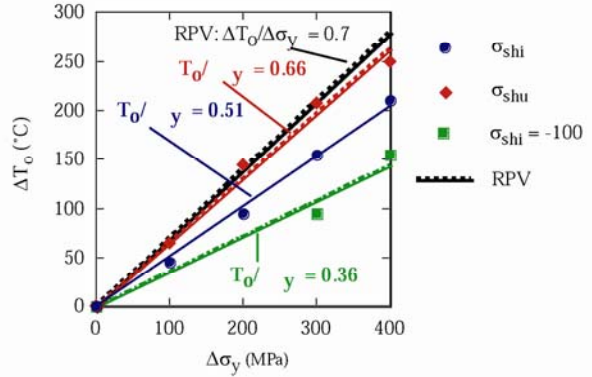


Fig. 4. a) The corresponding  $\Delta T_0$  plotted against the  $\Delta\sigma_y$  for various strain hardening cases.

Clearly, irradiation induced decreases in  $\sigma_{sh}$  result in significant reductions in the  $C_0 = \Delta T_0/\Delta\sigma_y$  relation. Put simply, part of the  $\Delta\sigma_y (> 0)$  is wasted (or recovered) by simultaneous  $\Delta\sigma_{sh} (< 0)$ . In principle, this effect could be accounted for by defining  $\Delta T_0$  in terms of a  $\Delta\sigma_{fl}$  at a specified  $\varepsilon$ ,  $C_{0'} = \Delta T_0/\Delta\sigma_{fl}(\varepsilon)$  or averaged over a pertinent range of  $\varepsilon$ ,  $\langle\Delta\sigma_{fl}\rangle$ ,  $C_{0'} = \Delta T_0/\langle\Delta\sigma_{fl}\rangle$ . Figure 4b shows  $\Delta T_{0'}$  as a function of the  $\Delta\sigma_{fl}(\varepsilon)$  for various  $\varepsilon$  as indicated in the legend. The calculated points approximately fall along the same line with different  $C_{0'}$  slopes. The  $C_{0'} = 0.69^\circ\text{C}/\text{MPa}$  at  $\varepsilon = 0.03$ , which close to the  $C_0$  for the case where  $\Delta\sigma_{fl} = \Delta\sigma_y$ , with no reduction in strain hardening. However, it is not clear that a single specified strain is applicable in all cases, and the  $C_{0'} = \Delta T_0/\langle\Delta\sigma_{fl}\rangle$  based on averaging  $\Delta\sigma_{fl}$  may be more general.

We have shown elsewhere that there is a universal relationship between indentation hardness ( $H$ ) and the average  $\sigma_{fl}$  between  $\varepsilon = 0$  to 0.1,  $\langle\sigma_{fl}\rangle_H$  [24,25]. Figure 4c plots  $\Delta T_0$  versus  $\langle\Delta\sigma_{fl}\rangle_H$  for both cases with and without reduction in  $\sigma_{sh}$ . The  $\Delta T_0$  all approximately fall along a single line with  $C_{0'} = \Delta T_0/\langle\Delta\sigma_{fl}\rangle_H = 0.68^\circ\text{C}/\text{MPa}$ . This suggests that there may be a universal relation between  $\Delta T_0$  and  $\Delta H$  (or its  $\langle\Delta\sigma_{fl}\rangle_H$  equivalent).

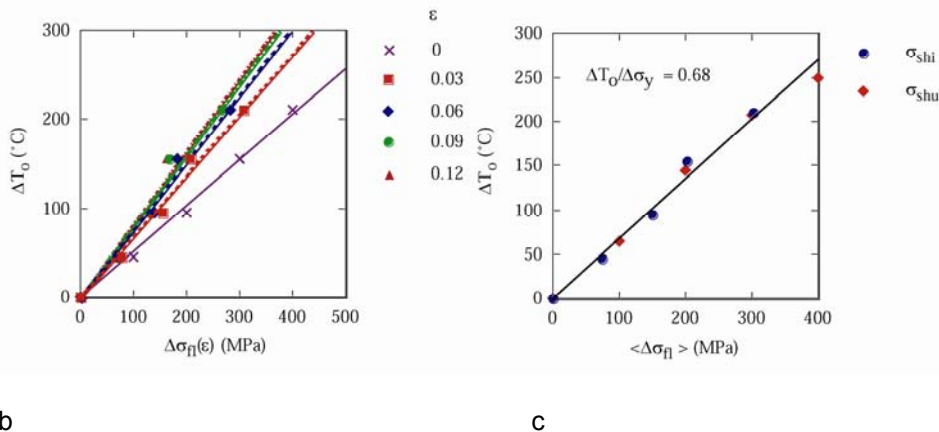


Fig. 4. b)  $\Delta T_{0'}$  as a function of the  $\Delta\sigma_{fl}(\varepsilon)$  for various  $\varepsilon$  and c)  $\Delta T_0$  versus  $\langle\Delta\sigma_{fl}\rangle_H$  for both cases with and without reduction in  $\sigma_{sh}$ .

## Concluding Remarks

In this work we addressed two key questions. First, how does  $\Delta\sigma_{sh}$  influence the  $C_o = \Delta T_o / \Delta\sigma_y$  relation? Second, is it possible to derive a universal relation between  $\Delta T_o$  and  $\Delta\sigma_{fl}$  averaged over a pertinent range of  $\varepsilon$ ,  $\langle\Delta\sigma_{fl}\rangle$ , such that a  $C_o = \Delta T_o / \langle\Delta\sigma_{fl}\rangle$  is independent of the individual values of  $\Delta\sigma_y$  and  $\Delta\sigma_{sh}$ . The results suggest that  $\langle\Delta\sigma_{fl}\rangle$  averaged between  $\varepsilon = 0$  to 0.1 provides a similar  $C_o$  for various assumptions about the effect of irradiation on  $\Delta\sigma_{sh}$ . Notably, changes in indentation hardness,  $\Delta H$ , are also directly related to this same  $\langle\Delta\sigma_{fl}\rangle$ . Hence, measurements of  $\Delta H$  should provide a good basis for assessing  $\Delta T_o$  for a wide range of alloys and irradiation conditions.

## References

- [1] G. R. Odette, T. Yamamoto, H. J. Rathbun, M. Y. He, M. L. Hribernik, and J. W. Rensman, *J. Nucl. Mater.* 323 (2003) 313.
- [2] M. A. Sokolov and R. K. Nanstad, *Effects of Irradiation on Materials-18<sup>th</sup> International Symposium*, ASTM STP 1325 (1999) 167.
- [3] G. R. Odette, T. Yamamoto, H. Kishimoto, M. Sokolov, P. Spätig, W. J. Yang, J-W. Rensman, and G. E. Lucas, *J. Nucl. Mater.* 329–333 (2004) 1243.
- [4] ASTM E 1921-05, *Standard Test Method for Determination of Reference Temperature,  $T_o$ , for Ferritic Steels in the Transition Range*, ASTM (2005).
- [5] T. Yamamoto, G. R. Odette, H. Kishimoto, J-W. Rensman, and P. Miao, *Journal of Nuclear Materials* (submitted).
- [6] R. Kasada, T. Morimura, A. Hasegawa, and A. Kimura, *J. Nucl. Mater.* 299 (2001) 83.
- [7] G. R. Odette, H. J. Rathbun, J. W. Rensman, and F. P. van den Broek, *J. Nucl. Mater.* 307–311 (2002) 1624.
- [8] G. R. Odette, K. Edsinger, G. E. Lucas, and E. Donahue, *ASTM STP 1329* (1998) 298.
- [9] G. R. Odette and M. Y. He, *J. Nucl. Mater.* 283–287 (2000) 120.
- [10] G. R. Odette and M. Y. He, *J. Nucl. Mater.* 307–311 (2002) 1624.
- [11] H. J. Rathbun, G. R. Odette, M. Y. He, and T. Yamamoto, *Engineering Fracture Mechanics* (submitted).
- [12] J-W. Rensman, *NRG Irradiation Testing: Report on 300°C and 60°C Irradiated RAFM Steels*, NRG Petten 20023/05.68497/P.
- [13] K. Edsinger, G. R. Odette, G. E. Lucas, and B. D. Wirth, *ASTM STP 1270* (1996) 670.
- [14] G. R. Odette, *J. Nucl. Mater.* 212–215 (1994) 45.
- [15] T. L. Anderson, *Fracture Mechanics: Fundamentals and Applications*, Third Edition, CRC Press, Boca Raton, Fla. (2005).
- [16] G. R. Odette, M. Y. He, E. G. Donahue, P. Spatig, and T. Yamamoto, *J. Nucl. Mater.* 307–311 (2002) 171.
- [17] A. F. Rowcliffe, J. P. Robertson, R. L. Klueh, K. Shiba, D. J. Alexander, M. L. Grossbeck, and S. Jitsukawa, *J. Nucl. Mater.* 258–263 (1998) 1275.
- [18] J. Rensman, H. E. Hofmans, E. W. Schuring, J. van Hoepen, J.B.M. Bakker, R. den Boef, F. P. van den Broek, and E.D.L. van Essen, *J. Nucl. Mater.* 307–311 (2002) 250.
- [19] (CM17 T18 SS).
- [20] P. Spätig, R. Schäublin, and M. Victoria, in *Material Instabilities and Patterning in Metals*, Eds., H. M. Zbib, G. H. Campbell, M. Victoria, D. A. Hughes, and L. E. Levine, *Mater. Res. Soc. Symp. Proc.*, Vol. 683E (MRS, Warrendale, Pa., 2001) BB1.10.1.
- [21] P. Spatig, G. R. Odette, G. E. Lucas, and M. Victoria, *J. Nucl. Mater.* 307–311 (2002) 536.
- [22] M. Nevalainen, R. H. Dodds, and J. R. Rice, *J. Mech. Phys. Solids* 21 (1973) 131.
- [23] M. L. Hribernik, G. R. Odette, and M. Y. He, *Fusion Materials Semiannual Report DOE/ER-313/38* (2005) 109.
- [24] G. R. Odette, M. Y. He, and D. Klingensmith, *Fusion Materials Semiannual Report DOE/ER-313/37* (2005) 109.
- [25] M. Y. He, G. R. Odette, T. Yamamoto, and D. Klingensmith, *Journal of Nuclear Materials* (submitted).

## ON THE INTRINSIC INITIATION AND ARREST CLEAVAGE FRACTURE TOUGHNESS OF FERRITE—M. L. Hribernik, G. R. Odette, and M. Y. He (University of California, Santa Barbara)

### OBJECTIVE

The primary objective is to assess the hypothesis that a universal master toughness temperature curve shape,  $K_{Jc}(T - T_o)$ , observed in structural steels derives from an underlying universal temperature dependence of the intrinsic ferrite lattice micro-arrest toughness,  $K_{\mu}(T)$ . These results also represent the first database on the fundamental toughness properties of Fe and will provide critical insight on the atomic processes governing the brittle-to-ductile transition (BDT).

### SUMMARY

The results of the crack arrest fracture toughness ( $K_a$ ) measurements on cleavage oriented Fe single crystals from -196 to 0°C are reported. Arrest measurements were performed on four low toughness cleavage orientations; (100)[010], (100)[011], (110)[001] and (110)[110]. Reliable and consistent measurements were obtained for the (100) cleavage planes, however inconsistent measurements were observed for the (110) planes as cleavage cracks always reverted back to the (100) planar orientation. The corresponding static ( $K_{ic}$ ) and dynamic ( $K_{id}$ ) cleavage initiation toughness for the (100) planes from -196 to 50°C were also measured over a range of applied stress intensity rates ( $\dot{K}$ ) from  $\approx 0.1$  to  $10^4$  MPa $\sqrt{m/s}$ . The  $K_{ia}(T)$ ,  $K_{ic}(T)$  and  $K_{id}(T)$  gradually increase with temperature from a minimum average  $K_{ia}$  value of approximately 4 MPa $\sqrt{m}$  up to a rapid BDT at  $\approx 0^\circ\text{C}$ . The BDT temperature increases with higher  $\dot{K}$ , and is highest for  $K_{ia}$ . The  $\dot{K}$  dependence of  $K_{ic/d}(T)$  is consistent with the strain rate dependence of thermally activated flow stress of Fe. The  $K_{ic}(T)$  for single crystal Fe and W are also reasonably similar when plotted on a homologous temperature scale. The  $K_{ia}(T)$  for Fe at  $\approx -40^\circ\text{C}$  is similar to that for Fe-3wt%Si at  $\approx 110^\circ\text{C}$ . This 150°C shift can be reasonably rationalized by the solid solution lattice strengthening of Si. The  $K_{ia}(T)$  for Fe must be shifted up by  $\approx 220^\circ\text{C}$  to approximate the temperature dependence of the  $K_{\mu}(T)$  that is consistent with a universal  $K_{Jc}(T)$  master curve shape. This magnitude of shift may be caused by a combination of thermally activated (rate-dependent) solid solution lattice strengthening, complemented by long-range internal stress fields.

### PROGRESS AND STATUS

#### Introduction

The brittle-to-ductile transition (BDT) in bcc metals and alloys is of both technological and scientific importance. Almost no reliable experimental data are available on the BDT in unalloyed Fe. Also, in spite of a large modeling literature, a fundamental understanding of the BDT remains one of the most elusive material science challenges. A corollary fundamental challenge is to rationalize the empirical observation that the shape of the macroscopic fracture toughness-temperature curve,  $K_{Jc}(T - T_o)$ , of structural steels is approximately the same when scaled by reference temperature  $T_o$ . The universal master curve (MC) shape appears to apply to a very wide range of alloy microstructures and strength levels, thus a correspondingly large span of  $T_o$ . The ASTM Standard E 1921 [1] for measuring fracture toughness in the transition is based on the MC concept. However, there are a number of questions concerning the MC method. The most fundamental pertains to the existence of a universal MC shape, which is not understood [2]. Relevant background has been presented in previous reports, so a brief summary is given here.

Cleavage in steels involves a sequence of events ultimately associated with the unstable propagation of a microcracks formed at brittle trigger particle. The high stresses and strains in the blunting crack tip process zone crack these particles, such as grain boundary carbides. While many particles may exist in the process zone, only those with sufficiently large size and favorable

orientation with respect to low toughness crystallographic planes and directions in the adjoining ferrite are 'eligible' for a microcrack propagation event. That is, the propagation versus arrest of a dynamic microcrack into the adjacent ferrite matrix is the critical event for macroscopic cleavage [3,4] and is associated with a critical stress,  $\sigma^*$ . The  $\sigma^*$  can be expressed in terms of a modified Griffith criteria in Equation 1 [2-4]:

$$\sigma^* = CK_{\mu}/\sqrt{d} \quad (1)$$

Here, C is a geometric factor of order unity, that depends on the crack shape and d is the characteristic trigger particle size. Thus the macroscopic cleavage  $K_{Jc}$  is controlled, by the  $K_{\mu}$  ( $\ll K_{Jc}$ ) of ferrite. The traditional model assumption is that  $\sigma^*$  is approximately independent of temperature. This assumption is consistent with MC behavior at low temperatures. However, at high temperatures and with  $\Delta\sigma_y$  shifts caused by irradiation hardening this assumption is not consistent with observed MC shape. This inconsistency is a consequence of the decreasing temperature dependence of  $\sigma_y(T)$  at higher  $T_0 \geq \approx 0^\circ\text{C}$ , and can be remedied by incorporating a modest temperature dependence, as  $\sigma^*(T)$ .

The temperature dependence of  $\sigma^*(T)$  demands a corresponding temperature dependence of  $K_{\mu}(T)$ . The fact that the position ( $T_0$ ), but not the shape, of the MC depends on microstructure and alloy strength leads to the hypothesis that  $K_{\mu}(T)$  is independent of the fine, nano-scale features introduced by irradiation. This further suggests that some intrinsic property of the ferrite matrix controls  $K_{\mu}(T)$ . Thus the focus of this work is on assessing  $K_{\mu}(T)$  in Fe. While it can be inferred from the trigger particle size distribution and  $\sigma^*$ ,  $K_{\mu}$  cannot be directly measured [2-4]. However, it is possible to measure various toughness parameters of single crystal Fe oriented for cleavage, including the static ( $K_{Ic}$ ) and dynamic ( $K_{Id}$ ) initiation toughness for sharp cracks, and the arrest toughness ( $K_{Ia}$ ) for propagating cracks. While not identical properties, we propose that the  $K_a(T)$  is a good surrogate for  $K_{\mu}(T)$ .

In spite of the paucity of data, many models have been proposed to describe the BDT in Fe and other bcc metals and alloys. Regardless of detail and level of approximation, however, most BDT models are based on the interaction between a (usually) sharp crack tip under increasing remote loading ( $K_I$ ) and the evolution of local dislocation structures. The first successful attempt to model the BDT, based on an energy criterion mediating the nucleation of a single dislocation (ductile) prior to bond breaking (brittle), was proposed by Rice and Thomson (RT) [5]. The RT model and its progeny focusing on the nucleation and glide of dislocations, coupled with some detailed experimental observations, have helped to clarify the specific crystallographic slip processes involved in shielding a stationary crack tip. However, the various BDT models involve a number of assumptions and approximations and predict a wide range of behavior. The models and model parameters can be adjusted to match wide range of experimental results. Further, the BDT models have generally not addressed the crack tip processes involved in continued propagation of a cleavage crack, or arrest of the crack by the evolution of crack tip shielding dislocations. Thus, it is clear that the atomic level processes that govern the BDT are not fully understood in general, and for crack arrest in particular. Hence, our major objective is to develop a unique toughness database of unalloyed Fe single crystals over a wide range of temperature.

## Experimental Procedure

The following section only very briefly outlines the challenging experimental techniques used in this study, and greater detail is given in previous reports. Single crystal rods sectioned into thin rectangular slices with the desired (100)[010], (100)[011], (110)[001] and (110)[110] cleavage orientations were procured from Monocrystals Co. The slices were incorporated into composite specimens reflecting two different approaches to testing, referred to as the 'bridge' and 'wedge' techniques. In both cases, the composite specimens were fabricated by diffusion bonding the

single crystal slices to high strength steel sections that served both to transmit loads and store and release elastic energy.

The bridge technique was a modified compression precracking method, where the beam initially contains a shallow fatigue pre-crack [6]. Figure 1 (blue line) shows the variation in the corresponding normalized stress intensity factor ( $K_I/\sigma W^{1/2}$ ) versus the crack depth to beam width ratio ( $a/W$ ) determined from a detailed finite element (FE) analysis. The major limitation of the compression anvil bridge technique is that at higher test temperatures ( $T > -100^\circ\text{C}$ ) it is not possible to initiate a dynamic crack from a shallow fatigue pre-crack at a compressive  $\sigma$  that does not damage or deform the specimen.

Thus a second method was developed based on the wedge loading of a composite chevron specimen with short double cantilever arms [7]. The wedge technique allowed access to higher test temperatures up to  $\approx 0^\circ\text{C}$ , and has the advantage that multiple initiation and arrest events can be measured with a single specimen. Implementation of this test method also required a detailed FE analysis and optimization, leading to the normalized stress intensity factor ( $K_I B^{1/2}/E\Delta$ ) shown by Figure 1 (red lines), where  $\Delta$  is the wedge opening displacement at the end of the beam arms. One very important detail about the double cantilever beam chevron wedge test determined in the FE analysis was that the  $K_I$  is higher at the edge corners (solid red line) of the crack front in the chevron than in the center (dashed red line). Thus cracks tend to initiate at the corners (at  $K_{Ic}$ ) and arrest (at  $K_{Ia}$ ) in the middle of the crack front.

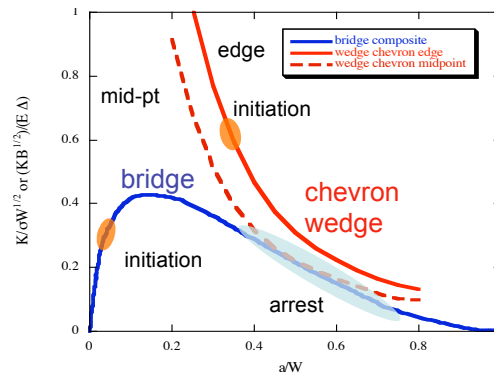


Figure 1. Finite element assessment of the stress intensity for the bridge and wedge specimens.

Following bridge testing, the beam specimens are left with a deep and very sharp pre-crack, providing the opportunity to obtain initiation toughness measurements over a range of loading rates from static ( $K_{Ic}$ ) to dynamic ( $K_{Ia}$ ). The initiation tests were carried out in 4-point bending through servo-hydraulic load frame and drop tower loading schemes at  $\dot{K}$  from  $\approx 1\text{-}10^4$  MPa $\sqrt{\text{m/s}}$ . Note the corresponding  $\dot{K}$  for the chevron wedge specimen tests was  $\approx 0.1$  MPa $\sqrt{\text{m/s}}$  thereby increasing the overall  $\dot{K}$  range of this study.

## Results

The average  $K_{Ia}$  results for the four cleavage orientations are shown in Figure 2. The standard deviations of the  $K_{Ia}$  data scatter are not shown, but are in the range of  $\pm 1.0$  to  $1.5$  MPa $\sqrt{\text{m}}$ . There is good agreement between the two techniques, so the data is combined where they overlap below  $-100^\circ\text{C}$ . The (100)[011] orientation is in general slightly lower than the (100)[010], and the (100) plane data is much lower than the (110). Also the transition for the (100) plane data occurs at a higher temperature than the (110) plane. However, while an attempt was made to force cleavage onto the (110) planes, the cracks always propagated along the (100) plane. Therefore, the toughness levels are not truly representative of this cleavage system.

The results of the (100) plane  $K_{Ic}$  over the range of  $\dot{K} = 0.1-10^4$  MPa $\sqrt{m/s}$  are summarized in Figure 3a. In general the [011] direction is slightly less tough than the [010], but they are very similar and are combined to reflect the (100) plane. As expected, the  $K_{Ic}$  decrease with rising  $\dot{K}$ .

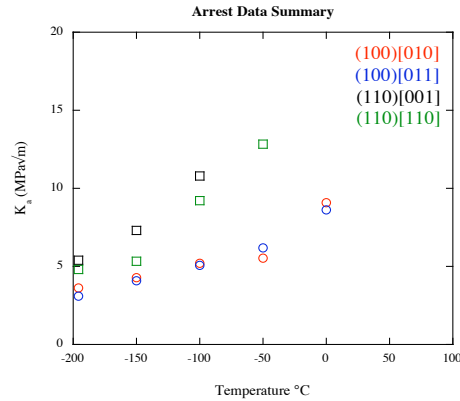


Figure 2. Results of arrest toughness measurements on Fe single crystal.

It is expected that the  $\dot{K}$  dependence of  $K_{Ic}$  derives from the corresponding strain rate dependence of  $\sigma_y$  (or, more precisely, the critical resolved shear stresses for the glide of screw dislocations on pertinent slip systems). To test this hypothesis the data from Figure 3a, along with the  $K_{Ic}$  from the double cantilevered beam chevron wedge specimen test are re-plotted in Figure 3b on a  $\dot{K}$  compensated temperature scale  $T'$ , analogous to a strain rate compensated temperature.  $T'$  (°K) is given by:

$$T' = T[1 - C \ln(\dot{K}/\dot{K}_r)] \quad (2)$$

Here  $\dot{K}$  is the loading rate for a specific test and  $\dot{K}_r$  is a reference rate of 1000 MPa $\sqrt{m/s}$ . The  $C$  is 0.035 consistent with the corresponding strain rate dependence of  $\sigma_y$ . While the data remain scattered, the  $K_{Ic/d}$  data fall in a common band, except possible at the lowest temperature where the  $K_{Ic}$  data remains higher than the  $K_{Ic}$  results. However, These results lend powerful support to the hypothesis that the BDT in Fe (and other bcc metals and alloys) is controlled by thermally activated dislocation glide processes.

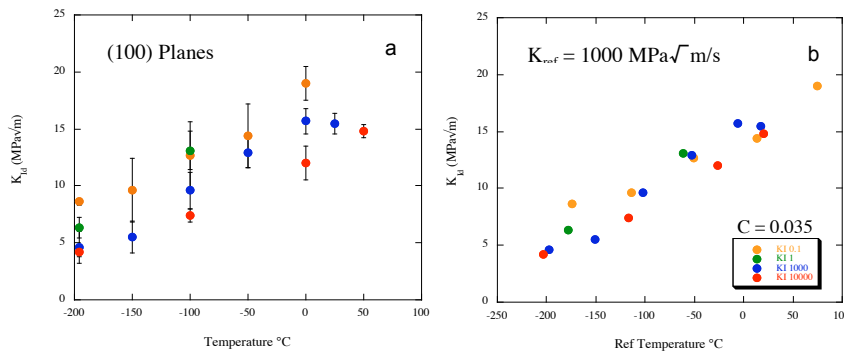


Figure 3a-b. a) Results of (100) planar orientation rate effect dynamic toughness study. b) Rate adjustment of dynamic data to a reference state similar to a strain rate compensated  $\sigma_y$ .

Figure 4 compares  $K_{Ic}$  data from each of the orientations in the quasi-static loading condition (0.1 MPa $\sqrt{m/s}$ ) to that of W single crystals reported by Gumbsh [8] plotted on a homologous  $T/T_m$  scale, where  $T_m$  is the melting temperature. Overall the initiation toughness data are similar, with the exception of the (110)[110] system, but issues with the (110) plane data have been

addressed. At low temperatures, the W data are somewhat lower than the Fe  $K_{Ic}$  data. Agreement is better at higher temperatures although an abrupt BDT for W occurs at a lower  $T/T_m$ .

Figure 5a compares the  $K_{Ia}$  data for Fe and Fe-3wt%Si single crystal reported by Argon (unfilled diamonds) [9]. At comparable  $K_{Ia}$  levels the Fe data (green circles) is  $\approx 150^\circ\text{C}$  lower in temperature. This difference could be rationalized by the solid solution strengthening contribution of the 3%Si to the alloy  $\sigma_y$  (or, more properly, the critical resolved shear stresses for screw

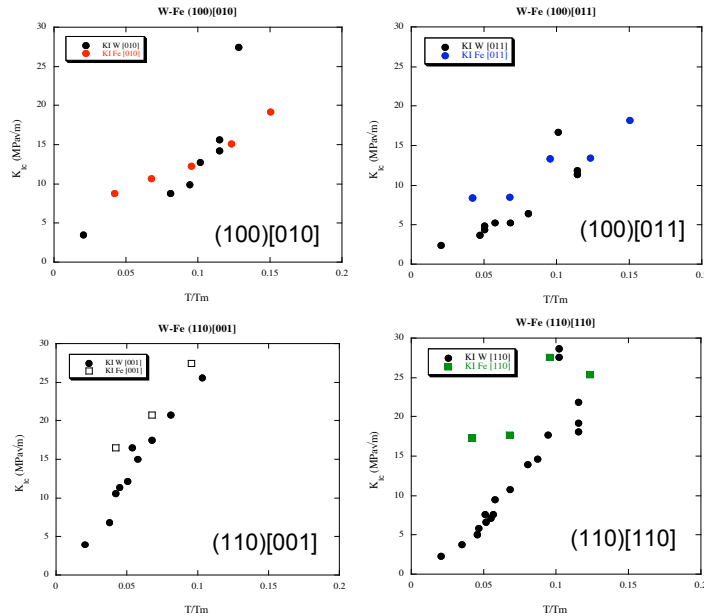


Figure 4. Comparison of quasi-static  $K_{Ic}$  Fe and W data on four low toughness orientations.

dislocation glide on the pertinent slip systems) compared to unalloyed Fe. If it is assumed that the Si contribution to the thermally activated (rate dependent) lattice resistance to dislocation slip is similar in consequences to the crystal lattice contribution (the Peirls stress) in unalloyed Fe at lower temperatures, the corresponding temperature shift in the  $K_{Ia}$  can be evaluated at the difference in the temperatures,  $\Delta T$ , for equivalent  $\sigma_y$  in Fe and Fe-3wt%Si [10]. The corresponding  $\Delta T$  is estimated to be  $\approx 150^\circ\text{C}$ , as shown by the red symbols in Figure 5a, which are in good agreement with the Fe-3wt%Si  $K_{Ia}$  data. Note, Si is spaced less than one nm apart on the slip and two adjoining planes, hence, might be expected to produce a friction like lattice resistance stress. There are, however, complications in this simple hypothesis, like the fact that Si produces softening at low temperatures. Thus additional research is needed to understand the role of solutes in mediating the BDT.

Figure 5b compares the Fe  $K_{Ia}(T)$  data to the  $K_{\mu}(T)$  derived (blue line) from a fitted  $\sigma^*(T)$  that is consistent with an invariant MC shape in low alloy C-Mn-Mo-Si-Ni and C-Cr-Mo-W steels. As in the case with the Fe-3wt%Si  $K_{Ia}$  data, the  $K_{\mu}(T)$  data (green circles) are either: a) simply totally inconsistent with the measured  $K_{Ia}(T)$  for Fe; or b) the  $K_{Ia}(T)$  in typical alloys are shifted up (red circles) in temperature by approximately  $220^\circ\text{C}$ , due to mechanisms such as solid solution strengthening and, possibly, long range stress fields. Of course, the latter interpretation is not fully consistent with our previous hypothesis that there is a completely intrinsic  $K_{Ia}(T)$ -BDT curve for ferrite that is relatively independent of the microstructure, such as changes induced by irradiation. Further, even with a large shift the adjusted Fe  $K_{Ia}$  data show a somewhat stronger temperature dependence than the normalized  $K_{\mu}(T)$  curve, especially at the highest temperature. However, it is noted that the  $K_{\mu}(T)$  curve depends on the assumed temperature dependence of  $\sigma_y$ , which was taken from the average of many steels and other details that are not accounted for in this simple

analysis, like the effects of temperature and irradiation on strain hardening as well as the effective strain rate in the process zone. Further, there is little valid  $K_{Jc}$  data to test the hypothesis of a MC shape at temperatures above  $\approx 100^\circ\text{C}$ .

A weak effect of microstructure versus a stronger effect of solutes on the BDT might be attributed to the corresponding difference between discrete, moderately strong to strong athermal dislocation obstacles that are much more widely spaced (typically  $>$  to  $\gg \approx 10$  nm) compared to closely spaced ( $< 1$  nm) dissolved solutes, that contribute to a thermally activated and rate dependent lattice friction type flow stress. Finally, we re-emphasize that  $K_a(T)$  and  $K_\mu(T)$  are not identical properties, and possible differences between them will also be explored in the future. Thus the solute BDT temperature shift concept is a plausible but not proven hypothesis.

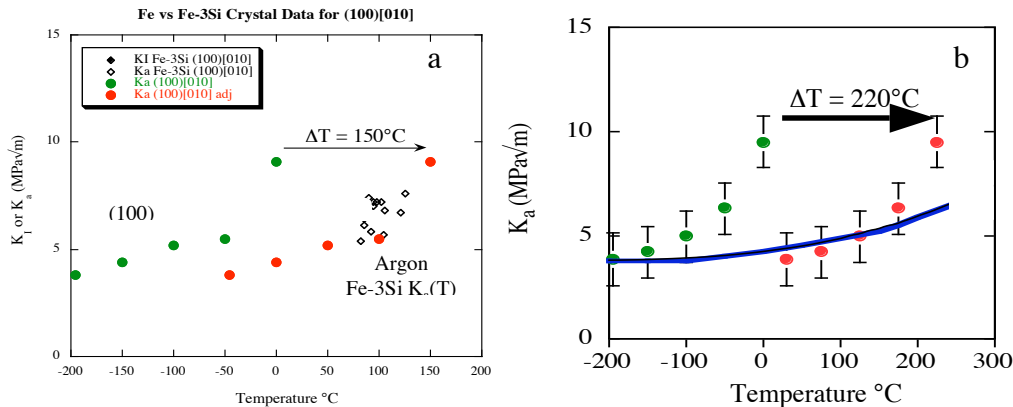


Figure 5a-b. a) Comparison of Fe and Fe-3Si arrest toughness levels showing an approximate  $150^\circ\text{C}$  difference in equivalent toughness levels. b) Comparison of Fe arrest toughness to that predicted to alleviate discrepancy between model and observed MC shape.

### Future Work

The toughness measurements will be complemented by detailed characterization of the fracture surface features, side slip traces, and dislocation structures using optical and scanning electron microscopy. The main goal is develop a catalog of images from combinations of orientation, temperature and applied loading rate. The results of the characterization studies will be correlated with general trends in fracture surface topology, such as arrest front depth, apparent amount of dislocation activity on the surface, and size of the arrest/re-initiation boundary. Finally, etch pit studies of fracture and side slip surfaces have been initiated in attempt to identify the type of dislocations active and quantify the dislocation densities of the various regions of the crack trace.

### References

- [1] ASTM Standard E 1921-97, ASTM 2003.
- [2] G. R. Odette and M. Y. He, *J. Nucl. Mater.* 283-287 (2000) 120.
- [3] G. R. Odette, T. Yamamoto, H. J. Rathbun, M. L. Hribernik, and J. W. Rensman, *J. Nucl. Mater.* 323 (2003) 313.
- [4] G. T. Hahn, *Metall. Trans.* 15A (1984) 987.
- [5] J. R. Rice and R. Thomson, *Philos. Mag.* 29 (1974) 73.
- [6] ASTM Standard C 1421-99, ASTM 2000.
- [7] ASTM Standard E 1304-97, ASTM 1998.
- [8] P. Gumbsch, J. Riedle, A. Hartmaier, and H. F. Fischmeister, *Science* 282 (1998) 1293.
- [9] Y. Qiao and A. S. Argon, *Mech. Mater.* 35 (2003) 903.
- [10] P. B. Pickering, in *Physical Metallurgy and the Design of Steels* (1978) 65.

**SWELLING AND MICROSTRUCTURE OF PURE Fe AND Fe-Cr ALLOYS AFTER NEUTRON IRRADIATION TO ~26 DPA AT 400°C**—Yu V. Konobeev, A. M. Dvoriashin, S. I. Porollo (The Institute of Physics and Power Engineering, Russia), F. A. Garner (Pacific Northwest National Laboratory)

**OBJECTIVE**

The object of this effort is to expand our understanding of the factors that determine the response of ferritic alloys to radiation.

**SUMMARY**

The microstructures of pure Fe and various Fe-Cr binary alloys in both the annealed and heavily cold worked conditions were investigated after irradiation to 25.8 dpa at  $4 \times 10^{-7}$  dpa/s in the BR-10 fast reactor. Microscopy has shown that the largest swelling of 4.5% was observed in the cold worked pure iron while that of annealed Fe is only 1.7%. Additions of 2% chromium resulted in a decrease of swelling, but the swelling of cold worked Fe-2Cr alloy was still higher than that of the annealed condition. Independent of the initial starting condition, swelling in the Fe-6Cr alloy was completely suppressed. In alloys with higher chromium content swelling of 0.04–0.05% was observed only in samples irradiated in the annealed condition. There were also significant changes in dislocation and precipitate microstructure following irradiation.

**PROGRESS AND STATUS**

**Introduction**

Metals and alloys possessing a b.c.c. lattice have traditionally been considered as materials with high resistance to swelling, especially when compared to that of f.c.c. metals and alloys. Experimental data provided by Gelles on model iron-base alloys showed low swelling levels after irradiation to doses as high as 200 dpa when irradiated at relatively high displacement rates in the Fast Flux Test Facility (FFTF) [1]. There has been a general perception that the low swelling rate of b.c.c. materials is an intrinsic property of bcc crystal lattice [2]. However, recent data have cast doubt on the general validity of such a perception. The first contrary data showed that V-5%Fe swelled ~100% after neutron irradiation to 52 dpa at an average swelling rate of ~2%/dpa [3] while the steady state swelling rate in iron-base alloys with fcc lattice does not exceed 1%/dpa [4].

In one of our earlier reports, pure Fe and Fe-Cr alloys in the lightly cold-worked (5–15%) condition were irradiated near the top of the BR-10 fast reactor to 6 dpa at  $\sim 1 \times 10^{-7}$  dpa/s, which is a relatively low displacement rate for a fast reactor. Microstructural examination showed that the swelling of pure iron reaches 3%, implying an average swelling rate of ~0.5%/dpa, although the same study showed that additions of Cr resulted in partial but strong suppression of swelling [5]. At that time it was suggested that the high average swelling rate of ~0.5%/dpa in pure Fe might be related to the combined effects of cold work as well as to the relatively low dose rate of  $\sim 1 \times 10^{-7}$  dpa/s.

Garner and co-workers later showed that cold working often accelerates the onset of void swelling in metals and alloys, both f.c.c. and b.c.c., when irradiated under conditions where void nucleation was otherwise rather protracted [6,7]. Garner also showed that the swelling of both Fe-Cr-Ni and Fe-Cr alloys was a transient-dominated process, with the transient duration decreasing very strongly as the atomic displacement rate decreased [7–10]. More importantly, it was shown that the steady state swelling rate of Fe-Cr alloys was at least 0.2%/dpa, significantly larger than previously reported by Gelles after irradiation at higher displacement rates.

Fortunately, the alloys of immediate interest were irradiated in several positions in BR-10 at different dpa rates. In order to check the possibility that cold-working and lower dpa rates could increase swelling, another set of the same Fe and Fe-Cr alloys were irradiated in-core to 25.8 dpa at  $4 \times 10^{-7}$  dpa/s. While this dpa rate is higher by a factor of four compared to that of our previous study, it is still lower by an order of magnitude compared to studies conducted in FFTF by Gelles [1]. To study the

effect of thermal-mechanical treatment, these Fe and Fe-Cr alloys were irradiated in both solution treated and heavily cold-worked conditions

### Experimental Procedure

Strips of pure iron with < 0.015 C, < 0.005 P, < 0.05 S, 0.012 Si, 0.001 Al, 0.0015 Cr, 0.0015 Cu, 0.007-0.03 Ni, < 0.0015 Mg, 0.001 Mo, 0.18 O, 0.002 - 0.004 N (wt%), and four Fe-Cr alloys (2; 6; 12, 18 at % Cr) with similar low levels of impurities (> 99.9% Cr) were used to prepare the specimens. These strips were originally 0.5 mm in thickness and were rolled in one pass to 0.12 to 0.15 mm thickness. The average level of cold work in these foils was ~250%. Half of these foils were then annealed at 1100°C for 5 min and then quenched in water. Plates of 6×15 mm were prepared from both cold-worked and annealed material. A package containing both types of plates was loosely bound with Nichrome wire and placed vertically in a perforated capsule at 140–155 mm above the core midplane of the BR-10 fast reactor. The irradiation was performed in flowing sodium at 400°C, reaching 25.8 dpa at  $4 \times 10^{-7}$  dpa /s.

After irradiation, disks of 3 mm diameter were punched from these plates and thinned for electron microscopy using a STRUERS jet device. Unirradiated archive specimens were similarly prepared. The specimens were investigated using a JEM-100CX electron microscope equipped with a side-entry goniometer stage. The first details describing the microstructure of the pure Fe specimens irradiated to 25.8 dpa were reported earlier [11]. This report covers the final phase of the experiment where all Fe-Cr alloys were examined.

### Results

In the unirradiated condition (both annealed and cold-worked) Fe and Fe-18Cr were found to have ferritic structure, Fe-6Cr was completely martensitic, and the Fe-2Cr and Fe-12Cr alloys had two-phase structure with 70–80% of ferrite and 20–30% martensite. The ferrite and martensite phase fractions were determined by measuring the grain sizes on micrographs at a low magnification. In the heavily cold-worked materials, ferritic grains were observed to have undergone fragmentation and formation of clearly expressed sub-grain structure. Data on the initial dislocation density in both cold-worked and annealed materials are shown in Tables 1 and 2. The grain size in cold-worked materials was 20–50 microns. The grain size in annealed materials was larger at 50–100 microns.

Neutron irradiation resulted in significant structural changes, namely, formation of voids, dislocation loops and precipitates, and redistribution of dislocations. Data on microstructural characteristics of the irradiated materials are also shown in Tables 1 and 2.

Table 1. Characteristics of the microstructure in Fe-Cr alloys (250% C.W.) irradiated in BR-10 at 400°C to 25.8 dpa

Chromium content, at %		0	2	6	12	18
Structure		F	F+M	M	F+M	F
Dislocation density $\rho_d^{unirr}$ , $10^{14} \text{ m}^{-2}$	F	10–20	10–20	-	10–20	10
	M	-	10–20	10–20	10–20	-
Dislocation density $\rho_d^{irr}$ , $10^{14} \text{ m}^{-2}$	F	0.4	0.5	-	10	10
	M	-	10	10	10	-
Mean void diameter $\langle d_v \rangle$ , nm		120	44	-	-	-
Void number density $N_v$ , $10^{20} \text{ m}^{-3}$		0.32	1.2	-	-	-
$\Delta V/V$ , %		4.5	1.1	-	-	-
Mean loop diameter $\langle d_l \rangle$ , nm		85	36	-	-	-
Loop number density $N_l$ , $10^{20} \text{ m}^{-3}$		0.9	10	-	-	-
Mean diameter of $\alpha'$ -precipitates $\langle d_p \rangle$ , nm		-	-	-	n.m.	10
Number density of $\alpha'$ -precipitates $N_p$ , $10^{22} \text{ m}^{-3}$		-	-	-	n.m.	2

n.m. = not measured; F = ferrite, M = martensite

Table 2. Characteristics of the microstructure of Fe-Cr alloys (1100°C/5 min. + quenched) irradiated in BR-10 at 400°C to 25.8 dpa

Chromium content, at %		0	2	6	12	18
Structure		F	F+M	M	F+M	F
Dislocation density $\rho_d^{unirr}$ , $10^{14} \text{m}^{-2}$	F	<0.1	1	-	2	0.1
	M	-	5–10	10	10	-
Dislocation density $\rho_d^{irr}$ , $10^{14} \text{m}^{-2}$	F	0.3	0.5	-	0.5–1.0	0.5
	M	-	5	5	5	-
Mean void diameter $\langle d_v \rangle$ , nm		55	16	-	8	5/30–100
Void number density $N_v$ , $10^{20} \text{m}^{-3}$		1.2	5	-	5	$\approx 1.7/0.1$
$\Delta V/V$ , %		1.7	0.3	-	0.04	0.05
Mean loop diameter $\langle d_l \rangle$ , nm		117	40	-	25	12
Loop number density $N_l$ , $10^{20} \text{m}^{-3}$		0.75	6	-	5	20
Mean diameter of $\alpha'$ -precipitates $\langle d_p \rangle$ , nm		-	-	-	14	14
Number density of $\alpha'$ -precipitates $N_p$ , $10^{22} \text{m}^{-3}$		-	-	-	0.7	2

### Voids

As seen from data shown in Tables 1 and 2, pure iron exhibits the highest swelling, with cold-worked iron at 4.5%, but annealed iron is only 1.7% (Figs. 1a, b). Adding 2% chromium results in a decrease of swelling for both conditions, but the swelling of cold-worked Fe-2Cr is still higher than that of the annealed alloy, however. Voids and dislocation loops formed only in ferritic grains in Fe-2Cr. The swelling of Fe-6Cr was suppressed completely, independent of the initial thermal-mechanical treatment. The relative swelling behavior of the two starting conditions was reversed at higher chromium contents, with swelling of 0.04–0.05 % observed in the annealed condition and none in the cold-worked condition.

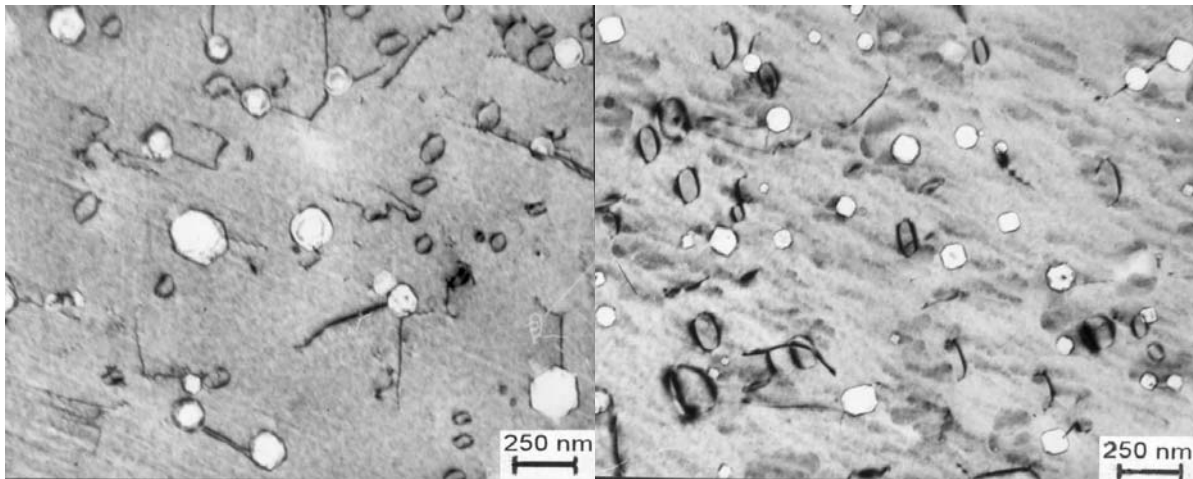


Fig. 1. Microstructure of pure Fe after irradiation in BR-10 at 400°C to 25.8 dpa. a) Specimen in ~250 % cold deformed condition; b) annealed condition.

### Dislocation structure

After irradiation the dislocation evolution was different in martensite and ferrite grains. The character of dislocation structure changes in martensite grains was similar in both cold-worked and annealed conditions, and was expressed in an approximately two-fold decrease of the initial dislocation density and also in the formation of clusters of small dislocation loops (Fig. 2a).

The dislocation structure of ferrite grains irradiated in the annealed condition consisted of quite uniformly distributed dislocation lines, segments and loops with the total length per unit volume in the

range of  $3$  to  $7 \times 10^{13} \text{ m}^{-2}$  (without counting of loops) (Fig. 2a). The largest loops were formed in pure iron with a mean loop diameter of  $117 \text{ nm}$ . With increasing chromium content the loop size decreases monotonically to  $12 \text{ nm}$ . The lowest loop concentration was observed in pure iron. Alloying of iron with chromium has resulted in a substantial increase of loop concentration.

In pure Fe and Fe-2Cr irradiated in the cold-worked condition the initial cellular dislocation structure of  $(10-20) \times 10^{14} \text{ m}^{-2}$  in density has transformed to a uniform dislocation network with density of  $(4-5) \times 10^{13} \text{ m}^{-2}$ . Meanwhile, the dislocation structure of ferrite grains in Fe-12Cr and Fe-18Cr alloys in the cold-worked condition has demonstrated a high resistance to irradiation, having kept the initial dislocation density after the irradiation. In all cases, the habit planes and Burgers vectors of loops in ferrite grains were identified as  $\{100\}$  planes and a  $\langle 100 \rangle$  Burgers vectors. From observations conducted in martensite grains one can conclude that some dislocation loops lay also on planes of  $\{100\}$  type.

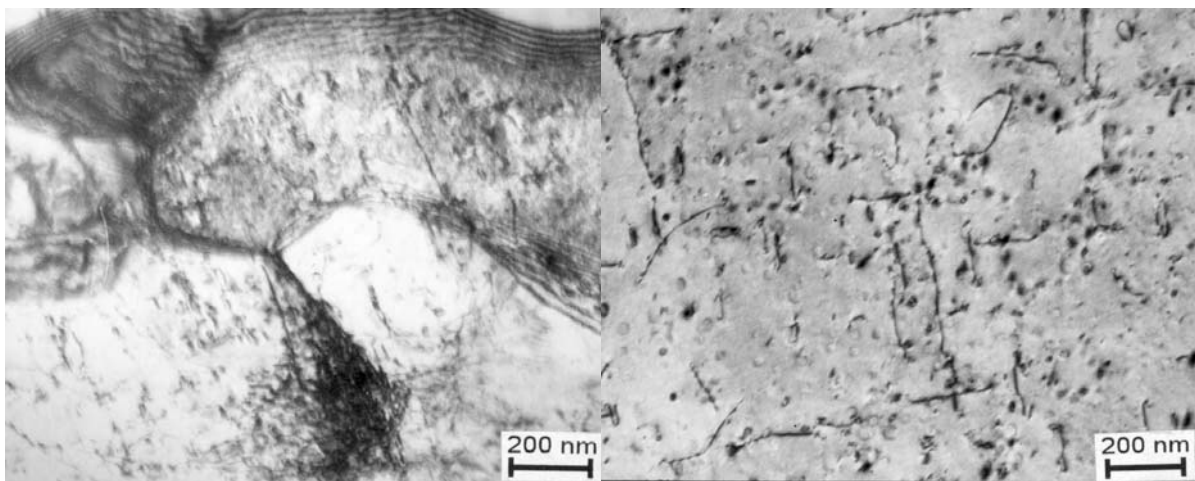


Fig. 2. Dislocation structure of Fe-Cr alloys after irradiation in BR-10 at  $400^\circ\text{C}$  to  $25.8 \text{ dpa}$ . a) Fe-6Cr alloy,  $\sim 250\%$  cold deformed, martensite, b) Fe-12Cr alloy, annealed condition, ferrite.

### Precipitates

After irradiation finely dispersed precipitates of  $\alpha'$ -phase formed the Fe-12Cr and Fe-18 alloys in the bulk of grains in both cold-worked and annealed specimens (Fig. 3a). Precipitate-free zones of  $\leq 150 \text{ nm}$  in width were observed along grain boundaries. In annealed samples the mean precipitate diameter was approximately identical at  $\sim 14 \text{ nm}$ . In cold-worked alloys the  $\alpha'$ -phase precipitates have a slightly smaller size,  $\sim 10 \text{ nm}$ . Along with the  $\alpha'$ -phase precipitates, a low concentration of rod-like or plate-like precipitates of  $100-500 \text{ nm}$  in length and  $10-40 \text{ nm}$  in thickness was observed at grain boundaries and in the matrix of annealed Fe-12Cr and Fe-18Cr alloys. In many cases these precipitates were attached to largest voids (Fig. 3a). An analysis of micro-diffraction patterns has shown that these precipitates are  $\text{M}_7\text{C}_3$  carbides. The chemical composition of both the  $\alpha'$ -phase precipitates and  $\text{M}_7\text{C}_3$  precipitates was not determined in the present work. The structures of these precipitates were determined using micro-diffraction methods.

### **Discussion**

Having reached  $3\%$  swelling in pure, lightly cold-worked iron at  $6 \text{ dpa}$  and  $1 \times 10^{-7} \text{ dpa/s}$ , one might expect to reach more than  $4.5\%$  swelling in heavily cold-worked pure iron at  $25.8 \text{ dpa}$  and  $4 \times 10^{-7} \text{ dpa/s}$ . However, such an expectation is not necessarily warranted, when one considers not only that the cold-work level is very different, but also there is a significant difference in dpa rate. Garner and coworkers have shown that relatively small increases in dpa rate can strongly extend the transient regime of both f.c.c. and b.c.c. iron-base alloys and thereby lower the swelling [7–10].

The most significant observation is that in pure Fe and Fe-2Cr irradiated side-by-side, cold-working strongly increased swelling, consistent with the earlier observations of Garner [6,7]. At higher chromium levels no swelling or very small levels of swelling were observed. In the high-chromium specimens containing radiation-induced  $\alpha'$ -phase, voids were observed only in the annealed specimens and not in the cold-worked specimens. Unlike the observations at 0–2% Cr, this behavior is in agreement with the general perception that cold working suppresses swelling.

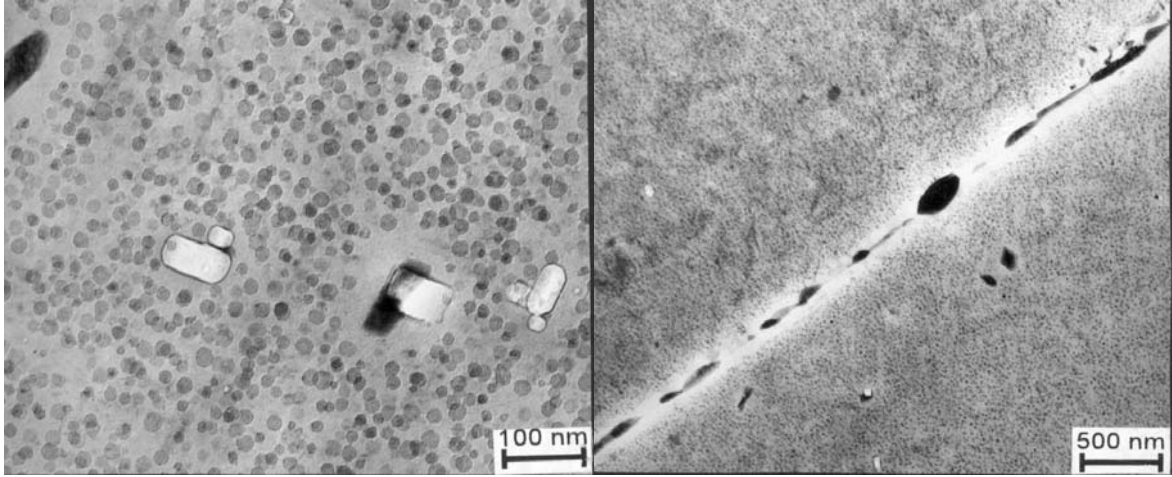


Fig. 3. Precipitation of  $\alpha'$ -phase a) and  $M_7C_3$  b) in annealed Fe-18Cr after irradiation in BR-10 at 400°C to 25.8 dpa.

The other significant observation of these studies was the radiation-induced decrease in dislocation density. In order to describe the radiation-induced recovery of dislocation structure in cold-worked materials one can write the following equation for the rate of change in the total length of dislocations and dislocation loops per unit volume  $L(t)$ :

$$\frac{dL(t)}{dt} = I(t) - R_d \nu L^2(t), \quad (1)$$

where  $I(t)$  is the dislocation source which is determined by the rates of loop nucleation and growth,  $\nu$  is the dislocation climb velocity (assumed be equal to the loop growth rate),  $R_d$  is the effective radius of annihilation. The velocity  $\nu$  can be expressed in terms of the voidage rate as follows:

$$\frac{d}{dt} \frac{\Delta V}{V} = b \nu L(t), \quad (2)$$

where  $b$  is the Burgers vector length.

Inserting the Eq. (2) in Eq. (1) and integrating, one obtains the following solution satisfying the initial condition:

$$L(t) = L(0) \exp\left(-\frac{R_d}{b} \frac{\Delta V}{V}(t)\right) + \int_0^t I(t') \exp\left(\frac{R_d}{b} \left[\frac{\Delta V}{V}(t') - \frac{\Delta V}{V}(t)\right]\right) dt'. \quad (3)$$

Because of the lack of information on both  $I(t)$  and dose dependence of voidage in the Fe-2Cr alloy (250% C.W.), the expression (3) can be used for determining the ratio  $R_d/b$  only for iron in the cold-worked condition. In the cold-worked iron a relatively low dislocation loop length per unit volume of  $0.23 \times 10^{14} \text{ m}^{-2}$  has formed after irradiation to 25.8 dpa, so that only the first term in the right side of Eq. (3) is of significance. Taking for iron in the 250% cold-worked condition  $L(0) = (10 - 20) \times 10^{14} \text{ m}^{-2}$ ,

$L(t) = 0.4 \times 10^{14} \text{ m}^{-2}$  and  $\Delta V/V = 4.5\%$  one obtains  $R_d/b=61-76$ , which is a relatively large number compared to the original dislocation spacing in this heavily cold-worked material, thereby providing a strong driving force for reduction in dislocation density, as was observed in this study.

## Results

The results of the present work confirm our perceptions that relatively high neutron-induced swelling levels can be reached in pure iron compared with Fe-Cr alloys, and that cold-working leads to an enhancement of swelling in iron and low-chromium alloys. It also appears that unexpectedly high levels of swelling can be reached when the irradiation is conducted at displacement rates that are significantly lower than those of many earlier studies.

## Acknowledgements

The Civilian Research and Development Foundation under Grant RE2-2224 sponsored the Russian portion of this work. The Office of Fusion, U.S. Department of Energy provided support for the U.S. portion of this research under contract DE-AC06-76RLO 1830 with Battelle Memorial Institute.

## References

- [1] D. S. Gelles, *J. Nucl. Mater.* 225 (1995) 163–174.
- [2] E. A. Little and D. A. Stow, *Proceedings of the International Conference on Irradiation Behavior of Metallic Materials for Fast Reactor Core Components*, Ajaccio, Corsica, France, June 4–8, 1979, pp. 17–24.
- [3] H. Matsui, D. S. Gelles, and Y. Kondo, *Proceedings of Effect of Radiation on Materials: 15th International Symposium*, ASTM STP 1125, R. E. Stoller, A. S. Kumar, and D. S. Gelles (eds.), American Society for Testing and Materials, Philadelphia, 1992, pp. 928–941.
- [4] F. A. Garner, *J. Nucl. Mater.* 122–123 (1984) 459–471.
- [5] S. I. Porollo, A. M. Dvoriashin, A. N. Vorobyev, and Yu. V. Konobeev, *J. Nucl. Mater.* 256 (1998) 247–253.
- [6] F. A. Garner, C. A. Black, and D. J. Edwards, *J. Nucl. Mater.* 245 (1997) 124–130.
- [7] F. A. Garner, M. B. Toloczko, and B. H. Sencer, *J. Nucl. Mater.* 276 (2000) 123–142.
- [8] T. Okita, N. Sekimura, F. A. Garner, L. R. Greenwood, W. G. Wolfer, and Y. Isobe, *Proceedings of the 10th International Conference on Environmental Degradation of Materials in Nuclear Power Systems--Water Reactors*, 2001, CD format.
- [9] F. A. Garner, N. I. Budykin, Yu. V. Konobeev, S. I. Porollo, V. S. Neustroev, V. K. Shamardin, and A. V. Kozlov, *The Influence of DPA Rate on Void Swelling of Russian Austenitic Stainless Steels*, 11th International Conference on Environmental Degradation of Materials in Nuclear Power Systems--Water Reactors, 2003, pp. 647–656.
- [10] T. Okita, N. Sekimura, T. Sato, F. A. Garner, and L. R. Greenwood, *J. Nucl. Mater.* 307–311 (2002) 322–326.
- [11] A. M. Dvoriashin, S. I. Porollo, Yu. V. Konobeev, and F. A. Garner, *J. Nucl. Mater.* 283–287 (2000) 157–160.

#### **4.0 COPPER ALLOYS**

**No contributions.**

## **5.0 REFRACTORY METALS AND ALLOYS**

**No contributions.**

## **6.0 AUSTENITIC STAINLESS STEELS**

**THE MECHANISM OF STRESS INFLUENCE ON SWELLING OF 20% COLD WORKED 16Cr15Ni2MoTiMnSi STEEL**—I. A. Portnykh, A. V. Kozlov, V. L. Panchenko (FSUE Institute of Nuclear Materials), V. M. Chernov (A. A. Bochvar Institute of Inorganic Materials), and F. A. Garner (Pacific Northwest National Laboratory)

## OBJECTIVE

The object of this effort is to explore new mechanisms whereby environmental variables such as applied stress can affect radiation-induced microstructural evolution of structural alloys of fusion devices. New insight on these mechanisms will lead to better predictions in fusion environments.

## SUMMARY

Argon-pressurized tubes of 20% cold-worked 16Cr15Ni2MoTiMnSi steel were irradiated at hoop stresses of 0, 100, and 200 MPa at ~740K in the BN-600 fast reactor to 108 dpa. Following nondestructive measurements of strain, density measurements and microscopy were conducted. Voids were categorized into three types depending on their association with other microstructural features. Stress enhanced the nucleation of all void types, but nucleation of voids associated with dislocations was increased the most. Swelling increased as a consequence, even though the average size of each type void decreases. Swelling measured by TEM and density change gave identical results.

A stress-enhanced void nucleation model is presented to explain these results. It invokes collection and diffusion of helium-vacancy complexes in dislocation cores and intersections to produce void nuclei, followed by stress-induced breakaway of the pinned dislocation to reach new obstacles and initiate the next sequence of helium collection and void nucleation.

## PROGRESS AND STATUS

### Introduction

Applied mechanical stress is one of the important variables that are known to accelerate the onset of void swelling [1]. Most studies show that stress results in a significant increase of swelling [2] while a few other studies show a very small or no effect [3]. At present, there is no quantitative model for confident prediction of the influence of stress on swelling. Additional data are required to develop a predictive model. Toward this objective, this paper examines the effect of a biaxial stress state on the swelling of 20% CW 16Cr15Ni2MoTiMnSi austenitic steel at very high neutron exposure.

### Experimental Procedure

Three argon-pressurized tubes of 70 mm length, 6.9 diameter, and 0.4 mm wall thickness were fabricated from 20% cold-worked steel of composition Fe-15.45Cr-14.80Ni-2.37Mo-1.29Mn-0.44Si-0.06C-0.014P-0.004S in wt %. Internal pressures of 0, 52, and 104 atm were used to produce hoop stresses of 0, 100, and 200 MPa during side-by-side irradiation in flowing sodium at ~740K in the BN-600 fast reactor to 108 dpa at  $1.9 \times 10^{-6}$  dpa/sec [4]. The outer diameters were measured before and after irradiation by a profilometry technique. Measurements were made at 12 axial locations and 5 radial positions and the measurements were averaged. After irradiation, the tubes were destructively examined. After removing the end caps, the density change of the tube was determined via hydrostatic weighing. Electron microscopy was used to study the microstructure. The quantitative method employed for microscopy analysis was presented previously [5, 6].

### Results

Table 1 and Fig. 1 present the diameter and density change measurements as well as the microscopy determinations of swelling. While swelling increases almost linearly with stress, the creep deformation may exhibit some small nonlinearity but could be approximated by a linear relationship. With only three data points, these two possibilities can not be distinguished. The creep deformation CD was

calculated as  $CD = \frac{\Delta d}{d} - \frac{1}{3} \cdot S$ , where  $S = S_d$ , the swelling determined by density change. The

swelling determined by microscopy is subjected to greater measurement errors and scatter, but appear to be in agreement with the bulk-averaged density change results.

TEM examination of multiple areas of each specimen showed that different porosity distributions developed as a function of stress. Figure 2 shows typical void micrographs at each stress level.

Voids were identified in four categories as described elsewhere [5, 6]: *a*-type voids are arrayed on dislocations, *b*-type voids are associated with precipitates, usually involving two separate distributions, and free-standing *c*-type voids formed on gas-vacancy complexes in the crystal matrix.

Table 1. Results of diameter and density measurements

Cladding stress, MPa	Mean value of diameter, mm	Diameter change $\Delta d/d_0$ , %	Density, $g/cm^3$	Swelling %, Density $S_d$	Swelling %, TEM $S_{TEM}$	Creep deformation, CD %
Unirradiated specimen	6.92	-	7.94	-	-	-
0	7.12	2.89	7.30	8.8	8.6	0.0
100	7.30	5.49	7.17	10.7	10.5	1.9
200	7.57	9.39	7.07	12.3	12.5	5.3

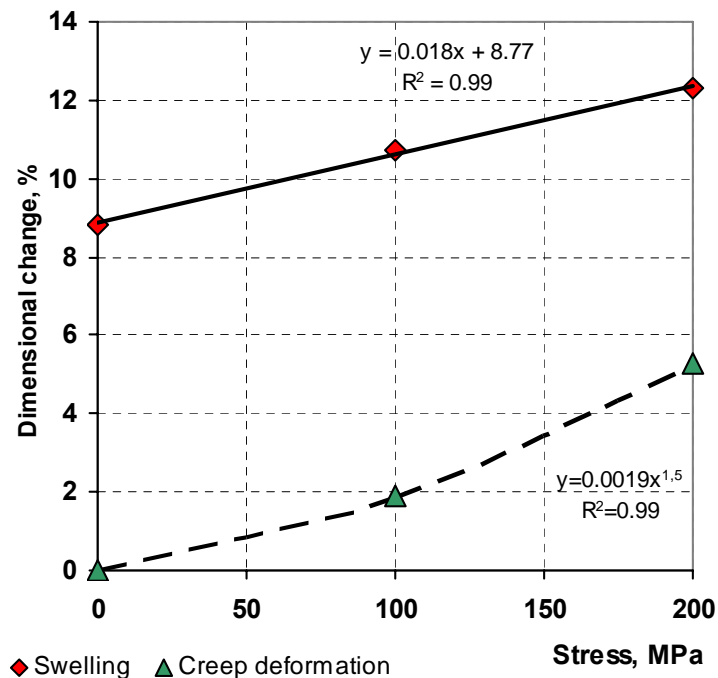


Fig. 1. Swelling and creep deformation as a function of stress.

Electron-microscopy examinations revealed different porosity characteristics for specimens irradiated without stress and under stress. Fig. 2 presents typical micrographs. In general, homogeneous distributions of voids were observed in specimens irradiated at 0 and 200 MPa, with somewhat more heterogeneity observed at 100 MPa. The largest volume fraction of voids in the specimens without stress was the *b*-type voids connected with G-phase precipitates, while the largest voids were usually located on twins.

Histograms of the void-size distribution are shown in Fig. 3 with single distributions obtained by the  $\chi^2$  criterion [4], described as the sum of the four single distributions as follows: *a*-type voids are formed on dislocations, *b*-type voids of two types connected with precipitates, and *c*-type voids formed on gas-vacancy complexes in the crystal matrix, the latter having smallest sizes [5]. A summary of mean sizes and concentrations of each void type is shown in Fig. 4. Note that the contribution of *b*-type voids to total swelling decreases with increasing stress as shown in Fig. 5. The enhancement of void swelling by stress is reflected in a pronounced increase in void density, especially in the density of *a*-type voids, but the increase is not reflected in the void sizes, which uniformly decrease with stress.

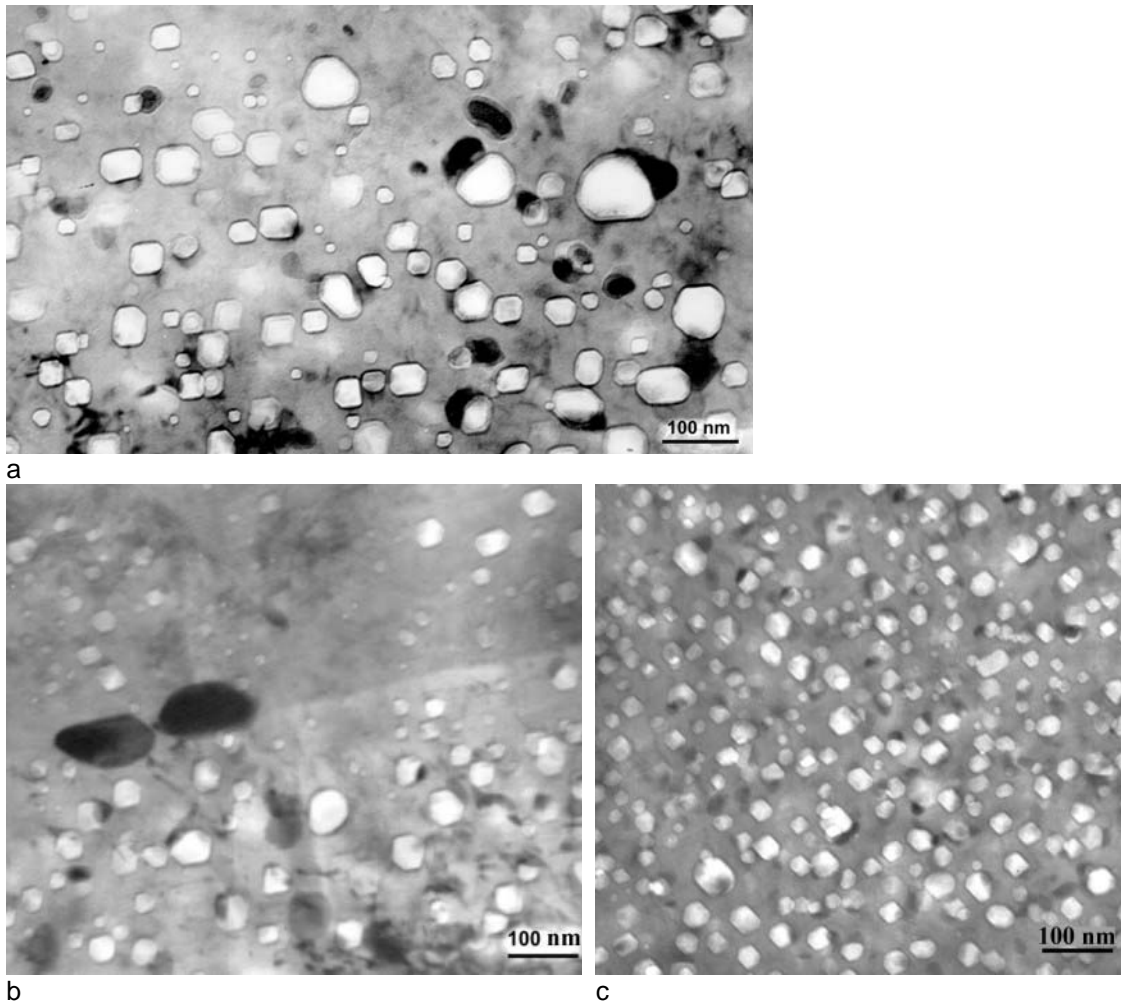


Fig. 2. Voids and precipitate microstructures observed at a) 0, b) 100, and c) 200 MPa. Most of the precipitates are G-phase.

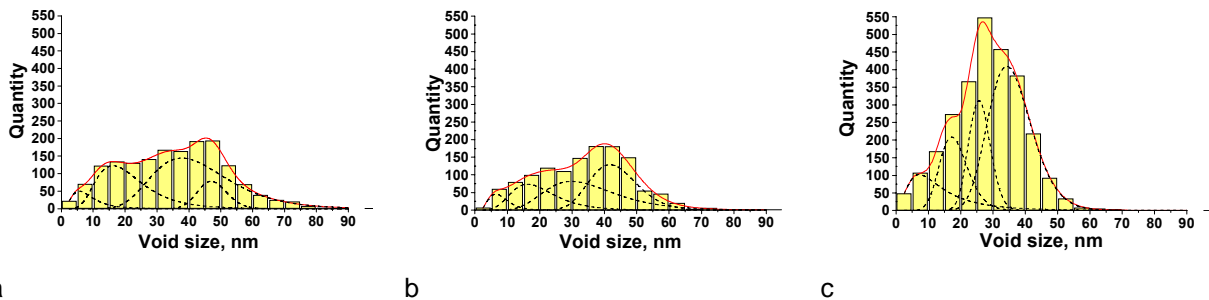


Fig. 3. Void-size distributions at a) 0 MPa, b) 100 MPa, and c) 200 MPa. The total number of voids measured was 1600, 1300, and 2700, respectively. ■ - experimental data, --- - single log-normal distribution, — - sum of single log-normal distributions.

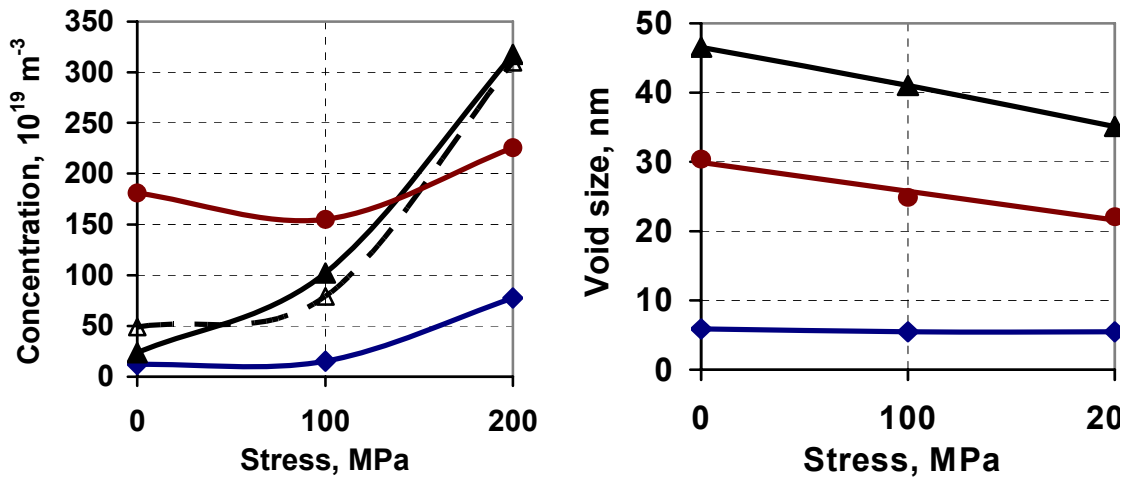


Fig. 4. Dependence of concentration (a) and mean size (b) on stress for each type of voids:  $\blacktriangle$  - a-type,  $\bullet$  - b-type, and  $\blacklozenge$  - c-type,  $\triangle$  - theoretical prediction of a-type based on our model.

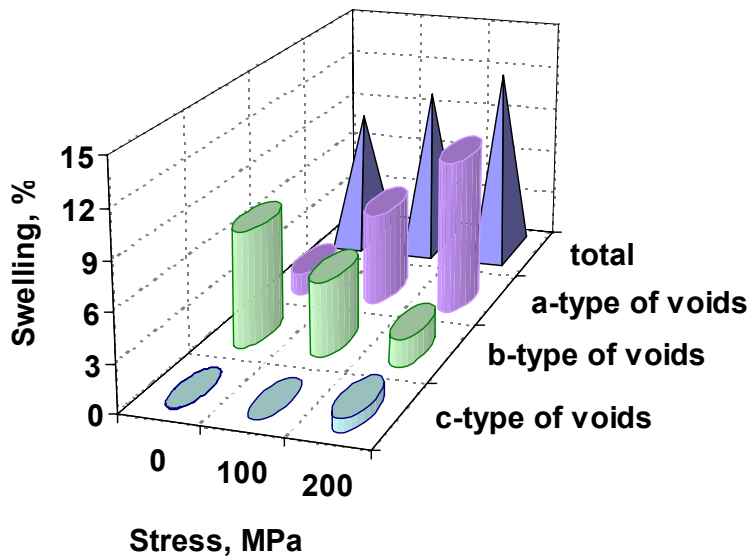


Fig. 5. Contribution to total swelling of each type of void.

### Discussion

It can be shown that stress at  $\sim 200$  MPa cannot significantly influence the diffusion characteristics of point defects and therefore, cannot significantly change the growth rate of voids, but stress can strongly influence void nucleation, as demonstrated in this experiment. It appears that void nucleation of the a-type voids is particularly sensitive to the stress level. We advance here a new explanation to explain this result. This model assumes that stabilization of void nuclei requires helium and stress can alter the way in which helium is collected and bubbles distributed.

Transmutant helium (with concentration determined as 1 appm/dpa for the BN-600 reactor [7]), when combined with a vacancy, migrates as a gas-vacancy pair, with mobility determined by the vacancy migration energy of  $\sim 1.2\text{--}1.3$  eV [7]. In the dislocation core, this pair diffuses with migration energy of  $\sim 0.6$  eV. This pipe diffusion causes He-vacancy bubbles to be formed on dislocations, especially where dislocations intersect, producing void nuclei after reaching a critical size. This mechanism was proposed earlier to explain a-type void growth, especially in the early stages of swelling at 650–800K [8].

When the local stress exceeds a critical value  $\sigma_c$ , the dislocation slips over any obstacles that pin it and then glides to the next group of obstacles. Voids or bubbles earlier formed on a dislocation stay in their original position and continue to grow. The dislocation in its new location begins to collect He-vacancy pairs and generate new nuclei. This process is repeated each time the dislocation moves, leading to stress enhancement of voids.

If an external stress  $\sigma$  is applied to a dislocation and requires an additional stress ( $\sigma_c - \sigma$ ) by accumulation of point defects to overcome the obstacles, then  $\tau$  is mean time required to achieve dislocation separation and is proportional to the additional stress. The number of voids forming per time  $t$  can be expressed as follows:

$$n_a = n_{a_0} + \xi_n \cdot \rho_d \cdot \frac{t}{\tau} = n_{a_0} + \frac{\xi_n \cdot \rho_d \cdot v_\sigma \cdot t}{(\sigma_c - \sigma)} = n_{a_0} + \frac{A}{(\sigma_c - \sigma)} \quad (1)$$

where

$\xi_n$  – number of voids per length unit, formed on dislocation during its immovable state,

$\rho_d$  – dislocation density,

$v_\sigma$  – coefficient characterizing the rate of internal stress accumulation due to defect accumulation, and

$n_{a_0}$  – concentration of voids, formed on a stationary dislocation in absence of applied stress.

Figure 4a contains a theoretical prediction of a-type behavior using this model, where  $A$  and  $\sigma_c$  were determined by optimization to fit the experimental data. One can see a qualitative coincidence between experimental and calculated curves illustrating some success of the proposed model to describe stress-induced swelling. The dependence of mean size of a-type voids on stress exhibited in Fig. 4b is additional indirect confirmation of this model.

## Conclusions

Void swelling of pressurized tubes constructed from 20% cold-worked 16Cr15Ni2MoTiMnSi austenitic steel and irradiated at 740 K to 108 dpa in the BN-600 fast reactor clearly show that applied stress enhances swelling. The enhancement is manifested primarily as a strong increase in the void density, especially those voids which are associated with dislocations. A new model is presented to explain these results that involve collection and diffusion of helium in dislocation cores, followed by stress-induced breakaway from pinning points, leading to a new sequence of collection and nucleation.

## Acknowledgements

This work was supported by a grant of the Russian Federation President for State Support of Young Scientists, No. MK-20011.2005.2. F. A. Garner's participation was funded by the U.S. Department of Energy, Office of Fusion Energy.

## References

- [1] F. A. Garner, Chapter 6: Vol. 10A of Materials Science and Technology: A Comprehensive Treatment, VCH Publishers (1994) 419.
- [2] H. R. Brager, F. A. Garner, and G. L. Guthrie, J. Nucl. Mater. 66 (1977) 301.

- [3] K. Herschbach, W. Schneider, and H.-J. Bergman, Effects of Radiation on Materials: 14th International Symposium (Vol. II), ASTM STP 1046 (1990) 570.
- [4] S. A. Averin, A. V. Kozlov, N. I. Budylnkin, and V. V. Romaneev, Investigations of Structural Materials of Fast Sodium Reactor Core, collected articles, RAS UD, Ekaterinburg (1994) 153, in Russian.
- [5] I. A. Portnykh and A. V. Kozlov, VANT quarterly report series: Material science and new materials, No.1 (59) (2002) 41, in Russian.
- [6] I. A. Portnykh, A. V. Kozlov, and L. A. Skryabin, Perspective Materials No. 2 (2002) 50, in Russian.
- [7] A. G. Zalyzhnyi, Lu. N. Sokyrskiy, and V. N. Tebys, Energoatomizdat, Moscow (1988) 224, in Russian.
- [8] I. A. Portnykh, V. Sagaradzhe, A. V. Kozlov, and L. A. Skryabin, PhMM, Vol. 94, No. 1 (2002) 105, in Russian.

## **THE INFLUENCE OF COLD-WORK LEVEL ON THE IRRADIATION CREEP AND SWELLING OF AISI 316 STAINLESS STEEL IRRADIATED AS PRESSURIZED TUBES IN THE EBR-II FAST REACTOR—**

E. R. Gilbert and F. A. Garner (Pacific Northwest National Laboratory)

### **OBJECTIVE**

Pressurized tubes of AISI 316 stainless steel irradiated in the P-1 experiment in the EBR-II fast reactor have been measured to determine the dependence of irradiation-induced strains resulting from plastic deformation, irradiation creep, void swelling and precipitation. It is shown that the Soderberg relation predicting no axial creep strains in biaxially-loaded tubes is correct for both plastic and creep strains. Swelling strains are shown to be isotropically distributed both for stress-free and stress-affected swelling, while precipitation strains are somewhat anisotropic in their distribution. When corrected for stress-enhancement of swelling, the derived irradiation creep strains appear to be identical for both annealed and 20% cold-worked specimens, and also for tubes strained by rise to power increases in pressure. For relatively small creep strains it is often difficult to separate the creep and non-creep components of deformation.

### **PROGRESS AND STATUS**

#### **Introduction**

Void swelling and irradiation creep of neutron-irradiated metals are intimately linked phenomena that interact with each other through their response to the local stress state [1]. While void swelling in the absence of stress can be easily measured by various nondestructive and destructive techniques, it is somewhat more difficult to separate irradiation creep strains from non-creep strains such as void swelling, texture-induced recovery, lattice parameter changes resulting from precipitation, plastic strains induced by stresses in excess of the yield strength and the enhancement of swelling by stress. Analysis of irradiation creep experiments is further complicated by the onset of the "creep cessation" phenomenon at higher swelling levels [1–3], the known anisotropy of precipitation-induced strains at low exposures [1, 4] and the suspected anisotropy of strains associated with stress-affected swelling [5, 6]. The situation is further complicated by limitations of funding, reactor space and specimen type chosen to conduct irradiation creep experiments.

While creep specimens can take many forms (rods, springs, bent beams, etc.) the favorite form for most creep experiments for the last several decades has been the pressurized tube. Its major advantages are its small size and simplicity of construction and measurement, its nearly constant biaxial stress state even in the presence of substantial swelling, and its lack of need for external mechanical connections.

However, some of its disadvantages are apparent when one attempts to cleanly separate the strains arising from creep and non-creep components. Two general approaches have been taken in the design of creep-swelling experiments and each approach has limitations in this regard. The approach taken in the FFTF-MOTA experiments was to place a series of tubes at different stress levels in an actively-controlled volume where variations in neutron flux and temperature are minimized [7]. The tubes were irradiated, removed and measured, and then returned for further irradiation, repeating the process a number of times. This approach minimizes specimen-to-specimen scatter but does not allow either a clean separation of strains or a determination of the stress-enhancement of swelling.

The approach taken in other experiments conducted in the much smaller EBR-II reactor was to place tubes at different stress levels as close as possible, accepting small variations in flux and temperature, but then to extract and destructively examine each tube after irradiation. This approach allows better separation of strains at the expense of increased data specimen-to-specimen scatter. A similar approach was used by the British in PFR and the French in PHENIX, but the tubes in the French program were welded together into long pins. A review of these studies is published elsewhere [8, 9].

Most of the experiments involving irradiations of austenitic stainless steels in FFTF have been published previously [3, 8–12]. In a joint U. S. Department of Energy effort involving the Nuclear Energy Research Initiative and Fusion Materials programs, an effort is underway to harvest data and insight from previously unpublished studies conducted decades earlier in the liquid metal reactor program. This first paper of a series addresses selected results of the P-1 experiment.

### Experimental Procedure

Both 20% cold worked and solution annealed 316 (prepared by heating 20% cold worked cladding for six minutes at 1010°C) stainless steel cladding were irradiated in the P-1 test. Specimens were manufactured from N-Lot (Heat V87210) and consisted of 25 mm long sections of helium-pressurized cladding as shown in Fig. 1. The fill pressure was verified by measurement of the elastic strain induced during pressurization and also by measurement of the He contained in the specimens after irradiation. The fill gas pressure introduced at room temperature rose as the irradiation temperature was attained, producing mid-wall hoop stresses ranging from 0 to 400 MPa.

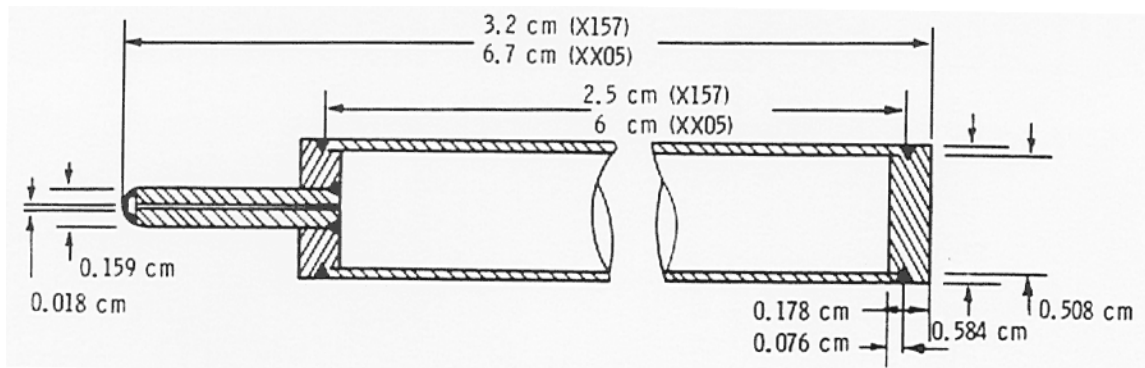


Fig. 1. Pressurized tube specimen design for Test P-1 (EBR-II Subassembly X157) and Test P-5 (EBR-II Subassembly XX05).

Thick-walled capsules, each containing three pressurized tube specimens immersed in static sodium, were stacked and centered in long stainless steel tubes that extended through the EBR-II core. Temperatures were estimated from the calculated gamma heating rate and the thickness of the helium gas gap between the thick-wall capsule and the outer tube. Irradiation temperatures were chosen to span the range 375 to 577°C, with uncertainties of  $\pm 10$  to  $\pm 20^\circ\text{C}$  with increasing target temperatures.

After irradiation the diameter and length changes of the tubes were measured using a laser measurement technique [7]. The end caps were then removed and the density of the tube section determined by an immersion technique accurate to  $\pm 0.1\%$ .

In Fig. 2 are shown three examples of measurements of length and diameter changes in comparison with one-third of the density conducted on stress-free tubes. Within the accuracy of the measurements it appears that strains arising from stress-free swelling are isotropically distributed, with some indication of possibly small densification in the annealed tubes. This finding suggests that length changes can be used to estimate swelling in stressed tubes where diameter changes include creep strains. In the cold-worked tube, however, the diametral and density strains agree but once swelling begins, the longitudinal strains are measurably larger. This suggests that the anisotropy of precipitation-induced strains reflects the strong texture of cold-worked tubes and resultant orientation of carbide formation [1, 4].

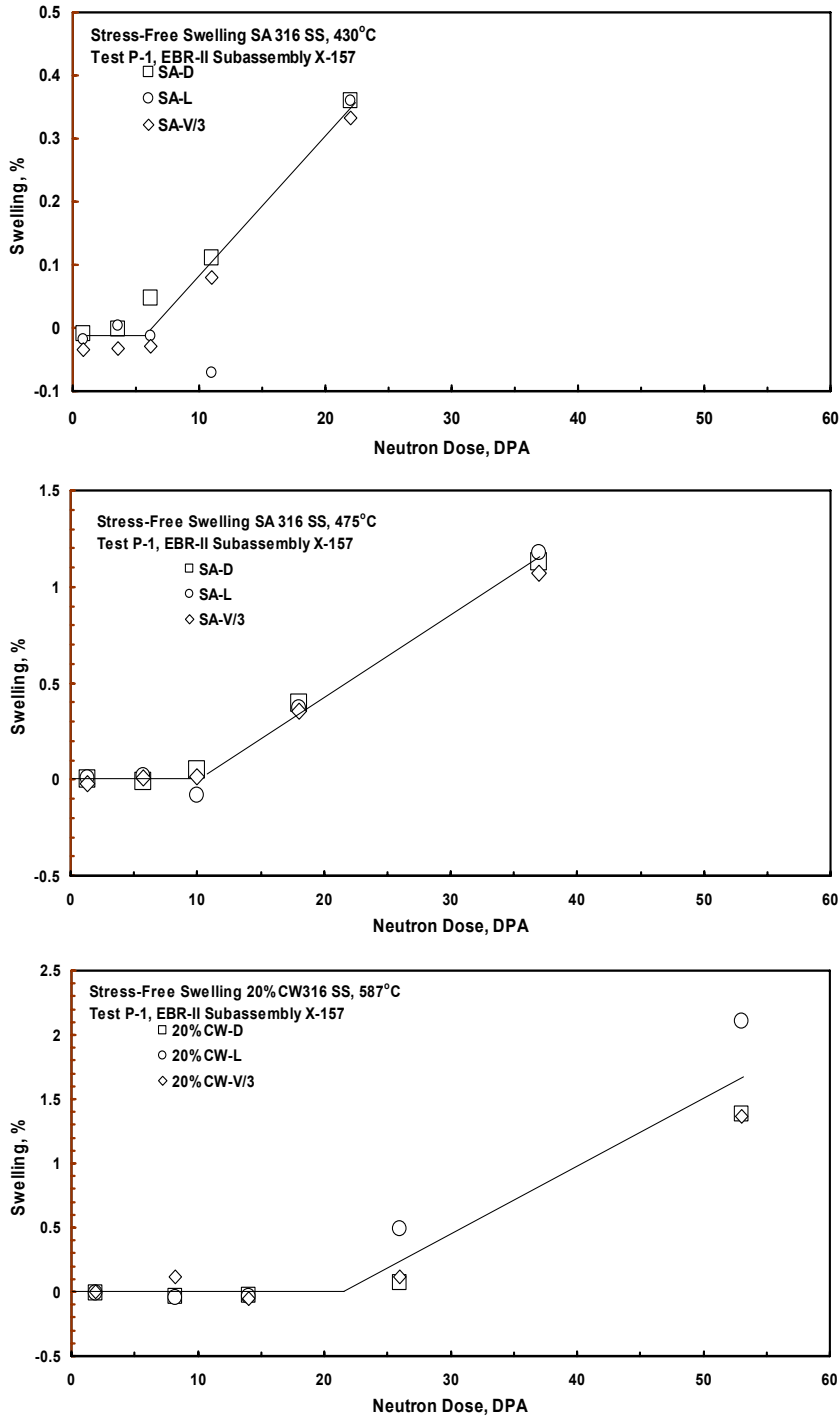


Fig. 2. Comparison of diametral and diameter strains for three sets of stress-free tubes with one-third of the swelling strains as determined by immersion density.

In the two sets of annealed tubes, all strains appear to be isotropically distributed, but in the cold-worked tubes (bottom), the length strains are larger, probably arising from anisotropy associated with texture induced during drawing of the tube.

Figure 3 shows the results of a series of annealed tubes irradiated under stress in the range 454–474°C and 46 dpa to hoop stresses of 95–254 MPa. Note that no comparable specimen is available at 0 MPa. It can be seen that the length changes compare well with one-third of the density changes, indicating that swelling continues to be isotropically distributed, even though swelling is clearly accelerated by stress. The well known Soderberg relationship states that the creep strain developed in biaxial stress states experienced by these tubes will be zero in the axial direction [13], but the distribution of the stress-enhanced portion of swelling has not been well defined in previous studies.

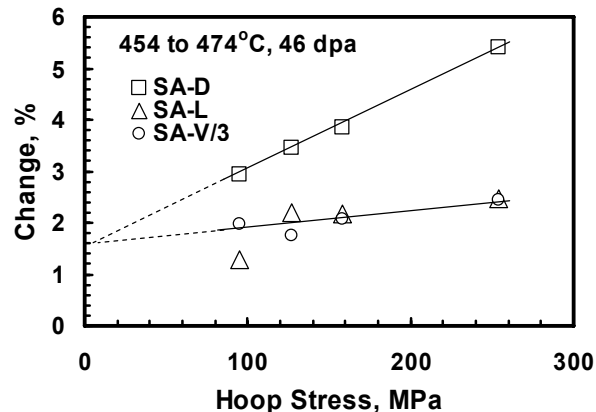


Fig. 3. Comparison of the diameter and length strains of annealed 316 tubes irradiated at 454–474°C and 46 dpa to hoop stresses of 95–254 MPa, showing stress-affected swelling, isotropy of swelling strains, and swelling-enhanced creep.

Figure 4a shows, however, that there is a limit to the application of stress and its effect on swelling and creep. Note that at 400 MPa the yield stress of the annealed tube was exceeded when the tube reached 419°C, producing an immediate plastic strain of ~2% in the diameter but not in the length. This strain produced sufficient cold-working to delay the onset of swelling, however. Densification is not easily visible with such large plastic strains and may be present but overwhelmed by a small amount of swelling. Note that once again the length and density change data agree, indicating that stress-enhanced swelling was isotropic.

Figure 4b shows that the cold worked tubes did not exceed the yield strength at the same nominal irradiation condition and initially densified, developing a low rate of swelling after ~15 dpa. Both annealed and cold-worked tubes thereafter exhibited a similar rate of diameter change, indicating that the eventual creep rates were largely unaffected by the starting condition of the tubes when the swelling is relatively low.

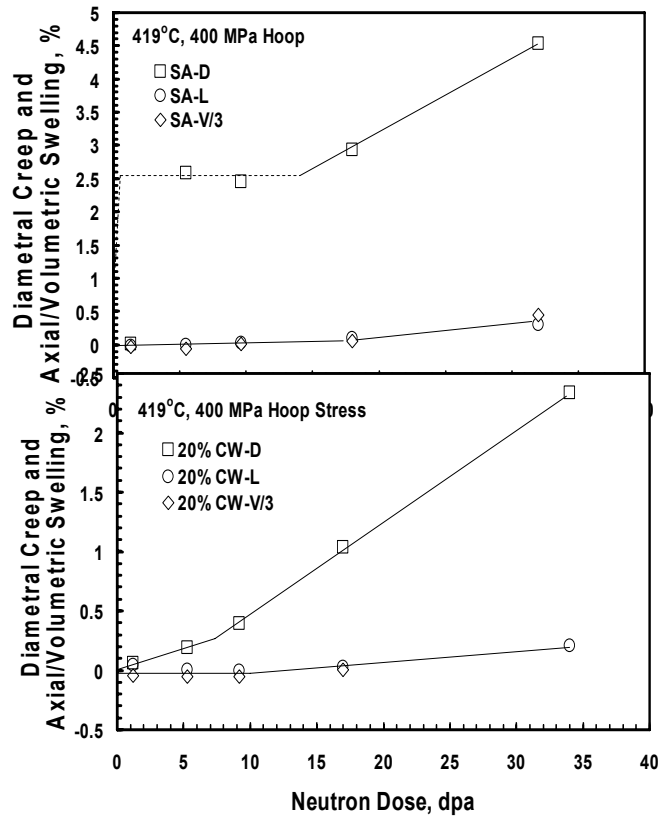


Fig. 4. Comparison of annealed (top) and cold-worked (bottom) tubes irradiated together at 419°C and 400 MPa hoop stress. The yield strength of the annealed tube was exceeded during the rise to temperature but the cold-worked tube did not exceed its yield strength.

Figure 5a demonstrates the complexity that arises for lower stress levels that marginally exceed the yield stress of annealed steel and produce lower levels of plastic strain. Note that an initial strain of ~0.4% occurs, but the strain decreases thereafter, with some recovery or densification processes occurring. The densification is clearly occurring, reaching ~0.2%, as shown in Fig. 5c. Swelling becomes dominant only above ~10 dpa.

Figure 5b shows that cold-worked tubes at identical irradiation conditions do not plastically deform but densify initially to about the same level, ~0.2%, but then appear to recover the density loss thereafter, as seen in Fig. 5c. The length changes also show densification occurring to a lesser extent, but also show that swelling is not significant up to ~22 dpa.

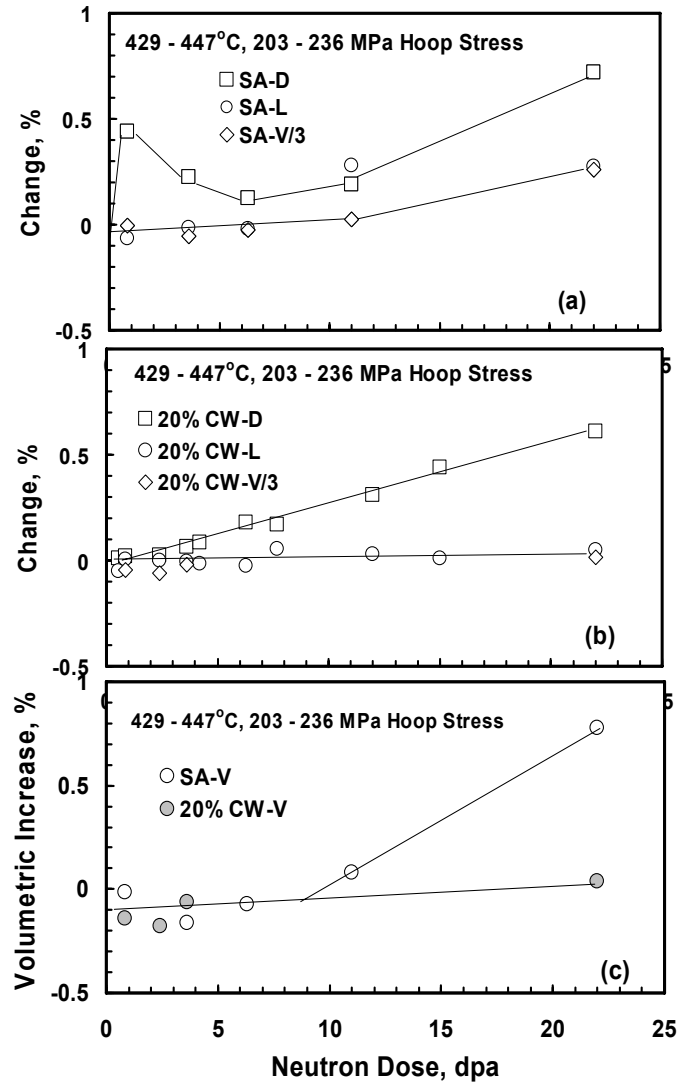


Fig. 5. Comparison of annealed (top) and cold-worked (middle) tubes irradiated at 429–447°C and 203–236 MPa hoop stress.

The yield strength of the annealed tube was slightly exceeded during the rise to temperature but the cold-worked tube was not. The bottom figure compares measured changes in density of both annealed and cold-worked tubes, showing strong densification to  $\sim 0.2\%$  early in the irradiation.

Figure 6 presents a summary of the stress-normalized diametral creep strains calculated for both annealed and cold-worked tubes, calculated by subtracting the swelling strains from the diameter changes. The large scatter band, especially at lower doses, reflects primarily the strong influence of anisotropic strains associated with precipitation. Note that the creep rates of the annealed and cold-

worked steel do not appear to be significantly different once swelling has been removed. The creep coefficient associated with the least squares fit is  $1.5 \times 10^{-6} \text{ MPa}^{-1} \text{ dpa}^{-1}$ , somewhat larger than the value of  $1 \times 10^{-6} \text{ MPa}^{-1} \text{ dpa}^{-1}$  anticipated in the absence of swelling [1].

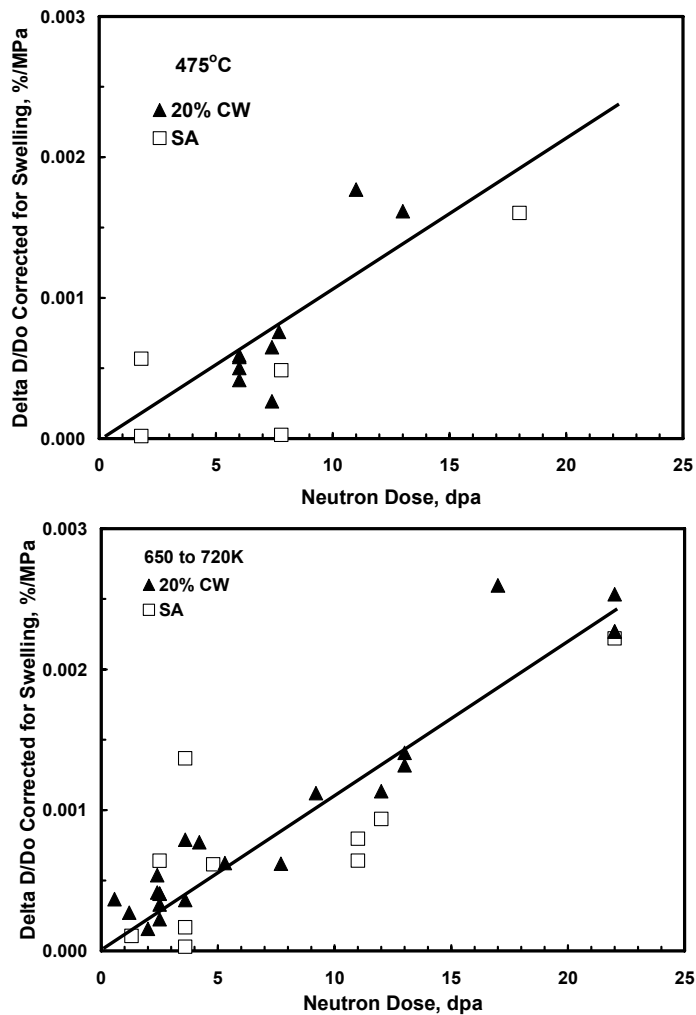


Fig. 6. Diametral strain per unit stress are presented for both annealed and cold-worked tubes after correction for density changes, showing that while scatter can be large at relatively low neutron exposures, the creep strains of annealed and cold-worked tubes are very similar. Data in top figure was derived at 377–447°C and in bottom figure at 477°C.

## Results

The use of individual pressurized tubes that are irradiated for one period and then destructively examined provides relatively clear separation of the various components of strain, but in order to get different values of dpa or stress one must accept greater data scatter. The scatter arises primarily from three sources. The first source arises from the use of multiple specimens to reach one dose level, adding specimen-to-

specimen variability. The second is particularly important in small reactors with large flux gradients and varying temperature histories, leading to larger uncertainties in irradiation condition. The third source is due to void swelling. Based on other studies it is known that the creep compliance of stainless steels in the absence of swelling is relatively independent of irradiation temperature and dpa rate at  $1 \times 10^{-6} \text{ MPa}^{-1} \text{ dpa}^{-1}$ , but when swelling occurs the creep rate is accelerated by an amount proportional to the swelling rate [1]. It is well known that the onset of swelling and the instantaneous swelling rate are very sensitive to every material variable and especially to minor differences in dpa rate and temperature [1]. Thus the swelling-affected creep rate is highly variable in its response to the local irradiation conditions, introducing additional scatter into the data ensemble.

Much of the reported variation in creep compliance actually results from the inability to separate the creep strains from the non-creep strains, most of the latter tending to saturate at relatively low doses. In most of the FFTF experiments there was no direct measurement of the stress-induced swelling component, which was incorrectly but necessarily treated as a component of irradiation creep. In most creep experiments the swelling values, whether measured by density change or by dimensional change, include precipitation contributions, introducing additional uncertainties in separation of creep strains.

Within the limitations of this experiment, however, we were able to show that void swelling, both without and with stress, appears to distribute its strains isotropically. It was also shown that both plastically-induced and irradiation creep-induced strains obey the Soderberg relationship, allowing the separate measurement of actual swelling under stress. In addition, it appears that the creep compliance at temperatures below  $\sim 500^\circ\text{C}$  is independent of material starting state, in agreement with earlier studies conducted in FFTF on effects of cold-work level [14,15]. While the scatter is relatively large, especially at relatively low dose levels, the measured creep coefficient is  $\sim 1.5 \times 10^{-6} \text{ MPa}^{-1} \text{ dpa}^{-1}$ , just slightly larger than the usually accepted creep compliance of  $1 \times 10^{-6} \text{ MPa}^{-1} \text{ dpa}^{-1}$ , reflecting the relatively small and correctly separated amount of swelling in the selected tubes.

## Conclusions

This experiment has shown that the Soderberg relation predicting no axial creep strains is correct for both plastic and irradiation creep strains measured in AISI 316 stainless steel irradiated in EBR-II. Swelling is shown to be accelerated by stress and its strains are shown to be isotropically distributed both for stress-free and stress-affected swelling, while precipitation strains are somewhat anisotropic in their distribution. When corrected for stress-enhancement of swelling, the derived irradiation creep strains appear to be identical for both annealed and 20% cold-worked specimens.

## Acknowledgements

This work was sponsored by the U.S. Department of Energy, Office of Fusion Energy, and the Office of Nuclear Energy, Science, and Technology, NERI Project 01-137.

## References

- [1] F. A. Garner, Chapter 6: Vol. 10A of *Materials Science and Technology: A Comprehensive Treatment*, VCH Publishers (1994) 419–543.
- [2] F. A. Garner, D. L. Porter, and B. J. Makenas, *J. Nucl. Mater.* 148 (1987) 279–287.
- [3] M. B. Toloczko and F. A. Garner, *J. Nucl. Mater.* 212–215 (1994) 509–513.
- [4] F. A. Garner, W. V. Cummings, J. F. Bates, and E. R. Gilbert, Hanford Engineering Development Laboratory Report HEDL-TME-78-9 (1978).
- [5] J. F. Bates, W. V. Cummings, and E. R. Gilbert, *J. Nucl. Mater.* 99 (1981) 75–84.
- [6] J. E. Flinn, M. M. Hall, Jr., L. C. Walters, and F. A. Garner, Influence of In-reactor History on the Swelling of Type 304 Stainless Steel Fast Reactor Fuel Cladding, *Journal of Nuclear Materials* (in preparation).
- [7] E. R. Gilbert and B. A. Chin, in *Proceedings of Effects of Radiation on Materials: Tenth Conference*, ASTM STP 725 (1981) 665–679.

- [8] F. A. Garner, M. B. Toloczko, B. Munro, S. Adaway, and J. Standing, in Proceedings of Effects of Radiation on Materials, 18th International Symposium, ASTM STP 1325 (1999) 713–724.
- [9] M. B. Toloczko and F. A. Garner, in Proceedings of Effects of Radiation on Materials: 19th International Symposium, ASTM STP 1366 (2000) 655–666.
- [10] F. A. Garner, M. B. Toloczko, and R. J. Puigh, in Proceedings of Effects of Radiation on Materials: 19th International Symposium, ASTM STP 1366 (2000) 667–678.
- [11] M. B. Toloczko and F. A. Garner, *J. Nucl. Mater.* 212–215 (1994) 509–513.
- [12] F. A. Garner and R. J. Puigh, *J. Nucl. Mater.* 179–181 (1991) 577–580.
- [13] C. R. Soderberg, *Trans. ASME* (1963) 737.
- [14] F. A. Garner, M. L. Hamilton, C. R. Eiholzer, M. B. Toloczko, and A. S. Kumar, in Proceedings of 16th International Symposium on Effects of Radiation on Materials, ASTM STP 1175 (1992) 696–713.
- [15] F. A. Garner, M. L. Hamilton, C. R. Eiholzer, M. B. Toloczko, and A. S. Kumar, *J. Nucl. Mater.* 191–194 (1992) 813–817.

**RECENT EXPERIMENTAL RESULTS ON NEUTRON-INDUCED VOID SWELLING OF AISI 304 STAINLESS STEEL CONCERNING ITS INTERACTIVE DEPENDENCE ON TEMPERATURE AND DISPLACEMENT RATE**—F. A. Garner (Pacific Northwest National Laboratory), B. J. Makenas (Fluor Hanford Company)

**OBJECTIVE**

The objective of this effort is to explore the response of austenitic steels in diverse nuclear environments. Since light water reactors generate helium/dpa levels comparable to fusion devices, there is considerable overlap in relevance. In addition, the focus on AISI 304, while not of direct application to fusion devices, is useful because this simple steel does not have a very complicated phase evolution, allowing study of radiation-induced microstructural evolution without the complications associated with precipitation.

**SUMMARY**

Almost all data on the void swelling of AISI 304 stainless steel relevant to PWR applications were derived from examination of structural components or experimental assemblies irradiated in the EBR-II fast reactor. However, many more components and assemblies were not fully analyzed and often were not published as the fast reactor program moved to research on more swelling-resistant alloys. In this paper a number of these lost opportunities have been rescued and examined with an eye toward their relevance to predicting behavior of AISI 304 in PWRs.

Swelling of annealed AISI 304 stainless steel initially proceeds at a rate of  $\sim 0.07\%/dpa$  in the range of  $370\text{--}390^\circ\text{C}$  and then begins to accelerate toward a rate of  $\sim 1\%/dpa$ , with the breakaway dose dependent on dpa rate, temperature, temperature gradient and stress in roughly that order. The interactive effects of dpa rate and temperature are very strong and produce “loops” which allow visualization of the conditions under which swelling will be the strongest. These conditions are lower dpa rate and higher temperatures, but temperature gradients and stresses can also accelerate the onset of swelling. While no additional data are available below  $370^\circ\text{C}$ , the insight acquired will allow better extrapolation down into the full range of PWR-relevant temperatures.

**PROGRESS AND STATUS**

**Introduction**

The major portions of baffle-former assemblies of PWRs are constructed from annealed AISI 304 stainless steel. This steel is known to swell rather easily compared to other steels such as cold-worked AISI 316 frequently used for baffle bolts [1,2]. Swelling in AISI 304 is known to increase monotonically as the temperature rises above  $370^\circ\text{C}$  [1]. Relatively small isolated volumes of the baffle-former assembly at reentrant corners may therefore experience significant amounts of void swelling that arise due to localized higher temperatures generated by gamma-heating in thick plates, especially at reentrant corners [3].

Essentially all data on the swelling of AISI 304 was generated in the now-decommissioned EBR-II fast reactor. The data base suffers from three significant deficiencies. First, there are no data available below  $370^\circ\text{C}$  which was the inlet cooling temperature. Most of the PWR baffle-former assembly will experience temperatures less than  $350\text{--}360^\circ\text{C}$ . Second, irradiation in the EBR-II core proceeded at dpa rates on the order of  $0.5$  to  $1.0 \times 10^{-6}$  dpa/sec, fully an order of magnitude higher than the maximum dpa rate experienced by those portions of the baffle-former assembly that are closest to the PWR core. Third, most data were derived from components that spanned a range of temperatures and dpa rates, thus making it difficult to separate the simultaneous and synergistic effects of these two variables. Additionally, some of the examined components were subject to either constant or time-dependent stresses, and stress is the third most important variable in determining the onset of void swelling in austenitic steels [2].

In an attempt to determine the impact of lower PWR-relevant dpa rates, swelling measurements were made on hexagonal ducts from the EBR-II reflector region where the dpa rates are comparable to those found in PWR baffle-former assemblies [4,5]. As shown in Fig. 1, these measurements clearly show that the onset of accelerated swelling in AISI 304 in the range 373–388°C is clearly accelerated as the dpa rate decreases. This implies that swelling equations developed in the 1970–1980 period for in-core fast reactor application will strongly under-predict the swelling of components operating at comparable temperatures but PWR-relevant dpa rates. The swelling equations published earlier, however, were not designed to separate the interactive effects of dpa rate and temperature. In fact these equations did not incorporate any dependence on dpa rate, with swelling depending only on temperature and total dpa. These earlier swelling equations also did not incorporate the insight developed in the 1980s that swelling of all austenitic alloys approaches a terminal swelling rate of  $\sim 1\%/dpa$  over a wide range of material and environmental variables [2,6].

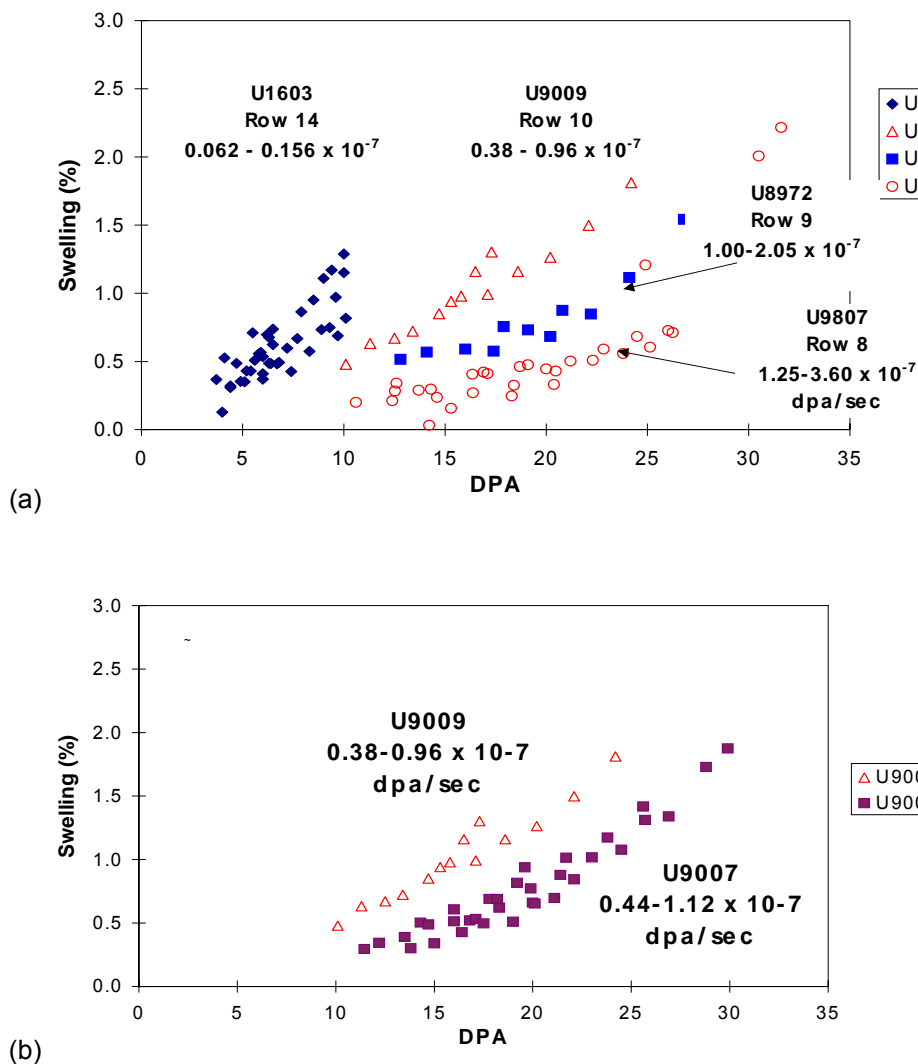


Fig. 1. Swelling of annealed 304 stainless is strongly dependent on dpa rate at a given irradiation temperature [5]. Note that each data set spans a range of dpa rates. The lowest dpa levels correspond to the lowest dpa rates and lowest temperatures. a) At temperatures of 373–388°C the transient regime of swelling is progressively decreased when moving from row 8 to row 14. b)

When comparing two row 10 assemblies with dpa rates varying only ~16%, the strong effect of dpa rate can easily be observed with swelling accelerating faster at the lower dpa rate.

Returning to Fig. 1, note that there is no indication in the data field that AISI 304 will reach 1%/dpa or that it will do so at all dpa rates. The highest rate reached in this data set is perhaps 0.3%/dpa in row 14, although there appears to be enough upward curvature in the data field to allow a subsequent increase in swelling rate to 1%/dpa at higher doses.

Also note that the data shown in Fig. 1 are only confidently applicable to those isolated regions of the baffle-former assembly where gamma heating has elevated the temperature above 370°C. The possibility exists that there might be some lower PWR-relevant temperature below which the swelling rate falls below 1%/dpa. In such a case, the majority of the baffle-former assembly might never reach the terminal swelling rate. While this possibility can not be confirmed, there are some data that appear to suggest hope of such a beneficial behavior.

Older previously unanalyzed and largely unpublished studies from the U.S. fast reactor program conducted in EBR-II are now being examined to address these possibilities. The insight gained from these studies will aid in the extrapolation of fast reactor data to PWR application. A few of the on-going studies are highlighted below.

#### Transient swelling regime

In earlier published studies by Porter and Garner it appeared that at ~390°C annealed 304L stainless steel tubes at constant internal pressure and irradiated at  $5.3 \times 10^{-7}$  dpa/sec at the mid-plane of row 7 were swelling. In the absence of applied stress the rate was only ~0.18%/dpa up to perhaps 75 dpa [7,8]. This implies either the operation of a long transient regime of swelling or possibly a lower swelling rate condition. However, the tubes also appeared to be experiencing swelling at higher rates when stress was applied via gas pressurization. Destructive examination was conducted on both unstressed and stressed tubes to study swelling over their length and therefore over a range of dpa rates. These studies showed, however, that lower dpa rates along the tube were clearly shortening the transient duration. One consequence of this shortening is that such "constant time" experiments where data is collected along a component with a strong gradient in dpa rate will always give an artificially low estimate of the swelling rate.

One way to avoid the difficulty associated with such internal flux-effects in the low-dose transient regime is to perform multiple measurements on fixed positions of components at increasing exposure levels. Microscopy data are needed for such a study in order to provide swelling data that is not obscured by densification arising via carbide precipitation. Walters and coworkers have performed such a study and reported the results of the CREEP 1 experiment conducted in row 7 of EBR-II. This study showed that up to ~6 dpa the swelling rate of AISI 304L was roughly linear at 0.060%/dpa [9]. Although not reported in the open literature, a subsequent reevaluation of this experiment after reaching ~10 dpa yielded 0.067%/dpa [10].

Johnson and Hofman later showed that these data could be combined with data from three other experiments and again observed a very linear behavior over ~50 dpa, with a swelling rate of ~0.067%/dpa as shown in Fig. 2 [11]. Since this latter experiment covered a range of dpa rates and temperatures of 370–390°C, it appears that they have defined a relatively flux-independent swelling rate for the incubation regime of annealed AISI 304.

In a more recent compilation by Allen and coworkers [12] it appears that both the earlier and newer data from row 12 [13] could be plotted as shown in Fig. 3. The authors of this paper have added the line representing the correlation of Johnson and Hofman corrected for carbide densification. This figure shows that there appears to be a relatively fixed transient swelling rate of ~0.06%/dpa, and the primary influence of dpa rate is to determine at what dpa level the post-transient behavior begins and the swelling rate accelerates thereafter.

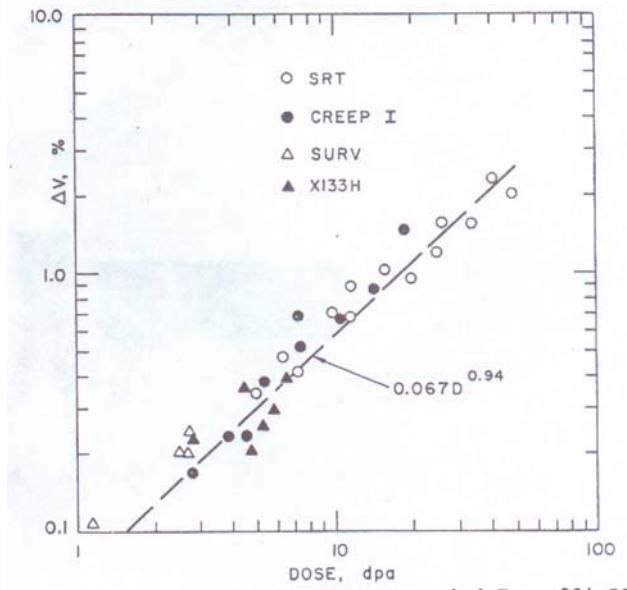


Fig. 2. Swelling (measured by microscopy) vs. dose as plotted by Johnson and Hofman for four sets of experiments conducted in rows 3 to 12 of EBR-II [11]. The swelling rate of this prolonged transient regime is  $\sim 0.067\%/dpa$ .

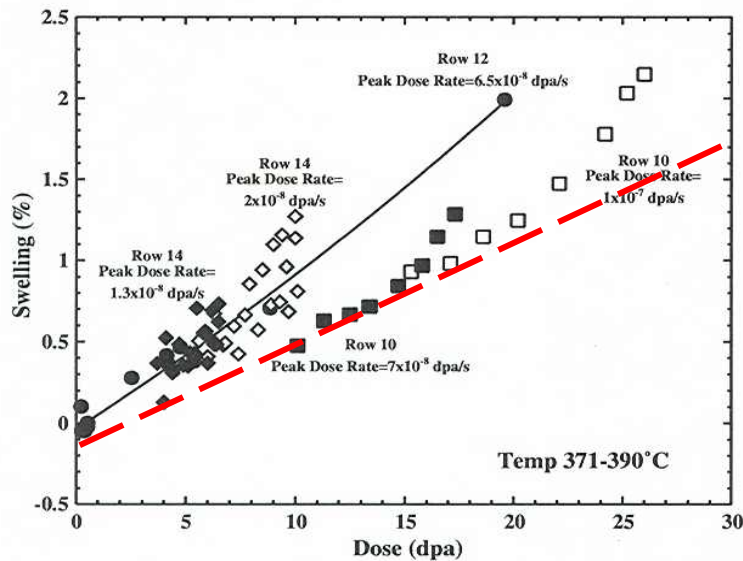


Fig. 3. Data compilation of Allen and coworkers showing swelling of annealed AISI 304 stainless steel [12].

The red line is the microscopy correlation of Johnson and Hofman corrected for carbide densification and was added by authors of this paper to show that a transient swelling rate of  $\sim 0.06\%/dpa$  persists until the swelling rate begins to accelerate. At higher dpa rates the swelling rate begins to turn up at much higher dpa levels than occurs at lower dpa rates.

In order to address the question of whether the post-transient swelling rate approaches  $1\%/dpa$  independent of the dpa rate, it is necessary to evaluate the swelling behavior of EBR-II

components that reached much higher exposures. It is important to note that such components represent “constant-time” experiments with monotonic increases in temperature from bottom to top of the component, but possessing a dpa rate and dpa distribution that peaks near the mid-plane of the component as shown in Fig. 4. Three types of components are considered in the following sections. These are hexagonal cans, stress-free tubes and fuel pin cladding.

### Hexagonal wrappers

The hexagonal cans enclosing safety rods and control rods in the core of EBR-II were the first components to be measured for swelling in the USA after learning of swelling from the British in the late 1960s. There was extensive measurements of these components made at three U.S. national labs but surprisingly little reporting of these data in the open literature was accomplished.

One significant exception was a paper by Fish and coworkers [14] and Fig. 5 from that work shows the peaked profiles for a number of control (CRT) and safety (SRT) rod thimbles, which are thin-walled (~1 mm) hexagonal cans with each face measuring ~3 cm wide. The opposing faces are 6 cm apart which is relatively large compared to the diameter of the core active zone (~30 cm). Each curve shown represents the axial swelling profile of only one face of each can, although 2–4 faces were measured on most cans.

Surprisingly, with again one exception by Fish and coworkers, no comparisons were made between different faces of the same can. Note that hex cans are relatively unstressed, have moderate temperature rises along the axial direction, but at any one elevation have very small difference in temperature from face to face. There also is no significant gradient in temperature across the wall.

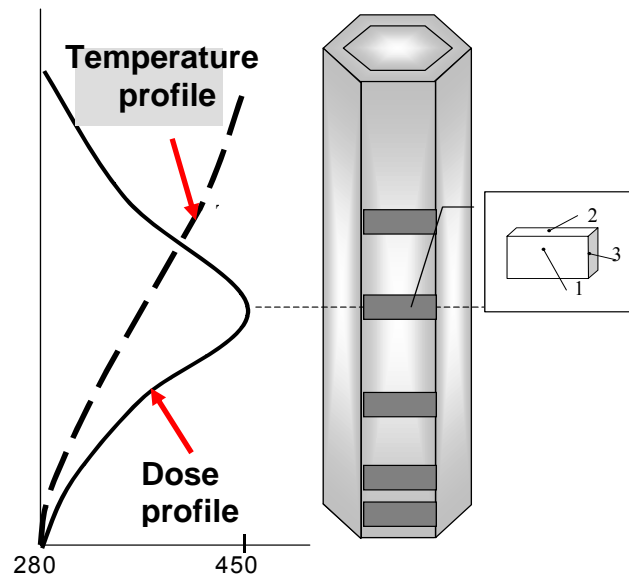


Fig. 4. Schematic representation of a hexagonal duct being sliced to prepare specimens for density measurements. Note that the temperature profile is monotonic in nature but the dose profile is peaked along the axial direction. Thus, neutron flux and dpa rate first rise from the core bottom to mid-plane but then fall thereafter.

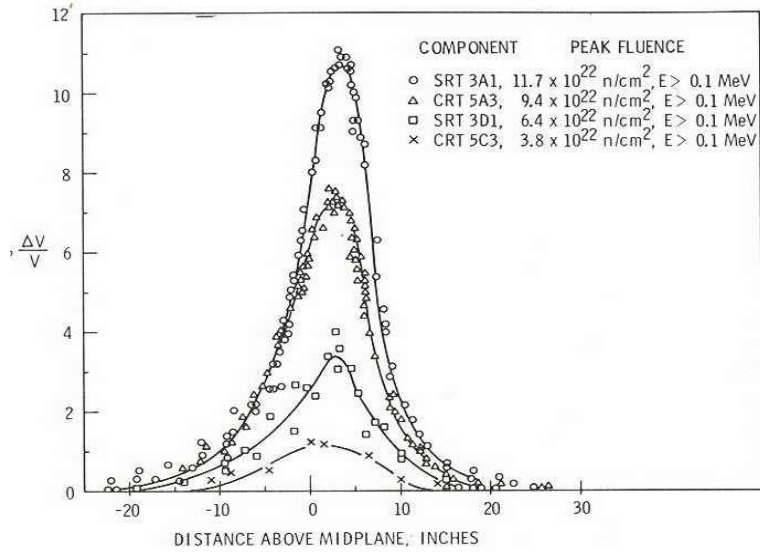


Fig. 5. Swelling in % (measured by immersion density) of individual faces of hexagonal cans enclosing safety rods and control rods as reported by Fish and coworkers [14].

Figure 6 shows the swelling of non-adjacent two faces of SRT 3A1, plotted as a function of dpa only. Note that “loops” are formed on any one face as the dose increases from the bottom to the middle of the can, and then as the dose decreases when moving toward the top of the can. This loop is the consequence of the transient duration increasing with increasing dpa rate on the bottom half of the pin, and then decreasing as the dpa rate falls along the top half of the pin. If there were no effect of irradiation temperature the loop would have zero “width”, but increasing temperature in this steel is always trying to shorten the transient duration [1]. The larger the temperature change along the duct axis, the more pronounced will be the loop width.

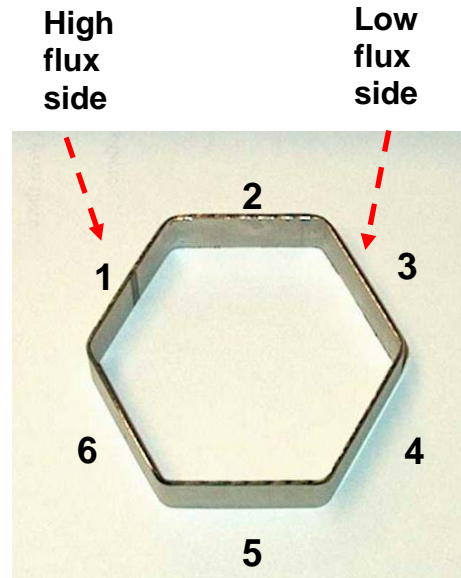
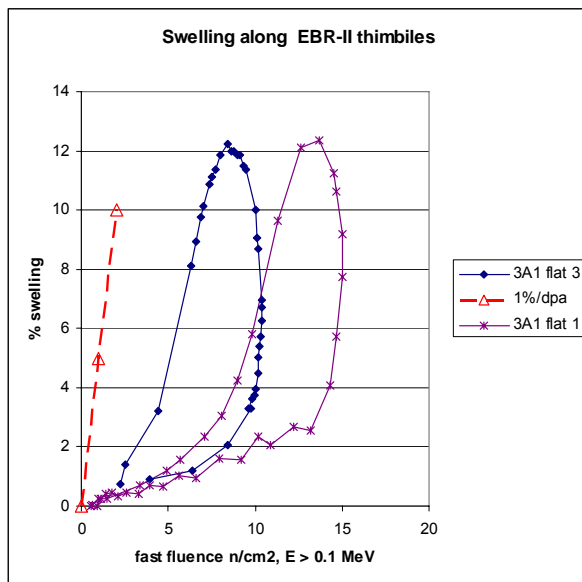


Fig. 6a. Swelling loops produced by plotting swelling vs. dpa from the bottom to top of the duct. Note that the duct face #1 having the highest dpa rates actually swells later than does the low flux face #3. The terminal swelling rate of 1%/dpa is shown for comparison.

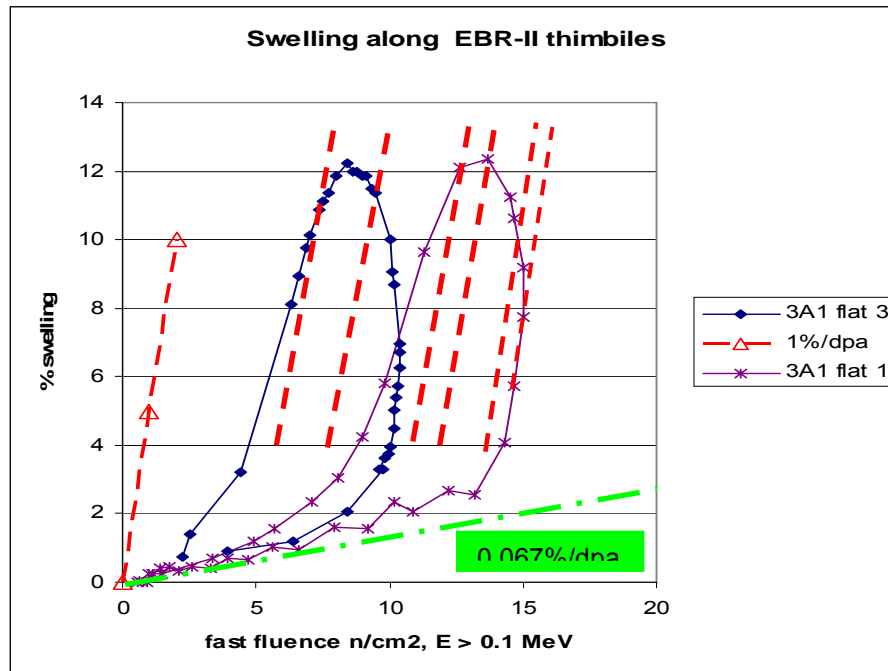


Fig. 6b. Interpretation of loops as formed by swelling curves rising to  $\sim 1\%/dpa$  after a transient swelling rate of  $0.067\%/dpa$ . The transient duration is determined by the combination of dpa rate and temperature unique to each point on the duct face.

Note that as the flux effect increases on the right side of the loop, its effect is partially counteracted by that of increasing temperature, allowing the clear observation of a tangent on the order of  $\sim 1\%/dpa$ . Each data point on the loop at high swelling levels is thought to reside on a separate  $1\%/dpa$  curve with the transient duration determined by the combined effect of temperature and dpa rate. Also note that the low-dpa transient described in the previous section can be seen on the both sides of the higher-flux loop.

Most importantly, however, note that the loop corresponding to the lower-flux face is clearly displaced to lower dpa compared to the higher-flux face. This is a dramatic example of the power of dpa rate to change strongly the transient duration of swelling. Other hex cans show the same face-to-face behavior, but are not shown in this paper.

### Stress-free capsules

Flinn and Kenfield presented a large amount of swelling data on annealed 304L from EBR-II irradiation in a U.S. workshop held in 1976, but very little of the data was analyzed or reported in the open literature [15]. These data were derived from thin-walled cylindrical cladding of 7.37 mm outer diameter that was used to encapsulate fuel pins of 4.42 mm diameter, with the gap filled by sodium.

While there is no stress on the capsule, there is a moderate temperature gradient across the capsule wall, and the axial temperature gradient is much steeper than that of the hex can, with both gradients arising from the heat generation of the encapsulated fuel pin. While the capsule diameter is smaller than the hex can there is still a measurable gradient in dpa rate across some but not all tubes, depending on their location in the fuel pin assembly.

The experimental procedure was to cut ~1 inch sections of the tubes and measure the density of the entire ring, thereby averaging out any swelling variations across the tube diameter. Therefore if loops are observed they are composite loops averaged over the capsule circumference.

Given the variability in a given fuel pin assembly of heat generation rates, dpa gradients, residence time in the assembly and other factors, a wide variety of dpa rate-temperature combinations are possible. In addition, it is now known that temperature gradients across cladding walls accelerate the onset of swelling [16,17] adding one more contributing factor to determine the transient duration.

For the current paper we will focus only on the question of whether the loops are still formed and whether they support the 1%/dpa independence of temperature and dpa rate. In Fig. 7 are presented a selection of loops observed along the length of these pins. Once again the loops, especially at higher swelling levels, develop tangents on the order of 1%/dpa. This is especially clear in capsule #232. Also seen are the low swelling rates characteristic of transient swelling.

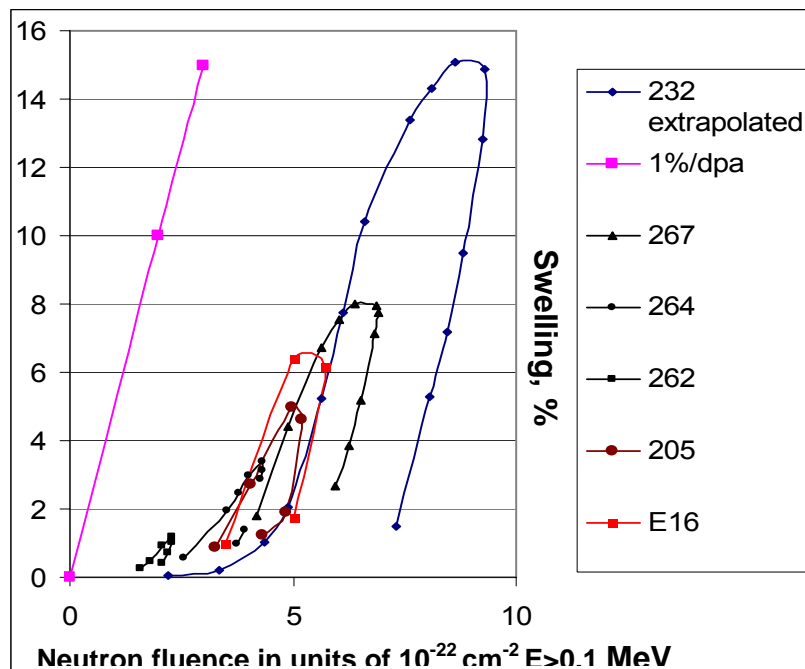


Fig. 7. Loops observed in stress-free capsules at various combinations of pin power, time in reactor and temperature-flux coupling. Note that transition between the lower transient swelling rate and the eventual 1%/dpa terminal rate can be observed in some but not all pins. Capsule identification numbers are provided on the right.

#### MOX fuel pins

Since EBR-II was constructed with annealed 304 stainless steel and had functioned for years without obvious problems, this steel was originally slated for use in building the FFTF fast reactor. There was to be a change, however, moving away from metal fuel used in EBR-II to mixed oxide (MOX) fuel in FFTF. When swelling was discovered in EBR-II in double-digit amounts, the possible use 304 in FFTF was abandoned in favor of cold-worked 316 stainless steel, a steel which swelled much less.

Years before, however, three 37-pin fuel assemblies designated PNL-3, PNL-4, and PNL-5 were put into EBR-II to test the fuel characteristics of 304-clad MOX fuel pins. Although the

experiments were destructively examined and data compiled as part of the swelling evaluation of AISI 304, the data were never analyzed or reported since the decision to abandon the future use of AISI 304 in both EBR-II and FFTF had already been made.

Fuel pins are smaller than the stress-free capsules so the flux gradient across the diameter is smaller, but the temperature gradients across the cladding are larger and the axial temperature gradients were larger. In addition, stresses gradually develop on the cladding that arise from fission gas accumulation and fuel swelling to cause fuel-clad interaction. All of these factors will act to accelerate the onset of swelling to produce different behavior than that of stress-free tubes.

Again ~1 inch long sections of cladding were cut and cleaned of fuel prior to measurements of density. Usually 3 to 5 sections were cut from each pin, and pins were removed at 2–3 exposure levels. Once again the data represent the average swelling across the diameter. Examples of the results for two of the three fuel assemblies are presented in Fig. 8. A full report on this experiment will be made at a later date.

Note that the loops take time to develop, with the transient swelling rate dominating the loop shape at low exposures. Once again the loops are clearly seen at high exposures with tangents on the order of 1%/dpa. Note that when clusters of adjacent pins are removed, the flux-dependent shift of the loops can be seen even within the cluster.

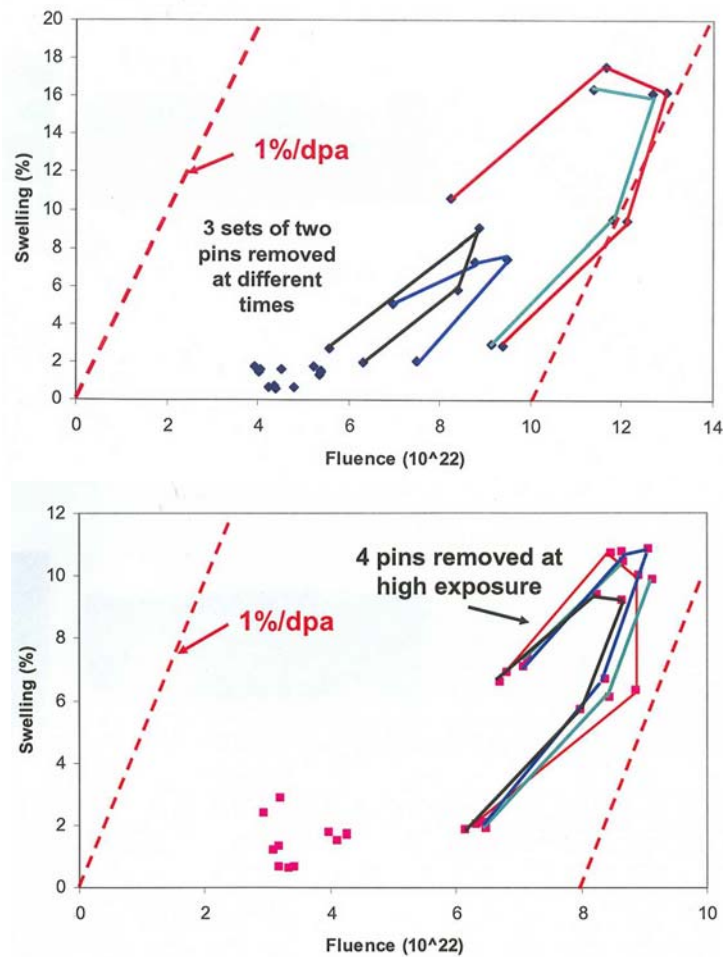


Fig. 8. Selected swelling data sets drawn from fuel assemblies designated PNL-3 (top) and PNL-4 (bottom).

In these pins the combined influence of dpa rate, temperature gradients and stress all serve to develop rather “wide” loops. Note that the loops at lower exposures in the top figure are not yet approaching 1%/dpa but reflect the dominant influence of the lower transient swelling rate.

## Results

Swelling of annealed AISI 304 stainless steel initially proceeds at a rate of  $\sim 0.07\%/dpa$  in the range of 370–390°C and then begins to accelerate toward a rate of  $\sim 1\%/dpa$ , with the breakaway dose dependent on dpa rate, temperature, temperature gradient and stress, in roughly that order.

Swelling of PWR baffle-former assemblies is expected to be most pronounced at those locations where the temperature is highest. The data presented in this paper confirm the general tendency of swelling to have the shortest transient duration with increasing temperature. Also shown however is the stronger tendency of the transient duration to shorten with decreasing dpa rate.

Perhaps the most important conclusion of this study is that swelling correlations developed for PWR application must include dpa rate as an explicit variable. Use of correlations published earlier by the fast reactor community will seriously under-predict swelling at 370–390°C under PWR-relevant flux conditions.

## Acknowledgements

The U.S. portion of this work was jointly supported by the Materials Sciences Branch, Office of Basic Energy Sciences, and the Office of Fusion Energy, U.S. Department of Energy, under Contract DE-AC06-76RLO 1830. Support from H. T. Tang of EPRI is also acknowledged, allowing the lead author to focus this work toward PWR applications.

## References

- [1] F. A. Garner and D. L. Porter, A reassessment of the swelling behavior of AISI 304L stainless steel, Proceedings of the International Conference on Dimensional Stability and Mechanical Behavior of Irradiated Metals and Alloys, April 11–13, 1983, Brighton, England, Vol. II, pp. 41–44.
- [2] F. A. Garner, Chapter 6: Irradiation Performance of Cladding and Structural Steels in Liquid Metal Reactors, Vol. 10A of Materials Science and Technology: A Comprehensive Treatment, VCH Publishers, 1994, pp. 419–543.
- [3] H. T. Tang and J. D. Gilreath, “Aging research and management of PWR vessel internals, Proceedings of the Fontevraud 5, Contribution of Materials Investigation to the Resolution of Problems Encountered in Pressurized Water Reactors, September 23–27, 2002, paper #19, CD format.
- [4] G. M. Bond, B. H. Sencer, F. A. Garner, M. L. Hamilton, T. R. Allen, and D. L. Porter, Void swelling of annealed 304 stainless steel at  $\sim 370\text{--}385^\circ\text{C}$  and PWR-relevant displacement rates, 9<sup>th</sup> International Conference on Environmental Degradation of Materials in Nuclear Power Systems–Water Reactors, 1999, pp. 1045–1050.
- [5] F. A. Garner, D. J. Edwards, S. M. Bruemmer, S. I. Porollo, Yu. V. Konobeev, V. S. Neustroev, V. K. Shamardin, and A. V. Kozlov, Recent developments concerning potential void swelling of PWR internals constructed from austenitic stainless steels, Proceedings of the Fontevraud 5, Contribution of Materials Investigation to the Resolution of Problems Encountered in Pressurized Water Reactors, September 23–27, 2002, paper #22, CD format.
- [6] F. A. Garner, Recent insights on the swelling and creep of irradiated austenitic alloys, J. Nucl. Mater. 122–123 (1984) 459–471.
- [7] D. L. Porter, G. D. Hudman, and F. A. Garner, Irradiation creep and swelling of annealed type 304L stainless steel at  $\sim 390^\circ\text{C}$  and high neutron fluence in EBR-II, J. Nucl. Mater. 179–181 (1991) 581–584.
- [8] D. L. Porter and F. A. Garner, Swelling of AISI type 304L stainless steel in response to simultaneous variations in stress and displacement rate, Effects of Radiation on Materials: Twelfth International Symposium, ASTM STP 870, F. A. Garner and J. S. Perrin (eds.), ASTM, Philadelphia, 1985, pp. 212–220.

- [9] L. C. Walters, C. M. Walter, and M. A. Pugacz, The in-reactor creep of helium-pressurized 304L stainless steel tube, *J. Nucl. Mater.* 43 (1972) 133–142.
- [10] L. C. Walters and C. M. Walter, In-reactor creep experiments on stainless steel tubing, in Quarterly Progress Report: Irradiation Effects on Reactor Structural Materials, February–April 1973, HEDL-TME-73-4, Hanford Engineering Development Laboratory, 1973, pp. ANL 1–3.
- [11] D. L. Johnson and G. L. Hofman, Property changes in fast reactor core support components due to low dose rate, long-time irradiation, *Trans. 4th International Conference on Structural Materials in Reactor Technology*, Vol. L, paper L8/7, August 1977.
- [12] T. R. Allen, J. I. Cole, C. L. Trybus, D. L. Porter, H. Tsai, F. A. Garner, E. A. Kenik, T. Yoshitake, and J. Ohta, The effect of dose rate on the response of austenitic stainless steels to neutron radiation, *J. Nucl. Mater.* 348 (2006) 148–164.
- [13] T. R. Allen, J. I. Cole, C. L. Trybus, and D. L. Porter, The effects of long-term irradiation and thermal aging on 304 stainless steel, *J. Nucl. Mater.* 270 (1999) 290–298.
- [14] R. L. Fish, J. L. Straalsund, C. W. Hunter, and J. J. Holmes, Swelling and tensile properties of high-fluence EBR-II thimbles, *Effects of Radiation on Substructure and Mechanical Properties of Metals and Alloys*, ASTM STP 529, 1973, pp. 149–164.
- [15] J. E. Flinn and T. A. Kendall, Neutron swelling observations on austenitic stainless steels irradiated in EBR-II, *Proceedings of Workshop on Correlation of Neutron and Charged Particle Damage*, CONF-760673, Oak Ridge National Laboratory, June 8–10, 1976, pp. 253–289.
- [16] J. L. Seran, H. Touron, A. Maillard, P. Dubuisson, J. P. Hugot, E. Le Boulbin, P. Blanchard, and M. Pelletier, The swelling behavior of titanium-stabilized austenitic steels used as structural materials of fissile subassemblies in Phenix, *Effects of Radiation on Materials: 14<sup>th</sup> International Symposium (Vol. II)*, ASTM STP 1046, 1985, pp. 736–752.
- [17] N. Akasaka, I. Yamagata, and S. Ukai, Effect of temperature gradients on void formation in modified 316 stainless steel cladding, *J. Nucl. Mater.* 283–287 (2000) 169–173.

**7.0 MHD INSULATORS, COATINGS, INSULATING CERAMICS,  
AND OPTICAL MATERIALS**

## **INVESTIGATION OF Pb-Li COMPATIBILITY FOR THE DUAL COOLANT TEST BLANKET MODULE—** B. A. Pint and J. L. Moser (Oak Ridge National Laboratory)

### **OBJECTIVE**

The objective of this task is to assess the long-term, high-temperature compatibility of various materials with Pb-Li. One proposed fusion reactor concept uses SiC/SiC composites with a self-cooled Pb-17Li blanket. Another concept uses a SiC/SiC flow channel insert with a dual coolant of He and Pb-Li at ~800°C. These concepts also require piping to carry the Pb-Li between the first wall and the heat exchanger. To evaluate compatibility issues in these systems, monolithic SiC, SiC/SiC composites and potential piping and coating materials are being exposed to isothermal Pb-17Li in capsule tests at 700°-1200°C.

### **SUMMARY**

Static capsule tests in Pb-17Li were performed on coated and uncoated type 316 stainless steel and Al-containing alloys at 800°C and the Pb-Li was analyzed after each capsule test. Chemical vapor deposited (CVD) aluminide coatings on type 316 substrates reduced dissolution by ~50X at 800°C compared with uncoated samples. Little effect of pre-oxidation was observed for the performance of the coating. These results indicate that aluminide coatings may be a viable option to allow conventional Fe- or Ni-base tubing alloys to carry PbLi from the first wall to the heat exchanger. Future work will need to include testing in a flowing system with a thermal gradient to fully determine the compatibility of these materials. In order to test the viability of using a thermal convection loop made of quartz, a quartz ampoule was filled with Pb-Li and exposed for 1000h at 800°C. No Si was detected in the Pb-Li after the test indicating that quartz may be a low cost construction option.

### **PROGRESS AND STATUS**

#### **Introduction**

One proposed test blanket module (TBM) concept for ITER is a dual coolant (He and Pb-Li) system using advanced ferritic steels as the structural material and a silicon carbide composite as a flow channel insert [1,2]. Although the TBM design will operate at <500°C, thereby limiting compatibility problems, ultimately this blanket concept would be more attractive with a maximum operating temperature of 700-800°C. In this temperature range, critical compatibility issues need to be addressed. Recent effort has focused on the compatibility of ferritic-martensitic steels in Pb-Li at 400-600°C [3,4]. However, there has been less work examining corrosion-resistant coatings needed at higher temperatures.

Because of the low activity of Li in Pb-17Li, thermodynamic calculations have shown that Al<sub>2</sub>O<sub>3</sub> should be stable [5], indicating that alloys or coatings that form an adherent external alumina scale should be resistant to dissolution in Pb-Li. Such coatings would be required for conventional piping materials to carry Pb-Li from the first wall to the heat exchanger at ~700°C. While a SiC flow channel insert could protect the steel walls from Pb-Li dissolution, it is unlikely this strategy could be used through the entire flow path. Contact of Fe- or Ni-base, alloys with flowing Pb-Li at this temperature would result in unacceptably high dissolution rates [3,4,6]. Although the use of refractory metals is one option [7], fabrication and durability of Nb or Mo tubing could be an issue. However, a protective coating could allow a conventional Fe- or Ni-base tubing alloy to be used.

Baseline compatibility data is being developed using static capsule tests and model materials in order to assess the performance of an aluminide coating or Al-containing alloys. Based on positive results at

Table 1. Alloy chemical compositions (atomic% or ppma) determined by inductively coupled plasma analysis and combustion analysis.

Material	Fe	Ni	Cr	Al	O	C	N	S	Other
316SS	65.1	8.9	19.9	0.02	490	3360	2380	68	1.94Si, 1.67Mn, 1.38Mo, 0.21Cu
ODS FeCrAl	67.8	0.02	20.0	10.6	7430	340	210	50	0.44Ti, 0.23Y, 0.04Si, 0.04Mn
Fe-28Al-2Cr+Zr	70.0	<	2.0	27.9	70	400	<	46	0.026Zr, 0.005Hf
Ni-42.5Al	<	57.3	<	42.6	40	380	<	<	<

< indicates below the detectability limit of <0.01% or <0.001% for interstitials

700°C [8] CVD aluminide coatings on type 316 stainless steel substrates were tested at 800°C. Both sets of experiments show promising results, consistent with the thermodynamic assessment.

### Experimental Procedure

Capsule tests with static PbLi (detailed elsewhere [8,9]) were performed on alloy coupons with a 1.5mm thickness, a surface area of 4-5cm<sup>2</sup> and a 600grit SiC surface finish. The chemical composition of the alloys tested at 800°C are shown in Table 1. A Fe<sub>3</sub>Al composition was selected as being similar to aluminide coatings formed on Fe-base alloys [10] and a Ni-42Al composition is similar to the composition of a CVD aluminide coating on a Ni-base alloy [11]. In addition, an oxide dispersion strengthened (ODS) FeCrAl (Plansee alloy PM2000) was tested as this class of alloy could be used without a coating. The alloy specimens were pre-oxidized for 2h at 1000°C in 1 atm dry O<sub>2</sub> before exposure to Pb-Li. Two specimens of type 316 stainless steel were CVD aluminized for 4h at 1050°C in a laboratory scale reactor and then immediately annealed for 2h at the same temperature [10]. These conditions produce a coating approximately 200µm thick with an Al-rich outer layer, ~( $\text{Fe,Ni}$ )<sub>3</sub>Al, about 20µm thick. One of the coated specimens was pre-oxidized for 2h at 800°C in air. All of the specimens were suspended in a welded Mo capsule using Mo wire. For these tests, the inner Mo capsule was loaded with high purity (99.9999%) Pb shot and Li in an argon-filled glove box. The Mo capsule was protected by an outer type 304 stainless steel capsule. Specimen mass was measured before and after exposure on a Mettler-Toledo balance with an accuracy of ±0.04 mg. The 1000h exposures were performed in resistively heated box furnaces. After exposure, the specimens were soaked in a mixture of acetic acid, hydrogen peroxide and ethanol for 24-72h to remove any residual Pb-Li. The composition of the Pb-Li after testing was determined by inductively coupled plasma analysis and combustion analysis. Post-test characterization of the specimens has not yet been performed.

### Results and Discussion

**Capsule results.** Table 2 shows the mass changes for the specimens exposed at 800°C [12]. Compared

Table 2. Mass change of specimens after 1000h at 800°C in Pb-17Li with a Mo capsule.

Specimen	Pre-oxidation	Mass Change	
		(mg)	(mg/cm <sup>2</sup> )
316SS	none	-79.51	-17.30
316SS + CVD Al	none	- 1.55	- 0.34
316SS + CVD Al	2h at 800°C	- 1.93	- 0.43
ODS FeCrAl	2h at 1000°C	+ 1.58	+ 0.24
Fe-28Al-2Cr+Zr	2h at 1000°C	- 1.55	- 0.37
Ni-42.5Al	2h at 1000°C	-12.12	- 2.72

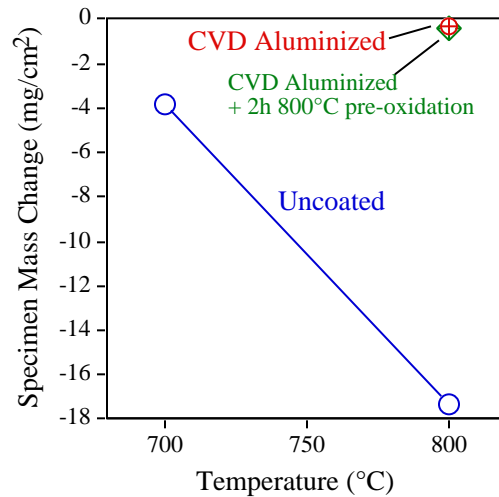


Figure 1. Specimen mass loss after 1,000h in Pb-17Li as a function of temperature for uncoated and coated type 316 stainless steel.

to the uncoated 316SS specimen, the aluminized 316SS specimens showed dramatically lower mass losses. Pre-oxidizing the coating for 2h at 800°C to form an alumina layer did not have a beneficial effect on dissolution. Figure 1 summarizes the 700° and 800°C results for uncoated and coated type 316 stainless steel in Pb-Li showing the ~50X reduction in dissolution at 800°C with the CVD aluminide coating.

The Al-containing alloys also showed lower amounts of dissolution. The mass gain for the ODS FeCrAl specimen may be due to entrapped metal, i.e., incomplete cleaning, however, the specimen appeared unaffected by the exposure. The Fe<sub>3</sub>Al specimen had one ~3mm area where the oxide was removed causing some degree of mass loss. This selective attack area may be due to incomplete initial mixing of the Pb and Li. Undoped lithium would quickly attack alumina and any of these alloys at 800°C. The highest mass loss was for NiAl where ~90% of the oxide appeared to be spalled after exposure. One reason for the higher mass loss may be that Ni dissolves more readily than Fe in PbLi. This hypothesis was confirmed by the chemical analysis which showed a detectable Ni level in the PbLi after exposure of the NiAl sample, Table 3. Another factor is that this alloy did not contain a reactive element addition (Y, Zr, Hf, etc.) which improves the adhesion of the alumina layer formed during pre-oxidation, Table 1. Spallation of the alumina could have resulted in more attack for this specimen.

Table 3. Chemical composition using inductively coupled plasma and combustion analysis of the starting Pb, commercial Pb-Li ingot and the Pb-Li after capsule exposures at 800°C for 1000h (in ppma except for Li in atomic%).

Test	Li	Fe	Cr	Ni	Mn	Si	Al	Mo	C	O	N	S
Starting Pb	n.d.	<4	<4	<4	<4	<40	<8	<2	<170	1270	<40	<50
Comm. PbLi	14.3%	<30	<70	<30	<30	<120	<60	<40	750	4820	180	<50
316SS	16.5%	<30	<30	<b>270</b>	<30	<120	<60	<20	480	2040	<40	<50
316SS+Al	17.6%	<30	<30	<30	<30	<120	<60	<20	590	1370	<40	<50
316SS+Al/O	17.5%	<30	<30	<30	<30	<120	<60	<20	730	2100	<40	<50
FeCrAl	17.3%	<30	<30	<30	<30	<120	<60	<b>90</b>	460	5280	<40	<50
Fe <sub>3</sub> Al	16.3%	<30	<30	<30	<30	<120	<60	<20	540	1230	<40	<50
NiAl	16.7%	<30	<30	<b>150</b>	<30	<120	<60	<20	520	2640	<40	<50
Quartz	14.5%	<30	<30	<30	<30	<120	<60	<20	430	4550	<40	<50

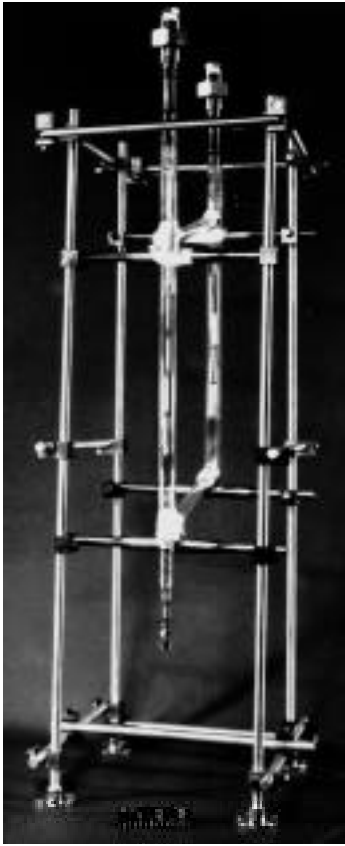


Figure 2. Photograph of a quartz thermal convection loop at ORNL [14].

**Loop experiment planning.** Future work will eventually include flowing liquid metal experiments with a temperature gradient. Static capsule experiments can only be expected to produce a limited assessment of the compatibility issue because saturation of the liquid metal with the element or elements dissolving eventually inhibits further dissolution [6,8]. Since low-cost quartz loops (Figure 2) were previously used for testing Pb [13] and Bi-Li [14], the possibility of constructing Pb-Li loops out of quartz was investigated by testing Pb-17Li in a quartz ampoule at 800°C. A mass change could not be determined in this test but the post-test PbLi chemistry showed no detectable Si dissolved in the liquid metal, Table 3. Thus, a quartz loop appears to be a viable, low-cost option, at least for an initial assessment of compatibility of SiC composites and Al-containing alloys and coatings, for tests in flowing Pb-Li.

The current procedure of in-capsule melting of Pb and Li to form the Pb-17Li composition would not be viable for a loop testing program. Therefore, purchase of pre-alloyed Pb-Li has been investigated and commercial Pb-Li was obtained from N. Morley at UCLA. The chemical composition of the as-received commercial PbLi is shown in Table 3. In particular, O and N are much higher than in the starting Pb used in the capsule experiments. Based on the high Li-O affinity and prior results, the high O content likely suppressed the measured Li in the commercial material. The commercial PbLi is being used in two recently started capsule experiments examining monolithic SiC at 1000°C.

## References

- [1] P. Noajitra, L. Buhler, U. Fischer, S. Malang, G. Reimann, and H. Schnauder, *Fusion Eng. Des.* 61-62 (2002) 449.
- [2] M. Abdou, D. Sze, C. Wong, M. Sawan, A. Ying, N. B. Morley, and S. Malang, *Fusion Sci. Technol.* 47 (2005) 475.
- [3] G. Benamati, C. Fazio, and I. Rikapito, *J. Nucl. Mater.* 307-311 (2002) 1391.
- [4] J. Konys, W. Krauss, Z. Voss, and O. Wedemeyer, *J. Nucl. Mater.* 329-33 (2004) 1379.
- [5] P. Hubberstey, T. Sample, and A. Terlain, *Fusion Sci. Technol.* 28 (1995) 1194.
- [6] T. Flament, P. Tortorelli, V. Coen, and H. U. Borgstedt, *J. Nucl. Mater.* 191-194 (1992) 132.
- [7] H. Feuerstein, H. Gräbner, J. Oschinski, and S. Horn, *J. Nucl. Mater.* 233-37 (1996) 1383.
- [8] B. A. Pint, J. L. Moser, and P. F. Tortorelli, *Fusion Eng. Des.* 81 (2006) 901.
- [9] B. A. Pint, L. D. Chitwood, and J. R. DiStefano, DOE/ER-0313/35 (2003) 13.
- [10] Y. Zhang, B. A. Pint, J. A. Haynes, I. G. Wright, and P. F. Tortorelli, *Oxid. Met.* 62 (2004) 103.
- [11] Y. Zhang, W. Y. Lee, J. A. Haynes, I. G. Wright, B. A. Pint, K. M. Cooley, and P. K. Liaw, *Met. Trans.* 30A (1999) 2679.
- [12] B. A. Pint, J. L. Moser, and P. F. Tortorelli, DOE-ER-0313/39 (2005) 128.
- [13] J. V. Cathcart and W. D. Manly, *Corrosion* 12 (1956) 43.
- [14] J. R. DiStefano and O. B. Cavin, ORNL/TM-5503, 1976, Oak Ridge National Laboratory, Oak Ridge, Tenn.

**8.0 BREEDING MATERIALS**

**No contributions.**

**9.0 RADIATION EFFECTS, MECHANISTIC STUDIES,  
AND EXPERIMENTAL METHODS**

**MODELLING THERMODYNAMICS OF ALLOYS FOR FUSION APPLICATION**—A. Caro, M. Caro, J. Marian (Lawrence Livermore National Laboratory), E. Lopasso (Centro Atomico Bariloche, Argentina), and D. Crowson (Virginia Polytechnic Institute)

## OBJECTIVE

This research has two main objectives:

- The development of computational tools to evaluate alloy properties, using the information contained in thermodynamic functions to improve the ability of classic potentials to account for complex alloy behavior, and
- The application of these to predict properties of alloys under irradiation.

## SUMMARY

Atomistic simulations of alloys at the empirical level face the challenge of correctly modeling basic thermodynamic properties. In this work we develop a methodology to generalize many-body classic potentials to incorporate complex formation energy curves. Application to Fe-Cr allows us to predict the implications of the *ab initio* results of formation energy on the phase diagram of this alloy and to get a detailed insight into the processes leading to precipitation of  $\alpha'$  phase under irradiation.

## PROGRESS AND STATUS

Four main activities were developed in the period covered by this report.

1. Continuing the work described in the previous report, namely the procedure to build a classic model for Fe-Cr alloys from the perspective of thermodynamics, we derived the phase diagram of that system that has been sent for publication and accepted in applied Physics Letters. This diagram provides an explanation to several experimental observations that were at odds with the traditional phase diagram.
2. We started the study of precipitation of  $\alpha'$  phase, using the recently developed Monte Carlo code and the potential for the alloy. We explore homogeneous nucleation first and determine some properties of the precipitates.
3. We started the study of point defects in the alloy, with a careful comparison with *ab initio* results from P. Klaver – M. Finnis group in UK.
4. We started the study of radiation damage in the alloy with a new collaboration with S. Srinivasan from Los Alamos National Lab.

In what follows, we briefly describe the achievements.

### Phase Diagram of the Fe-Cr Empirical Potential

We analyzed the implications of the recently reported results of *ab initio* calculations of formation energies of the Fe-Cr alloy. The formation energies show a change in sign from negative to positive as Cr composition increases above  $\sim 10\%$ . By developing a classic potential to evaluate the thermodynamic properties [1], we determine the location of the solubility limit and compare it with earlier results. A significant difference appears in a region of temperature and composition that is relevant for the nuclear applications of this alloy. Experimental results seem to confirm the validity of the location of the new *solvus* line.

The Phase diagram we obtained is shown in Fig. 1 below. It shows the low T - low x region of interest  $0K < T < 1000K$  and  $0\% < x_{Cr} < 20\%$ . A continuous followed by a dotted line is our results for the *solvus* in the FM phase, while the dashed line is the *solvus* as it appears in SSOL, the database of Thermocalc.

Our *solvus* is plotted with a solid line only for temperatures below the invariant line suggested by the experiments, that we report in the figure as a horizontal solid line; above it, the *solvus* is shown with a dotted line, indicating that other effects determine the diagram at those T-x values, namely, the  $\sigma$  phase and the magnetic transition.

In Fig. 1 we have added the experimental results of Kuwano et al. [2] and those of Mathon et al. [3]. The discrepancy between the SSOL [4] *solvus* and the *solvus* implied in the *ab initio* results is obvious, as is the agreement between the experimental results and our prediction. The most striking difference is the fact that the *solvus* line, if extrapolated to zero temperature, does not cross the x-axis at  $x = 0$ , as explicitly assumed in the CALPHAD treatment. This fact can easily be understood if one considers a very low T, where excess free energy is essentially equal to the excess heat of formation (hof); then the solid line in Fig. 2, that shows the formation energy of the alloy, can be reinterpreted as a free energy curve and the common tangent construction would show that the miscibility gap at  $T = 0K$  closes at  $x \sim 0.04$ , i.e., the location of the minimum of that curve. This fact can be considered as the main consequence of the *ab initio* result giving a change in sign in the hof.

The implications of this are as follows: Fig. 1 shows how the phase diagram at low T and low x is modified if one considers the heat of formation predicted by *ab initio* calculations. This diagram is calculated using a classic potential that reproduces the energetics (in particular the change in sign at some low Cr concentration), and by doing the thermodynamics exactly via switching Hamiltonians and thermodynamic integration techniques. The fact that the miscibility gap closes at finite x and that the maximum in the hof is higher than the SSOL value implies that the location of the *solvus* is significantly affected.

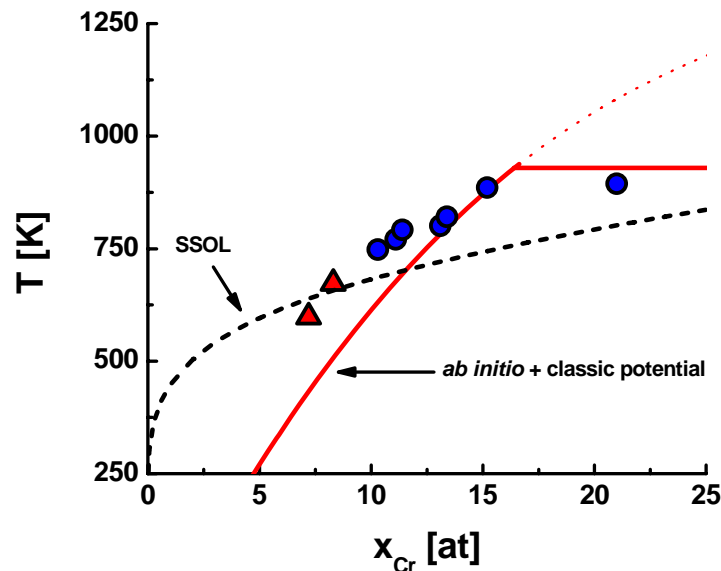


Fig. 1. Portion of the phase diagram as predicted by our methodology, showing the location of the *solvus*, together with experimental results from Ref [2, 3], and the *solvus* as appears in SSOL, the database of CALPHAD [4].

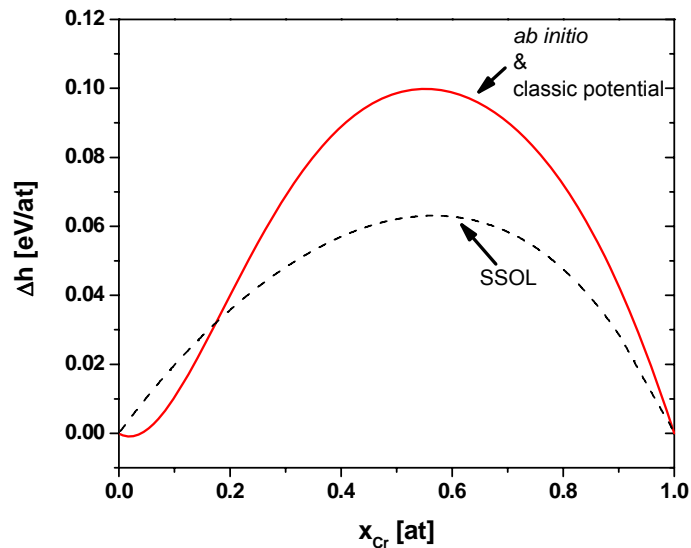


Fig. 2. Formation energy of the alloy as predicted by ab initio calculations (solid line) and as reported in the database of CALPHAD.

In summary, we observe that the change in sign of the heat of formation at about 6% Cr modifies the location of the *solvus* in the phase diagram by making it much steeper than the SSOL value. The solubility limit above  $\sim 700\text{K}$  is much less than the value in SSOL and conversely, below  $\sim 700\text{K}$  it is much higher. In particular, at low temperature, even at 0 K, there is a finite Cr solubility because the *solvus* does not go to  $x_{\text{Cr}} = 0$  at  $T = 0$  but to  $x_{\text{Cr}} \sim 0.04$ .

As we pointed out above, the finite Cr solubility at 0 K is a result that is not affected by the controversy regarding the value of the hof around equiatomic composition. However how steep the *solvus* is at both ends of the diagram strongly depends on that value. The solubility of Fe in the  $\alpha'$  phase, as we predict it, is too low compared to experiments [3] and SSOL [4], a result also related to the high hof predicted *ab initio*.

#### Precipitation of $\alpha'$ Phase

The predictions of the Fe-Cr alloy potential regarding segregation of supersaturated solid solution can be assessed by using the Monte Carlo code with displacements developed in this work. Figure 3, below, shows the phases  $\alpha$  and  $\alpha'$  with a flat interface in a heterogeneous sample during a MC run used to determine the equilibrium composition of the two coexisting phases. By averaging in time the composition profiles, we determine the composition shown in Fig. 4.

In addition to composition, Fig. 4 also shows that the nature of this particular interface between coherent  $\alpha$  and  $\alpha'$  precipitates is quite sharp, only about one lattice parameter.

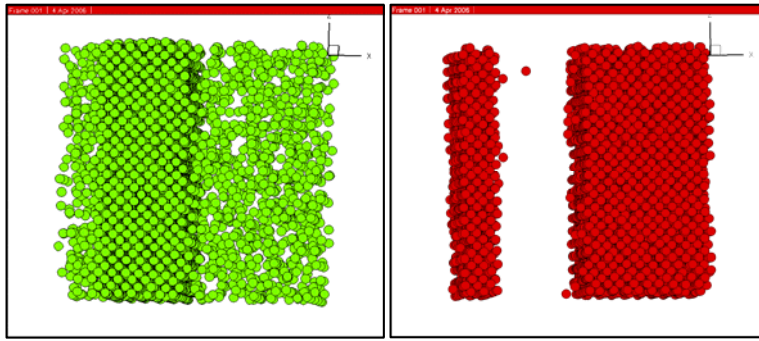


Fig. 3. Composition of a  $\alpha$  and  $\alpha'$  precipitates in contact in a two phase sample. The figures represent in green the Cr atoms and in red the Fe atoms. In the figure on the left we see  $\alpha'$ , Cr rich precipitate, and similarly for  $\alpha$  on the right.

This result gives an insight on the morphology of  $\alpha'$  precipitates. Further studying the mechanisms of precipitation, we are at present analyzing the process of nucleation and growth. Figure 5 shows a precipitate of a few nanometers in a saturated solution at 750K. The precipitate is spherical, coherent and with a sharp interface.

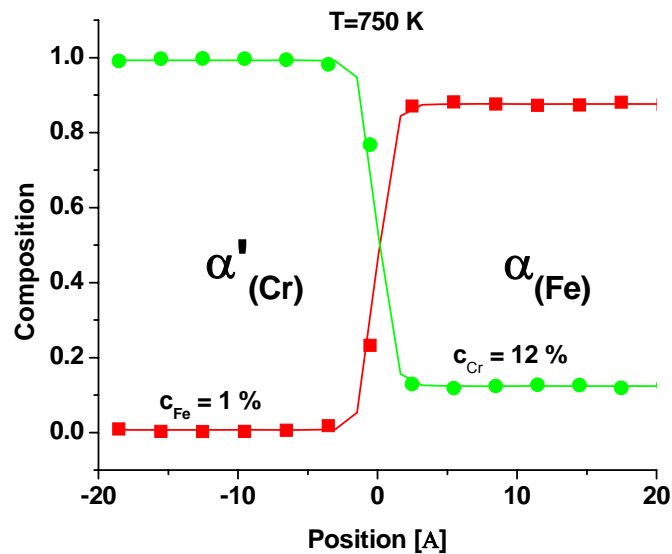


Fig. 4. Composition of a  $\alpha$  and  $\alpha'$  precipitates in contact in a two phase sample. Comparison of these saturation solubilities with the location of the solvus in Fig. 1 indicates a perfect agreement between the MC result and the prediction of the thermodynamics calculations.

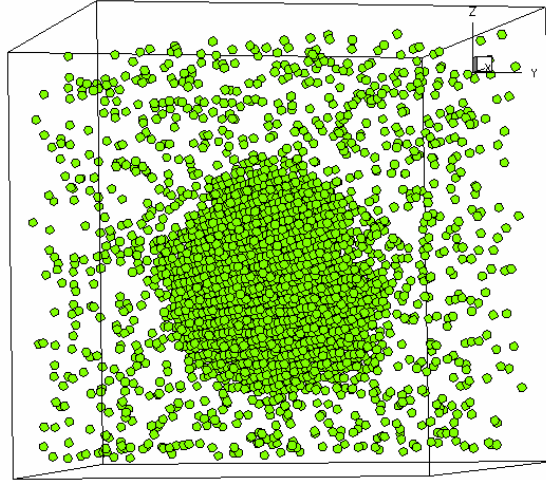


Fig. 5. Homogeneous precipitation of a saturated solution produces spherical precipitates, coherent with the matrix and with sharp interfaces. These are the first results obtained with the MC code developed for this project.

Similarly, we explored precipitation in a solution close to 50% composition where spinodal decomposition instead of nucleation and growth is the precipitation mechanism. Figure 6 shows the microstructure of such precipitation process.

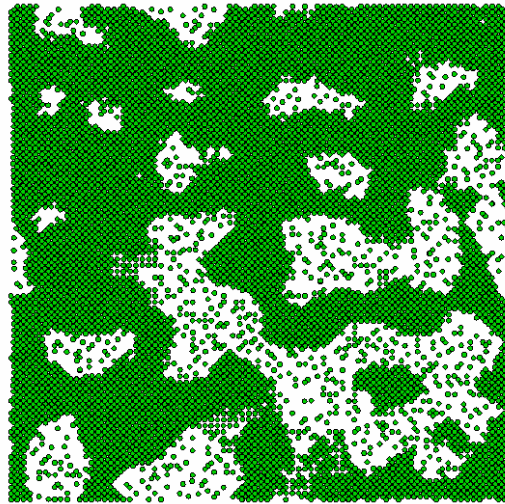


Fig. 6. For compositions inside the spinodal region (i.e., around 50%) the model predicts decomposition by the spinodal mechanism. This result of a MC simulation shows the microstructure after that process took place. Green atoms are Cr atoms.

#### Point Defects in the Alloy

It has recently been proved by colleagues from the UK that the complex nature of this alloy is due to magnetic effects in competition between ferromagnetic Fe and antiferromagnetic Cr. The ability to capture the essence of these interactions is one of the main challenges for the development of a classic approach to this alloy useful for large-scale molecular dynamics. At the present stage of

our project, we are systematically studying point defects in the alloy and comparing the results with ab initio calculation from P. Klaver – M. Finnis group in UK.

One of the most salient features is the fact that a dilute solution of Cr in Fe is exothermic, i.e., it has a negative heat of formation. However, when the composition rises above  $\sim 10\%$  the alloy turns into a segregating system with endothermic heat of formation. This property appears in a different scenario when two substitutional Cr atoms in a dilute alloy approach each other. Ab initio calculations show that significant repulsion occurs. Figure 7 shows the excellent agreement between this important feature in the ab initio calculation and in our classic approach, giving a strong support to the validity and utility of the potential developed.

This result is the first step of a series of test we are performing at present to explore diverse configurations of point defects in the alloy, trying to identify the relevant parameters that describe point defects in a concentrated alloy, in view of the future development of approximate methods to treat longer time scales using kinetic Monte Carlo approaches.

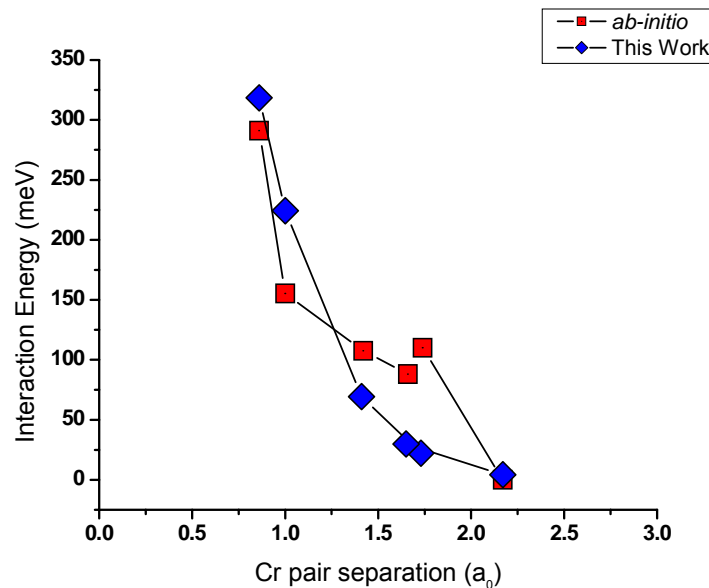


Fig. 7. Interaction energy (repulsion) between two substitutional Cr atoms in an otherwise perfect Fe lattice. Squares represent ab initio results from P. Klaver [Queen's University, Belfast, unpublished] and rhombuses are the predictions of our classic potential. The agreement is remarkable considering that the origin of this repulsion is of magnetic origin, only captured qualitatively in the classic approach.

### References

- [1] A. Caro, D. A. Crowson, and M. Caro, Classical many-body potential for concentrated alloys and the inversion of order in iron-chromium alloys, *Phys. Rev. Lett.* 95 (2005) 075702.
- [2] H. Kuwano and Y. Hamaguchi, *J. Nucl. Mater.* 155 (1988) 1071.
- [3] M. H. Mathon, Y. de Carlan, G. Geoffrey, X. Averty, and A. Alamo, *J. Nucl. Mater.* 312 (2003) 236.
- [4] N. Saunders and A. P. Miodownik, *CALPHAD: A comprehensive guide*, Ed., R. W. Cahn, Pergamon Materials Series (Oxford, New York, 1998).

**THERMAL HELIUM DESORPTION OF HELIUM-IMPLANTED IRON**—D. Xu, T. Bus, S. C. Glade, and B. D. Wirth (University of California, Berkeley)

## OBJECTIVE

The objective of this work is to understand the kinetics and energetics of helium in iron implanted with He ions at different energies and fluences.

## SUMMARY

Following the last report, we have performed new implantations at energies lower than 100 keV, with an aim of reducing the penetration depth of helium atoms and the structural damage, and thus reducing the He-point defect interaction complexity during desorption experiments. Initial measurements on the new samples have revealed a large number of desorption peaks within both the bcc and fcc temperature ranges. These peaks are well fit with first order reaction kinetics, which reveal activation energies ranging from ~1.9 to ~3.5 eV. The number and the relative intensities of detected desorption peaks within the bcc temperature range appear to increase with decreasing implantation energy. Previously reported spurious peaks and a non-1<sup>st</sup>-order sharp peak are now better understood and described in the current report.

## PROGRESS AND STATUS

### Introduction

Helium effects on the microstructure and mechanical properties are among the most critical subjects in fusion materials research. It has been shown that implanted or internally produced (by neutron radiation) helium can cause formation of voids and bubbles in the materials and thus result in significant mechanical property degradation [1–4]. A crucial aspect, therefore, is to understand how helium atoms migrate and are trapped by microstructural features in irradiated materials. While a large amount of theory, modeling and experimental research has been performed in the past years, the understanding of this problem is still far from complete.

In iron and ferritic alloys, computer simulations have been performed on defect production in collision cascades during helium injection [5], effect of He-vacancy complexes on the mechanical properties [6], thermal stability of He-vacancy and/or He/self-interstitial-atom (SIA) clusters [7–10], helium clustering at dislocations [11,12], and the He-grain boundary interaction [13–14]. Experimentally, nuclear reaction depth profiling [15], transmission electron microscopy [16], positron annihilation lifetime and coincidence Doppler broadening (CDB) techniques [17,18] and thermal helium desorption spectrometry (THDS) [7,19–20] have been used to study the He migration and He-induced defect clusters in iron.

Despite the above works, there are still many unresolved questions regarding the helium behavior in iron. For example, for the dissociation of the simple substitutional helium (i.e., HeV); different researchers have reported very different values of activation energy, such as 3.9 eV by v.d. Berg et al. [11] and Morishita et al. [7,8], 2.4 eV by Fu et al. [10], and even 1.4 eV by Vassen et al. [20]. The current knowledge about helium behavior in iron and ferritic alloys remains incomplete and is certainly less than necessary to establish a predictive model for the performance of these materials in future fusion reactors.

In our previous report [21], preliminary work on the THDS study of the kinetics and energetics of helium in iron implanted with 100 keV He to three different fluences,  $1 \times 10^{11}$ ,  $1 \times 10^{13}$ , and  $1 \times 10^{15}$  He/cm<sup>2</sup> was presented. In that report, it was observed that certain unknown spurious peaks which were apparently not related to the desorption of implanted helium appeared on the measured helium signals from all the 100 keV samples. From the two lower fluence ( $1 \times 10^{11}$  and  $1 \times 10^{13}$  He/cm<sup>2</sup>) samples, particularly, no clear signals were observed that could be unambiguously associated with real desorption of implanted helium within the entire temperature range of measurement (from room temperature up to 1330°C). For the

highest fluence ( $1 \times 10^{15}$  He/cm<sup>2</sup>) sample, however, two major real desorption events were observed with the first event peaking at  $\sim 1017^\circ\text{C}$  (upon continuous heating at a rate of 1 K/s) and the second starting at  $\sim 1100^\circ\text{C}$  but not ending even up to the upper limit of the measurement temperature (i.e.,  $1330^\circ\text{C}$ ). Detailed kinetic analysis showed that the low temperature desorption event of the 100 keV and  $1 \times 10^{15}$  He/cm<sup>2</sup> sample consists of two components (or sub-events), one with a broad peak and the other with a sharp peak. The broad component can be described by 1<sup>st</sup>-order kinetics using either conventional reaction model or Johnson-Mehl-Avrami (JMA) model, while the sharp component can only be described by a high ( $n \sim 5.8$ ) order JMA model. It was also observed that a similarly sharp desorption event appeared during immediate cooling from  $1330^\circ\text{C}$  at the end of first heating ramp and even during subsequent re-heating and re-cooling of the 100 keV and  $1 \times 10^{15}$  He/cm<sup>2</sup> sample. Only after the sample was held isothermally at a very high ( $1330^\circ\text{C}$ ) temperature for a long time ( $\sim 30$  min) did the event disappear completely during immediate cooling and subsequent re-cycling.

Following this previous report, we have performed new implantations at energies lower than the previous 100 keV. Some of the new samples have been measured and their data has been analyzed which has yielded new information, particularly for the bcc-iron temperature range, as we will elaborate in the following.

### Instrumentation

Figure 1 is a picture of the THDS system at University of California, Berkeley [22]. The construction and the operating principle have been explained in detail in the previous report [21]. Briefly, however, under the dynamic operating mode, the system measures the instantaneous gas partial current ( $I$ ) by a quadrupole mass spectrometer which can be converted easily to the instantaneous desorption rate ( $d\bar{N}/dt$ ) of that gas using the proportional relation:  $d\bar{N}/dt \propto (P - P_{base}) \propto (I - I_{base})$ . The proportion coefficient can be determined using a calibration procedure [21].



Fig. 1. Picture of the Berkeley THDS instrument.

### Theory

After implantation, helium atoms are trapped by various microstructural defects inside the implanted material. The trapping defects include those created during implantation such as vacancies, self-interstitial-atoms (SIAs) and their clusters, and those already existent prior to the implantation such as thermal vacancies, dislocations, grain boundaries, impurities, etc. During subsequent thermal annealing,

three different kinetic processes may occur: diffusion, detrapping and retrapping. A general description of the overall kinetics can be represented by (in 1-D case):

$$\vec{J}(x,t) = -\sum_i D_i(t) \vec{\nabla} C_{mob,i}(x,t) \quad (1)$$

$$\frac{\partial C_{mob}(x,t)}{\partial t} = -\vec{\nabla} \vec{J}(x,t) + \sum_j \frac{\partial C_{detrapp}^j(x,t)}{\partial t} - \sum_k \frac{\partial C_{retrap}^k(x,t)}{\partial t} \quad (2)$$

where the first summation (in Eq. (1)) refers to the diffusion by different mechanisms, the second to the detrapping from different traps, and the third to the retrapping by different traps. Assuming that the diffusion of mobile helium atoms is fast until they are retrapped or reach the sample surfaces (i.e., neglecting the slow diffusion through the collective movement of a helium-containing trap which might happen if the migration energy of the trap as a whole is much lower than its dissociation energy), then the total number of mobile helium atoms inside the sample remains very low, and we have approximately (where  $A$  is surface area)

$$\frac{\partial \int C_{mob}(x,t) A dx}{\partial t} \sim 0. \quad (3)$$

Integrating Eq. (2) over the length of the sample then yields

$$AJ_{tot} = A[J(0,t) + J(l,t)] \sim \sum_j \frac{\partial \int C_{detrapp}^j(x,t) A dx}{\partial t} - \sum_k \frac{\partial \int C_{retrap}^k(x,t) A dx}{\partial t} \quad (4)$$

which means the instantaneous total outflux through the two surfaces is linearly related to the instantaneous detrapping (dissociation) and retrapping rates. Therefore, by measuring the total outflux (i.e., desorption signal), one can easily obtain information about the detrapping and retrapping kinetics inside the sample.

It has been reported that the interaction (detrapping and retrapping) between inert gas atoms and microstructural defects generally obeys the first order chemical reaction model, i.e.,

$$\frac{\partial}{\partial t} C_{detrapp}^i = (C_0^i - C_{detrapp}^i) v_i \exp\left(-\frac{E^{D,i}}{k_B T}\right), \quad (5)$$

where  $E^{D,i}$  is the activation energy for the detrapping (dissociation) from the  $i$ th trap type. Then we expect to be able to derive the activation energies  $E^{D,i}$ , as well as the initial concentration  $C_0^i$  and the attempt frequency  $v_i$  of various traps (defects) from desorption signals.

However, as we see from Eq. (4), the measured desorption signals from THDS experiments may have contributions from both detrapping and retrapping, which can make the data analysis very difficult since, with strong interference of retrapping, some of the detrapping events will not be detected at all. Therefore, in order to extract the kinetic parameters more reliably and easily, we shall minimize the probability of retrapping of the detrapped helium atoms before they diffuse to the surfaces. This can be done by lowering the implantation energy which simultaneously has two positive effects: reducing the penetration

depth of helium (so that the diffusion path across the damaged layer is shorter) and reducing the amount of damage (so that the number of potential retrapping sites is lower).

## Results and Discussion

### TRIM/SRIM calculations

TRIM (SRIM 2003) software [23] was used to calculate the damage and helium concentration profiles with respect to depth for 5, 20, and 100 keV (as shown in Fig. 2, from left to right) helium implantations in iron at a common fluence of  $1 \times 10^{15}$  He/cm<sup>2</sup>. Helium peak concentration depth is determined to be 26, 96, 335 nm, respectively, in the order of increasing implantation energy. The number of vacancies created per helium is 20, 50, and 87. It is clear that as the implantation energy increases the penetration depth of helium and the average damage produced per helium both increase. For the reasons discussed earlier, we shall expect less interference of retrapping with our desorption signals.

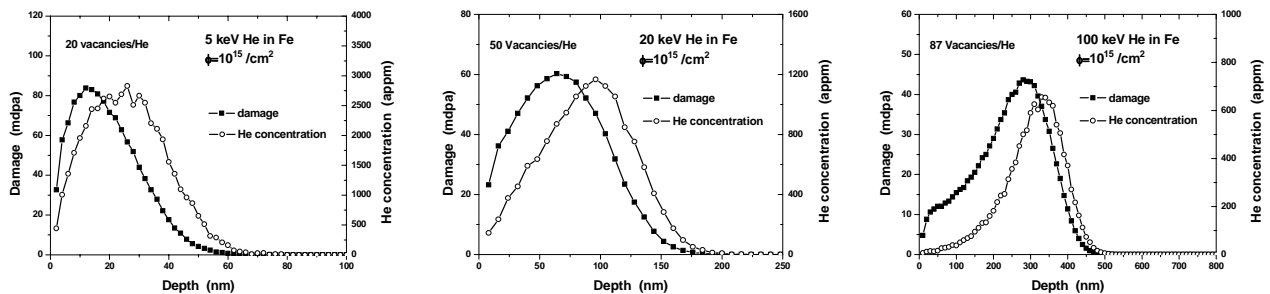


Fig. 2. (from left to right) Damage and helium concentration vs. depth for 5, 20, and 100 keV helium implantations in iron. The fluence used is  $1 \times 10^{15}$  He/cm<sup>2</sup> for all the three energies.

Based on the calculation and previous experience that signals from a sample with a fluence below  $1 \times 10^{13}$  He/cm<sup>2</sup> might be too difficult to measure using our system, we have performed new implantations with 9 new combinations of energy and fluence: 5, 10, and 20 keV for energy vs.  $1 \times 10^{13}$ ,  $1 \times 10^{14}$ , and  $1 \times 10^{15}$  He/cm<sup>2</sup> for fluence. At present, we have performed measurements and data analysis on some of the newly implanted samples, while the rest of the new samples will be studied soon.

### 100 keV and $1 \times 10^{15}$ He/cm<sup>2</sup> helium implanted iron

We shall briefly recall some of the THDS signals presented in the last report [21]. Figure 3 (left) shows the helium signal measured by the mass spectrometer from a 100 keV and  $1 \times 10^{15}$  ion/cm<sup>2</sup> helium implanted iron, and shows certain 'spurious peaks' (marked by the oval in the figure). They are considered not real desorption peaks of implanted helium but 'spurious peaks' based on two facts: (1) these peaks not only appeared in the He channel but also in other channels such as the N<sub>2</sub> channel as well as in the total pressure (2) these peaks were also observed even during an experiment on a non-implanted iron (shown in Fig. 3 right).

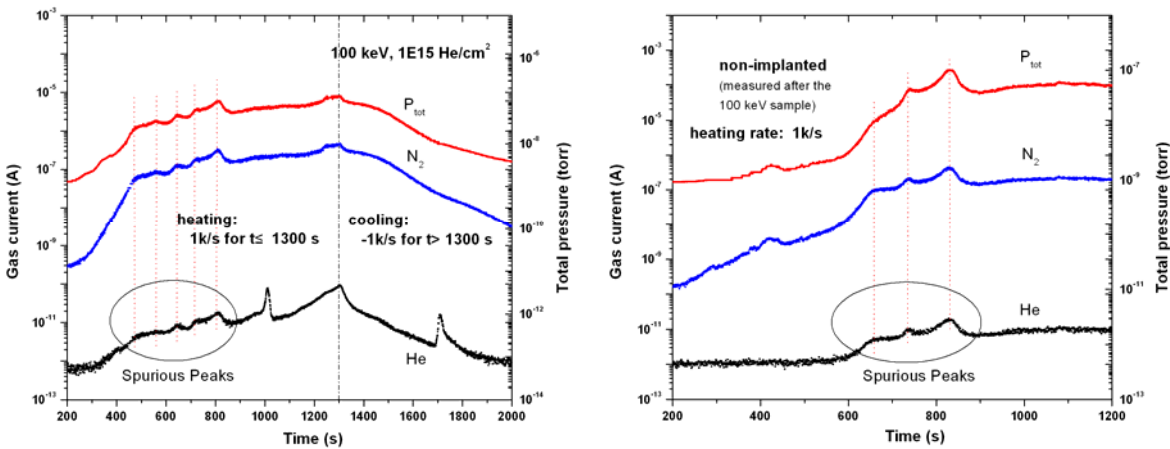


Fig. 3. Left: total pressure (measured by an ion gauge) and  $N_2$  and He gas current (measured by a mass spectrometer) recorded during a THDS experiment on an iron sample implanted with 100 keV helium ion to a fluence of  $1 \times 10^{15}$  He/cm<sup>2</sup>; right: total pressure and  $N_2$  and He gas current recorded during a THDS experiment on non-implanted iron following the experiment shown on the left.

Besides these obvious ‘spurious peaks’, there is essentially no real desorption signal from the 100 keV and  $1 \times 10^{15}$  He/cm<sup>2</sup> sample that can be clearly identified below 912°C—the ideal transition temperature between alpha (bcc) and gamma (fcc) iron. Above 912°C and during subsequent cooling, as we discussed in the Introduction, certain major events distinguish the He channel from other channels (as well as distinguishing the implanted sample from the non-implanted sample) and thus should be considered as real desorption signals of implanted helium.

#### 5 keV and $1 \times 10^{15}$ He/cm<sup>2</sup> helium implanted iron

Figure 4 (left) shows the signals recorded during a similar THDS experiment on a newly implanted 5 keV and  $1 \times 10^{15}$  He/cm<sup>2</sup> sample. The thermal scheme used was 1k/s heating up to 1330°C followed by 1k/s cooling immediately after. In the high temperature (above 912°C) regime during heating as well as in the cooling process, we see clearly different features in the He channel than in other channels, as for the case of the previous 100 keV and  $1 \times 10^{15}$  He/cm<sup>2</sup> sample. Therefore, we consider these high temperature helium signals are at least mostly, if not all, real desorption signals. However, two noticeable differences between the 5 keV sample and the 100 keV sample in this regime should be pointed out: (1) the He desorption rate already starts to drop after 1274°C (before cooling starts) for the 5 keV sample while it is still increasing at 1300°C where cooling starts for the 100 keV sample and (2) the relative intensity and thus the integrated area underneath (corresponding to the number of desorbed helium in an event) of the sharp peak around 1000-1080°C with respect to those of the even higher temperature (>1100°C) signal are larger for the 5 keV than for the 100 keV sample.

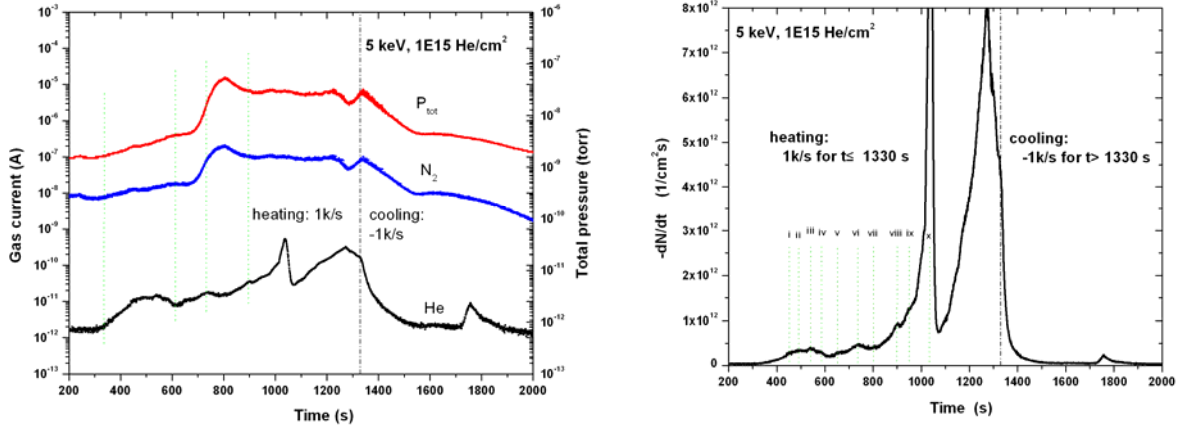


Fig. 4. Left: total pressure and  $N_2$  and He gas current recorded during a THDS experiment on a 5keV and  $1 \times 10^{15}$  He/cm<sup>2</sup> implanted iron; Right: linearly scaled desorption rate of the 5keV and  $1 \times 10^{15}$  He/cm<sup>2</sup> sample converted from the He gas current shown on the left.

In the low temperature (below 912°C) regime during heating, we can also identify a series of small peaks on the helium signal recorded for the 5 keV sample. But what makes the 5 keV sample different from the previous 100 keV sample in this regime is that these small peaks for the new sample only appeared in the helium channel but not in other channels or in system pressure. Therefore, we consider these low temperature peaks for the 5 keV sample as real desorption signals of implanted helium.

The right of Fig. 4 shows the converted desorption rate of helium from the 5keV and  $1 \times 10^{15}$  He/cm<sup>2</sup> sample with 10 peaks denoted, including the sharp peak above 1000°C. Since most of the present simulation of helium behavior has been performed in bcc iron, and because of the unknown complexities following the bcc to fcc structural transition, we are most interested in analyzing the low temperature signals than the high temperature ones.

Since previous studies (e.g., [24]) have shown that inert gas dissociation from traps generally follows the first order reaction kinetic model, we can first base our data analysis on this assumption. In the model, the desorption rate (in terms of number per unit time) is proportional to the remaining number of helium atoms in the particular type of traps, i.e.,

$$dN/dt = -K_0 \exp(-Q/K_B T) * N, \quad (6)$$

where  $K_0$  is the attempt frequency, usually on the order of  $10^{13}$  /s,  $K_B$  is the Boltzmann constant, Q is the activation energy for the given type of traps. In comparison with Eqs. (4) and (5), Eq. (6) is actually a spatially integrated form of the concentration-represented version of the model. The temporal integration of Eq. (6) then gives,

$$N = N_0 \exp\left[-\int_0^t K_0 \exp(-Q/K_B T) dt\right]. \quad (7)$$

By virtue of Eq. (6) and Eq. (7), using three parameters, namely,  $K_0$ , Q, and  $N_0$  for each of the identifiable desorption events, and summing all the individual desorption rates up, one can in principle fit the measured desorption rate numerically and thus determine the best values of the parameters for each individual event.

To facilitate the data fitting, we shall make initial estimates for the parameters for each event. The first step is to identify the peak positions  $T_p$  (as denoted on the right of Fig. 4). Second, we calculate  $Q$  according to the following equation

$$\ln(\beta / T_p^2) = -Q / K_B T_p + \ln(K_0 K_B / Q), \quad (8)$$

which is derived by solving the equation  $d^2 N / dt^2 = 0$  under the constant rate ramping condition (i.e.,  $dT / dt = \beta$ ) (note that we seemingly need to know  $K_0$  in order to calculate  $Q$ , however, the dependence of  $Q$  on  $K_0$  is actually fairly weak around  $K_0 = 10^{13}$  /s; hence we can first estimate  $Q$  using this particular value of  $K_0$ ). Third, the initial number of atoms  $N_0$  can be estimated from the peak height (matching the calculated and the experimental heights for each peak).

Figure 5 displays the experimentally measured and numerically simulated (according to first order reaction model) helium desorption rates together with the individual desorption events/components. The agreement between the measured and the simulated desorption rates is excellent up to  $\sim 1000^\circ\text{C}$  where the non-1<sup>st</sup>-order sharp signal starts to dominate. The fitting-optimized activation energies  $Q$  for the individual events are listed in Table 1, together with the corresponding  $Q_{\text{corr}}$  values which were calculated from Eq. (8) using corrected peak positions. The correction to the peak positions will be explained later.

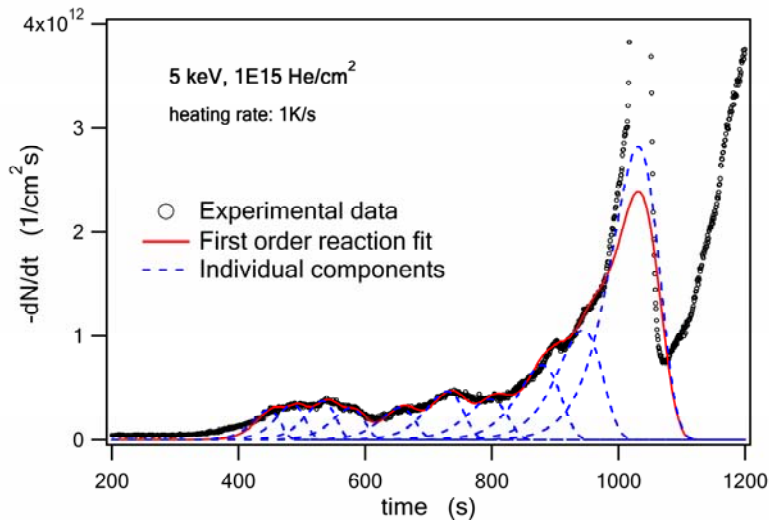


Fig. 5. Experimentally measured (circles) and numerically simulated (according to first order reaction model) (red solid line) helium desorption rates together with the individual desorption events (blue dashed line).

Table 1. Activation energies  $Q$  determined through curve fitting, and  $Q_{\text{corr}}$  calculated from Eq. (8) using peak positions corrected according to alpha to gamma transition temperature, for the 5 keV and  $1 \times 10^{15}$  He/cm<sup>2</sup> iron.

	I	II	III	IV	V	VI	VII	VIII	IX	X
$Q$ (eV)	2.1	2.2	2.3	2.5	2.7	2.9	3.1	3.4	3.5	3.7
$Q_{\text{corr}}$ (eV)	1.85	1.9	2.1	2.2	2.4	2.7	2.9	3.2	3.3	3.5

### 20 keV and $1 \times 10^{15}$ He/cm<sup>2</sup> helium implanted iron

We have also measured and analyzed 20 keV and  $1 \times 10^{15}$  ion/cm<sup>2</sup> helium implanted iron. Shown on the left of Fig. 6 are the recorded total pressure and N<sub>2</sub> and He gas current during the experiment using the same thermal cycling scheme as for the 5 keV and  $1 \times 10^{15}$  ion/cm<sup>2</sup> sample.

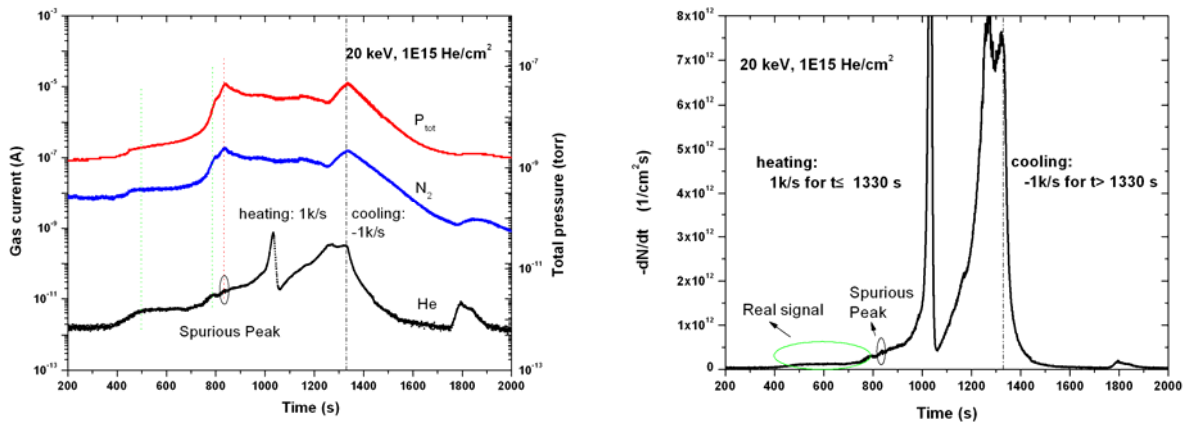


Fig. 6. Left: total pressure and N<sub>2</sub> and He gas current recorded during a THDS experiment on a 20keV and  $1 \times 10^{15}$  He/cm<sup>2</sup> implanted iron; Right: linearly scaled desorption rate of the 20keV and  $1 \times 10^{15}$  He/cm<sup>2</sup> sample converted from the He current shown on the left.

In the high temperature regime (above 912°C) during heating and during cooling, we again see the helium signal distinct from N<sub>2</sub> or system pressure indicating that the helium signal in this regime is mostly a real desorption signal from implanted helium. Comparing with the high temperature helium signal from the 100 keV sample, we can still see the two differences we pointed out earlier when we compared the 5 keV sample with 100 keV sample, although they are more subtle here.

In the low temperature regime (below 912°C) during heating, we see (Fig. 6, left) an initial rise in helium signal at ~390°C followed by a plateau extending from ~500°C to ~680°C after which a few small peaks can be identified. Although there are also an initial rise and a plateau in N<sub>2</sub> channel and the system pressure, the positions of the rising and leveling-off points are clearly different from those for the helium signal. Thus we can also consider the helium signal of the 20 keV sample in this regime mostly a real desorption signal with only one peak possibly being spurious as marked out with the vertical oval in Fig. 6.

Since it is not easy to clearly identify individual peak positions from the measured desorption signal of the 20 keV sample, we choose to start with the peak positions and activation energies previously obtained from the 5 keV sample. It appears, as shown in Fig. 7, that with the same number of component events we can only get a fair agreement between the simulated and the measured signal for the 20 keV sample. More specifically, there are always a few separated intervals on the simulated curve for this 20 keV sample, including one near the marked 'spurious peak,' that cannot match the measured signal well.

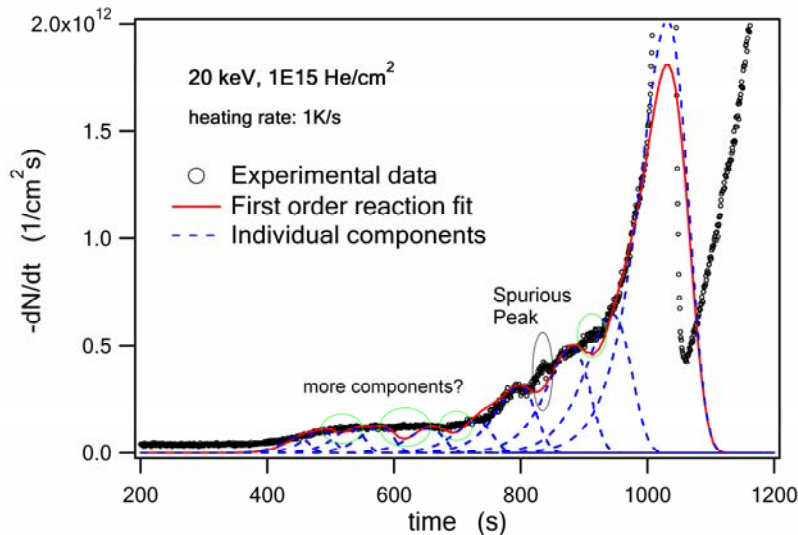


Fig. 7. Experimentally measured (circles) and numerically simulated (according to first order reaction model) (red solid line) helium desorption rates together with the individual desorption events (blue dashed line).

There are several explanations that might be possible for this non-perfect fitting of the 20 keV sample. First, the easiest explanation would be that there are more individual desorption events involved in the 20 keV sample than in the 5 keV sample. If we add in a few more individual events in our simulation, we can certainly improve the quality of the matching. Second, it may be possible that there is more contribution from spurious signal than what we have recognized. Third, but not least probable, there may be non-negligible retrapping encountered by some desorbed helium before they could reach the surfaces. One might be tempted to rule out the retrapping from possible explanations upon noticing that the simulated signal shown in Fig. 7 is actually lower than the measured signal at the mismatched spots. However it should be clarified that the relative height of the simulated and the measured signals may be reversed at mismatched spots if we change the values of initial number of atoms  $N_0$  of the relevant components. Further investigations are required to understand this result.

#### Source of Non-1<sup>st</sup>-order Sharp Peak

We have seen a very similar sharp peak around 1020°C on each of the signals recorded from the 5, 20, and 100 keV helium implanted iron samples. In the previous report [21] we have left this question unanswered: what is the source of the non-1<sup>st</sup>-order sharp peak? Putting together all the observations and analysis results, including those presented in the last report, we now believe that this sharp peak, or, more appropriately, the irregularly rapid release of helium, is due to the alpha  $\leftrightarrow$  gamma structural phase transition.

First, the repetitive appearance of this sharp peak during heating and cooling and subsequent re-heating and re-cooling (if all the implanted helium is not completely desorbed during the first cycle) resembles the reversibility of the alpha  $\leftrightarrow$  gamma phase transition very well. In fact, without the reversible phase transition, we can only expect a monotonically decreasing desorption rate without any peak during cooling process since both the reaction constant  $K_0 \exp(-Q/K_B T)$  and the remaining number to be desorbed  $N$  in the rate equations of any order (for 1<sup>st</sup> order, see Eq. (6); for  $n$ th order, replace the  $N$  in Eq. (6) with  $N^n$ ) decrease as temperature decreases.

Second, we have shown in the previous report that the peak sharpness can be very well reproduced using a Johnson-Mehl-Avrami kinetic model [25,26]. Considering that the JMA model is primarily applied to phase transitions, this in fact provides additional supportive evidence for the above claim. It should be pointed out that the JMA model is limited to diffusional phase transitions proceeding by nucleation and

growth and thus it can not describe diffusionless martensitic phase transitions which are often encountered in iron or ferritic alloys. However, the martensitic phase transition can occur in elemental iron only at extremely high ramping rates on the order of  $10^4$  K/s [27], far above the rates used in our studies. It should be mentioned that Sugano et al. [28] and Ono et al. [29] have also reported recently the observation of the non-1<sup>st</sup>-order rapid release signals from iron and certain ferritic alloys and attributed them to phase transitions, although they did not perform cooling or re-cycling studies or JMA analysis.

Having concluded that the sharp peak is due to the  $\alpha \leftrightarrow \gamma$  phase transition, we can then use this characteristic peak to calibrate our temperature readings at different ramping rates, and this approach is currently being carried out. For each of the interested heating rates, we measure the peak transition temperature using an accurate differential scanning calorimetry (DSC) facility and then compare with the measured temperature using our THDS system. An additional standard point for calibration,  $577^\circ\text{C}$ , can be obtained by using an Al-film-on-Si-wafer eutectic reaction method.

While the calibration has not been completed at present, we have made a rough estimate for the effect of correcting temperature readings on the derived activation energies. Table 1 also lists the corrected values,  $Q_{\text{corr}}$ , of individual activation energies for the  $5 \text{ keV}$  and  $1 \times 10^{15} \text{ He/cm}^2$  sample. The  $Q_{\text{corr}}$  values were calculated from Eq. (8) using corrected peak positions. The correction to the peak positions is performed by simply subtracting  $81^\circ\text{C}$  from the fitting-derived values. This  $81^\circ\text{C}$  subtraction is based on the assumption that the sharp peak temperature measured as  $993^\circ\text{C}$  during a heating ramp at  $0.5 \text{ K/s}$  corresponds to the literature value of the  $\alpha \leftrightarrow \gamma$  iron phase transition point at  $912^\circ\text{C}$ . Even though this is apparently an overcorrection, it turns out that the activation energies are changed by only  $0.2$  or  $0.3 \text{ eV}$ .

#### Source of spurious peaks

It should be pointed out that all of the above experiments were performed with the sample/crucible, the filament and the thermocouple being surrounded by a molybdenum thermal shield. During a more recent experiment on a non-implanted iron sample without the presence of the thermal shield, we have observed a significant reduction in the magnitude and curvature of the total pressure as shown in Fig. 8. The He signal became quite flat with no identifiable spurious peaks until the temperature was so high as to counteract the cooling of the chamber wall (realized by flowing liquid nitrogen inside) and to begin desorbing physically-adsorbed molecular species off of the chamber wall. Meanwhile, a spurious peak still can be recognized on the total pressure and other gas signals at a common temperature.

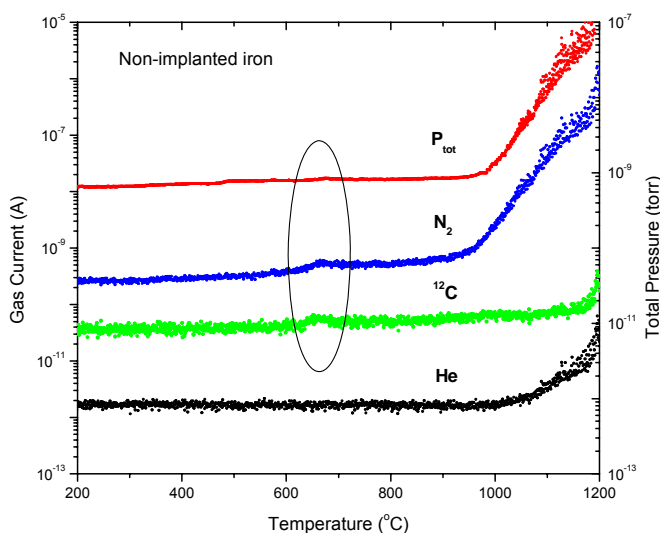


Fig. 8. Signals recorded during an experiment on a non-implanted iron sample without the presence of thermal shield.

It appears that both the old thermal shield and the samples themselves were responsible for the appearance of the spurious peaks on He signal in previous experiments. The sample surfaces always contain physically adsorbed molecular gas species while being exposed in the open atmosphere. These molecular species can then desorb at certain temperatures and, depending on the total pressure in the system, can or can not produce spurious peaks in the helium signal. With the old thermal shield, the total pressure was quite high and consequently, the helium signal was influenced by the desorption of other species from the sample surfaces.

However, performing experiments without a thermal shield may cause other problems, e.g., non-uniform temperature distribution around the sample/crucible, and over-heating of the chamber wall. We have observed some inconsistency in temperature readings while experimenting without the shield which may be caused by large temperature gradient around the thermocouple junction. In order to get a reliable reading, the measurement junction of a thermocouple and the portion of its wires close to the junction should normally be kept at a uniform temperature field. Therefore, instead of experimenting without a shield, it may be better to replace the old shield with a new and clean one. Efforts to improve the signal to noise ratio and to reduce the number of spurious desorption events will continue.

## Conclusions

Following our previous report, we have performed new implantations at energies lower than 100 keV. Initial measurements on the new samples have revealed a large number of desorption peaks within both bcc and fcc Fe temperature ranges. The peaks in the bcc range are generally well fit with first order reaction kinetics which discloses a series of activation energies ranging from ~1.9 to ~3.5 eV. The number and the relative intensities of detected desorption peaks within the bcc temperature range appear to increase with decreasing implantation energy. The non-1<sup>st</sup>-order sharp peaks previously reported for 100 keV and  $1 \times 10^{15}$  He/cm<sup>2</sup> and also observed for the 5 keV and  $1 \times 10^{15}$  ion/cm<sup>2</sup> and 20 keV and  $1 \times 10^{15}$  ion/cm<sup>2</sup> implanted iron have been attributed to the alpha ↔ gamma phase transition. Causes for the spurious peaks reported previously are also now better understood.

## Acknowledgements

This work has been supported by the Office of Fusion Energy Sciences, U.S. Department of Energy, under Grant DE-FG02-04ER54750.

## References

- [1] L. K. Mansur and W. A. Coghlan, J. Nucl. Mater. 119 (1983) 1.
- [2] H. Ullmaier, Nucl. Fusion 24 (1984) 1039.
- [3] L. K. Mansur and M. L. Grossbeck, J. Nucl. Mater. 155 (1988) 130.
- [4] H. Trinkaus and B. N. Singh, J. Nucl. Mater. 323 (2003) 229.
- [5] I. Mori, T. Morimoto, R. Kawakami, and K. Tominaga, Nucl. Instrum. Methods Phys. Res. Sect. B 153 (1999) 126.
- [6] A. A. Selezenev, V. G. Golubev, and N. S. Ganchuk, Chem. Phys. Rep. 17 (1998) 295.
- [7] K. Morishita, R. Sugano, B. D. Wirth, and T. D. de la Rubia, Nucl. Instrum. Methods Phys. Res. Sect. B 202 (2003) 76.
- [8] B. D. Wirth et al., J. Nucl. Mater. 329–333 (2004) 103.
- [9] L. Ventelon, B. D. Wirth, and C. Domain, J. Nucl. Mater. 351 (2006) 119.
- [10] C. C. Fu and F. Willaime, Phys. Rev. B 72 (2005) 064117.
- [11] F. v.d. Berg, W. V. Heugten, L. M. Caspers, and A. V. Veen, Solid State Commun. 24 (1977) 193.
- [12] H. L. Heinisch, F. Gao, R. J. Kurtz, and E. A. Le, J. Nucl. Mater. 351 (2006) 141.
- [13] R. J. Kurtz and H. L. Heinisch, J. Nucl. Mater. 329 (2004) 1199.
- [14] F. Gao, H. Heinisch, and R. J. Kurtz, J. Nucl. Mater. 351 (2006) 133.
- [15] M. B. Lewis and K. Farrell, Nucl. Instrum. Methods Phys. Res. Sect. B 16 (1986) 163.
- [16] K. Arakawa, R. Imamura, K. Ohota, and K. Ono, J. Appl. Phys. 89 (2001) 4752.

- [17] T. Ishizaki, Q. Xu, T. Yoshiie, and S. Nagata, *Mater. Trans.* 45 (2004) 9.
- [18] T. Iwai, Y. Ito, and M. Koshimizu, *J. Nucl. Mater.* 329 (2004) 963.
- [19] R. Sugano, K. Morishita, A. Kimura, H. Iwakiri, and N. Yoshida, *J. Nucl. Mater.* 329 (2004) 942.
- [20] R. Vassen, H. Trinkaus, and P. Jung, *Phys. Rev. B* 44 (1991) 4206.
- [21] D. Xu, T. Bus, S. C. Glade, and B. D. Wirth, *Fusion Materials Semiannual Progress Report DOE/ER-0313/39* (2005) 151.
- [22] S. C. Glade, B. D. Wirth, and H. Schut, *Fusion Materials Semiannual Progress Report DOE/ER-0313/37* (2004) 136.
- [23] J. F. Ziegler, J. P. Biersack, and U. Littmark, *The Stopping and Range of Ions in Matter* (Pergamon, New York, 1984).
- [24] A. van Veen, A. Warnaar, and L. M. Caspers, *Vacuum* 30 (1980) 109.
- [25] W. A. Johnson and R. F. Mehl, *Trans. Am. Inst. Min. Metall. Engs.* 135 (1939) 416.
- [26] M. Avrami, *J. Chem. Phys.* 7 (1939) 1103.
- [27] *ASM Handbook*, ASM International, Vol. 9 (2004) 148.
- [28] R. Sugano, K. Morishita, and A. Kimura, *Fusion Sci. Technol.* 44 (2003) 446.
- [29] K. Ono, K. Arakawa, H. Shibasaki, H. Kurata, I. Nakamichi, and N. Yoshida, *J. Nucl. Mater.* 329–333 (2004) 933.

**HELIUM IN IRRADIATED IRON: A MULTI-SCALE STUDY**—T. Seletskaya, Yu. N. Osetsky, R. E. Stoller, and G. M. Stocks (Oak Ridge National Laboratory)

## OBJECTIVE

A new empirical He-Fe potential was obtained by fitting to results obtained from first principles calculations. Both the formation and relaxation energies of single He defects and small He clusters were accounted for in the fitting process. The new potential consists of a repulsive pair-potential term and a three-body interaction term and was applied in combination with three commonly-used iron interatomic potentials (Finnis-Sinclair, Ackland, Mendeleev et al.) and a potential for helium in vacuum by Aziz et al. As an application of the new potential, we evaluated the stability of He-vacancy clusters at zero temperature. The calculated results were similar for all three Fe-Fe potentials. The results obtained with the new potential are consistent with *ab initio* calculations as well as experimental observations of helium desorption reported in the literature.

## SUMMARY

Helium is produced in neutron-irradiated metals as the result of  $(n, \alpha)$  transmutation reactions and plays a significant role in microstructure evolution and mechanical properties degradation [1,2]. Due to helium's high mobility via an interstitial migration mechanism and its strong binding with vacancies, information on its atomistic behavior is hard to assess from experiments. The only way to obtain such information is from first-principles electronic structure calculations. However, electronic structure calculations can not be used on the time and size scales needed to simulate the important evolution of helium-vacancy clusters that ultimately leads to bubble formation. A multi-scale approach, based on constructing an empirical potential and employing this potential in classical molecular dynamics, seems to be the only practical approach currently available to study He behavior in metals on the desired scale.

The only previous attempt to construct empirical potentials for He in iron resulted in an Fe-He potential obtained by Wilson [3] in the late 1960s. The potential was defined as a pairwise interaction energy for a Fe-He<sup>0</sup> dimer completely ignoring bulk properties of the metal matrix. The latter makes it inappropriate for simulating energy and dynamic properties of He defects in the iron matrix. Electronic structure calculations [4,5] have demonstrated that the Wilson potential predicts the wrong site preference for the He interstitial defect and significantly overestimates the binding energy of one He atom with a vacancy. A pair potential model is not suitable for Fe-He interaction in general because there a pair potential can not accurately describe both the forces and formation energies of He defects [6]. Fe-He interaction originates by electronic hybridization between Fe  $d$ - and He  $s$ - electrons. The hybridization is strong enough to change the magnetic moment of He iron neighbors [4] telling us about the complexity of the potential.

In our previous work [7], we presented a Fe-He empirical potential fitted to first-principles results with the high accuracy. The potential consisted of a pair potential part and an embedded energy. The later modifies He-He interaction and makes the potential inapplicable to the problems considering a low density He gas inside the iron void. In this case, He gas is expected to have its vacuum properties. Here we introduce a different model that does not have this deficiency. The form of the potential was inferred from the electronic structure calculations. The potential was used to study He-vacancy cluster stability at zero temperature using the classical molecular statics (MS) technique.

## Methodology

In our empirical model of a Fe-He system consisting of  $I_{Fe}$  iron atoms and  $I_{He}$  helium atoms, we have chosen the following functional form for the total energy:

$$E = \sum_{i \in I_{Fe}} \Phi_{Fe}(\rho_i) + \sum_{\substack{i \in I_{Fe} \\ j \neq i, j \in I_{Fe}}} \varphi_{FeFe}(r_{ij}) + \sum_{\substack{i \in I_{He} \\ j \in I_{Fe}}} \varphi_{HeHe}(r_{ij}) + \sum_{\substack{i \in I_{He} \\ j \neq i, j \in I_{He}}} \varphi_{FeHe}(r_{ij}) \quad (1)$$

$$+ \sum_{\substack{i \in I_{He} \\ j \in I_{Fe} \\ k \neq j, k \in I_{Fe}}} Y_{He}(r_{ij}, r_{ik}, \Theta_{jik})$$

where the first two terms describe Fe-Fe interaction; the third and the fourth terms represent a He-He and a Fe-He pair potentials, respectively; and the fifth term introduces a Fe-He three-body interaction. In our calculations we included three potentials describing the Fe-Fe interaction, *viz.*, those by Finnis and Sinclair [8], Ackland [9], and Ackland et al. [10] based on the work of Mendeleev et al. [11]. All Fe-Fe potentials have a many-body term as described by the first term in Eq. 1 which depends on the atomic density  $\rho_i$  and a repulsive pair potential, given by the second term as function of the interatomic distance  $r_{ij}$ . The discrepancies between *ab initio* calculations and the empirical potentials for pure iron were reduced according to [7]. For He-He interaction term, we use a He-He vacuum pair potential of Aziz et al. (1995) [12].

The empirical Fe-He potential consisting of a pair potential term,  $\varphi_{FeHe}(r_{ij})$ , and a three-body term,  $Y_{He}(r_{ij}, r_{ik}, \Theta_{jik})$ , was obtained by fitting the results of first-principles calculations. The calculations were performed using the Vienna *ab initio* simulation package (VASP) as described in previous publications [4,7]. Our objective was to fit formation and relaxation energies of the single He defect and small He clusters. Interstitial He in both the octahedral and tetrahedral positions and the substitutional He defect (He octa, He tetra, and He sub) [4] were evaluated. He clustering behavior was investigated for both interstitial and vacancy-type defects. These included a He di-interstitial and clusters with two and three He atoms located inside one vacancy (2He, 2He-vac, and 3He-vac) [7].

The long-range part of the pair potential was fitted first using a simple and relatively flexible mathematical form:

$$\varphi_{FeHe}(r_{ij}) = p_1 \left(1 - p_2 \left(\frac{r_{ij}}{p_3} - 1\right)\right) e^{-p_4 \left(\frac{r_{ij}}{p_3} - 1\right)} \cdot f_{cut}(r_{ij}), \quad (2)$$

where  $f_{cut}(r_b, r_c, r_{ij})$  is a cutoff function whose first and second derivatives vanish when  $r_{ij}=r_b$  and  $r_{ij}=r_c$ :

$$f_{cut}(r_{ij}) = (1-x)^3(1+3x+6x^2), \text{ where } x = \frac{r_{ij}-r_b}{r_c-r_b}. \quad (3)$$

For  $r_{ij} < r_b$ ,  $x=0$ , and for  $r_{ij} > r_c$ ,  $x=1$ .  $\varphi_{FeHe}(r_{ij})$  has three fitting parameters ( $p_1$ ,  $p_2$ , and  $p_4$ ) since  $p_3$  is simply a scaling factor.

The parameters were obtained using a least-squares method. Since the three-body interaction is acting only in the interstitial region, the parameters of the pair potential were fitted to the formation energies of He substitutional defect and the formation energies of 2 and 3 He atoms in a vacancy. The smallest Fe-He separation in these configurations is equal to 1.68 Å. Initial guesses for the potential parameters  $\{p_i\}$  were used to estimate the sum of squared differences. The minimization of the sum of squared differences was performed by the conjugate-gradient method. However, this procedure does not

guarantee zero forces for the relaxed configurations. Therefore, the obtained potential was used to relax the above configurations by classical MS in a 128-atom supercell as was used in VASP calculations [4,9]. Then the parameters  $\{p_j\}$  were varied and relaxation repeated until the minimum sum of squared differences between *ab initio* and MS simulations was reached.

The derived pair potential reproduced He behavior in vacuum but strongly underestimated the formation energies of He interstitials. To fit the energies of the interstitial, we used an exponential function for interatomic distances less than 1.6 Å and a simple polynomial to smoothly join this function with the long-range part of the pair-potential. As a result, the pair-potential is written:

$$\varphi_{FeHe}(r_{ij}) = \begin{cases} \exp(b_1 + b_2x + b_3x^2 + b_4x^3 + b_5x^4), & r_{ij} < 1.6\text{Å} \\ a_1 + a_2x + a_3x^2 + a_4x^3 + a_5x^4 + a_6x^5, & 1.6\text{Å} \leq r_{ij} < 2.2\text{Å} \\ \varphi(r_{ij}), & 2.2\text{Å} \leq r_{ij} < 4.4\text{Å} \end{cases} \quad (4)$$

where  $\varphi(r_{ij})$  is given by Eq. 2. The parameters of the potential are given in the Table 1.

Table 1. Parameters for pair potential given by Eq. 2 and 5

$b_1 = -2.142600207811$	$a_1 = -285.7450302953, \text{ eV}$	$p_1 = 0.167753, \text{ eV}$
$b_2 = 32.965470333178, \text{ Å}^{-1}$	$a_2 = 794.5913355517, \text{ eVÅ}^{-1}$	$p_2 = 0.000000$
$b_3 = -52.893449935488, \text{ Å}^{-2}$	$a_3 = -856.9376372455, \text{ eVÅ}^{-2}$	$p_3 = 2.432258, \text{ Å}$
$b_4 = 30.970079966695, \text{ Å}^{-3}$	$a_4 = 452.5323035795, \text{ eVÅ}^{-3}$	$p_4 = 3.727249$
$b_5 = -6.398785336260, \text{ Å}^{-4}$	$a_5 = -117.6519447529, \text{ eVÅ}^{-4}$	$r_b = 4.1, \text{ Å}$
	$a_6 = 12.0878858024, \text{ eVÅ}^{-5}$	$r_c = 4.4, \text{ Å}$

The three-body potential term was introduced to improve the fitting for the interstitial properties. It has the following form:

$$Y_{He}(r_{ij}, r_{ik}, \Theta_{jik}) = \sum_{\substack{j \in I_{Fe} \\ k \neq j, k \in I_{Fe}}} f^Y(r_{ij}) f^Y(r_{ik}) \cos^2(\Theta_{jik} - 0.44), \quad (5)$$

where the summation is performed over the Fe neighbors of He atom separated by the distances  $r_{ij}$  and  $r_{ich}$ , with the functions  $f^{eY}(r)$  representing the distance-dependence of the three-body potential and  $\Theta_{jik}$  is the angle between the radius-vectors  $r_{ij}$  and  $r_{ich}$  drawn from the He atom as the centre. To guarantee the preference for the tetrahedral site over the octahedral, we subtract an angle of 0.44 rad which is equal to the average angle formed by He-Fe vectors in the tetrahedral position minus  $\pi/2$ . The functions  $f^{eY}(r)$  in Eq. 5 are given by Eq. 3, with the right-hand side multiplied by the parameter  $a^{Ye}$ . The values of  $a^{Ye}$  and  $r_b^j$  were obtained from the fitting process; their values are  $0.7 \text{ eV}^{e/2}$  and  $1.75 \text{ Å}$ , respectively. The cutoff of the three-body energy,  $r_{eK}^e$ , was chosen to be  $2.2 \text{ Å}$ .

## Results

The results of the fitting procedure for a single He defect and small He clusters are presented in Table 2. It is clear that when the Fe-He potential is used in combination with different Fe-Fe potentials similar results are obtained for the He defects. Since the potential does not have a many-body part that is different in different Fe potentials, it automatically gives the same formation energies of He defects in unrelaxed structures. The relaxation of Fe atoms around a He defect depends on the stiffness of the Fe potential. Since all three empirical potentials used here were fitted to experimental elastic constants, they yield similar atomic relaxation around the He defect.

Table 2. Results of fitting He defect formation energies (eV) in Fe

Defect	VASP*	Fe-Fe potentials		
		Finnis-Sinclair	Ackland	Mendelev
Unrelaxed Structures				
He octa	6.37	6.40	6.40	6.55
He tetra	5.70	5.72	5.72	5.83
He sub	3.99	3.98	3.82	3.74
Relaxed Structures				
He octa	4.60	4.74	4.70	4.57
He tetra	4.36	4.37	4.33	4.26
He <sub>i-mid</sub>	4.42	4.40	4.37	4.29
He sub	3.73	3.82	3.70	3.75
He-He-vac	6.29	6.49	6.35	6.46
He-He-He-vac	9.09	9.39	9.23	9.37
He-He inter.	8.72	8.59	8.54	8.24

\*VASP results for He defects in a vacancy were scaled for the Ackland potential [7].

The formation energies are reproduced to within an accuracy of 0.2 eV. The tetrahedral He interstitial is the most stable in all of the iron matrices. Based on a comparison with the *ab initio* simulation of He migration by Fu and William [13], the new potential accurately describes He interstitial migration [13]. The He migration path from one tetrahedral position to another lies in a  $\langle 110 \rangle$  direction that does not pass through the octahedral site. The formation energy of a He interstitial at the midpoint of this migration path is denoted by He<sub>i-mid</sub> and is given in Table 2. The new potential somewhat underestimates the formation energy of a He di-interstitial, while overestimating its binding by about 0.2 eV. However, we believe that this inaccuracy for very closely spaced He atoms should have only a weak effect on its future application. Atomic helium clusters are unlikely to be created in significant numbers because He is easily trapped by vacancies. Overall the potential accurately describes the formation energies before and after relaxation which also indicates its good performance in describing Fe-He forces.

The new Fe-He potential was used to study the properties of He-vacancy clusters at 0 K. The dependence of the binding energy of additional He atoms to a He-vacancy cluster (substitutional He) and the binding energy of an Fe SIA to a He-di-vacancy cluster were investigated as a function of cluster size. The definitions of the binding energies are given in [7]. Periodic boundary conditions were applied to a cubic  $10a_0 \times 10a_0 \times 10a_0$  computational cell ( $a_0$  is bcc iron equilibrium lattice parameter). The atomic coordinates were relaxed using a conjugate-gradient method to zero force at constant volume. The results for He atom and Fe SIA binding are presented in Figs. 1(a) and (b), respectively, for simulations performed with the Ackland [9] and Mendelev [10] Fe potentials. The results are qualitatively the same with either iron matrix, with a strong atomic relaxation observed around the He-vacancy complex. The binding energies for small He-vacancy clusters calculated from first principles [7] are also shown in Fig. 1(a). The binding energies calculated with the new potential agree with *ab initio* calculations to within 0.25 eV. The binding energies obtained from Wilson's Fe-He pair potential [13] are also presented for comparison. Wilson's potential systematically overestimates the binding of a He atom to the He-vacancy cluster and underestimates the binding of an Fe SIA.

The binding energy of a He atom to the He-vacancy cluster does not exhibit a simple dependence on the number of He atoms. It initially decreases and then increases, with a local maximum when a total of six He atoms (five He bound to substitutional He) are involved. In this case, a compact He octahedron is formed with a vacant site at the center. For larger numbers of He atoms, the local dilatations produced by the He-vacancy complex are strong enough to begin displacing iron atoms at the periphery of the cluster.

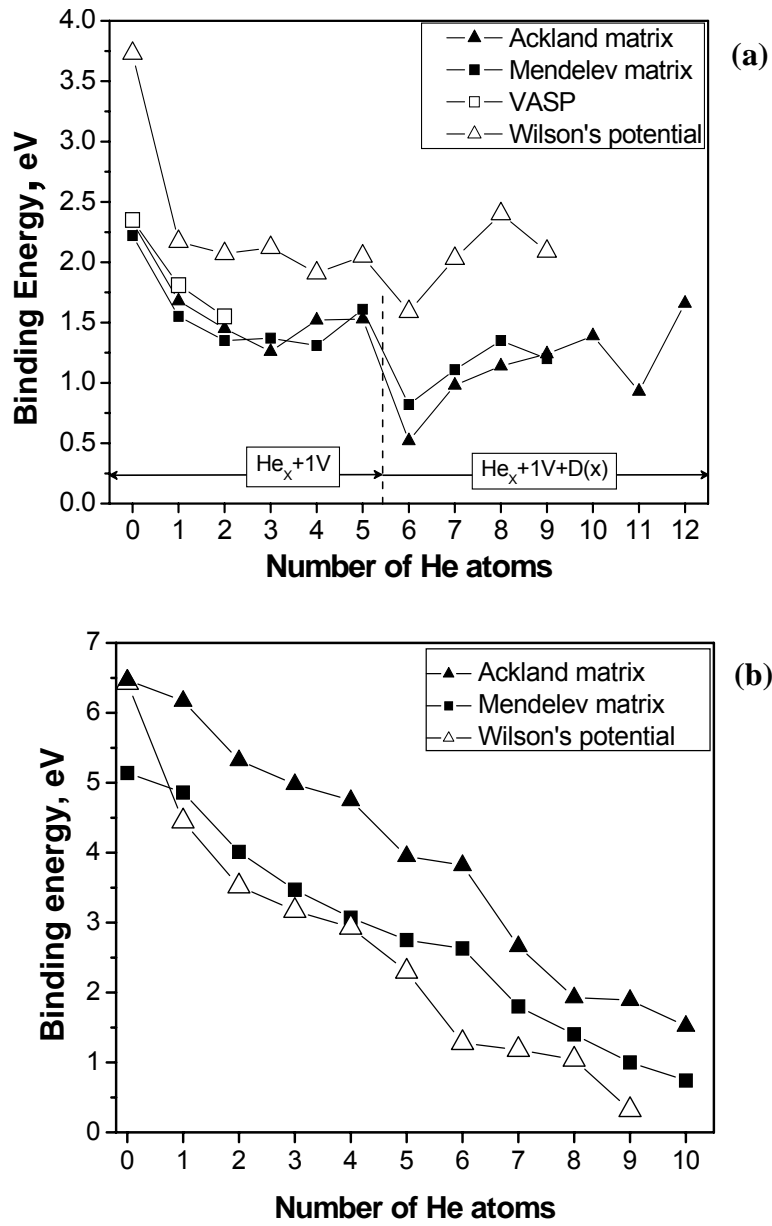


Fig. 1. Binding energy: (a) of He atom to a He-vacancy cluster and (b) an Fe SIA to a He-di-vacancy cluster versus the number of He atoms in the cluster.

This leads to the decrease in binding energy shown when the sixth He atom (a total of seven He) is added to the He-vacancy cluster. The notation  $D(x)$  in Fig. 1(a) is meant to indicate that significant matrix distortions occur for the larger He contents. An example of these distortions is shown in Fig. 2 for the case of 11 He atoms bound to the He-vacancy cluster. Eight Fe atoms are displaced by  $\sim 0.2 a_{\text{Fe}}$  in approximately  $\langle 110 \rangle$  directions to create the extra volume required to accommodate the He. These distributed displacements rather than true Frenkel pair were observed in all the static simulations, and the configuration shown in Fig. 2 suggests the possibility of directly producing Fe interstitial clusters (so-called loop punching) for clusters with greater He content. Dynamic simulations at finite temperature are required to determine if Frenkel pair or interstitial cluster formation is favored.

The strong He binding behavior contrasts with that of an Fe SIA. As shown in Fig. 1(b), the binding energy of an SIA to a He-di-vacancy cluster decreases continuously as the number of He atoms increases. The weaker SIA binding is ultimately a necessary condition for He bubble growth since it

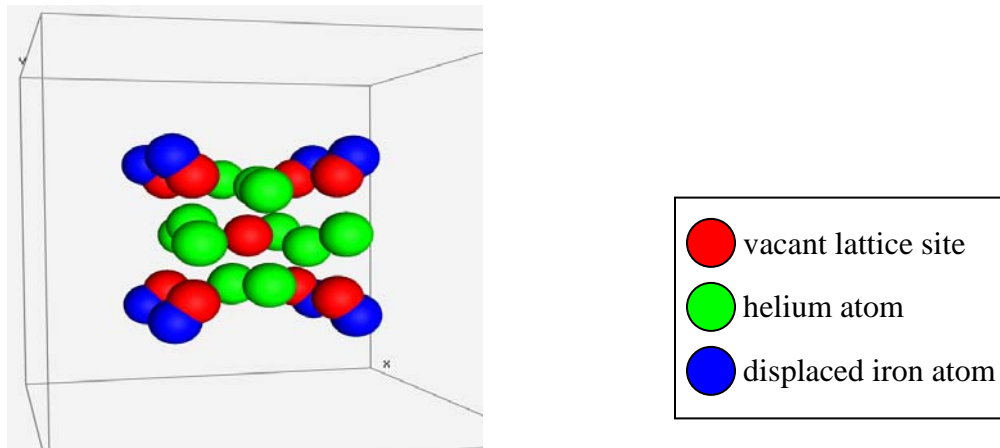


Fig. 2. He-vacancy cluster with a total of 12 He atoms. Initial, true vacancy is shown at center and dilatation-induced defects at the periphery.

favors He-vacancy agglomeration relative to SIA-vacancy recombination for larger He-vacancy clusters.

## Conclusions

A multi-scale approach has been applied to study He defect properties in iron. An empirical Fe-He potential, consisting of a pair potential and a three-body term, was fitted to *ab initio* data. When used in combination with different iron potentials, it accurately reproduces the energies of a single He defect and small He clusters. The potential was used to study the zero-temperature properties of helium-vacancy clusters. Depending on the size of the cluster, He atoms are bound with an energy that is generally greater than 1.0 eV, while the binding of a Fe self-interstitial to a He-di-vacancy cluster decreases continuously with increasing cluster size. Although the details of the He-vacancy configurations must be potential dependent to some degree in these static simulations, the physical mechanisms are believed to be accurately predicted. The Fe-He potential that has been developed represents a substantial improvement over currently-available pair potentials, is relatively simple, and can be efficiently applied in large-scale molecular dynamics simulations.

## Acknowledgements

This research was sponsored in part by the Materials Science and Technology Division (Seletskaya, Osetsky, and Stocks).

## References

- [1] R. E. Stoller, J. Nucl. Mater. 174 (1990) 289–310.
- [2] R. Vassen, H. Trinkaus, and P. Jung, Phys. Rev. B 44 (1991) 4206–4213.
- [3] W. D. Wilson, in Conference on Fundamental Aspects of Radiation Damage in Metals, Eds., F. W. Young and M. T. Robinson, USERDA-CONF-751006-P2 (1975) 1025.
- [4] T. Seletskaya, Yu. N. Osetsky, R. E. Stoller, and G. M. Stocks, Phys. Rev. Lett. 94 (2005) 046403.
- [5] C. C. Fu and F. Willaime, presented at TMS Symposium on Microstructural Processes in Irradiated Materials, February 14–17, 2005, San Francisco, Journal of Nuclear Materials (in press).
- [6] T. Seletskaya, Yu. N. Osetsky, R. E. Stoller, and G. M. Stocks, Second International Conference on Multiscale Materials Modeling, October 11–15, 2004, Los Angeles.
- [7] T. Seletskaya, Yu. N. Osetsky, R. E. Stoller, and G. M. Stocks, presented at TMS Symposium on Microstructural Processes in Irradiated Materials, February 14–17, 2005, San Francisco, Journal of Nuclear Materials (in press).
- [8] M. W. Finnis and J. E. Sinclair, Philos. Mag. A 50 (1984) 45–55.
- [9] G. J. Ackland, D. J. Bacon, A. F. Calder, and T. Harry, Philos. Mag. A 75 (1997) 713–732.
- [10] G. J. Ackland, M. I. Mendeleev, D. J. Srolovitz, S. Han, and A. V. Barashev, J. Phys., Condens. Matter 16 (2004) S2629–S2642
- [11] M. I. Mendeleev, S. Han, D. J. Srolovitz, G. J. Ackland, D. Y. Sun, and M. Asta, Philos. Mag. 83 (2003) 3977–3994.
- [12] R. A. Aziz, A. R. Janzen, and M. R. Moldover, Phys. Rev. Lett. 74 (1995) 1586–1589.
- [13] C. C. Fu and F. Willaime, Phys. Rev. B 72 (2005) 064117.
- [14] K. Morishita, R. Sugano, B. D. Wirth, and T. Diaz de la Rubia, Nucl. Instrum. Methods Phys. Res. Sect. B 202 (2003) 76–81.

## MODELING THE INTERACTION OF HELIUM WITH DISLOCATIONS AND GRAIN BOUNDARIES IN ALPHA-IRON—H. L. Heinisch, F. Gao, and R. J. Kurtz (Pacific Northwest National Laboratory)

### OBJECTIVE

The objective of this research is to understand the fate of helium atoms produced in metals and alloys by the neutrons in a fusion reactor in part by studying the migration and diffusion mechanisms of He atoms in dislocations and grain boundaries in  $\alpha$ -Fe using atomic-scale methods of molecular dynamics and statics.

### SUMMARY

Molecular statics, molecular dynamics and the dimer method of potential surface mapping are being used to study the fate of helium in the vicinity of dislocations and grain boundaries in alpha-iron. Even at very low temperatures interstitial helium atoms can migrate to dislocations and grain boundaries, where they are strongly bound. The binding energies of helium to these microstructural features, relative to the perfect crystal, and the migration energies of helium diffusing within them have a strong correlation to the excess atomic volume that exists in these extended defects. Helium atom migration energies within the dislocations and grain boundaries studied are in the range of 0.4–0.5 eV. Helium “kick out” mechanisms have been identified within dislocations and grain boundaries by which interstitial helium atoms replace a Fe lattice atom, creating a stable He-vacancy complex that may be a nucleation site for a He bubble.

### PROGRESS AND STATUS

#### Introduction

In the development of structural materials for nuclear energy production, including fission and fusion, the production and presence of helium (He) and its effects on the properties of structural materials under irradiation have long been a concern [1–4]. Computer simulations of He production, diffusion, trapping and clustering can provide valuable insights into the effects of He on the properties of nuclear materials. Although atomic-scale simulation of rare gases in metals has a history spanning half a century [5], progress has been spotty over the years. However, recently, interest in computational modeling of He-metal interactions and the development of relevant computational capabilities has increased significantly, primarily as part of the efforts to develop advanced materials that have minimum deleterious effects of He accumulation. The primary input information for these models is the interatomic potentials. In the past few years molecular dynamics (MD) simulations using Embedded Atom Method (EAM) type interatomic potentials have been performed to study He clustering [6,7] and He migration and interactions with extended defects [8–10] in  $\alpha$ -Fe. Recent *ab initio* calculations [11,12] are providing new insights and quantitative information on He-Fe interactions.

According to MD modeling results single interstitial He atoms are extremely mobile in  $\alpha$ -Fe, having migration energy of less than 0.1 eV in a perfect Fe crystal [9]. Interstitial He atoms are strongly trapped at vacancies, and they can also be trapped—less strongly but significantly—by features in the microstructure where there is much less excess volume than at a vacancy. Interstitial locations in and near grain boundaries (GBs) and dislocations can have sufficient excess volume to trap He atoms. The purpose of our modeling is to determine the binding energies of He to these extended defects and the migration energies of He within them, as well as to determine the kinetics of He clustering and the stability of He clusters in and near them.

Multiscale modeling, from *ab initio* computer simulations through analytical reaction rate theory computations, is required for comprehensive quantitative modeling of He disposition in an irradiated metal. Recently *ab initio* calculations are providing more critical information, but they are still restricted to atom configurations that comfortably fit within extremely small volumes and, usually, periodic boundary conditions, which limits their usefulness for studies of extended defects such as dislocations or grain

boundaries. MD suffers from a lack of realistic interatomic interactions, simply because much of the important physics of the interactions cannot be directly included. However, because of the large size of models that can be dealt with relatively efficiently, MD models can easily be applied to situations that include long-range fields and the essential features of large, non-symmetric defected regions of the material. It is often possible to tailor the potentials used in MD to more realistically represent some specific aspect(s) of the defect interactions--but with a concomitant loss of general applicability. Knowing which things to get exactly right and which details can be safely ignored--tempered by the possibility of even implementing these things quantitatively--is the essential dilemma of multiscale modeling.

Time scales are important. *Ab initio* and static molecular interaction models have no time scale, and MD can model times of perhaps nanoseconds, usually at nearly unphysically high interaction rates. Kinetic Monte Carlo (KMC) methods can be used to model macroscopic time intervals, if only for a very small volume of material and a limited number of events. The quantitative details of each category of defect migration and interaction in KMC and analytical rate theory models must be supplied by lower scale models, e.g., *ab initio*, MD, or input from experiments.

### Interatomic Potentials

The present work is aimed at determining the fundamental aspects of the interaction of helium atoms with the existing microstructural features, as well as radiation-induced microstructure changes in alpha-Fe (and eventually in ferritic steels for fusion power applications). In particular, we have studied He atom interactions with edge and screw dislocations as well as with several types of grain boundaries. Potentials for Fe-Fe, Fe-He and He-He suitable for use in MD simulations are needed for these studies. Our studies so far have been performed using the set of potentials consisting of the Fe-Fe potential of Ackland et al. [13], the Wilson and Johnson potential for Fe-He [14], and the He-He potential used by Beck [15]. These potentials were used by Morishita et al. [9,10] and others in studies of He bubble formation, and the Ackland potential has been widely used in other MD simulations of radiation damage and defect interactions in  $\alpha$ -Fe. Thus, for consistency in comparing our simulations of He in grain boundaries and dislocations to that body of work, we have used them in the present simulations.

EAM potentials have functional forms with parameters that can be fitted to a set of material properties (usually for the perfect crystal and often to some defect configurations) determined by experimental measurements or *ab initio* calculations. There is no guarantee that any of the existing EAM potentials for Fe adequately represent all non-equilibrium or non-symmetric atom configurations. Mendeleev et al. [16] developed a number of EAM potentials for Fe that describes properties of both crystalline and liquid Fe. The various versions of the potential were fitted to different sets of measured and *ab initio*-calculated properties. These potentials are on average in better agreement with those properties than other EAM potentials for Fe. The Mendeleev Potential #2 appears to be the best for computation of defect properties of interest to the present study. We have re-done some of our He-dislocation calculations using the Mendeleev #2 potential for Fe-Fe. Results are compared and discussed below.

## **Calculations**

### He-Dislocation Interactions

He-dislocation interactions were studied by doing molecular statics to determine defect formation energies, and Dimer [17] calculations to determine transition state energies and configurations. Some MD simulations were also done to study the intermediate range behavior of interstitial He-dislocation interactions at low temperatures. Models of the  $a/2[111]$ [-1-12] edge dislocation and the  $a/2[111]$  screw dislocation were constructed using cylindrical computational cells, each containing a dislocation along (or parallel to) the cylinder axis and having periodic boundaries in the direction of the dislocation line, with fixed boundaries at the surface of the cylinder. See Fig. 1. All atoms in the cell were displaced according to the anisotropic displacement field of the dislocation, and the cell was relaxed to allow the dislocation core field to develop. To determine He defect formation energies, a He atom was placed at a specific

position within the relaxed cell and the cell was relaxed again. Starting from a specific relaxed configuration, Dimer calculations were performed to determine the energies, saddle points, and final configurations of all possible transitions. More details of how these calculations were performed are in [9]. To study He-core interactions MD simulations were performed for picoseconds at 100 K for single migrating He atoms near the edge dislocation core. To study the effects of different Fe-Fe potentials, separate test cells were constructed for the Ackland and Mendelev Fe-Fe potentials because their equilibrium lattice parameters for perfect Fe are slightly different (0.28665 nm Ackland; 0.28553 nm Mendelev).

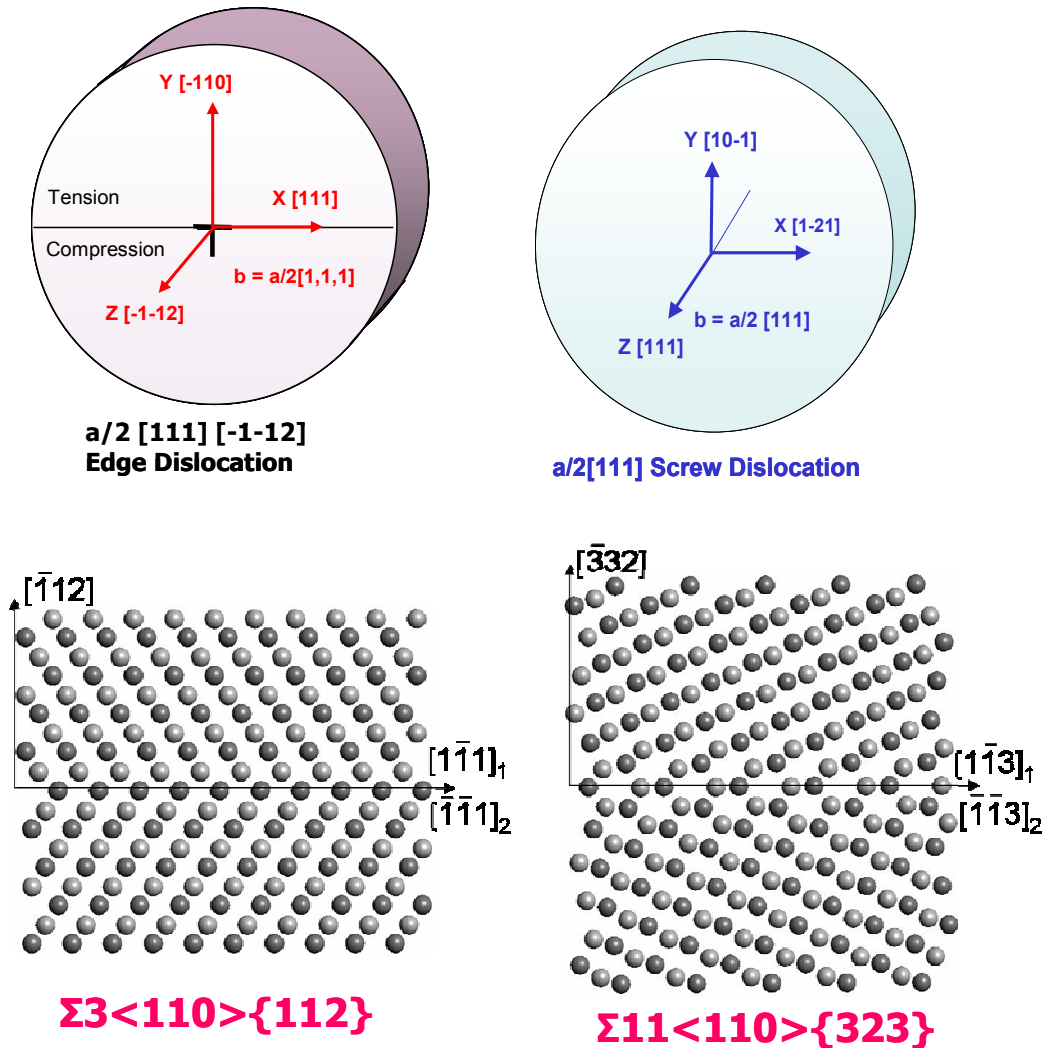


Fig. 1. Schematic drawings of the computational cells and orientations of the models of the  $a/2\langle 111 \rangle [-1-12]$  edge dislocation, the  $a/2\langle 111 \rangle$  screw dislocation, and the  $\Sigma 3\langle 110 \rangle \{112\}$  and  $\langle 110 \rangle \{323\} \Sigma 11$  grain boundaries.

#### He-Grain Boundary Interactions

Simulations of He interactions within two tilt GBs,  $\Sigma 3 \{112\}$   $\Theta = 70.53^\circ$  and  $\Sigma 11 \{323\}$   $\Theta = 50.48^\circ$ , were performed to study the diffusion of He interstitials and small clusters in the temperature range from 600 to 1200 K. Only the Ackland interatomic potential was used for Fe-Fe interactions. The MD migration

simulations were followed for 1–14 ns, depending on the temperature. The diffusivity,  $D$ , of He atoms can be determined from the sum of the mean square displacements (MSD) of He atoms. To accurately calculate the diffusion coefficient of He atoms, the method used here is based on decomposing the single trajectory into a set of shorter independent segments with equal duration, and then an average MSD,  $D_i$  ( $i$  indicates the  $i$ th time interval for the segment) for each segment, is calculated. The time interval of segments varies from 10 ps to 500 ps, and then  $D_i$  is averaged over all time intervals. With the diffusion coefficients of He atoms obtained at different temperatures, the activation energy for He migration in GBs,  $E_m$ , can be estimated from the Arrhenius Relation

$$D = D_0 \exp(-E_m / k_B T) \quad (1)$$

where  $D_0$  is the pre-exponential factor,  $T$  is the absolute temperature, and  $k_B$  is the Boltzmann constant.

The mean square displacements of a He interstitial are determined as a function of time for the  $\Sigma 3$  and  $\Sigma 11$  GBs using the method described above. More details of how the He-GB simulations were performed are in [10]. Using the same techniques, interactions of He di-interstitials with these GBs have also been studied [19].

## Results and Discussion

### Dislocations

The binding energies and migration energies calculated for He near the edge and screw dislocations and in the grain boundaries described above are summarized in Fig. 2, which is a table of energies for various types of He defects arranged in relation to the energy scale in the far left column. The binding energy is defined as the difference of the formation energy of the He defect when it is in a perfect crystal and when it is in the dislocation or GB. Migration energies of He atoms near and within the dislocations are determined from Dimer analysis. The binding energies are very position dependent, and only maximum binding energies are reported in Fig. 2.

The maximum binding energy of single interstitial He atoms to the edge dislocation is 2.3 eV, with a maximum binding of 2.9 eV at the corner of a jog on the dislocation. The binding energies represent the differences in the formation energies of the stable defect configurations in the perfect and dislocated regions. As expected, interstitial He atoms approaching the core region on the tensile side of the edge dislocation migrate more favorably toward the dislocation line, initially as octahedral interstitials. An octahedral interstitial He placed about three Burgers vectors from the dislocation center has migration energy toward the center on the order of 0.2 eV. As excess volume increases, the He atom is more likely to occupy tetrahedral locations, ultimately going into the lowest energy interstitial configuration near the dislocation, which is a [111] crowdion. As a crowdion, the He preferentially migrates along the dislocation line, which is perpendicular to the crowdion direction, by hopping to crowdion positions in adjacent rows with a migration energy of 0.4–0.5 eV, depending on the initial position. The activation energy for He jumping out of the crowdion configuration to an octahedral interstitial site (as a first step of migrating away from the dislocation) is about 1.5 eV.

Binding energies of single interstitial He atoms to the screw dislocation are less than half that to the edge dislocation, and the He interstitials near the screw are never observed in the crowdion configuration. This is probably because the excess interstitial volume in the vicinity of the screw dislocation is significantly less than that found near the edge dislocation.

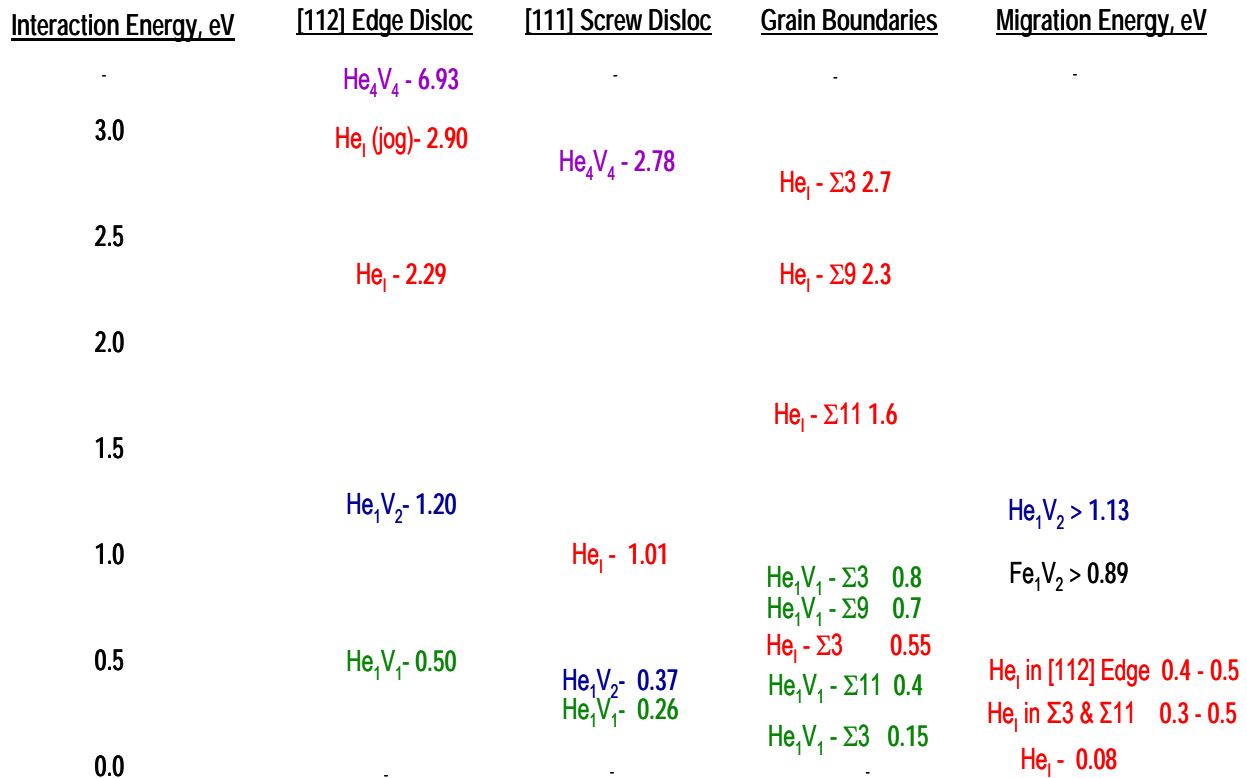


Fig. 2. A “map” of binding energies and migration energies in eV for He in dislocations and grain boundaries.

Entries in the binding energy part of the map are labeled according to the numbers of He and vacancies in the defect, He<sub>i</sub>V<sub>j</sub>. For example, He<sub>1</sub> is a single interstitial He atom and He<sub>1</sub>V<sub>1</sub> is a substitutional He atom. The relative positions of the entries are related to the interaction energy scale on the left.

### Grain Boundaries

The GBs do not have the long range fields associated with the single dislocations, but there is excess atomic volume dispersed throughout the boundary region that provides a sink for migrating interstitial He atoms. In the GBs the maximum binding energies of interstitial He atoms are somewhat less than in the dislocations, and they vary with the boundary type and orientation. See Fig. 1. Interstitial He has a binding energy to the Σ3 GB of 0.55 eV, and the dimensionality of its migration is temperature dependent. In the high temperature MD simulations [10], the interstitial He atom migrates one-dimensionally within the Σ3 GB at lower temperatures, and two-dimensionally above 800 K. At 1200 K the He atom was observed to migrate out of the GB three-dimensionally, reflecting the relatively smaller binding energy of He to the Σ3. He atoms have a higher binding energy to the Σ11 GB, and He atom migration is observed to be one-dimensional within the GB throughout the 800-1200 K temperature range studied. The migration energies of He atoms within the grain boundaries are in the range of 0.3–0.5 eV, depending on the He atom location and defect type.

Two interstitial He atoms placed in close proximity in the Σ3 GB migrate one-dimensionally as a di-interstitial He cluster at temperatures of 600–1000K without dissociation [19]. At 1200 K an interesting phenomenon is observed in that the di-interstitial He cluster “kicks out” an Fe atom and occupies the resulting vacancy, forming a very stable, stationary He<sub>2</sub>V defect. The Fe atom becomes a crowdion interstitial that quickly migrates along the [1–11] interface axis one dimensionally. A similar kick out

mechanism is observed at 1200 K in the  $\Sigma 11$  GB, where the kicked out Fe atom migrates within the GB as a [110] dumbbell. Depending on its long-term stability, the He<sub>2</sub>V defect might be the smallest He bubble nucleus.

### Comparing Interatomic Potentials

Results of calculations of some Fe and He defect formation energies using the Mendeleev version of the Fe-Fe potential were compared to the values obtained using the Ackland Fe-Fe potential, with the same Fe-He potentials for both cases. Table 1 gives the values of the He octahedral and tetrahedral interstitial formation energies and the He binding energies in a crowdion interstitial position near the edge dislocation. These results are also compared to results of *ab initio* calculations [11]. The formation energies using the Mendeleev potential are somewhat smaller than those using the Ackland potential, but in both cases the octahedral position is more stable than the tetrahedral, in contrast to the *ab initio* results. The magnitude of the difference is greater for the Mendeleev potential than for the Ackland potential. Evidently, the relative stability of these two He interstitial positions is not strongly influenced by the Fe-Fe interaction. Very recently Seletskiaia et al. [18] have shown results of similar calculations using a new empirical Fe-He potential fitted to results of *ab initio* calculations. The close agreement of their results using the empirical and *ab initio* methods indicates that the stability of the He interstitial in Fe is, not surprisingly, most strongly influenced by the Fe-He potential. Based on this success, it will be very interesting to incorporate the new Fe-He potential function into our further studies of He in dislocations and grain boundaries.

Table 1. Comparison of He interstitial formation energies in eV at octahedral and tetrahedral sites calculated in this study using Ackland[13] and Mendeleev[16] versions of EAM Fe-Fe interatomic potentials. The MD results are compared to results of *ab initio* calculations for these configurations by Seletskiaia et al. [11].

	<u>Ackland</u>	<u>Mendeleev</u>	<u><i>ab initio</i></u>
He Octahedral	5.25	4.99	4.60
He Tetrahedral	5.33	5.13	4.37

The results of our simulations indicate that the behavior of interstitial He within dislocations and GBs is strongly influenced by the excess volume found in the atomic arrangements of these extended defects. Moreover, the excess volume in the defected Fe lattice is determined solely by the Fe-Fe interatomic interactions, and the Mendeleev Fe-Fe potential #2 is fitted to many properties of Fe, including the *ab initio* values of self-interstitial atoms [16]. It is tempting to think that one could predict the behavior of He in any configuration of extended defects based solely on the magnitude and spatial distribution of excess volume in that configuration. However, according to results using the new Fe-He empirical potential [18], the response of He atoms to the atomic arrangements they experience in Fe appears to depend strongly on the He-Fe interactions. On the other hand, all the tests of this new He-Fe potential were performed on configurations where the excess volume is negative. It would be of great interest to have results of *ab initio* calculations performed for atom configurations containing excess volume that is representative of that found in dislocations or GBs.

### Conclusions

Molecular dynamics simulations have been performed for binding energies and migration energies of He in dislocations and grain boundaries. He is strongly trapped in regions of excess volume found in these extended defects. Details of the trapping and migration mechanisms of He observed in these simulations will be corroborated in further simulations using the latest interatomic potentials based on results of *ab initio* calculations. These simulations provide essential elements of the defect interaction information required for multiscale modeling of the fate of He in  $\alpha$ -Fe.

## Acknowledgements

This research is supported by the US Department of Energy, Office of Fusion Energy Sciences, under Contract DE-AC06-76RLO 1830.

## References

- [1] E. E. Bloom, *J. Nucl. Mater.* 85–86 (1979) 795.
- [2] H. Ullmaier, *Nucl. Fusion* 24 (1984) 1039.
- [3] R. L. Klueh and D. J. Alexander, *J. Nucl. Mater.* 218 (1995) 151.
- [4] D. S. Gelles, *J. Nucl. Mater.* 283–287 (2000) 838.
- [5] D. E. Rimmer and A. H. Cottrell, *Philos. Mag.* 2 (1957) 1345.
- [6] K. Morishita, R. Sugano, and B. D. Wirth, *J. Nucl. Mater.* 323 (2003) 243.
- [7] K. Morishita, R. Sugano, B. D. Wirth, and T. Diaz de la Rubia, *Nucl. Instrum. Methods B* 202 (2003) 76.
- [8] R. J. Kurtz and H. L. Heinisch, *J. Nucl. Mater.* 329–333 (2004) 1199.
- [9] H. L. Heinisch, F. Gao, R. J. Kurtz, and E. A. Le, *J. Nucl. Mater.* 351 (2006) 141.
- [10] F. Gao, H. L. Heinisch, and R. J. Kurtz, *J. Nucl. Mater.* 351 (2006) 133.
- [11] T. Seletskaiia, Y. Osetsky, R. E. Stoller, and G. M. Stocks, *Phys. Rev. Lett.* 94 (2005) 046403.
- [12] T. Seletskaiia, Y. Osetsky, R. E. Stoller, and G. M. Stocks, *J. Nucl. Mater.* 351 (2006) 109.
- [13] G. J. Ackland, D. J. Bacon, A. F. Calder, and T. Harry, *Philos. Mag. A* 75 (1997) 713.
- [14] W. D. Wilson and R. D. Johnson, *Interatomic Potential and Simulation of Lattice Defects*, Plenum, 1972 (375).
- [15] D. E. Beck, *Mol. Phys.* 14 (1968) 311.
- [16] M. I. Mendeleev, S. Han, D. J. Srolovitz, G. J. Ackland, D. Y. Sun, and M. Asta, *Philos. Mag.* 83 (2003) 3977.
- [17] G. Henkelman and H. Jónsson, *J. Chem. Phys.* 111 (1999) 7010.
- [18] T. Seletskaiia, Y. Osetsky, R. E. Stoller, and G. M. Stocks, *Journal of Nuclear Materials* (in press).
- [19] F. Gao, H. L. Heinisch, and R. J. Kurtz, *Journal of Nuclear Materials* (in press).

**10. DOSIMETRY, DAMAGE PARAMETERS, AND  
ACTIVATION CALCULATIONS**

**No contributions.**

**11. MATERIALS ENGINEERING AND DESIGN  
REQUIREMENTS**

**No contributions.**

## **12. IRRADIATION FACILITIES AND TEST MATRICES**

## **IRRADIATION OF FUSION MATERIALS IN THE BR2 REACTOR: THE FRISCO-F EXPERIMENT—E. Lucon (SCK•CEN) and M. A. Sokolov (Oak Ridge National Laboratory)**

### **SUMMARY**

Tensile and miniature Compact Tension specimens of eight high chromium steels of fusion relevance have been irradiated in the BR2 reactor in the framework of a collaborative project between Oak Ridge National Laboratory (ORNL) and SCK•CEN.

All samples have been irradiated at a nominal temperature of 300°C in the in-pile section 2 (IPS-2) for five cycles (02/2005 to 01/2006) up to an average fast neutron fluence of  $8.02 \times 10^{20}$  n/cm<sup>2</sup> or 1.20 dpa. The rig was rotated three times by 180° in order to reduce the radial and azimuthal neutron flux gradients.

### **INTRODUCTION**

Material research represents a crucial issue for the assessment of fusion as a future source of energy. Structural materials, in particular, need to show a superior mechanical and chemical behavior to guarantee the safe operation of the reactor during its whole lifetime, while retaining low activation characteristics to minimize the environmental impact of the produced waste. For many aspects of the design, it is indeed material technology that will dictate the most viable concept for the commercial power plant.

In this context, specific efforts have been focused for the last twenty years, in Europe, Japan and the US, on developing suitable Reduced Activation Ferritic Martensitic (RAFM) steels as prominent structural materials. EUROFER97 has recently emerged in Europe as the reference material for the DEMO design, whereas activities in the US and Japan have been concentrating for several years on F82H. At the same time, research is in progress at Oak Ridge National Laboratory (ORNL) in the US using model alloys with chromium contents ranging from 3% to 9%.

While the final assessment of these materials under the actual reactor conditions will only occur in ITER (blanket module) and IFMIF, it is presently of primary importance to develop the scientific understanding of the mechanisms which control the physical, mechanical, and chemical behavior of such materials under radiation.

A representative selection of high chromium steels of fusion relevance has been irradiated in the Belgian Reactor 2 (BR2) located in Mol (Belgium), in the framework of a collaborative project between ORNL and SCK•CEN. The experiment, denominated FRISCO-F (Fusion and Reactor Materials Irradiation SCK•CEN/ORNL–Fusion Materials), included tensile and fracture toughness specimens of the following materials: EUROFER97, F82H, CLAM and four ORNL developmental alloys (9Cr, 5Cr, 3Cr, 3Cr+Ta); in addition, we also irradiated samples of the well-known ferritic/martensitic steel T91, which is not relevant for fusion (its chemical composition cannot be considered reduced-activation) but it's regarded as one of the reference materials for applications such as accelerated-driven systems (ADS) and future high temperature nuclear energy systems (Gen IV).

The irradiation campaign took place during five cycles of BR2 in the period June 2005/March 2006; the nominal irradiation temperature was 300°C.

On the basis of analytical calculations which have been verified by actual dosimetry measurements, the average fast neutron fluence ( $E > 1$  MeV) for all irradiated specimens is  $8.02 \times 10^{20}$  n/cm<sup>2</sup>, corresponding to 1.20 dpa.

#### Irradiation Conditions

The FRISCO-F irradiation has been conducted between April 15, 2005, and March 21, 2006, at a water temperature between 295 and 300°C in the D180 channel (IPS-2) of the CALLISTO rig in the BR2 reactor. In order to achieve uniform irradiation conditions (fluence and flux) in the radial direction, the rig has been rotated by 180° between the first and the second, the second and the third and the third and the fourth cycles.

The parameters relative to the coolant have been chosen in conformity with the technical specification of PWR primary water chemistry:

- Temperature 295–300°C
- Boron (boric acid)  $\pm 550$  ppm
- Lithium (lithium hydroxide)  $1.8 \text{ ppm} \leq [\text{Li}] \leq 2.2 \text{ ppm}$
- pH  $7.00 \leq \text{pH}_{25^\circ\text{C}} \leq 7.08$  or  $7.26 \leq \text{pH}_{300^\circ\text{C}} \leq 7.34$
- Dissolved hydrogen  $25 \text{ ccSTP/kg} \leq [\text{H}_2] \leq 35 \text{ ccSTP/kg}$

The specimens were in direct contact with the water.

#### Materials and Specimens Irradiated

The following materials have been irradiated in the FRISCO-F experiment:

- three reduced-activation ferritic/martensitic (RAFM) steels : EUROFER97 (9%Cr), F82H (8%Cr), CLAM (Chinese Low Activation Material, 9%Cr);
- four high Cr developmental alloys produced by ORNL: 9Cr-2WVTa, 5Cr-2W2.5V, 3Cr-3WV, 3Cr-3WVTa;
- one ferritic/martensitic steel denominated T91 (9Cr1MoVNb).

The chemical composition of the steels irradiated is given in Table 1 (weight %). Tensile properties at RT for the three RAFM steels and for T91 are shown in Table 2.

Table 1. Chemical composition of the steels irradiated in FRISCO-F

Material	C	Mn	Si	S	P	Cr	V	W	Ta	Al	B	N
F82H	0.090	0.16	0.11	0.002	0.002	7.71	0.16	1.95	0.02	0.003	0.0002	0.006
EUROFER97	0.12	0.42	0.06	0.003	0.004	8.87	0.19	1.10	0.14	0.008	<0.0005	0.018
CLAM	0.10	0.45	0.25	-	-	9.0	0.20	1.5	0.07	-	-	0.02
ORNL 9Cr-2WVTa	0.11	0.44	0.21	0.008	0.015	8.90	0.23	2.01	0.06	0.017	<0.001	0.0215
ORNL 5Cr-2W2.5V	0.12	0.49	0.23	0.009	0.015	5.04	0.24	2.01	-	0.010	<0.001	0.0171
ORNL 3Cr-3WV	0.10	0.39	0.16	0.004	0.010	3.04	0.21	3.05	<0.01	0.003	0.001	0.004
ORNL 3Cr-3WVTa	0.10	0.41	0.16	0.005	0.011	3.02	0.21	3.07	0.09	0.003	0.001	0.003
T91	0.099	0.43	0.32	0.004	0.020	8.8	0.24	<0.01	-	<0.01	<0.0005	0.03

Table 2. RT tensile properties for four of the steels irradiated in FRISCO-F

Material	Yield strength (MPa)	Tensile strength (MPa)	Total elongation (%)	Reduction of area (%)
F82H	562	664	18	81
EUROFER97	557	670	20	80
CLAM	1086	1428	15	70
T91	544	684	22	73

For each of the three RAFM steels and for the ORNL 9Cr-2WVTa material, the following samples have been irradiated:

- 3 miniature tensile specimens with cylindrical cross section and the following nominal dimensions:
  - overall length  $L = 24$  mm;
  - length of reduced section  $A = 12$  mm;
  - diameter of reduced section  $D = 2.4$  mm;
  - heads M4;
- 12 miniature Compact Tension MC(T) specimens with the following nominal dimensions:
  - height  $H = 10$  mm;
  - width  $W = 10$  mm;
  - thickness  $B = 4.2$  mm.

For T91, one tensile and 12 MC(T) samples have been irradiated. In the case of the remaining ORNL alloys, only tensile specimens (three for 5Cr-2W2.5V, four for 3Cr-3WV and 3Cr-3WVTa) were included in the rig.

Technical drawings of the samples are provided in Annex 1 (tensile) and Annex 2 (miniature C(T)).

#### Activation Dosimeters

In total, 4 activation dosimeters made of pure iron (discs of 9 mm diameter and 0.5 mm thickness) have been inserted in the rig, located between the tensile specimen boxes and the MC(T) stacks in both needles.

Each dosimeter had slightly different geometrical dimensions in order to be distinguished from the others.

#### Pre-irradiation Operations

In the case of F82H and the four developmental alloys, samples were prepared by ORNL according to SCK•CEN specifications and shipped to Mol before irradiation. The remaining specimens were machined at SCK•CEN.

The tensile samples have been assembled in boxes, three by three at the same axial position; the MC(T)'s have been stacked in groups of 15.

#### Operations During and Post-irradiation

The irradiation of the FRISCO-F specimens has proceeded as planned, without any significant problem.

After the conclusion of cycle 01/2006 and a short cool-down period, the rig has been transported to the hot cells of BR2 where all the specimens have been recovered.

The irradiated samples have been transferred to the storage facility of LHMA (Laboratory for High and Medium Activities of SCK•CEN), where they are currently stored before being tested and/or shipped back to ORNL.

#### Evaluation of Fast Neutron Fluences and Doses

The evaluation of fast neutron fluences and doses experienced by the specimens is based upon the power of BR2, the axial position of the samples in the rig and the duration of the irradiation cycles.

The maximum fast neutron fluences ( $E > 1$  MeV) and doses relative to the center channel of the CALLISTO rig (channel E) and the BR2 midplane (axial position  $Z = -72$  mm) have been calculated using the code GEXBR2-TRPT3, which has been developed and validated by SCK•CEN and is based on neutron transport theory.

The calculated values for the five BR2 cycles of the FRISCO-F irradiation are:  $\phi = 8.80 \times 10^{20}$  n/cm<sup>2</sup> ( $E > 1$  MeV) or 1.32 dpa

These values are rigorously valid only for samples located at the position of highest flux (midplane) and in the center channel of the rig (channel E); cosinusoidal axial distribution functions [1] are available and have been used to evaluate the fluence and dose associated to each individual specimen.

Fluences and fluxes measured by the 4 activation dosimeters loaded in the rig have been used to adjust the values calculated using the neutron transport code. The maximum deviation between calculated and measured fluence at the dosimeter position was 2%. Details of the dosimetry measurements are given in the Technical Note presented in Annex 3.

The values of fast fluence and dpa associated to each irradiated specimen are presented in the next section.

### Loading Plan/values of Fluence and dpa

The two needles (G and I) containing the specimens irradiated in FRISCO-F have been loaded into the basket ST 17 of IPS 2.

All loading and unloading operations have been performed in the BR2 hot cells; other operations in the reactor pool were standard manipulations.

The loading plan for the specimens irradiated in channels G and I is given in Table 3 and Table 4 respectively, with the values of fast fluence and dpa calculated for each individual sample.

The mean values of fast fluence and dpa associated to the entire specimen set and to each material and specimen type are presented in Table 5.

### **Acknowledgements**

The collaboration of the personnel of the BR2 and TCH departments of SCK•CEN for all pre-, during- and post-irradiation operations is acknowledged. Thanks also to Roger Mertens for the preparation of the specimens extracted from the materials provided by SCK•CEN.

Finally, personal thanks to Marcel Wéber who followed the preparation and execution of the irradiation campaign.

### **Reference**

[1] R. Chaouadi, A Simple Equation to Estimate the Neutron Flux Distribution in the Callisto Loop of the BR2 Reactor, SCK•CEN Open Report BLG-866 (2001).

---

\*The axial level in Tables 3 and 4 refers to the midplane position of the specimens.

Table 3. Loading plan with fluence and dpa values for needle G

Axial level (mm)	Material	Specimen		Fast fluence ( $10^{20}$ n/cm <sup>2</sup> , E > 1 MeV)	Dose (dpa)
		Type	Id.		
-209	ORNL 3Cr	Tensile	K1	7.56	1.13
	ORNL 3Cr	Tensile	K2	7.56	1.13
	ORNL 3Cr	Tensile	K3	7.56	1.13
-185	F82H	Tensile	F1	7.86	1.18
	EUROFER97	Tensile	E97-140	7.86	1.18
	CLAM	Tensile	CL28	7.86	1.18
-172.5	Fe	Dosimeter	NFE1	8.00	1.20
-147.5	T91	Mini-CT	T91-93	8.23	1.23
-143.3	T91	Mini-CT	T91-94	8.26	1.24
-139.1	T91	Mini-CT	T91-95	8.29	1.24
-134.9	F82H	Mini-CT	F4	8.32	1.25
-130.7	EUROFER97	Mini-CT	E97-128	8.35	1.25
-126.5	CLAM	Mini-CT	CL13	8.37	1.26
-122.3	ORNL 9Cr	Mini-CT	I4	8.40	1.26
-118.1	F82H	Mini-CT	F5	8.42	1.26
-113.9	EUROFER97	Mini-CT	E97-129	8.44	1.27
-109.7	CLAM	Mini-CT	CL14	8.46	1.27
-105.5	ORNL 9Cr	Mini-CT	I5	8.47	1.27
-101.3	F82H	Mini-CT	F6	8.49	1.27
-97.1	EUROFER97	Mini-CT	E97-130	8.50	1.27
-92.9	CLAM	Mini-CT	CL15	8.51	1.28
-88.7	ORNL 9Cr	Mini-CT	I6	8.52	1.28
-61.5	F82H	Mini-CT	F7	8.53	1.28
-57.3	EUROFER97	Mini-CT	E97-131	8.52	1.28
-53.1	CLAM	Mini-CT	CL16	8.51	1.28
-48.9	ORNL 9Cr	Mini-CT	I7	8.50	1.27
-44.7	F82H	Mini-CT	F8	8.49	1.27
-40.5	EUROFER97	Mini-CT	E97-132	8.48	1.27
-36.3	CLAM	Mini-CT	CL17	8.46	1.27
-32.1	ORNL 9Cr	Mini-CT	I8	8.45	1.27
-27.9	F82H	Mini-CT	F9	8.43	1.26
-23.7	EUROFER97	Mini-CT	E97-133	8.41	1.26
-19.5	CLAM	Mini-CT	CL18	8.39	1.26
-15.3	ORNL 9Cr	Mini-CT	I9	8.36	1.25
-11.1	T91	Mini-CT	T91-96	8.33	1.25
-6.9	T91	Mini-CT	T91-97	8.31	1.25
-2.7	T91	Mini-CT	T91-98	8.28	1.24
21	Fe	Dosimeter	NFE2	8.08	1.21
33.5	F82H	Tensile	F2	7.95	1.19
	EUROFER97	Tensile	E97-141	7.95	1.19
	CLAM	Tensile	CL29	7.95	1.19
37.5	ORNL 3Cr+Ta	Tensile	L1	7.90	1.18
	ORNL 3Cr+Ta	Tensile	L2	7.90	1.18
	ORNL 3Cr+Ta	Tensile	L3	7.90	1.18

Table 4. Loading plan with fluence and dpa values for needle I

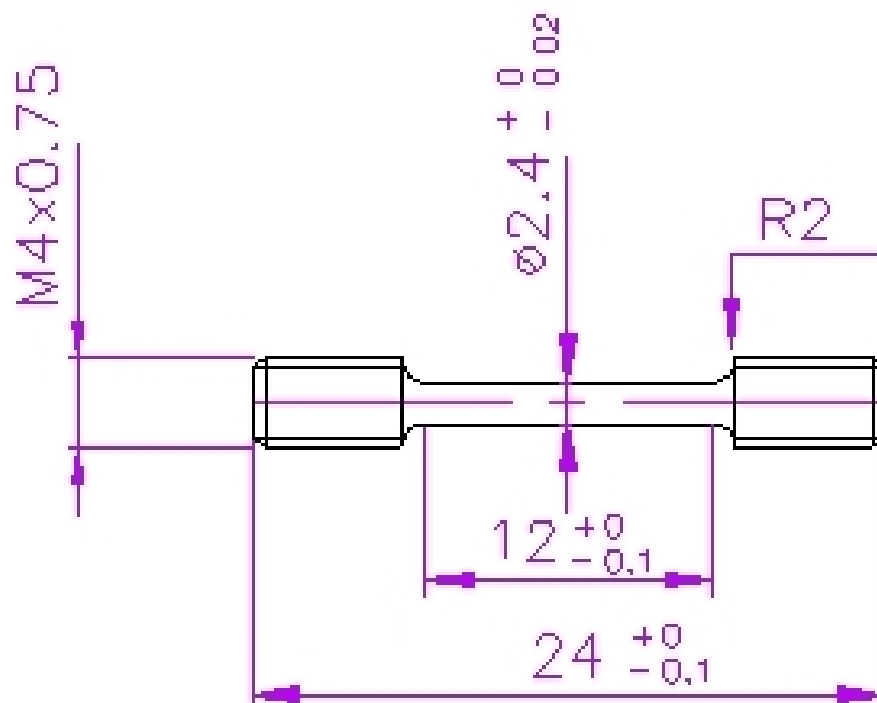
Axial level (mm)	Material	Specimen		Fast fluence ( $10^{20}$ n/cm <sup>2</sup> , E > 1 MeV)	Dose (dpa)
		Type	Id.		
-209	ORNL 5Cr	Tensile	J1	7.59	1.14
	ORNL 5Cr	Tensile	J2	7.59	1.14
	ORNL 5Cr	Tensile	J3	7.59	1.14
-185	F82H	Tensile	F3	7.89	1.18
	EUROFER97	Tensile	E97-142	7.89	1.18
	CLAM	Tensile	CL30	7.89	1.18
-172.5	Fe	Dosimeter	NFE3	8.03	1.20
-147.5	T91	Mini-CT	T91-99	8.26	1.24
-143.3	T91	Mini-CT	T91-100	8.29	1.24
-139.1	T91	Mini-CT	T91-101	8.32	1.25
-134.9	F82H	Mini-CT	F10	8.35	1.25
-130.7	EUROFER97	Mini-CT	E97-134	8.38	1.26
-126.5	CLAM	Mini-CT	CL19	8.40	1.26
-122.3	ORNL 9Cr	Mini-CT	I10	8.42	1.26
-118.1	F82H	Mini-CT	F11	8.45	1.27
-113.9	EUROFER97	Mini-CT	E97-135	8.47	1.27
-109.7	CLAM	Mini-CT	CL20	8.48	1.27
-105.5	ORNL 9Cr	Mini-CT	I11	8.50	1.27
-101.3	F82H	Mini-CT	F12	8.51	1.28
-97.1	EUROFER97	Mini-CT	E97-136	8.53	1.28
-92.9	CLAM	Mini-CT	CL21	8.54	1.28
-88.7	ORNL 9Cr	Mini-CT	I12	8.55	1.28
-61.5	F82H	Mini-CT	F13	8.55	1.28
-57.3	EUROFER97	Mini-CT	E97-137	8.55	1.28
-53.1	CLAM	Mini-CT	CL22	8.54	1.28
-48.9	ORNL 9Cr	Mini-CT	I13	8.53	1.28
-44.7	F82H	Mini-CT	F14	8.52	1.28
-40.5	EUROFER97	Mini-CT	E97-138	8.51	1.28
-36.3	CLAM	Mini-CT	CL237	8.49	1.27
-32.1	ORNL 9Cr	Mini-CT	I14	8.48	1.27
-27.9	F82H	Mini-CT	F15	8.46	1.27
-23.7	EUROFER97	Mini-CT	E97-139	8.44	1.26
-19.5	CLAM	Mini-CT	CL24	8.41	1.26
-15.3	ORNL 9Cr	Mini-CT	I15	8.39	1.26
-11.1	T91	Mini-CT	T91-102	8.36	1.25
-6.9	T91	Mini-CT	T91-103	8.33	1.25
-2.7	T91	Mini-CT	T91-104	8.30	1.24
21	Fe	Dosimeter	NFE4	8.10	1.21
33.5	ORNL 9Cr	Tensile	I1	7.97	1.20
	ORNL 9Cr	Tensile	I2	7.97	1.20
	ORNL 9Cr	Tensile	I3	7.97	1.20
37.5	ORNL 3Cr	Tensile	K4	7.93	1.19
	ORNL 3Cr+Ta	Tensile	L4	7.93	1.19
	T91	Tensile	T91-105	7.93	1.19

Table 5. Mean values of fast fluence and dpa calculated for the materials irradiated in the FRISCO-F experiment

Material	Specimen type	Fast fluence ( $10^{20}$ n/cm <sup>2</sup> , E > 1MeV)	Dose (dpa)
ORNL 3Cr	Tensile	7.65	1.15
ORNL 3Cr+Ta	Tensile	7.91	1.19
ORNL 5Cr	Tensile	7.59	1.14
	Tensile	7.97	1.20
ORNL 9Cr	MC(T)	8.46	1.27
	All	8.37	1.25
	Tensile	7.90	1.18
CLAM	MC(T)	8.46	1.27
	All	8.35	1.25
	Tensile	7.90	1.18
EUROFER97	MC(T)	8.46	1.27
	All	8.35	1.25
	Tensile	7.93	1.19
T91	MC(T)	8.30	1.24
	All	8.27	1.24
	Tensile	7.90	1.18
F82H	MC(T)	8.46	1.27
	All	8.35	1.25
	Tensile	7.83	1.17
All	MC(T)	8.43	1.26
	All	8.26	1.24

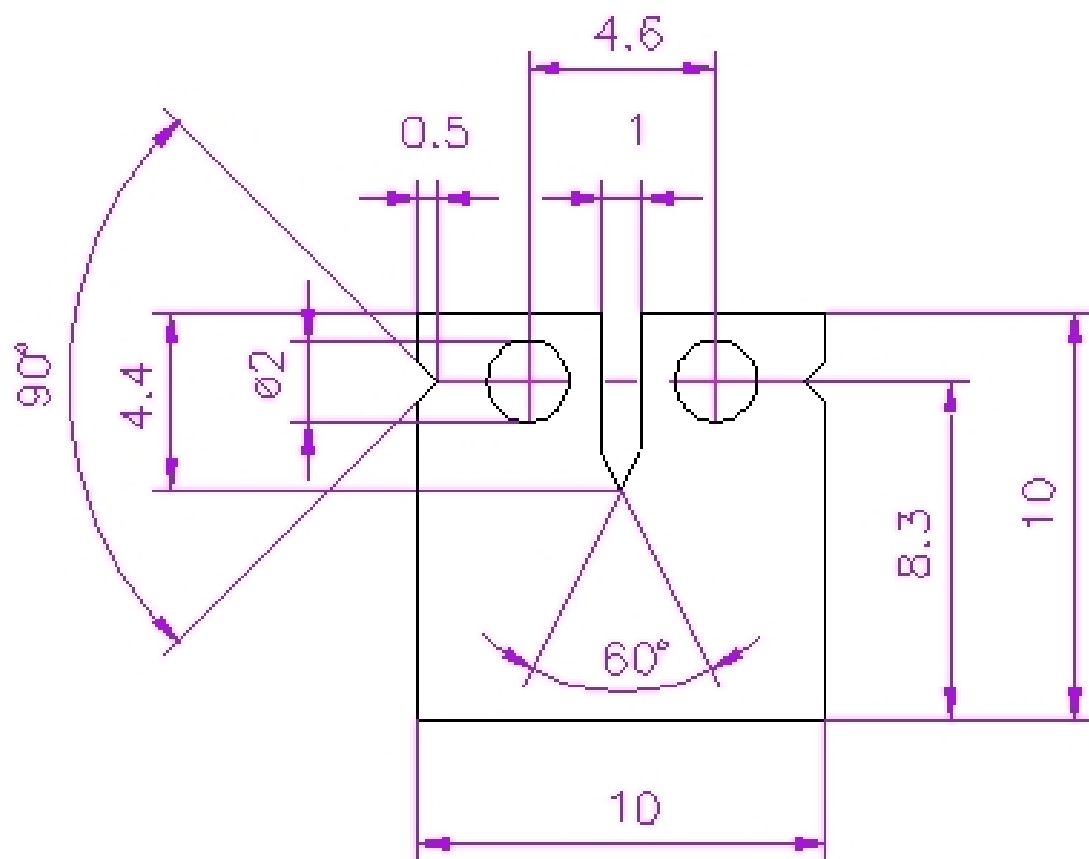
**ANNEX 1**

**Technical drawing of the  
sub-size tensile specimen**



**ANNEX 2**

**Technical drawing of the  
miniature C(T) specimen**



Thickness 4.2

**ANNEX 3**

**Dosimetry measurements**

**(Technical Note  
RF&M/Vwi/vwi RF&M/Vwi/vwi  
32.D049011-205/06 09)**

## Introduction

FRISCO stands for Fusion and Reactor material Irradiation SCK•CEN–ORNL. The specimens from the FRISCO-F experiment are made of different fusion materials.

The specimens were inserted in capsules which were assembled to a needle. These needles were loaded in the CALLISTO loop IPS2. Two needles were loaded with Fe dosimeters. The Fe dosimeters were inserted at the end of the specimens set in each capsule (see annex Fig. 1). Both dosimeters are small discs made of pure iron. Five irradiation cycles are foreseen for needles G and I in IPS2. This report describes how the fission flux and fluence is determined from the activity measurements of the dosimeters that have been irradiated during cycles 02A & 03A & 04B & 04C & 05A/2005 and 01A/2006.

## Irradiation

The irradiation was performed in the BR2 reactor in channel D180 (IPS2) of the CALLISTO loop at a nominal temperature of 295°C. The basket containing the FRISCO-F samples was rotated 180° between cycles 02A and 03A, 03A and 04B, 04C and 05A/2005 in order to get the most uniform fluence at the different specimen positions (see annex Fig. 2).

Fe activation dosimeters are used for the determination of the fast neutron flux and fluence. The dosimeters are discs with a diameter of 9 mm and a thickness of 0.5 mm.

Table 1 summarizes the identification, dosimeter name, needle number, axial position in the reactor, irradiation cycle, and rig (IPS).

Table 1. Overview of the dosimeters

Identification name	Dosimeter number	Needle	Reactor position	Irradiation cycle	Irradiation rig
FRIS-1	NFE1	G	-170	02A&03A&04BC&05A/2005 and 01A/2006	IPS 2
FRIS-2	NFE2	G	+20	02A&03A&04BC&05A/2005 and 01A/2006	IPS 2
FRIS-3	NFE3	I	-170	02A&03A&04BC&05A/2005 and 01A/2006	IPS 2
FRIS-4	NFE4	I	+20	02A&03A&04BC&05A/2005 and 01A/2006	IPS 2

The irradiation history is given in Table 2.

Table 2. Irradiation history

BR2 cycle	Start date of the irradiation	End date of the irradiation	Nominal Power (MW)	Duration (days)
02A/2005	2005-07-29 07:05	2005-08-23 21:15	57	25.48
03A/2005	2005-07-29 07:05	2005-08-23 21:15	57	25.48
04B/2005	2005-10-12 07:45	2005-10-20 10:11	60	8.02
04C/2005	2005-10-22 11:10	2005-11-02 18:42	60	11.31
05A/2005	2005-11-29 07:45	2005-12-19 00:48	60	19.39
01A/2006	2006-02-28 07:52	2006-03-21 23:19	57	19.73

A plot of the irradiation history is given in the annex (Fig. 3).

## Dismantling of the Dosimeters

The capsule with the dosimeters was unloaded in the hot cells of BR2. All the dosimeters were recovered.

## Results

The equivalent fission flux was calculated from the  $^{54}\text{Mn}$  activity formed by the following reaction:



The neutron flux was calculated using the  $^{235}\text{U}$  fission spectrum averaged  $^{54}\text{Fe}(n,p)^{54}\text{Mn}$  cross-section  $\langle\sigma\rangle = 81.7$  mb adopted from [1] (the  $^{54}\text{Fe}(n,p)$  reaction having an effective threshold energy of 2.80 MeV [1]).

The determined equivalent fission fluxes and fluences are given in Table 3 and Fig. 4. All neutron fluxes are calculated at reference power 57.0 MW.

Table 3. Dosimetry results obtained from the  $^{54}\text{Mn}$  activity measurements

Identification number	Needle	Position (mm)	Spec. activity (Bq/g)	Reaction rate ( $\text{s}^{-1}$ )	Eq. fis. flux ( $\text{n}/\text{cm}^2/\text{s}$ )	Eq. fis. fluence ( $\text{n}/\text{cm}^2$ )
NFE1	G	-170	7.18E+08	6.66E-12	8.15E+13	7.82E+20
NFE2		20	7.15E+08	6.62E-12	8.11E+13	7.79E+20
NFE3	I	-170	7.19E+08	6.66E-12	8.16E+13	7.83E+20
NFE4		20	7.19E+08	6.66E-12	8.15E+13	7.83E+20

The uncertainty ( $1\sigma$ ) on the specific activity  $< 3\%$ .

Due to the rotation of the basket between the cycles an error is introduced in the neutron flux (fluence) determination for all needles. In view of the small flux level differences expected between axial positions -170 mm and 20 mm this error is estimated to be  $\leq 5\%$ . This is confirmed by the converging results for the neutron fluence (see Table 3).

Table 4 summarizes how the equivalent fission flux (EFF) can be converted to flux  $> 0.1$  MeV, flux  $> 0.5$  MeV, and flux  $> 1$  MeV [2, 3].

Table 4. Fast neutron flux conversion factors

Irradiation rig	(flux $> 0.1$ MeV)/EFF	(flux $> 0.5$ MeV)/EFF	(flux $> 1$ MeV)/EFF
IPS 2	2.54	1.61	1.03

In order to obtain dpa rates, multiply the neutron flux  $> 1$  MeV by 1440 barn [2, 3].

## References

- [1] J. H. Baard et al., Nuclear Data Guide for Reactor Neutron Metrology, Kluwer (1989).
- [2] V. Kuzminov, SCK•CEN Technical Note BR2-SCU/VK/F04302/fluxes-dpa/23.06.04.
- [3] V. Kuzminov, private communication.

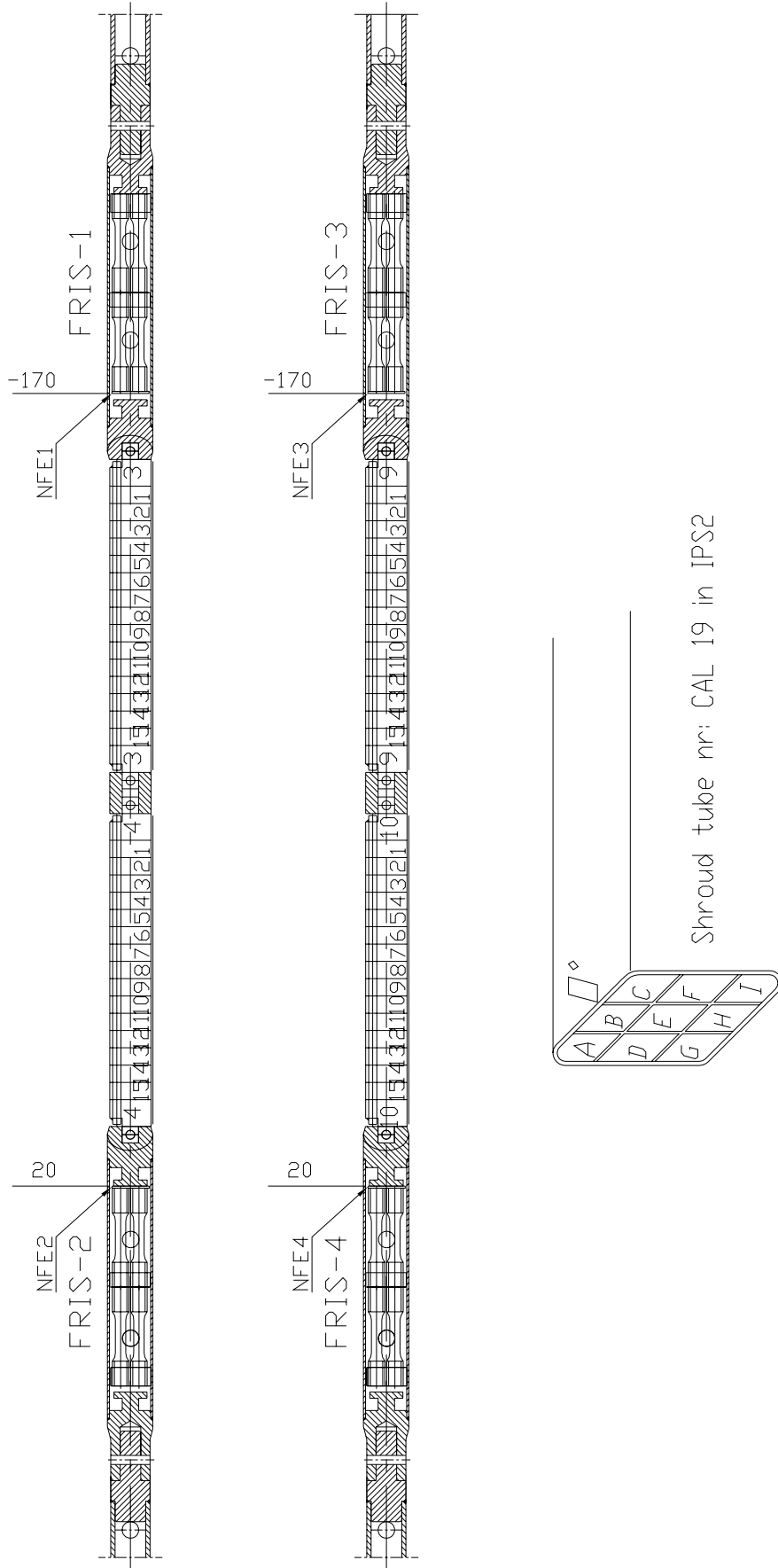


Fig. 1. Position of the dosimeters in needles G & I for experiment FRISCO-F (IPS2).

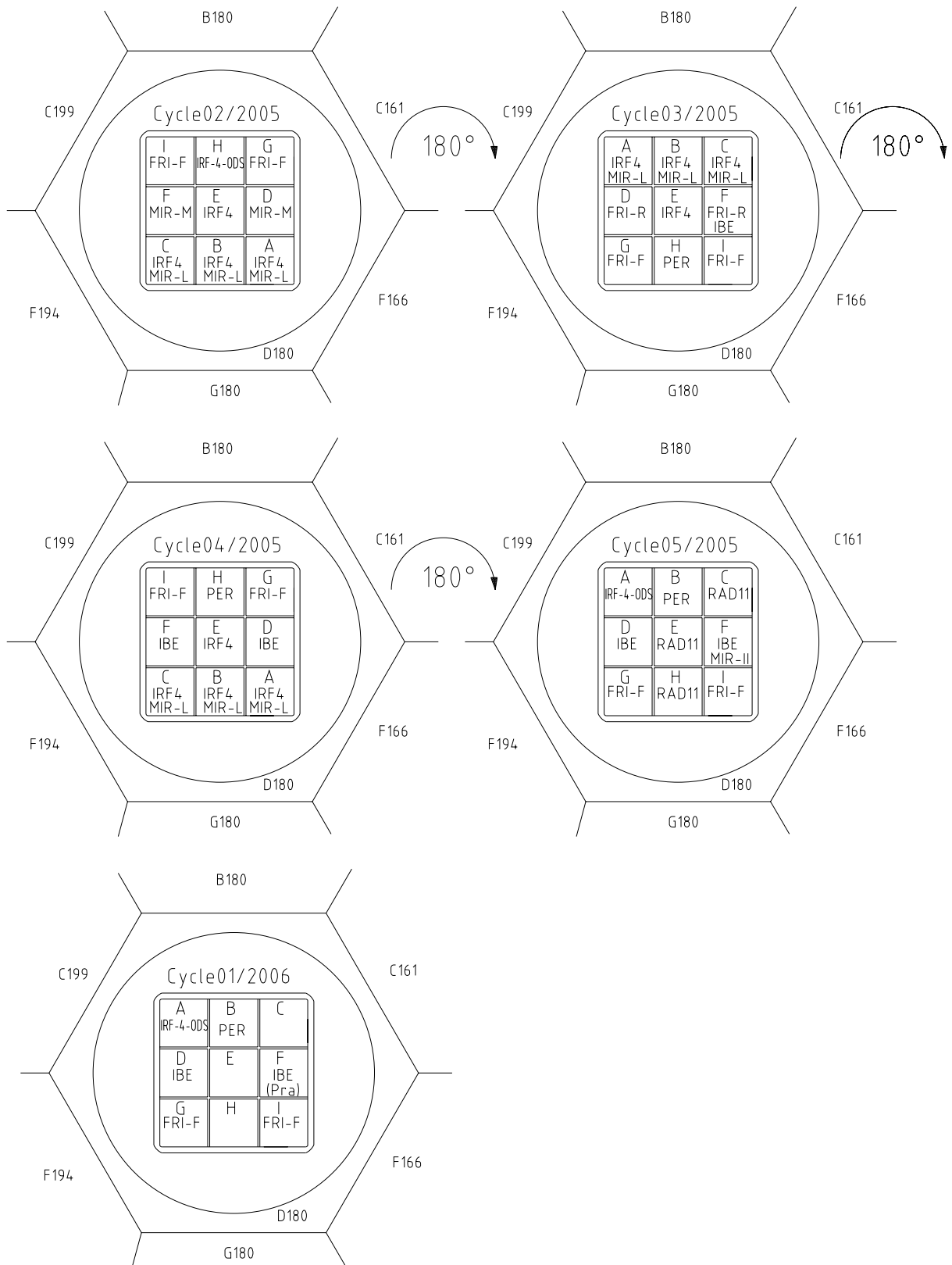


Fig. 2. Position of the needles in the Callisto rig for experiment FRISCO-F.

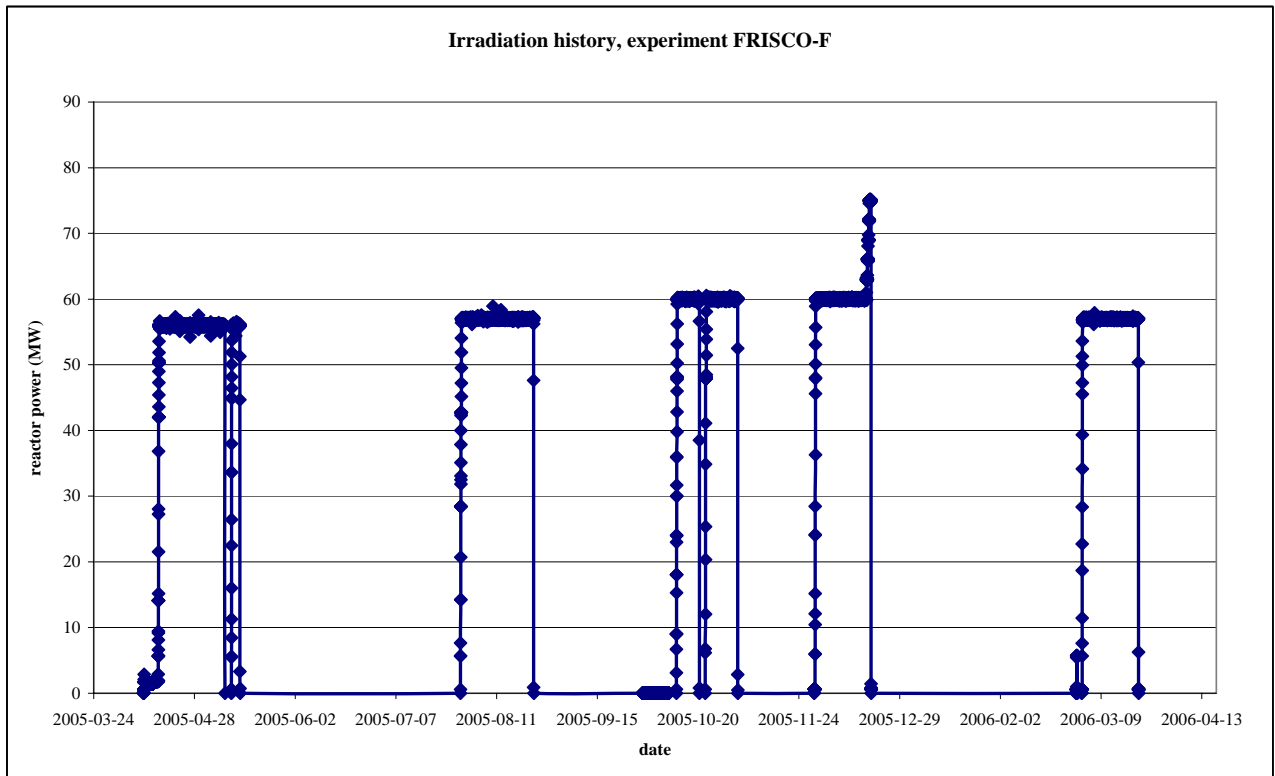


Fig. 3. Irradiation history for experiment FRISCO-F in the BR2 reactor.

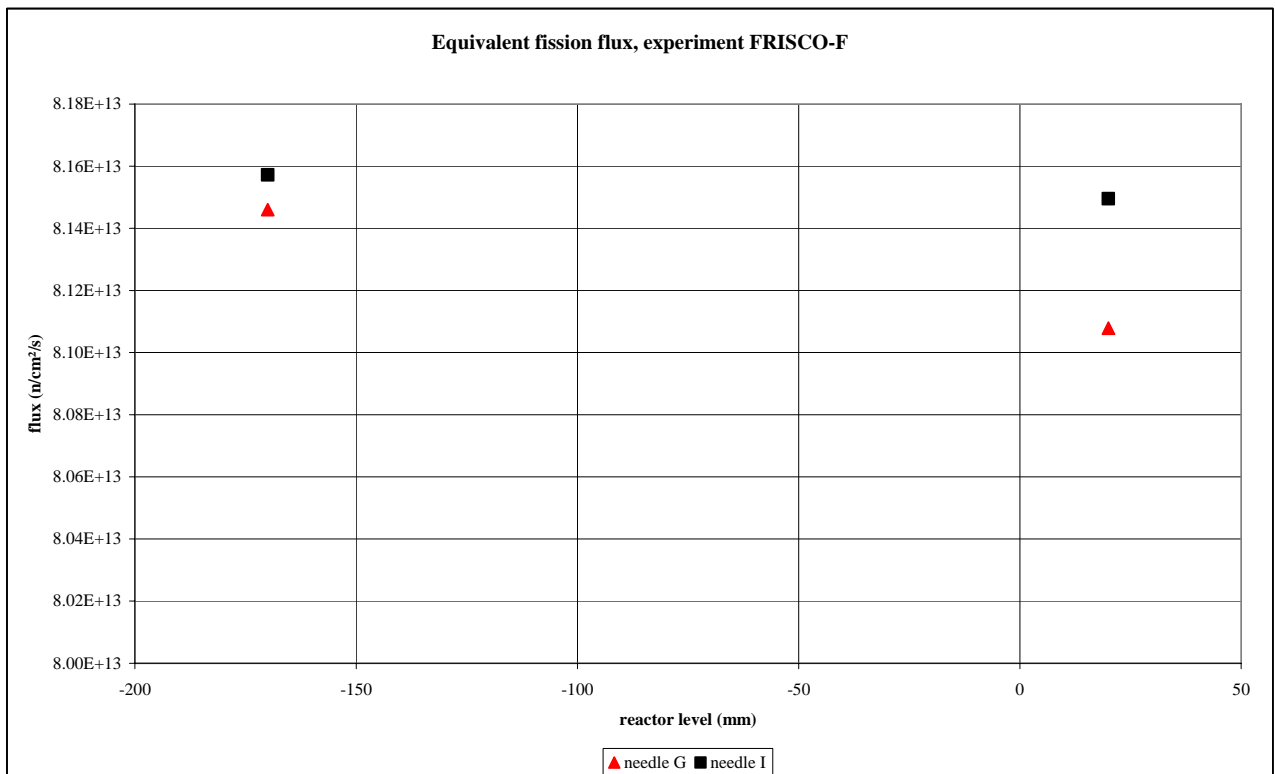


Fig. 4. The equivalent fission flux determined from the activity measurements.